Design and Synthesis of Hierarchical $B_xC_yN_z$ Nanotube Composites

A thesis submitted for the degree of Materials Science

Doctor of Philosophy



Dillon McGurty

Linacre College, University of Oxford

Michaelmas Term – 2023

Dedicated to my family and friends,

Everything I do, I do for you.

“If you don’t know where you’re going,
any road will take you there” **– George Harrison**

Declaration

This thesis is submitted for the degree of Doctor of Philosophy in Materials Science at the University of Oxford. No part of this thesis has been accepted or is currently being submitted for any degree, diploma, certificate or other qualification in this University or elsewhere. I can confirm that the work presented within this thesis is my own work. The use of any external contributions have been suitably indicated.

Abstract

The sub-class of carbonaceous nanomaterials, borocarbonitride nanotubes, have previously demonstrated encouraging performance with regard to a range of applications which include energy storage, electrocatalysis and environmental remediation. The promise they possess makes them suitable candidates for the development of, novel, next-generation hierarchical nanomaterials. Despite this, the field surrounding them has lacked substantial investigation into their further processing. This thesis looks to address some of the current shortcomings within the field and investigates processing techniques for the functionalisation and macroscopic arrangement of borocarbonitride nanotubes.

A two-step, aerosol assisted, synthesis route was developed for the production of borocarbonitride nanotubes. The effect of reaction temperature, heating rate and precursor crystallinity on the boron content of the nanotubes was investigated. The successful synthesis of borocarbonitride nanotubes and their properties, in comparison to the precursor nanotubes, were confirmed using a number of characterisation techniques which included x-ray photoelectron spectroscopy, transmission electron microscopy, scanning electron microscopy, Raman spectroscopy, thermogravimetric analysis and ultraviolet-visible spectroscopy. The importance of nitrogen doped sites, in the precursor material, to the success of the co-doping procedure was established experimentally and through computational modelling. This initial work thus allowed the exploration and development of further processing techniques by producing the borocarbonitride nanotubes on a suitable scale.

Borocarbonitride and nitrogen doped carbon nanotubes were functionalised with iron oxide nanoparticles. This was achieved using *ex situ* methodologies that exploited non-covalent interactions. The nanoparticle loading onto the nanotube was varied through alteration of the solvent medium, allowing for tuneable nanohybrid composition. The effect of solvent on the

nanoparticle loading was rationalised by comparing the results here with dielectric and surface energy-based models from the literature, that had not yet been corroborated for doped nanotubes. Both electrophoretic deposition and vacuum filtration techniques were then explored for the production of macroscopic borocarbonitride nanotube assemblies, with the latter being deemed more suitable. This method was then extended to the production of freestanding films from the borocarbonitride nanotube – iron nanoparticle hybrids.

The work that is detailed in this thesis presents advancements in the processing of borocarbonitride nanotubes, offering routes for converting them into hierarchical nanohybrids and assembling them into freestanding macroscopic arrangements.

Acknowledgements

As with most ventures in life, the completion of this project would not have been possible without the support that has been provided by a host of individuals, who have helped me in a variety of ways during my time as a student at the University of Oxford.

To begin with, I would like to thank Professor Nicole Grobert for offering me the opportunity to join this institute, providing access to the Nanomaterials by Design laboratory and guidance. Samantha Pearce, you have been so helpful in the face of the pandemic with lab organisation and checking on everyone's welfare and for that I am very grateful. I would like to thank Richard Turner and Greg Cook for being so inclusive and supportive during my time in Oxford, whether it be technical advice regarding equipment or to natter about where Richard was headed for the weekend, you both always offered great insight. I would like to thank the Oxford Materials Characterisation Service for access to their equipment, in particular a special thanks to Colin Johnston, Nicola Flanagan, Phil Holdway for their advice, training and hours dedicated to helping with the completion of this project. I would also like to thank the David Cockayne Centre for Electron Microscopy, in particular Neil Young and Ian Griffiths, for access to a variety of their microscopes and for training me to become a proficient microscopist. Thanks are also owed to the Swart Lab for hosting Eoin O'Sullivan whilst conducting the computational calculations.

Many thanks are owed to each of my peers within the Nanomaterials by Design group for making the office and laboratory a diverse and enjoyable place to work and complete my DPhil. In particular, Kai-Ling, Jesus, Ryan, Maya, Ruth & Dominique for offering fruitful conversation and scientific guidance throughout the duration of this project.

During my time at Oxford, I have met a number of people that I now consider friends and I would like to thank Albert, Jack, Pierre, Jasha, Lukas, Eboni, Mario, Sabrina and Lauren. We have shared a lot of good times together which has made my DPhil such an enjoyable experience. In particular, I'm extremely grateful to Pablo Quijano Velasco who has been a source of scientific guidance throughout my project and motivator when imposter syndrome took hold. Additionally, he has taught me an array of Spanish expletives to shout when experiments go wrong and introduced me to carnitas, and for that I'm indebted.

To my closest friends Matty, Hugo, Joel, Will, Tom, Mo and Hollie, thank you for standing by my side during this journey. Things that may seem small, like coming to visit me when I'd moved to a new city or popping out for a meal, meant a great deal to me and helped with adjusting to life in the south and made this a very enjoyable stint for me. While great distances may lie between us all, I have always felt your support and love you all very much.

Eoin O'Sullivan and John Ballentine, you both deserve a separate section, so don't tell the others. We started this journey together four and a half years ago and almost every day since we have spoken about our respective projects. Not only have we learnt how to become independent researchers, but we have also made many amazing memories together, the magnitude of which would warrant a thesis in itself. Holidays, pub-crawls, bops, camping, parties, balls, there's just too many to list. John, my shoes thank you for being a personal chauffer during my time here, without you they'd be in disarray and many of our outings would have been cut short. Also, thank you for bearing broad shoulders that have allowed you to deal with our crude humour. Eoin, thank you for everything. Thanks to you, my iron levels will not be depleted for the foreseeable which is a good thing considering the extensive bodily harm you have caused me over the years. You have been like a brother to me over the past few years and I'm proud to have you as my friend. I am leaving Oxford with two people who I now consider amongst my closest friends and for that, it's all been worthwhile.

To my family, who have always been so supportive throughout my studies, thank you. Aidan and Kieran; you are the funniest and best brothers I could ask for. Thank you for being there for weekends at home when I needed distraction from my worries and you delivered, in spades, with viral internet challenges amongst other things. To my pooches, the ones who started this journey with me, the ones who are no longer with us and the ones we have gained, you will never understand how loved you make me feel and that has always been a phenomenal source of encouragement for me. Mum, thank you for the lifts to and from Oxford, for the pies, for FaceTiming me on a Saturday morning, for our trips to Aldi and so much more. Dad, thank you for the constant proof reading, for texting me during the match, for sorting my internet, for rewatching sitcoms with me and so much more. These may seem like trivial things as parents, but I appreciate every single thing you've done to make my life easier during this project. To you both, thank you for being the most amazing parents and friends. I wouldn't be here without your support, guidance and love.

Finally and most importantly, I would like to thank my now wife, Mimi Yolande Williams. When I embarked on this journey to pursue a DPhil, you selflessly volunteered to uproot yourself and move away from your family and friends. Words can't describe how much that meant to me. Whilst the phrase 'I couldn't do it without you' is perhaps overused, it really does apply here. Whether it be ordering us a Sushi Corner after a long day in the lab and cooking seemed like an unsurmountable task, notes left around the flat, bringing me iced coffees when I had an afternoon of research talks to sit through, listening to me practice my presentations, your constant words of encouragement and unwavering belief in me, when mine disappeared; it all meant so much and I am eternally grateful. We came to Oxford as naïve children fresh out of university. We are leaving as naïve young adults who are about to embark on married life. After our experiences in Oxford together, I can't wait to jump into the next adventure that life has in store, with you.

Publications and Conferences

Ryan Schofield, Barbara Maciejewska, Shiling Dong, George Tebbutt, Dillon McGurty, Ruy Bonilla, Hazel Assender, Nicole Grobert, *Driving Fiber Diameters to the Limit: Nanoparticle-induced Diameter Reductions in Electrospun Photoactive Nanofiber for Organic Photovoltaics.*

Submitted.

Dillon McGurty, Eoin O'Sullivan, Pablo Quijano Velasco, John Ballentine,
Ryan Schofield, Nicole Grobert, *Effect of Solvent Medium on the Production of Hierarchical BCN-NT – Iron Nanoparticle Hybrids.*

Dillon McGurty, Eoin O'Sullivan, John Ballentine, Kai Ling NG, Nicole Grobert, *Two-Step Aerosol Assisted Synthesis of Structurally Uniform $B_XC_YN_Z$ Nanotubes: Tuning Properties via Co-Doping*

In preparation.

'$B_XC_YN_Z$ Nanotubes: Introductory Research Talk', University of Oxford – Imperial College London Mingle, June 2019.

'Two-Step Aerosol Assisted Synthesis of Structurally Uniform $B_XC_YN_Z$ Nanotubes: Tuning Properties via Co-Doping', International Conference on the Science and Application of Nanotubes and Low-Dimensional Materials, Rice University, June 2021.

Contents

Declaration i

Abstract ii

Acknowledgements iv

Publications and Conferences vii

Chapter 1: Introduction 1

Introduction 2

1.1. Carbon Nanotubes 4

1.1.1. Background to Carbon Nanotubes

1.1.2. Properties and Applications of Carbon Nanotubes

1.2. Processing of Carbon Nanotubes 11

1.2.1. Modified Carbon Nanotubes

1.2.2. Hierarchical Carbon Nanotube Structures

1.2.2.1 CNT-Polymer Hybrids

1.2.2.2 CNT-Graphene Hybrids

1.2.2.3 CNT-Nanoparticle Hybrids

1.3. Introduction to BCN Nanotubes: Potential Applications and Current Outlook 20

1.4. Thesis Aims and Outline 24

Chapter 2: Methods 26

2.1. Introduction 27

2.2. Characterisation of BCN-NTs and BCN-NT - Nanoparticle Hierarchical Nanostructure 27

2.2.1. Scanning Electron Microscopy

2.2.2. Transmission Electron Microscopy

2.2.3. X-ray Photoelectron Spectroscopy

2.2.4. Energy Dispersive X-ray Analysis

2.2.5. Raman Spectroscopy

2.2.6. Ultraviolet - Visible Light Spectroscopy

2.2.7. Thermogravimetric Analysis 3

2.3. Characterisation of BCN-NTs Macrostructures and Iron Nanoparticles 38
2.3.1. Brunauer-Emmett-Teller Analysis
2.3.2. Four Point Probe Analysis
2.3.3. X-ray Diffraction and Dynamic Light Scattering

Chapter 3: Two-Step Synthesis of Boron & Nitrogen Co-Doped CNTs **44**

3.1. Introduction 45
3.1.1. Synthesis of BCN-Nanotubes
3.1.1.1. Arc-Discharge
3.1.1.2. Chemical Vapour Deposition
3.1.1.3. Pyrolytic Techniques
3.2. Materials and Methods 57
3.2.1. Chemicals
3.2.2. Characterisation
3.2.3. Synthesis of Multiwalled Nitrogen-Doped Carbon Nanotubes
3.2.4. Synthesis of Carbon Nanotubes
3.2.5. Synthesis of Multiwalled Borocarbonitride Nanotubes
3.2.6. Synthesis of Multiwalled Boron-Doped Carbon Nanotubes
3.3. Results and Discussion 61
3.3.1. Synthesis of BCN-NTs
3.3.1.1. SEM and TEM Analysis
3.3.1.2. Elemental Analysis of BCN-NTs
3.3.2. Computational Study of BCN Bonding Sites
3.3.3. Effect of Co-Doping on Crystal Structure
3.3.4. Effect of Co-Doping on Optical Properties
3.3.5. Effect of Co-Doping on Oxidation Resistance
3.3.6. Effect of Reaction Variables on Boron Doping
3.3.6.1. Reaction Temperature
3.3.6.2. Precursor Crystallinity
3.3.6.3. Heating Procedure
3.4. Conclusions 91

Chapter 4: Developing Methods for the Synthesis of Doped CNT – Nanoparticle Hybrids: The Effect of Solvent Medium 92

4.1. Introduction 93

4.1.1. Synthesis of Hierarchical Nanotube – Nanoparticle Composites

4.1.1.1. In-Situ Synthesis Techniques

4.1.1.2. Ex-Situ Synthesis Techniques

4.1.1.3. Synthesis Techniques for BCN-NT Hierarchical structures

4.2. Materials and Methods 106

4.2.1. Chemicals

4.2.2. Characterisation

4.2.3. Synthesis of Nitrogen-Doped & $B_XC_YN_Z$ Nanotubes

4.2.4. Synthesis of Iron Oxide Nanoparticles

4.2.5. Synthesis of Polymer/N-CNT Hybrids

4.2.6. Synthesis of Iron Oxide NP/BCN & N-CNT Hybrids

4.2.7. Effect of Solvent on Iron Oxide NP/BCN-NT & N-CNT Hybrids

4.2.8. Effect of Destabilising Agent on Iron Oxide NP/N-CNT Hybrid

4.2.9. Effect of Polymer Coating on Iron Oxide NP/N-CNT Hybrid

4.3. Results and Discussion 112

4.3.1. Synthesis of Iron Oxide Nanoparticles

4.3.2. Synthesis of Iron Oxide NP/N-CNT Hybrids

4.3.2.1. Standard Conditions

4.3.2.2. Effect of Solvent on Functionalisation

4.3.2.3. Effect of Destabilising Agent on Functionalisation

4.3.2.4. Effect of Polymer Additive on Functionalisation

4.3.3. Synthesis of Iron Oxide NP/BCN-NT Hybrids

4.4. Conclusions 142

Chapter 5: Macroscopic Assemblies of $B_XC_YN_Z$ Nanotubes 145

5.1. Introduction 146

5.1.1. Electrophoretic Deposition for CNT Films

5.1.2. Vacuum Filtration for CNT Films

5.2. Materials and Methods 156

5.2.1. Chemicals

5.2.2. Characterisation

5.2.3. Synthesis of Nanotubes

5.2.4. Oxidation of CNTs
5.2.5. Electrophoretic Deposition of Oxidised CNTs
5.2.6. CVD Functionalisation of Oxidised CNT Films
5.2.7. Dispersion of BCN-NTs in Common Laboratory Solvents
5.2.8. Production of Nanotube Dispersions & Buckypapers
5.2.9. Production of $B_XC_YN_Z$-FeO_xNP Hybrid Buckypapers
5.3. Results and Discussion 162
5.3.1. Part 1: Electrophoretic Assisted Production of Macroscopic BCN-NT Films
5.3.1.1. Oxidation of CNTs
5.3.1.2. Electrophoretic Deposition of CNTs
5.3.1.3. Attempted Conversion of CNT to BCN-NT Film via CVD
5.3.2. Part II: Vacuum Assisted Production of Macroscopic BCN-NT Films
5.3.2.1. Optimisation of Nanotube Dispersion in Common Solvents
5.3.2.2. Production of BCN-NT Film via Vacuum Filtration
5.3.2.2.1. Overview of BCN-NT Films
5.3.2.2.2. Properties of BCN-NT Films
5.3.2.3. Production of BCN/FeO_xNP Film via Vacuum Filtration
5.4. Conclusions 190

Chapter 6: Summary and Potential Future Work 193

Bibliography 201

Appendices 216

Chapter 1

Introduction

Introduction

The study of nanomaterials, or nanoscience, refers to the design, manipulation and understanding of matter on the *nano* scale. The *nano* prefix is derived from the Greek word *νᾶνος* which has the translation 'dwarf'. The modern-day definition of a nanomaterial describes something that is composed of particles, that account for over half the total composition, possessing at least one dimension on the nanoscale; where the term 'nanoscale' refers to a measurement of 1 to 100 nm.[1] Human interest regarding the nanoscale has been documented throughout history and perhaps derives from ancient philosophy, such as Leucippus' theory of atomism. The bottom up-approach to material design draws parallels with his theories, in principle. Examples of nanomaterials have appeared throughout history, for instance the Lycurgus cup and medieval church windows. Many view Faraday's "divided state of gold" synthesised in 1856, as the birth point of experimental nanoscience. Despite this, it wasn't until the early 1980's that modern nanomaterial research really took off. The advancements within this field coincided with developments being made to characterisation techniques, such as microscopy, which allowed visualisation and further understanding of these nanomaterials.[2]

Carbon nanotubes (CNTs) are a class of one-dimensional carbonaceous nanomaterial. The origin of these CNTs is a topic that is often subject to debate. Mentions of nanotube-like carbonaceous materials date back as early as the 1950's, whilst recent studies have shown that CNTs existed within ancient pottery.[3, 4] Generally, however, the report by Iijima in 1991 is attributed with their dissemination throughout the wider scientific community.[5] Following on from Iijima *et al.*'s work, an enormous upturn in research regarding carbonaceous nanomaterials was observed. The subsequent experimental and theoretical work concluded that CNTs are promising candidates for a variety of potential applications which includes

thermal management, energy storage, catalysis, electronics and medical, amongst others.[6-10] Three decades on from the initial promise and excitement that was promoted by this field of study, CNTs remain a popular area of material science research. However, advancements and alterations to the materials first reported have been made. These adjustments have often been offered through the chemical modification, such as heteroatom doping, of regular CNTs.[11] Further to this, through the interlinking of CNTs with additive materials, additional functionality can be introduced, essentially allowing the properties of the hybrid materials to be tuned for specific applications.[12] Research has also increasingly looked towards designing macroscopic arrangements of these nanomaterials, that would ease handling and allow their implementation in everyday products.[13]

Borocarbonitride nanotubes (BCN-NTs) are a sub-class of carbonaceous nanomaterial that can be essentially viewed as CNTs co-doped with boron and nitrogen, simultaneously. Alterations to their chemical composition allow various properties to be tuned and like regular CNTs, BCN-NTs have been considered for a number of applications such as energy storage devices, electrocatalysis and electronics.[14-16] Despite the promise these BCN-NTs have displayed within several fields of application research, their widescale implementation remains limited. Additionally, when compared to regular CNTs and even uni-doped CNTs for that matter, research into the processing of BCN-NTs remains comparatively trivial. This lack of study may be attributed to the absence of availability on a commercial scale and other practical considerations. This thesis looks to address some of the shortcomings within the field of BCN-NTs studies. More specifically we are looking to develop and understand further processing techniques for these BCN-NTs, attempting to functionalise them and implement them on the macroscale in the process. This first chapter looks to serve as a basic guide for the reader, introducing them to the field of CNTs before then moving on to

discussing some of the existing techniques used for their processing. Finally, we will touch on the subject of BCN-NTs and their potential applications.

1.1. Carbon Nanotubes

1.1.1. Background to Carbon Nanotubes

A graphene sheet is a nanomaterial made up of a sp^2 hybridised carbon network, that is arranged in a hexagonally ordered layer. In pristine graphene, each carbon atom is attached to three other carbons. In its simplest form, a CNT is a carbon allotrope that can be considered as a graphene sheet that has been 'rolled up' into a cylindrical formation. This results in the observed tubular structure. Additionally, helicity arises due to the curvature of the graphene sheet. A schematic diagram of a CNT, formed from a rolled graphene sheet, is shown in Figure 1.1(a). The orientation in which the sheet is 'rolled' determines whether the structure of the CNT is in either a chiral, armchair or zig-zag formation.[17] The CNT structure is therefore defined by the chiral vector and the chiral angle exhibited by the CNT, in relation to the hexagonal network of carbon atoms. The chiral vector can be characterised by the symbols *n* and *m* which refer to vectors along the hexagonal lattice. The criteria for each type of nanotube are as follows; the armchair configuration occurs when n = m, zig-zag when m = 0 and for every other value, chiral nanotubes arise.[18] The resulting CNT type influences properties such as if the nanotube is metallic or semiconducting. CNTs are referred to as one-dimensional nanomaterials, as one of the material dimensions falls within the range of 1 – 100 nm.[19] The length of these nanotubes are often significantly greater than their corresponding diameter, which affords their high aspect ratios. The end of these tubular structures are often capped with a structure that is akin to a bisected buckyball. The presence of five membered rings can promote the CNT closure and are attributed to the presence of breaks in the sp^2 graphitic network at the terminal points.[20] CNTs consisting of a single

carbon layer are referred to as a single walled CNTs (SWCNTs). These are not the only type of nanotube, however. Concentric carbon layers can form around a central nanotube structure and where this occurs, the resulting CNTs are referred to as multi walled CNTs (MWCNTs).

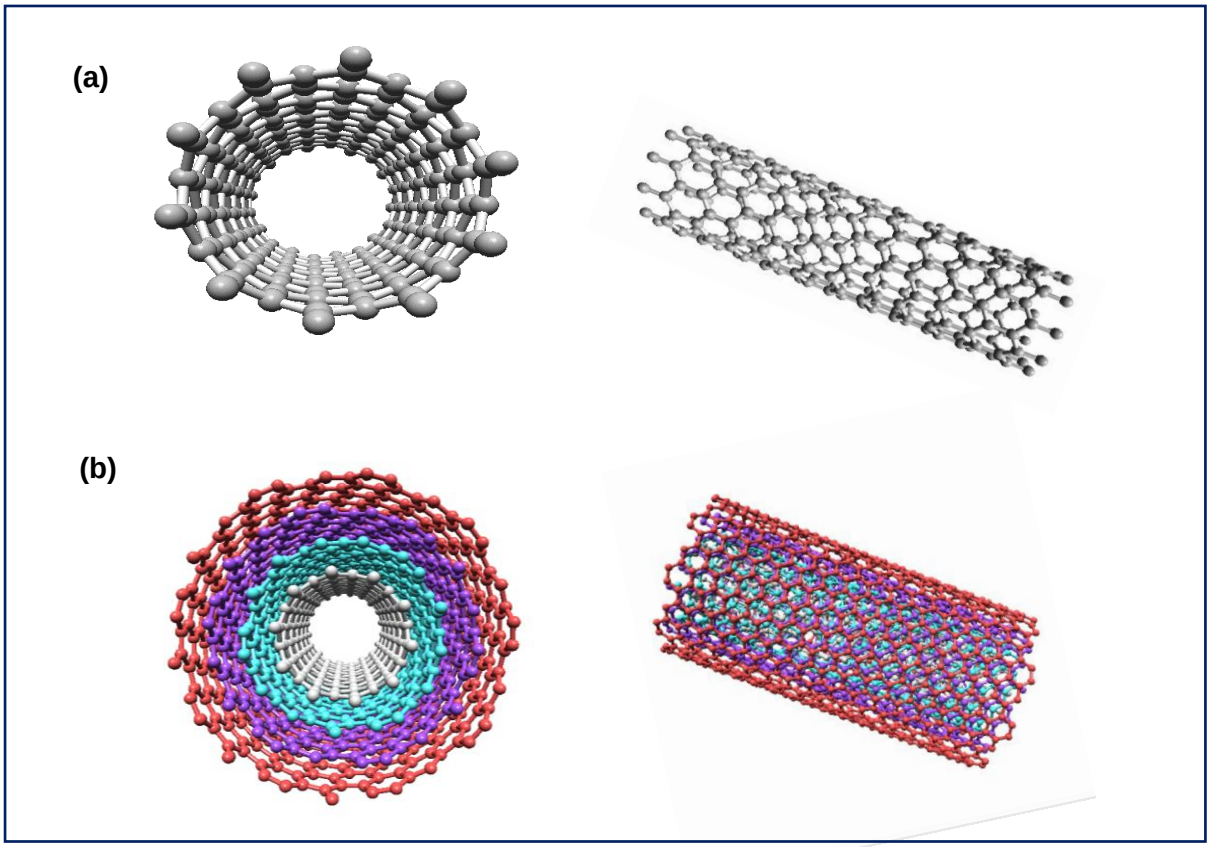


Figure 1.1: Schematic diagram showing pristine SWCNTs (a) and MWCNTs (b) from an internal and side profile view.

These MWCNTs, shown schematically in Figure 1.1(b), typically have a broader diameter than their single walled counterparts. There are a number of strategies that have been developed for the synthesis of CNTs which can include arc-discharge, chemical vapour deposition (CVD) and laser ablation, amongst others.[21-23] Depending on the synthesis route selected and the reaction conditions, we can select which type of nanotube, be it SWCNT or MWCNT, that is synthesised. Typically, the upscaling of SWCNT synthesis is more difficult when compared to that of MWCNTs.[18] The synthesis strategy employed will also influence

the purity of the product obtained and can be used to fine tune morphological properties of the nanotube such as length and diameter.

Like most things in life, perfect CNTs exist only in theory. Instead, CNTs often possess imperfections within their crystal structure known as defects. The quality of a CNT may be defined by the level of defects that are present within the structure. Whilst they can be detrimental to some properties, defects are desirable in some cases and are often intentionally introduced into the nanotube structure, post-synthesis.[24] Depending on the desired application therefore, the defective nature of CNTs is an important consideration. Defects can occur in various forms throughout the nanotube structure. Broadly speaking, these can be classified into four major categories; topological, bonding, hybridisation and elemental dopant defects.[25] The presence of these various defect types can influence the nanotube properties. Topological defects refer to the presence of five and seven membered rings, which promote disruption to the CNTs hexagonal lattice. Where a heptagon and pentagon appear adjacent to each other, the resulting site is known as a Stone-Wales defect.[26] The presence of these topological defects, within the carbon lattice, can promote areas of high strain and tube curvature.[27, 28] Bonding defects refer to gaps and breaks within the crystallographic bonding system. These defects may appear as dislocations, vacancies, interstitials, or as a combination, within the hexagonal lattice.[25, 29, 30] Hybridisation defects refer to the hybridisation state of carbon within the CNTs structure. In an ideal CNT system, all the carbon would be sp^2 hybridised. Rehybridisation, between the sp^2 and sp^3 states of carbon, can occur within CNT structures, however. Where a sp^3 carbon arises, a defect within the structure is present. As mentioned previously, researchers often introduce defects onto the CNT surface intentionally, the resulting type is most commonly a hybridisation type defect. Typically these sp^3 defects involve the carbon atom being bonded with an oxygen-containing or amine functional group on the exterior of the lattice.[31] Elemental dopants act as

substitutional impurities with a carbon lattice, the introduction of heteroatoms therefore introduce defects into CNTs. Intrinsically this makes doped CNTs more defective than their undoped counterparts. As we will see throughout this thesis, the presence of heteroatoms (such as boron and nitrogen) is often desired in CNT research and the resulting defective nature can be exploited.

1.1.2. Properties and Applications of Carbon Nanotubes

CNTs are renowned for possessing a number of unique properties that make them suitable for a host of applications. These properties are dictated by the type, quality and purity of CNT. Here we elucidate some of these interesting properties, in a more general sense to give the reader an overview of the unique characteristics of CNTs. Table 1.1 summarises these nanotube properties. Additionally, we look to highlight relevant applications that have been investigated due to said properties.

One of the most striking and obvious unique features of CNTs is the large length to diameter ratio they exhibit. This is otherwise known as a high aspect ratio. This property is related to the morphology of the nanotube itself and can be tuned through altering the diameter or type of nanotube (*i.e.* single or multi walled). Additionally, as with most nanomaterials, CNTs often possess very large surface areas. High aspect ratios are desirable for a host of applications as it means the benefits of CNTs can be typically exploited at relatively low loadings when used as an additive material. A material with lower aspect ratios would require higher loadings to achieve the same benefits displayed by CNTs. This effect has been demonstrated through tuning of the CNT aspect ratio.[32] When the aspect ratio of the CNTs were increased, improvements made to polymer composites were more significant than for lower aspect ratio CNTs. A number of applications also find the high surface area of CNTs

an extremely desirable property. Whilst a benefit for many applications, the high aspect ratios and surface areas, also contribute to the bundling of CNTs, a phenomena observed which can make them difficult to disperse.

Table 1.1 – A summary of physical properties displayed by CNTs that typically vary throughout the literature

Property	SWCNT	MWCNT
Structure	Single cylindrical carbon layer	Concentric carbon layers
Diameter	*ca.* 0.4 – 5 nm[33]	*ca.* 5 – 100 nm[34]
Length	*ca.* 10 nm[35] – 20 cm[36]	*ca.* 0.2 mm[37] – 3 mm[38]
Mechanical	Tensile Strength – up to 66 GPa[39]	Tensile Strength – up to 63 GPa[40]
Electrical	Metallic or Semiconducting[25]	Metallic and/or Semiconducting[41]
Thermal	Conductivity – 3500 W/m K[42]	Conductivity – 3000 W/m K[43]
Visual Appearance	Grey/Black	Grey/Black

The ‘honeycomb’ lattice of hexagonally arranged carbon atoms in CNTs are bridged by some of the strongest covalent bonds displayed in chemistry, which gives rise to a range of potentially excellent mechanical properties. For example the Young’s modulus displayed by CNTs, which is a mechanical property that relates to the ease in which a material is deformed, has been studied in great detail. The values reported for the Young’s modulus of CNTs can vary within the literature depending on the type of nanotube (single or multi - walled) or the type of study (theoretical or experimental based). In general however, the reported values are very large in comparison to other materials and typically fall around the 1.0 TPa value.[44-47] The tensile strength of a material refers to the amount of stress that can be

applied to a material before the breaking point is reached. Until recently, a tensile strength of 63 GPa that had been recorded for MWCNTs was the largest value recorded for any material.[40] This has recently been exceeded by a value of 66 GPa which has been recorded for SWCNTs.[39] As can be seen, the values reported for the tensile strength are found to vary within the literature depending on the nanotube type, as they do with Young's modulus. Despite this, the values reported are typically large and in terms of tensile strength, CNTs can be considered amongst the strongest materials to exist.[34] Due to the properties mentioned above, CNTs have been considered for a number of applications where mechanical reinforcement may be desired. There have been many efforts to incorporate CNTs into polymer composites. Examples of these include inclusion into polyvinyl acetate, polystyrene and polymethyl methacrylate composites, amongst others.[48-51] A review by Coleman *et al*.[52] provided a comparison of the reinforcements achieved by the addition of CNTs and highlighted the variation between composite and nanotube type as well as processing techniques. The presence of defects can diminish the intrinsic mechanical properties of CNTs which means that the quality of nanotube must be considered for specific applications.[34] Research into these CNT – polymer composites has reached a stage where there has been significant effort into processing these composites on the macroscopic scale, in the form of nanotube films.[53]

In addition to outstanding mechanical properties, CNTs are often hailed for their electronic properties. The electrical properties displayed by CNTs depend on a host of structural characteristics. Due to the bonding network, each of the carbon atoms in the hexagonal lattice possess a free outer electron that is available for conduction.[54] As mentioned previously, there are many types of CNT that can form depending on how the graphene sheet is rolled, ultimately relating to the chiral vector. Depending on the type of the nanotube, therefore, CNTs can fall into the category of semiconductors or metallic objects. In addition to chirality,

the nanotube diameter, composition and presence of defects can also influence the electronic properties of CNTs.[25] As such, individual CNTs have displayed excellent electrical conductivities up to 10^7 S/m, which is on the order of Cu and Au metal.[54] This value is typically lower for bulk CNTs, however, but still on the order of 10^4 S/m.[55] As a result of these excellent properties, CNTs are seen as attractive material candidates for a number of electronic applications. These can broadly be categorised into nanoelectronics and energy storage devices. For example, due to their conductivity, surface area and ability to intercalate, CNTs have been investigated as potential electrode materials for lithium ion batteries.[56] In particular, they have been investigated as potential scaffold networks, used to support high capacity active materials, as a result of their electrical conductivity.[57] The high aspect ratios of CNTs means that a relatively low mass loading of material is required to form a conductive support network, which is desirable for energy storage devices. As well as lithium batteries, CNTs are also seen as ideal candidates for other energy storage devices such as supercapacitors and further types of high energy density batteries.[58, 59] Where nanoelectronics are concerned, the high electrical conductivities and carrier mobilities have seen CNTs explored for use in field effect transistors which themselves have a host of applications which include chemical sensors and radio frequency devices.[60] Furthermore, due to the requirements of electrode materials (*i.e.* high electrical conductivity and surface area), CNTs have been considered as metal-free and catalyst supports in a variety of electrocatalytic applications.[61]

As far as thermal characteristics are concerned, CNTs are once again known to exhibit exceptional properties. The thermal conductivity of individual MWCNTs has been recorded at *ca*. 3000 W/m K which is higher than the carbon allotropes graphite and diamond.[43] Further to this, SWCNTs have displayed even more impressive thermal conductivities that approach 3500 W/m K.[42] This excellent thermal conduction observed in CNTs predominantly occurs through a phonon transport mechanism which is afforded by the sp^2 hybridised carbon

network.[62, 63] Together with the thermal conductivity they display, CNTs are also thermally stable at elevated temperatures. In air, the oxidation resistance typically ranges from *ca*. 400 – 700 ^{o}C for CNTs.[64, 65] Similarly, under an inert atmosphere, they can display structural stability at temperatures ranging from 1300 – 2000 ^{o}C, depending on the nanotube type.[66, 67] Like the other physical properties reported thus far, the thermal characteristics of CNTs are strongly affected by a number of nanotube parameters such as the diameter and morphology.[68] For example, the presence of defects have been found to facilitate the oxidation procedure and thus, reduce the thermal resistance of CNTs.[65] Once again, this highlights the importance of considering the CNT type and processing techniques when looking towards CNT applications. These potential applications may include thermal management devices and epoxy – composites that look to exploit the promising thermal properties that CNTs possess.[69]

1.2. Processing of Carbon Nanotubes

1.2.1. Modified Carbon Nanotubes

As has been established, carbon nanotubes typically consist of a pristine graphitic structure and display a number of unique properties. Despite the promise that regular CNTs have demonstrated for a host of applications, since their advent, there have been numerous research efforts that attempted to tune the properties of the nanotubes. The logical approach to tuning the properties of these CNTs came in the form of modifying their structure. Through alterations to the structure, the chemistry and properties of the CNTs could be altered. This can be achieved through various means, such as physical and chemical

treatments of the CNTs. The following sub-section will introduce some of the commonly employed techniques that are used in the modification of CNTs.

Perhaps the earliest, and most commonly employed, technique for the modification of CNTs involves treatment with chemicals. CNTs are notoriously difficult to disperse in a range of solvents, owing to their surface chemistry properties, resulting from the sp^2 hybridised carbon network they possess.[70] As-synthesised CNTs typically exist in a bundled form due to the Van der Waal forces experienced between them and their high aspect ratios which can drive aggregation, as a means for lowering the surface energy they experience.[71, 72] Poor dispersion and the aggregation of CNTs can hinder their performance when implemented in various applications, such as polymer composites.[53] Additionally, for applications such as electrocatalysis, activity is believed to be promoted at defect sites.[61] These chemical treatments were therefore developed in an attempt to activate the surface chemistry of CNTs and enhance their dispersibility in common laboratory solvents. Through a variety of chemical treatments, the sp^2 carbon bonding network can be disrupted and the CNTs can therefore be covalently modified. Covalent modification, thus, allows the introduction of functional groups that assist in the dispersion of CNTs.

The most common type of wet chemical modification involves the acid treatment of CNTs. Originally, this procedure was used in the purification of CNTs post synthesis. The oxidative character of the acids resulted in by-reactions that introduced oxygen – containing groups onto the surface of the nanotubes. A variety of oxidative acids have been utilised for this procedure which include nitric acid, sulphuric acid, a combination of the two and much weaker acids such as hydrogen peroxide.[73-75] In general, this type of acid treatment will incorporate oxygen – containing organofunctional groups, such as carboxyl, alcohol, ether and other forms of carbonyl groups on the sidewalls of the CNTs.[76] In each case, the presence of these oxygen groups improve the dispersion of CNTs in common solvents. Using this wet

chemical approach, the level of oxidation achieved can be tuned relatively easily by altering simple reaction parameters that include the acid concentration, reaction time and temperature.[77, 78] In addition to acid etching, oxygen – containing functional groups can be introduced through the use of other oxidising agents like potassium permanganate, or through controlled thermal oxidation.[79, 80] The oxygen functional groups can be utilised further than just aiding the dispersion of nanotubes. In particular, the carbonyl groups can act as sites for organic reactions to occur, as they would in standard chemistry. For example, carboxyl groups can undergo conversion through esterification, thioesterification and amidation.[81] Figure 1.2 demonstrates the oxygen functionalities that can be incorporated into a nanotube structure and how these can be modified further to introduce a range of functional groups on the nanotube surface.

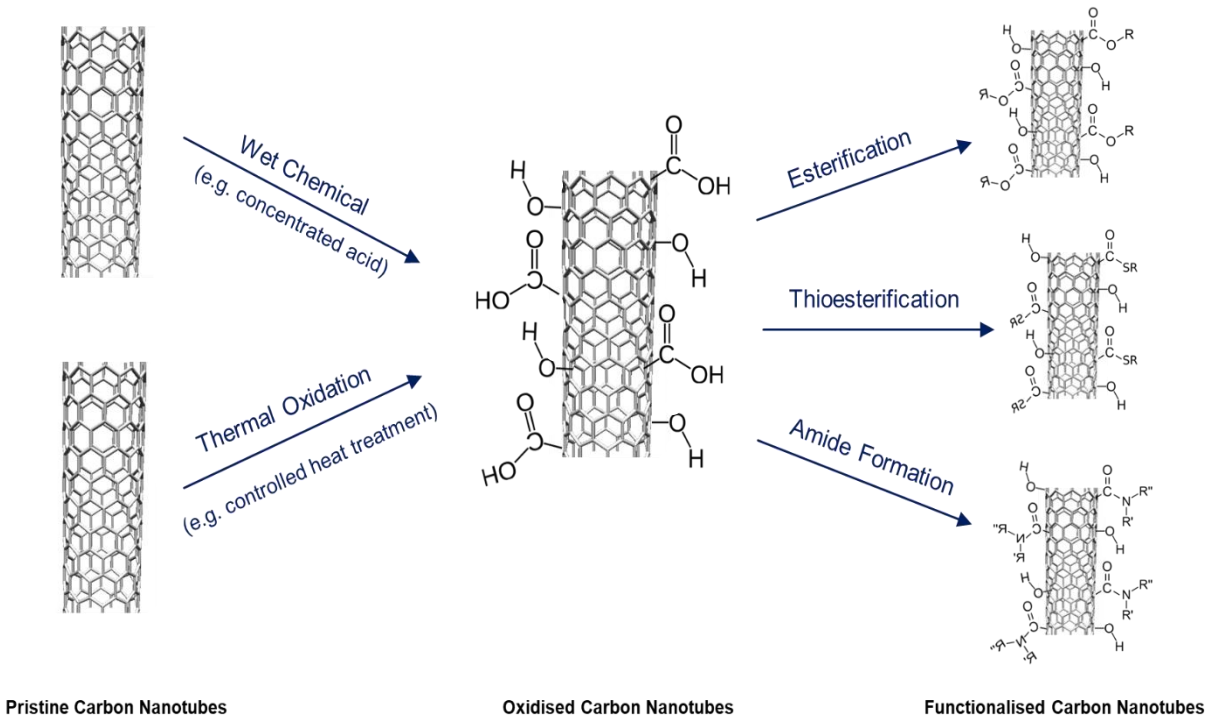


Figure 1.2. An overview of some of the reaction pathways available to introduce covalent functionalities on the surface of carbon nanotubes through chemical procedures.

Similar to oxygen containing groups, CNTs can be modified with other types of surface functionalities through chemical approaches. For example, nitrogen containing side groups can be introduced onto CNT surfaces through a wet chemical procedure that involves a reaction with the organolithium compound, lithium amine.[82] As with oxygen groups, the amine functionalities can be utilised for further chemical derivatisation. Similarly, solvent free reactions with amine reagents can take advantage of intrinsic defects on the nanotube surface to incorporate amine functionalities that once again enhance the dispersion of CNTs in solvents.[83] It is important to note that surface activation is not always required and, under the right conditions, CNTs can participate in a number of chemical reactions that introduce surface functional groups. These reactions may include radical additions, halogenation and cycloadditions.[81]

Further to chemical treatments that introduce functional groups, the surface structure of CNTs can be modified through the introduction of heteroatoms into the graphitic lattice that substitute for carbon atoms. As has been mentioned in the previous section, heteroatom sites incorporated into the carbon honeycomb essentially act as defects in the crystal structure which can alter the surface properties of the nanotube. Depending on the electron donating or accepting nature of the heteroatom, the dopants atoms may be considered as n or p type, respectively. These dopant atoms are predominantly introduced into the nanotubes lattice during the growth step but can also be added through further treatment of the nanotubes, post-synthesis.[84] By far, the most commonly incorporated heteroatom dopant into CNTs is nitrogen. The atomic radii of a nitrogen atom is similar to that of carbon which allows substitution to occur fairly readily. There have been a number of methodologies used to introduce nitrogen into CNTs. For the synthesis of nitrogen doped CNTs (N-CNTs) *via* arc-discharge, dopant atoms can be introduced through two main strategies; either through the incorporation of nitrogen containing compounds into the arcing electrodes, or by utilising a

nitrogenated atmosphere during the synthesis of the nanotubes.[85, 86] Where CVD is concerned, dopant atoms can be introduced through the use of nitrogen containing organic compounds, such as pyridine and its derivatives.[87, 88] Further to this, reactive nitrogen containing gases, like ammonia, can be used during the CVD growth process to dope the CNTs.[89] This can also be achieved by reacting ammonia with pre-formed CNTs, *ex-situ*, through a substitution reaction.[90] The incorporation of nitrogen into N-CNTs has been extensively studied and as such, the dopant content can be tuned by modifying synthesis parameters like reaction temperature and flow rate, for example.[89] It is important to investigate the effect of these reaction parameters on doping when exploring new synthesis techniques as it allows modification of dopant levels and ultimately, nanotube properties. Various types of nitrogen doping configuration exist within the carbon network; these are exemplified schematically in Figure 1.3. As with nitrogen, the atomic radius of boron is comparable to that of carbon and as a result, has also been extensively studied as a heteroatom dopant within CNTs. The strategies used to produce CNTs doped with boron are analogous to that of N-CNTs; with nitrogen containing reagents being replaced with boron alternatives (*i.e.* pyridine for triethyl borane and ammonia for diborane).[91, 92] Due to the contrasting nature of boron and nitrogen dopants, as we will see throughout this Thesis, there have been efforts to build on uni-doping which concerns introducing both dopants simultaneously, yielding BCN-NTs. These BCN-NTs look to utilise the synergistic effects that may arise through the incorporation of two types of dopant, simultaneously. The rationale for co-doping with boron and nitrogen will be discussed further in section 1.3. Aside from boron and nitrogen, a plethora of other heteroatoms have been investigated as potential dopants for CNTs. These dopants may include oxygen, sulphur and phosphorus, amongst many others.[84, 93] The doping of CNTs is an interesting area of research as the introduction of dopant atoms can alter the properties of nanotubes. For example, dopants have been shown to

activate the surface of CNTs for catalytic reactions, modified electronic properties and enhance surface chemistry for dispersion in solvents.[93]

1.2.2. Hierarchical Carbon Nanotube Structures

Whilst technically still a form of modified CNT, this next section refers to hierarchical nanotube structures, where an additive material has been attached to the nanotube in order to introduce additional functionality. These consist of, at least, two discrete phases that are composed from different materials. Here we will briefly introduce examples of these hybrid materials, an overview of the techniques used to produce them and some of their applications; a more detailed account of the synthesis routes available for nanoparticle – CNT hybrids will be provided as an introduction to Chapter 4, where the main focus is on producing this type of composite material.

After exploring ways to chemically modify CNTs, the most apparent research progression seemed to follow fusing supplemental materials with CNTs. The resulting products are generally referred to as hierarchical nanostructures or nanocomposites. Broadly speaking, construction of these materials can be achieved through the manoeuvring and coupling of individual nano-components, or by way of spontaneous organisation.[94] Throughout the work presented in this thesis, the latter approach is utilised for the production of these nanocomposites and as such we will focus on discussing self-assembly routes here. These additive materials differ from the chemical functional groups introduced onto nanotube surfaces, that were discussed in 1.2.1, and typically are a completely separate structure that is affixed to the nanotube. That being said, many research efforts utilise these functional groups for the effective coupling of these materials.

1.2.2.1. CNT – Polymer Hybrids

An early example of these hierarchical nanotube structures, and perhaps the most well studied, are polymer – CNT composites. These can be produced through covalent or non-covalent methodologies, with each typically involving wet-chemical processing. The former takes advantage of chemical groups on the nanotube surface, that have been covalently introduced, to attach the polymer or through direct reaction as detailed in the aforementioned text.[81] For example, covalently introduced carboxylic groups can be converted to acyl chlorides that undergo reaction with amine or hydroxyl – terminated polymers.[95] This route has yielded CNTs coated in polymer chains that aid dispersion and is referred to as the *grafting to* approach for polymer attachment. Alternatively, polymer chains can be formed on the surface of nanotubes through the covalent attachment of precursors, which is known as the *grafting from* approach. Polyethylene, for example, has been polymerised directly on the surface of CNTs after attaching reagents to oxygen containing functionalities on the nanotube.[96] Non-covalent polymer coating methodologies rely on the adsorption or wrapping of polymers on the nanotube surface which are moderated by non-covalent interactions. A common polymer utilised for non-covalent attachment is polystyrene, which interact with CNTs through π-π stacking.[97] This interaction is afforded by the aromatic ring component of the molecule and as such, other aromatic containing polymers, such as polyvinylpyridine, are suitable for non-covalent attachment to CNTs.[97] Depending on the type of polymer that is attached to the CNT, a variety of potential applications can be pursued for these nanocomposites, such as chemical sensors, biomedical devices and optoelectronics, amongst others.[98-100]

1.2.2.2. CNT – Graphene Hybrids

Since its discovery in 2004, there have been attempts by researchers to couple graphene, along with its oxidised equivalent, to CNTs.[101, 102] These hybrids look to combine some of the unique and excellent properties each of these carbonaceous materials possess. Graphene – CNT hybrids have been produced though a variety of techniques. For example, in a strategy similar to that used for polymer – CNT composites, graphene was coupled to the surface of CNTs using a wet-chemical procedure.[103] Graphene, that had been prepared *via* thermal reduction of graphene oxide, was coupled to oxidised CNTs through π-π stacking interactions experienced between the graphene sheet and nanotubes. The use of polymers has been explored as a mediator molecule that facilitates the coating of CNTs with graphene layers.[104, 105] Elsewhere, these graphene – CNT hierarchical nanostructures have been produced through CVD based, self-assembly routes. CNTs carpets have been grown on and covalently coupled to graphene sheets through successive deposition processes, for instance.[106] This has also been achieved when reversing the order of deposition (*i.e.* graphene growth on nanotubes), albeit with less significant adhesion between the carbon allotropes when compared to the covalent linkage the former method afforded.[107] The unique, synergistic properties afforded by these all-carbon nanocomposites has resulted in potential use within dye-sensitised solar cells, supercapacitors and optoelectronic devices, as well as a number of other applications.[102, 103, 105, 107] As we will see in the following section, CNTs can be conjoined with other carbon allotropes such as fullerenes and graphitic nanoparticles.

1.2.2.3. CNT – Nanoparticle Hybrids

A nanoparticle is generally considered as an object that does not exceed 100 nm in size. The properties of nanoparticles are distinct when compared to their bulk counterparts, which

arises from the improved surface to volume ratios they display. As such, like most nanomaterials, nanoparticles have garnered significant research attention. Examples of nanoparticles have been reported for a large proportion of elements in the periodic table, including transition metals, metalloids and non-metals.[108] These nanoparticles can be synthesised using a multitude of techniques that can broadly be categorised into *bottom – up* and *top – down* approaches, which each have their own sub-classes. Briefly, the former category involves assembling nanoparticles from smaller building – blocks, whilst the latter relies on their derivatisation from a larger bulk starting material.[108]

CNTs are seen as ideal nanoarchitecture building blocks for the attachment of nanoparticles. This is due to their aforementioned properties, such as high surface areas, mechanical robustness and excellent conductivity. The coupling of nanoparticles with nanotubes looks to combine the novel properties of each material type, in an effort to synergistically promote new functionality. Given the wide range of nanoparticles that exist, the field of nanoparticle – CNT hybrids is perhaps the most diverse type of CNT composite that is being studied, at present. Taking into account the considerable number of potential applications associated with various types of nanoparticles and CNTs themselves, a vast array of applications have arisen for these nanoparticle – CNT hybrids. These may include optoelectronics, heterogeneous catalysis, electrocatalysis and environmental remediation, amongst others.[109-112]

Many routes can be utilised for the construction of these hierarchical nanostructures, and these will be discussed in greater detail in later chapters. Briefly, however, pre-formed nanoparticles can be attached to the surface of the CNT (*i.e.* through wet-chemical means) or nanoparticles will be directly generated on the surface of the nanotube itself (*i.e.* through CVD).[113] The former procedure is referred to as *ex-situ* production whilst the latter is known as an *in-situ* approach. Furthermore, instead of coaxially decorating the surface of CNTs with

nanoparticles, some efforts look to fill the hollow cavity with nanoparticles. Again, this typically utilises the *in-situ* route, but these filled structures are beyond the scope of this work, however; detailed reviews can provide further insight into these composites if of interest to the reader.[114]

In order to fully take advantage of these nanoparticle – nanotube hybrid materials, a greater degree of sophistication is required in their production. By understanding the synthesis process further, we will be able to rationally design these hybrid materials with variable compositions and ultimately, tuneable properties. Where regular CNTs are concerned, there have been some preliminary research efforts that looked to rationalise the self-assembly of various nanoparticles onto the surface of the nanotube.[115] For doped nanotubes and BCN-NTs, in particular, this is not the case and as such a research gap remains within the literature.

1.3. Introduction to BCN Nanotubes: Potential Applications and Current Outlook

Borocarbonitrides are a sub-class of carbonaceous material that, as the name suggests, are composed of boron, nitrogen and carbon. After the advent of CNTs, the incorporation of boron and nitrogen into these nanotube soon followed with the resulting product being termed BCN-NTs. It is important to note that within the literature, borocarbonitride nanotubes is a broad encompassing term. For example, some may use it to refer to hybrid materials of BN/CNT, where the CNT is coated in a boron nitride layer. In this thesis, the BCN-NT materials that we will explore can essentially be viewed as CNTs that have been co-doped with both boron and nitrogen atoms, predominantly consisting of carbon. These dopant

atoms can exist in a variety of bonding configurations within the graphitic network; with some of these being exemplified in Figure 1.3.

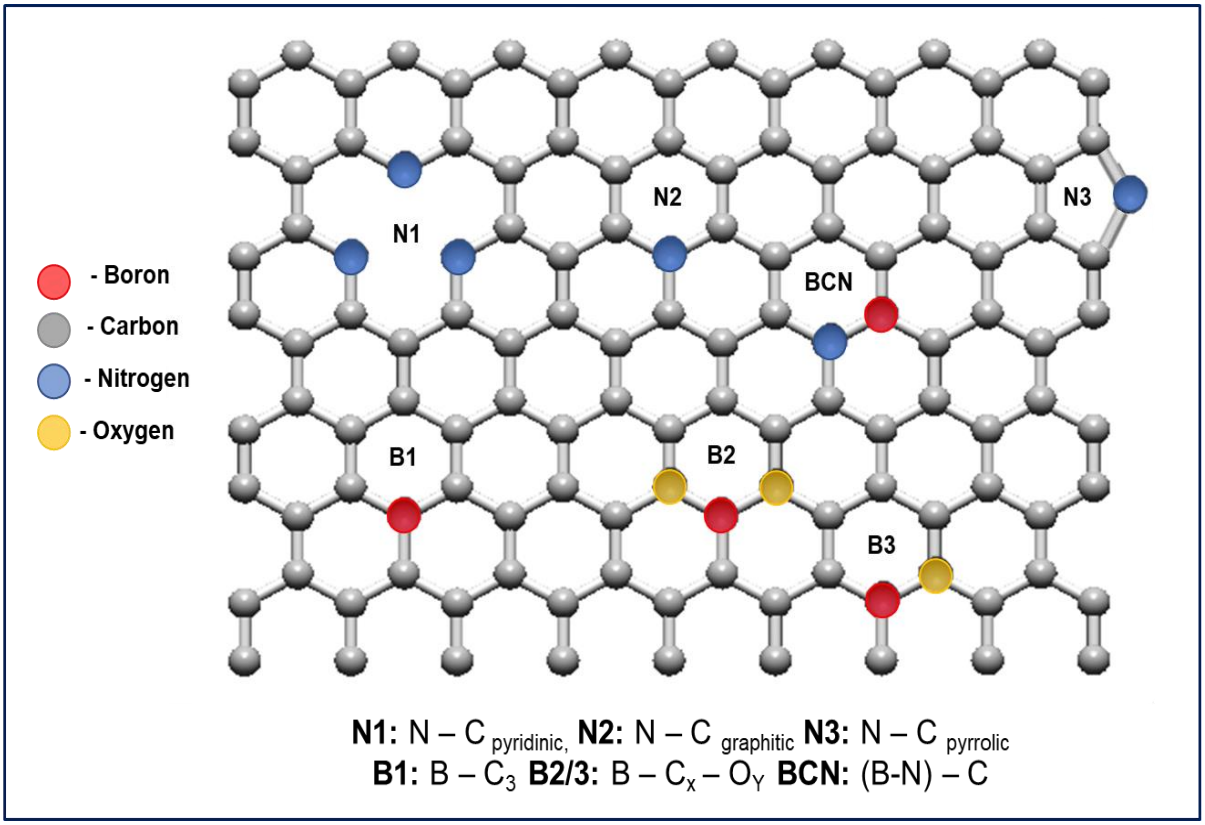


Figure 1.3: Schematic diagram highlighting some of the potential boron and nitrogen dopant site bonding configurations that exist within a graphitic carbon lattice.

Often the choice for simultaneous inclusion of co-dopants, and more specifically boron and nitrogen, is not discussed in great detail within the literature. Instead, the term 'synergistic effect' is typically ascribed to describe any positive results when both of these co-dopants are included. That being said, there is rationality behind the exploration of including both boron and nitrogen simultaneously. There have been a number of co-dopants explored within CNTs, but from a practical point of view, boron and nitrogen are the most logical given their similar atomic radii's.[116] These similarities facilitate inclusion more readily when compared to other heteroatoms. From a property perspective, the inclusion of both boron and nitrogen can

facilitate different modifications to CNTs that may be beneficial at the same time. Firstly, the chemistry of boron and nitrogen are different. The nitrogen possesses a free electron pair whilst boron has vacant p-orbital and both have different electronegativities. The lone pair and vacant orbital offer different routes of activation on the carbon nanotube surface which can enhance interactions and processes at these different sites, through alternating modes of action. Experimental and computational studies have shown that the inclusion of both co-dopants can modify the optical and electronic properties of carbonaceous nanomaterials.[117-119] For instance, simulations have suggested that the presence of both co-dopants can reduce the bandgap within nanotubes when compared to their pristine and uni-doped counterparts.[120] Material properties that are tuneable *via c*omposition are an intriguing prospect for many fields of research. Finally, the presence of a uni-dopant may lead to undesirable properties, at the price of a desired one. For example, nitrogen dopants can lower the oxidation resistance in carbonaceous materials whilst boron inclusion can improve this.[121] Therefore by incorporating both, we may be able to circumvent these drawbacks, and couple improved properties that would be afforded by each individual dopant.

Even though examples of BCN-NTs have been reported since the 1990's, it hasn't been until relatively recently that research into these BCN-NTs has matured to a point where they have been explored for a host of applications. Here we will look to briefly introduce the reader into some of the applications that have been explored for BCN-NTs and provide an outlook as to why they are material of interest.

As has been noted, the tuneable composition of BCN-NTs means the properties of these nanotubes can be varied. These composition dependent properties mean that a range of potential applications exist for BCN-NTs. Typically, these are related to those explored for regular CNTs, such as in energy storage devices. For example, BCN-NTs have been investigated for use in supercapacitors.[16, 122] Iyyamperuma *et al*. reported that the BCN-NTs

they synthesised displayed improved capacity when compared to their undoped counterparts.[16] The authors attribute the synergistic effect that arises from the presence of boron and nitrogen dopants to this enhanced capacity. Zhou *et al*.[122] also described improvements on this initial work with the specific capacitance they recorded for their BCN-NTs. It's interesting to note that the composition of the latter BCN-NTs had significantly more carbon present, with a ratio of 1:2:1, in comparison to 1:1:1. In each case, the synthesised nanotubes displayed good cycling durability and outstanding rate capabilities. Elsewhere, BCN-NTs have also been investigated as potential electrode materials for other energy storage devices such as lithium-ion batteries.[123] Once again, the authors note the excellent capacity and long-term cycling ability of these nanotubes when utilised as anode materials in the battery set-up, which they ascribe to the increased number of active sites presented by dopant atoms in the NT.

Aside from energy storage, BCN-NTs have found potential usage in electrocatalysis. Wang *et al*.[124] determined that BCN-NTs display superior catalytic ability and higher durability toward the oxygen reduction reaction when compared to the uni-doped CNTs tested for this reaction. This highlights the synergy that arises when introducing both boron and nitrogen simultaneously together. These synergistic effects, along with the surface area and functionality of BCN-NTs have made them promising materials for environmental remediation.[124] The dopant atoms enabled the nanotubes to interact with pollutants, which in turn enhanced their catalytic capability to degrade these molecules. Moreover, BCN-NTs have also displayed promising performance when considered for applications in gas storage and electromechanical devices.[125, 126]

As we have seen throughout this section, BCN-NTs have displayed promise with regard to a host of different applications, but as of yet, their wide scale usage remains unseen. In order to further the progression of BCN-NT implementation in everyday life, we need to perhaps look

to the natural research progression that followed regular CNTs. This would involve the design of hierarchical BCN-NT hybrid materials, which look to improve on the already promising performance of existing nano-scaffolds. Despite this, research into the functionalisation and processing of BCN-NTs remains significantly underdeveloped when compared to regular CNTs and uni-doped CNTs. This can likely be attributed to the lack of commercially available BCN-NTs which hinders the ability for researchers to investigate the synthesis and processing of these hybrid materials. Surprisingly, whilst some accounts existing for the further processing of BCN-NTs, very few studies investigate the production of hierarchical structures using *ex-situ* techniques or look towards their arrangement on the macroscale. As such this area of research remains at an early stage of development.

1.4. Thesis Aims and Outline

After reviewing the literature surrounding BCN-NTs, several things became apparent. Firstly, they are an extremely promising material class due to the performance they have exhibited within several potential applications to date. This makes them suitable candidates to explore as next-generation hierarchical materials. Secondly, there are significant research gaps regarding the processing of these BCN-NTs, which is likely due to the lack of commercial availability. For this reason, in this thesis, we are looking to tackle some of these issues. Broadly speaking, these can be defined by three main aims set out in this thesis:

(i) To investigate the exploitation of existing defects within AACVD grown N-CNTs for the production of BCN-NTs on a large scale, through a sequential doping procedure.

(ii) To determine if solvent selection has a significant impact on the attachment of iron oxide nanoparticles onto the surface of doped nanotubes, as it does in undoped systems. Furthermore, to assess if the presence of co-dopants influences the composition of these hybrid materials.

(iii) Develop practical arrangements of these nanomaterials and assess whether electrophoretic deposition or vacuum filtration techniques are more suitable for the production of macroscopic BCN-NT assemblies.

This thesis is split into three separate experimental sections that look to address areas of limitation, tackle each formal aim and offer new insight into the field of BCN-NTs. Whilst each chapter is principally independent from one another, some elements of research link between them. In particular, each chapter shares a common them of looking to make a contribution within the field of BCN nanomaterials. Prior to detailing the experimental work conducted for this thesis, I will first give the reader an introductory overview of some of the methods that will be encountered throughout this body of work.

Chapter 2

Methods

2.1. Introduction

There are a host of characterisation techniques available that can be used to analyse materials. A number of these techniques have, been used throughout the duration of this DPhil owing to their availability and significance to the materials that have been manufactured. In this chapter, I will introduce the basic theory behind each of the characterisation techniques that have been utilised in the experimental chapters of this thesis. Additionally, I will attempt to elucidate why they were used, by highlighting the relevance to the work that has been conducted within each chapter. For a more detailed account of each of these characterisation techniques, the reader can be pointed to a number of other resources that cover each of these techniques in greater detail.

2.2. Characterisation of BCN-NTs and BCN-NT - Nanoparticle Hierarchical Nanostructures

2.2.1. Scanning Electron Microscopy

When it comes to carbon nanomaterials, scanning electron microscopy (SEM) is one of the most common characterisation techniques employed after synthesis. As the name suggests, this form of microscopy involves the use of electrons to form an image of the product in question. This technique is useful for probing the surface morphology of synthesised materials over a relatively large sample area, in comparison to analysing individual nanotubes. SEM allows us to examine the orientation and size distribution of grown nanotubes which are important material properties to consider. Given that the wavelength of electrons can be significantly shorter than visible light, optical microscopy does not allow the

same level of resolution that can be achieved with SEM when imaging on nanoscale dimensions. Hence, when it comes to the characterisation of CNTs, SEM is preferred.

The basic operating procedure for SEM is schematically shown in Figure 2.1(a). An electron source is situated at the top of a column, under vacuum, which contains the sample of interest at the bottom. The column is fitted with lenses that are used to dictate the electron beam. An accelerated beam of electrons is passed through the column, until it reaches the sample and is scanned across a given area. The column is fitted with lenses that assist the focussing of the electron beam onto the sample. At this point the beam of electrons interact with the sample which promotes the generation of various signals, including backscattered and secondary electrons. These electron signals are collected by detectors and projected as an image of the sample. Bombardment of a material with electrons can lead to, what is known as, sample charging. This typically occurs when a non-conductive sample is used; as the sample is irradiated, a build-up of potential occurs on the material. This usually requires a conductive coating to be applied, to discharge the build-up of potential and to avoid any issues with

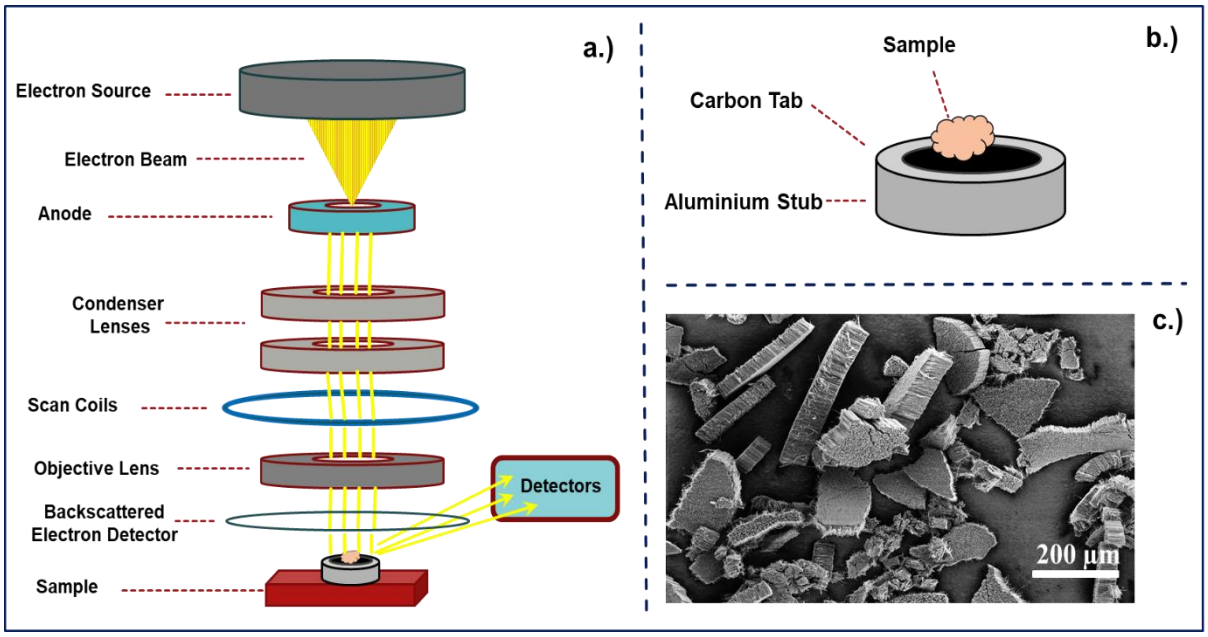


Figure 2.1 – A diagram illustrating schematics of the (a) operating principles for a scanning electron microscope and (b) sample preparation involved for this technique. We also see (c) an example of the imaging afforded by this technique.

imaging such as blurring or contrast issues. Given the nature of CNTs however, a conductive coating is not required meaning as prepared products can be analysed directly.

Sample preparation for SEM is relatively straightforward and is schematically shown in Figure 2.1(b). The as synthesised product is scattered on top of a conductive carbon-tab which is mounted to an aluminium stub. The entire tab is coated in sample to ensure an accurate representation for the bulk of material when examining with SEM. Where this body of work was concerned, SEM analysis was used to measure the length of the nanotubes and visualise the orientation of the product. These measurements give us an indication of uniformity across various batches of synthesised nanotubes. An example of SEM micrographs obtained for some of the CNT materials synthesised during this project are highlighted below in Figure 2.1(c). As we can see, this technique gives us an overview of the nanotube alignment and allows us to measure the length of the nanotubes.

2.2.2. Transmission Electron Microscopy

Like SEM, transmission electron microscopy (TEM) also involves the use of electrons to produce an image. TEM is one of the most commonly employed characterisation techniques to analyse nanomaterials. In particular for CNTs, it allows us to probe the innertube and give us a better idea of morphology for individual nanotubes as well as allowing us to measure diameters of the samples. Again, due to the use of electrons, the resolution afforded by TEM analysis is greater than that achieved by optical imaging and SEM, also.

Figure 2.2 shows a diagram that indicates the operating principles involved in TEM and the sample preparation. As we can see, the basic principles are similar to SEM. A beam of electrons is generated and passed through a series of electromagnetic lenses and apertures contained within a vacuum column. Whilst in SEM an image is formed by detecting electrons

signals produced after sample interaction with an electron beam, in TEM, an image is produced by detecting the transmitted electrons. The incident beam of electrons interact with the sample and the electrons transmitted through the sample are collected at a phosphor screen which generates an image. The contrast of the image is based on the density of electrons hitting the phosphor screen and thus, determined by the interaction with the sample. This contrast can be categorised into mass and thickness contrast which relate to the atomic weight of elements the electrons interact with and the thickness of the sample, respectively.

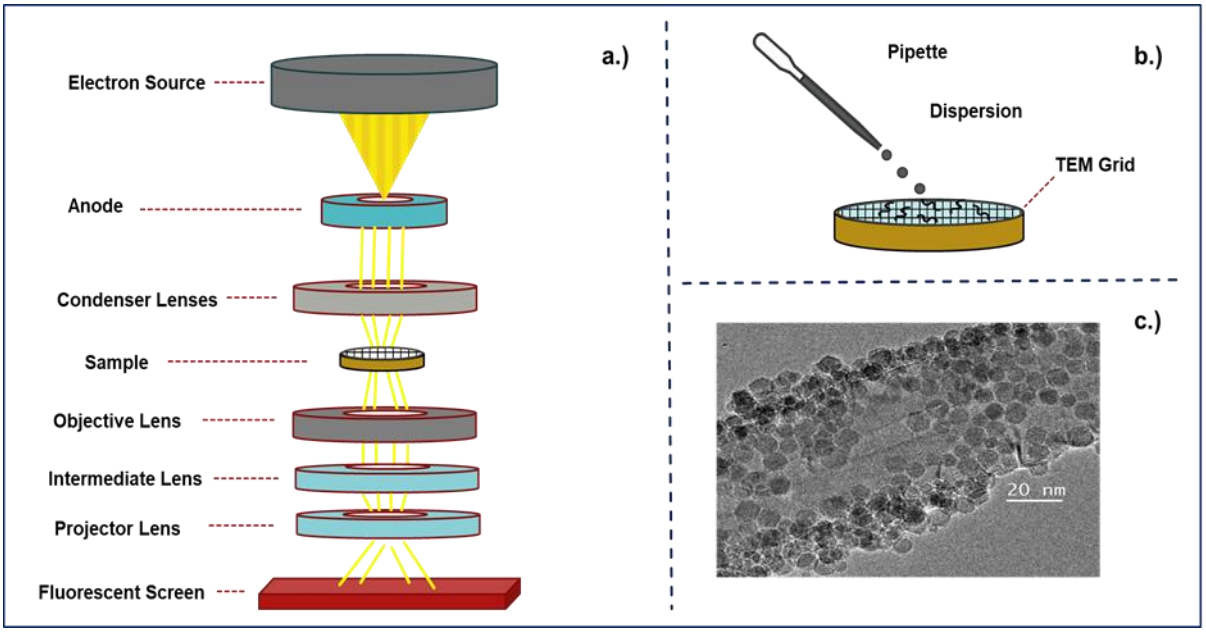


Figure 2.2 – A diagram illustrating schematics of the (a) operating principles for a scanning electron microscope and (b) sample preparation involved for this technique. We also see (c) an example of the imaging afforded by this technique.

TEM requires the sample of material to be relatively thin when compared to SEM. This means the carbonaceous products cannot be analysed as produced. Instead the nanotubes are dispersed in an organic solvent and cast onto a grid which, in essence, captures the material as a thin, even layer. The samples are dried under vacuum to remove excess solvent as this can interact with the beam. Here we have used TEM to monitor the effects that the co-doping

procedure, introduced in Chapter 3, had on the nanotube morphology and diameter. Due to the mass contrast, in Chapter 4, TEM was an extremely useful tool used to image the BCN-NT/FeO_xNP hybrid materials that were produced. In Figure 2.2(c) we see an example of one of these hybrid materials, imaged through TEM. The difference in atomic weight between the nanotubes and FeO_xNPs affords a sharp contrast which allows us to clearly visualise the level and distribution of functionalisation achieved.

2.2.3. X-ray Photoelectron Spectroscopy

X-ray photoelectron spectroscopy (XPS) is one of the most powerful surface analysis techniques available in materials science. It is useful in the study of nanomaterials as it allows us to determine what elements are present in a sample and analyse the composition.

XPS analysis relies on the photoelectric effect that was popularised by Albert Einstein.[127] Essentially it describes the excitation of atoms, followed by the emission of electrons observed when a material interacts with electromagnetic radiation. The kinetic energy of the ejected photoelectron is related to the energy of the incident radiation and the binding energy of the ejected electron. In XPS, a sample is irradiated with x-rays whilst the kinetic energy and magnitude of the emitted photoelectrons are then detected and analysed. From measuring the kinetic energy, we can determine the binding energy of the emitted electrons. These binding energies are characteristic of different elements and chemical environments; hence we can determine the composition of a sample using these detected electrons. XPS analysis is normally displayed as a spectrum of intensity against the binding energy of electrons. The greater the intensity, the larger the contribution of that specific electron binding energy, and thus element, to the overall composition. From XPS spectra we can deduce a relative composition presented within a material. This can be particularly useful in cases like this

study where low levels of heteroatom dopants are introduced into a predominantly carbon-based nanostructure. Due to the sensitivity of this technique we are able to detect the dopant atoms present.[128] Further to this, XPS affords information regarding the chemical environments of the electrons that are detected. The binding energy of electrons ejected will be affected by surrounding chemical sites that can be either electron withdrawing or donating, and result in bond polarisation. Electron withdrawing groups will typically increase the binding energy observed in the XPS spectrum and *vice versa* for donating groups.[129, 130] Through deconvolution of the peaks displayed in the XPS spectra we can gain further insight into the chemical and bonding environments present within the sample. The models used for the deconvolutions come from reviewing the literature and formulating a consensus on the relative peak positions for various bonds and their respective assignments. Throughout this thesis, XPS was used to confirm the successful incorporation of boron and nitrogen into the nanotubes to form BCN-NTs. We also probed the bonding configurations of each dopant type using the deconvolution of spectra approach detailed above.

2.2.4. Energy Dispersive X-ray Analysis

Energy dispersive x-ray (EDX) analysis is another characterisation technique that is used alongside SEM or TEM. It can be used to investigate the chemical composition of a sample. Whilst both EDX and XPS utilise x-rays in some way, the mode in which they do so differs. EDX is principally based on Moseley's law which relates emitted x-rays to atomic number.[131] In EDX analysis, after initially imaging with SEM or TEM, a sample is bombarded with electrons. The subsequent interaction with the electron beam results in the emission of x-rays from the sample. The electron beam ejects core electrons from the interacting atom, which in turn leads to the generation of holes in the innermost shell. These vacancies are then filled

with higher energy electrons from outer shells. Upon relaxing, energy is then released from the system, in the form of x-rays. The energy released relates to the energy gap between the shells. The ejected x-rays are characteristic of individual elements and can therefore be detected, analysed and assigned to specific elements. An element can be detected in a sample, using EDX, as long as there is a concentration greater than 0.1%.[132] By measuring these emitted x-rays we can therefore deduce the elements present within a sample and the relative amounts. When analysing bulk samples the electron-beam 'teardrop' interaction penetrates the sample on the order of a few μm which can limit spatial resolution and thus accuracy when compared to a thin sheet, for example. Additionally, sample topography in thick samples can also impede the path of generated X-rays and the detector which poses a potential limitation in detection. EDX mapping is however a useful analysis feature that allows us to visualise the distribution of the detected elements across the sample. Where XPS can be used to investigate the bonding type and chemical configurations present within a sample, EDX does not give us information regarding this. It is also a less sensitive technique than XPS, in particular for detecting lighter elements. This being due to a number of reasons, such as light elements emitting low numbers of x-rays. That being said, it is still a useful technique that can be used to complement XPS analysis, which is what was done in Chapter 3 of this thesis. We used it to probe analyse the incorporation of boron and nitrogen dopants within the BCN-NTs as well as for analysis of the macroscopic films in Chapter 5.

2.2.5. Raman Spectroscopy

Raman spectroscopy is a commonly employed characterisation technique in materials science that is used to evaluate the structure of synthesised materials. It is commonly used to assess the quality of carbonaceous nanomaterials through analysing the crystal structure.

The basic operating principles for the Raman spectroscopy involve irradiating a sample and analysing the light scattering response using a detector. Raman spectroscopy is based on Raman scattering, which is essentially the inelastic scattering of incident light. While the majority of incident light interacting with a sample will scatter at the same wavelength as the source *i.e.* Rayleigh scattering, a small fraction of inelastic scattering can be observed at altered wavelengths to the incident light. This inelastic, or Raman, scattering typically arises from molecular vibrations within the sample. Incident light promotes these molecular vibrations within the sample. The Raman shift is what we plot and analyse using this spectroscopy technique. This shift is measured as the difference between the incident and scattered light. This Raman shift can be subcategorised into Stokes and anti-Stokes scattering which refers to lower energy and higher energy wavelengths, when compared to the incident light, respectively. These observed shifts are characteristic of a material. This shift is plotted as a wavenumber against the intensity of the inelastic scattering causing the shift.

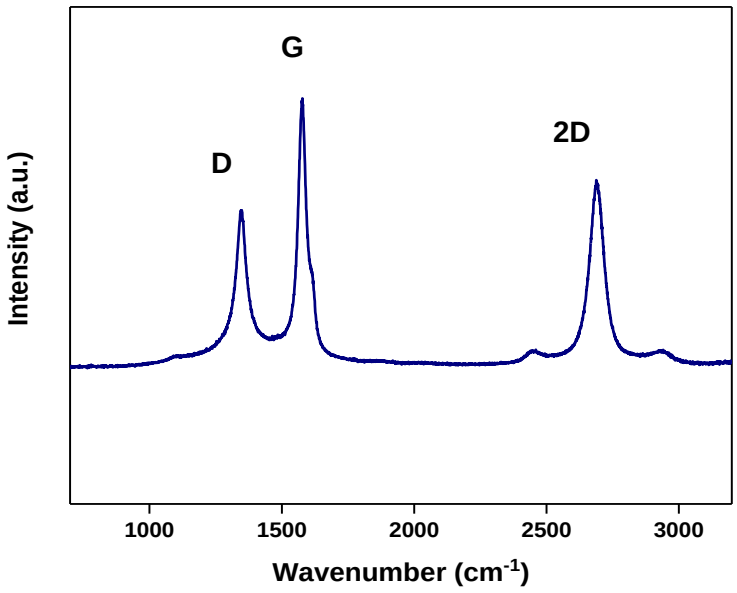


Figure 2.3 – A characteristic Raman spectrum recorded for a multi walled carbon nanotube sample. The three prominent peaks (D, G and 2D) are labelled accordingly.

Multi walled CNTs display characteristic features that are identifiable using Raman spectroscopy. Figure 2.3 shows a typical Raman spectrum obtained for a MWCNT sample. As we can see, three distinct peaks are displayed within the spectrum. The first peak which is apparent at the lowest wavenumber is known as the D peak. The presence of defects and disorder within the nanotube structure can lead to characteristic phonon scattering and hence, this peak is referred to as the D peak.[133] The second peak which appear at higher wavenumber of *ca*. 1550 cm^{-1} is known as the G peak and can be attributed to the high frequency E_{2g} mode, associated with in-plane stretching (tangential) vibrations within the graphitic bonding network of CNTs.[133] This peak appears in the Raman spectra for all carbon-based materials. The third peak appearing at *ca*. 2650 cm^{-1} is an overtone of the D peak and is referred to as the 2D (or G') peak and can be attributed to a double resonance scattering process.[133] Interpretation of these peaks, in particular the D and G, can be useful for assessing the properties of synthesised carbon nanomaterials such as the defect density.

Throughout this thesis, Raman spectroscopy is used to assess the relative crystallinity of the synthesised CNTs. In particular we use it to monitor how the co-doping procedure used to produce BCN-NTs influences the defect nature of the synthesised materials.

2.2.6. Ultraviolet - Visible Light Spectroscopy

Ultraviolet and visible light (UV-Vis) spectroscopy is a technique that measures the absorption of light through a material. This can be utilised to compare the quality of CNT dispersions and to probe optical properties of a material.

In UV-Vis spectroscopy, a sample is loaded into a spectrophotometer and positioned between a light source and detector. The light source, which includes wavelengths that range from the

UV to visible, is used to illuminate the sample. The detector can then collect information on the amount of light that is reflected, absorbed or transmitted through the material. The interaction with the incident light typically results in the presence of broad absorption bands which are related to optical transitions. These are characteristic of the material and in the case of carbon nanomaterials are often ascribed to π transitions.[134] These distinctive absorbances can be used to compare the quality and concentration of various CNT dispersions. The Beer-Lambert law is expressed in equation 2.1, where A = absorbance, c = concentration of the sample, l = path length and ε = is the absorption coefficient. This relationship essentially states that the concentration of a solution is proportional to the magnitude of absorbance. Further to this, through use of the Tauc relationship, researchers have previously probed the electronic properties of CNTs such as the optical band gap.[135, 136] This relationship is expressed in Equation 2.2 where, α = absorption coefficient, hν = energy, A = absorbance and E_g = optical band gap . The curves used to determine these optical properties are derived from UV-Vis absorption spectra.

$$A = \varepsilon c l \quad (2.1)$$

$$\alpha h\nu = A(h\nu - E_g)^n \quad (2.2)$$

In Chapter 3, the optical properties of the synthesised BCN-NTs are compared to the precursor material to determine the influence of the co-doping procedure. This was done through UV-Vis analysis. In Chapter 5, we used UV-Vis analysis to evaluate the suitability of various common laboratory solvents in dispersing synthesised BCN-NTs. This was done by comparing the apparent concentrations under various conditions. This work would later be

used to produce dispersions that were suitable for the fabrication of macroscopic BCN-NT assemblies.

2.2.7. Thermogravimetric Analysis

Thermogravimetric analysis (TGA) is a thermal based characterisation tool that can be used to analyse the thermal properties, as well as the composition, of nanomaterials. In theory, it is a relatively simple technique that involves monitoring the mass of a given sample under a specified heating procedure.

The basic principles of TGA involve a sample being packed into a pan that is loaded onto a hang-down wire which is connected to a precision balance. Typically, a minimum of a few mg of sample is required for the analysis. This pan is then placed inside a sealed furnace, which itself is flushed with either a reactive or inert gas throughout the analysis. Whilst inside the furnace, the sample can be heated to a desired temperature under a specific regime. The changes in mass across the sample are recorded as the heating procedure progresses, in a feedback style loop. These changes can then be plotted in a TGA curve. Given the sensitivity of the balance, it is important to ensure the sample pan is inert under the operating conditions and that it is free of impurities. Several pieces of information can be inferred from this analysis technique, such as chemical processes occurring or mass losses due to the presence of solvent, amongst others. Kinetics regarding these thermal events can also be deduced.

Throughout this thesis, as-produced samples were analysed using a combination of isothermal and dynamic procedures under an oxidising atmosphere. The maximum operating temperature utilised was 900 ^{o}C given that graphitic carbon nanomaterials are typically not thermally stable above this temperature.[65] TGA was used in Chapter 3 to monitor the effect co-doping had on the thermal properties after the synthesis of BCN-NTs. From the data curves produced during TGA, which is normally a plot of mass against sample temperature,

we can deduce thermal properties such as the oxidation resistance of a sample. The onset for such events can be defined as the point at which mass begins to significantly change.

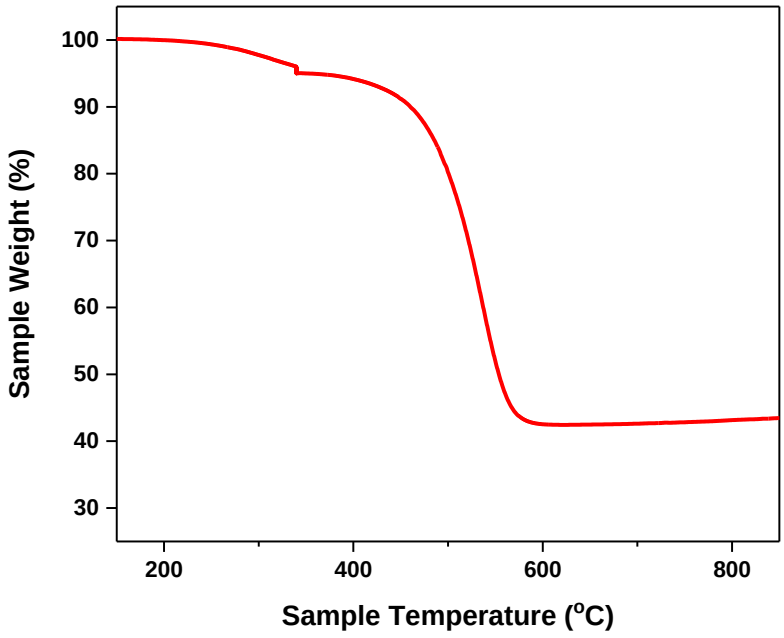


Figure 2.4 – A typical profile obtained after thermogravimetric analysis of a carbonaceous material which shows how the sample weight varies with sample temperature.

In Chapter 4, TGA was key to determining the composition of the BCN-NT/FeO_xNP hybrid materials we synthesised. An example of a TGA profile for one of these hybrids are shown in Figure 2.4. Given that the carbon based BCN-NTs oxidise at a lower temperature than FeO_xNPs, we are able to uncouple the decomposition of the BCN-NTs which allows us to quantify the loading of FeO_xNPs in the hierarchical hybrid materials synthesised. We could therefore assess the impact various solvents had on the functionalisation procedure.

2.3. Characterisation of BCN-NTs Macrostructures and Iron Nanoparticles

2.3.1. Brunauer-Emmett-Teller Analysis

Brunauer-Emmett-Teller (BET) analysis is a technique used to characterise the texture of a material and to evaluate the surface area and porosity. It is based on the adsorption of gas molecules onto the surface of a substance.

In BET analysis, a known mass of sample is initially degassed in order to remove potential contaminants, such as water molecules, that may affect the analysis. An inert gas, typically N_2, is then pumped into the sample analysis chamber. This is performed at low temperatures to maximise interaction. The pressure of this gas is gradually increased, and the amount of adsorbed gas is measured. Adsorption occurs where a gas molecule adheres to the surface of the material. Results are then displayed as an isotherm which is a plot of the adsorption magnitude against the relative pressure of the system. The isotherm can be used to calculate the surface area of the material analysed. This involves use of equation 2.3, otherwise referred to as the BET equation.

$$\frac{P/P^0}{n(1-P/P^0)} = \frac{1}{n_m} + \frac{C-1}{n_m C}(P/P^0) \quad (2.3)$$

Here P/P^0 = the relative pressure, C = a constant, n = the amount of gas adsorbed at a given relative pressure and n_m = the amount of gas adsorbed at standard temperature and pressure. By determining, n_m *i.e.* the specific monolayer capacity, the specific surface area can then be calculated. In addition to the surface area, the adsorption isotherms can also be used to infer information regarding the porosity of the material. The hysteresis loops typically exhibit a shape that is similar to one of six isotherms that have been previously defined.[137] The shape of these hysteresis loops are typically characteristic of the pore structure. The pore structure

can be further probed with the Barrett–Joyner–Halenda (BJH) method. In this thesis, we used BET and BJH analysis to probe the surface areas and porosity of the macroscopic film assemblies that were produced in Chapter 5.

2.3.2. Four Point Probe Analysis

Four-point probe analysis is often used in materials science to examine the electrical properties of a sample. It can be used to measure properties that include the electrical conductivity or sheet resistance of a material. The four-point probe apparatus, as the name suggests, involves a piece of equipment that houses four equally spaced probes arranged in a line. This is shown schematically in Figure 2.5. These probes are brought into contact with the material to be characterised.

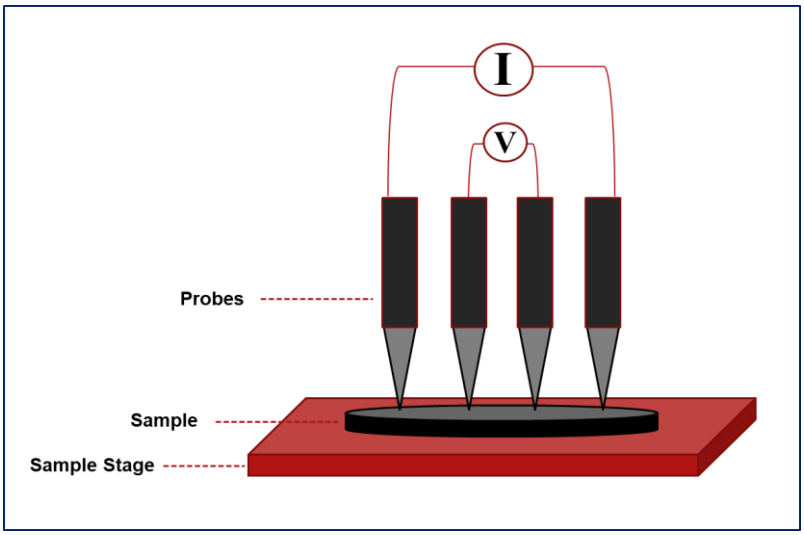


Figure 2.5 – A schematic illustration (not to scale) of the experimental set-up used for film conductivity measurements. A four point probe is brought into contact with a sample before measuring the change in potential.

This involves passing a current through the outer two probes which induces a change in potential difference between the two innermost probes. The change in potential across the

inner probes can be measured and used to calculate various electrical properties of the sample. In equation 2.4 we see how sheet resistance can be calculated.

$$(2.4) \quad R = \frac{\pi}{\ln(2)} \frac{\Delta V}{I}$$

$$(2.5) \quad \sigma = \frac{1}{R\,t}$$

Here, R = the sheet resistance of the material, I = the current applied to the outermost probes and ΔV = the change in voltage measured across the inner probes. The value obtained for sheet resistance can then be plugged into equation 2.5 to calculate the electrical conductivity of the material, where σ = electrical conductivity and t = the thickness of the sample in question. In Chapter 5, we used four-point probe analysis to analyse the macroscopic assemblies we produced to compare them with literature examples. It also allowed us to determine the effect co-doping had on electrical properties when comparing BCN-NTs to the pre-cursor material.

2.3.3. X-ray Diffraction and Dynamic Light Scattering

X-ray diffraction (XRD) is a chemical analysis technique in materials science that is employed to determine information regarding the crystalline properties of a nanomaterial sample. XRD is based on the principle of elastic scattering of x-rays across ordered structures. In XRD, a material is bombarded with x-rays and interaction with the structure of the material induces reflections of this incident beam. A detector is used to measure the angle and intensity of these diffractions. When diffracted x-rays constructively interact with one

another, an x-ray diffraction pattern can be recorded for the material. These constructive signals are observed when Bragg's law, shown in equation 2.6, is satisfied.

$$(2.6) \quad n\lambda = 2dsin\theta$$

Here n = a whole integer, λ = the wavelength of the x-ray source, d = the lattice spacing, and θ = the angle between the incident and diffracted beam. This relationship shows there is a link between the distance between atomic planes and the measured diffraction angle. The angle between the incident and diffracted beam (*i.e.* 2θ) is what the intensity is plotted against in an XRD diffractogram. The value of 2θ tells us about the spacing between the atoms in the crystallite. The XRD diffractogram recorded for a material can then be compared to a database of known values which allows us to assign the observed peaks. In Chapter 4, powder XRD was used to determine and analyse the crystal structure of the synthesised FeO_xNPs.

Dynamic light scattering (DLS) is an optical-based procedure used in the characterisation of nanoparticles. It can be used to assess the stability of a nanoparticle dispersion and to analyse the size of the nanomaterial. The theory behind DLS is centred on the Brownian motion of particles. Brownian motion states that particles are randomly moving due to constant collisions with solvent molecules. Brownian motion is faster for smaller particles and vice versa for larger particles. As the name suggests, DLS involves the measurement of scattered light. A solution of dispersed nanoparticles is irradiated using a laser which induces light scattering. The scattered light is detected at various angles, over time, and a flux of scattered light intensity is collected. The speed of the dispersed nanoparticles and the rate of these

fluctuations influence the signal that is detected. Using this information, the instrument can calculate a value for the hydrodynamic diameter of the dispersed nanoparticles.

XRD was used in Chapter 4 to analyse the crystallinity and phase of the produced FeO_xNPs. DLS was also used in Chapter 4 also, to measure the diameter of the nanoparticles produced to complement initial core diameter measurements made through TEM analysis. Where TEM allows us to measure the core diameter, the hydrodynamic diameter accounts for the exterior coating of the nanoparticle.

Chapter 3

Two-Step Synthesis of Boron & Nitrogen Co-Doped CNTs

3.1. Introduction

BCN-NTs have been considered for both energy storage and electrocatalytic technologies due to the promising performance they have displayed within each of these fields.[15, 138] The electronic and physical properties of BCN-NTs (for example the oxidation behaviour and chemical reactivity) can be tuned through modification of their chemical composition, which is useful for a host of potential applications.[14, 139] As has been established in section 1.3 of this thesis, BCN-NTs are essentially CNTs that have been co-doped with boron and nitrogen simultaneously. This dual doping opens up the possibility for synergistic effects to arise due to the differing dopant types. For example, carbon atoms can be activated *via* two modes owing to the electron accepting and donating nature of surrounding boron and nitrogen dopants, respectively.[140] These features of BCN-NTs make them an interesting material to explore for the bottom up production of hierarchical nanostructures, as these dopant sites may facilitate interactions with other nanomaterials and solvents.[141] Additionally, the presence of both nitrogen and boron dopant sites may also improve the processability of BCN-NTs with respect to the production of macroscopic assemblies. Despite the promise they have displayed, the development of processing techniques within the field of BCN-NTs is severely lacking when compared to CNTs, N-CNTs and BN-NTs. The lack of study into these processing techniques may lay with the commercial scarcity of BCN-NTs.

BCN-NTs have been synthesised using a variety of techniques including arc discharge, chemical vapour deposition and polymeric pyrolysis.[142-144] Despite the research into their synthesis, to date (*c.* 2023), BCN-NTs are not commercially available to purchase. There are some drawbacks associated with each of the existing fabrication methods listed, including high energy requirements, the use of corrosive and pyrophoric gases (e.g. ammonia and boranes) and non-uniform reaction products, respectively. The lack of commercial

availability has likely limited further research into the processing procedures for the production of BCN-NT nanohybrids and their macroscopic assembly. This ultimately has reduced further research into their potential applications and widespread implementation.

In this chapter, I introduce a two-step synthesis technique for BCN-NTs that attempts to overcome some traditional limitations associated with their synthesis. The aim of this chapter was to produce BCN-NTs on a sufficient scale that would allow us to develop methods for their further processing into hierarchical nanostructures and ultimately macroscopic assemblies. For nanotubes, and more specifically BCN-NTs, to be used on a wide-scale, it is important to have control over the nanotubes structural uniformity as the aspect ratio and composition often dictate the resultant material properties.[145] Therefore here we were interested in having a degree of control over the structure of the nanotubes synthesised here. N-CNTs, which are inherently defective, were produced *via* aerosol assisted chemical vapour deposition using a procedure that has previously been developed within our group.[146] These nanotubes, that are obtained in a vertically aligned arrangement, have been shown to possess structural uniformity and a homogenous distribution of nitrogen dopants across the sample. These N-CNTs were then utilised as a template for a subsequent boron doping procedure. It was envisaged that the intrinsic defects associated with the N-CNT precursor would assist this second step. A host of techniques, which included XPS, Raman and TGA were used to evaluate the synthesised BCN-NTs and to determine the effect the co-doping procedure had on the nanotube properties. Collaborative computational modelling was used to elucidate some of the experimental findings obtained here. Before detailing the experimental results gathered for this chapter, I will first provide an overview of some of the existing synthesis techniques that have been used for the production of BCN-NTs to date.

3.1.1. Synthesis of BCN Nanotubes

3.1.1.1. Arc-Discharge

When it comes to BCN nanomaterials and BCN-NTs, in particular, the literature is less comprehensive when compared to their uni-doped counterparts (*i.e.* boron or nitrogen doped nanomaterials). The earliest examples of BCN synthesis came in the early 1990's, inspired by the seminal discoveries detailed by Iijima in 1991 who utilised arc-discharge techniques to produce CNTs for the first time.[5] Arc-discharge is a procedure that involves two electrodes (typically the cathode is pure graphite whilst the anode is graphitic in nature and has a variable composition) being positioned adjacent to each other within an enclosed compartment. This is shown schematically in Figure 3.1. A small distance, on the millimetre scale, is maintained between these electrodes. The technique relies on the formation of plasma caused by electrical breakdown of a gas. The chamber encasing the electrodes is filled with an inert gas. When a large direct current is applied, an electrical arc-discharge is formed between the electrodes. This applied current causes perturbations within the graphitic networks of the electrodes. At this point, a high temperature plasma is formed (3500 – 5500 ^{o}C). The high temperatures generated by the plasma converts the anode material into gaseous carbon. The vapours are then drawn towards the cathode which is where they are deposited *via* sublimation. This 'cathode deposit' can then be collected manually. Due to build up at the cathode, the reaction therefore needs to be intermittently stopped and restarted in order for the removal of the product build-up on the electrode. There are a number of alterations that can be made to the set-up of the arc-discharge apparatus in order to vary the composition of the reaction product (*i.e.* selectivity between SWCNT and MWCNTs). These include the distance between the electrodes, the carrier gas, the chamber atmosphere, and the graphitic electrode quality.[147-150] Typically, the soot collected from the cathode requires further

purification to yield CNTs as it contains a number of impurities and by-products that remain from the synthesis. After purification of the raw material, the nanotubes can be characterised and observed.

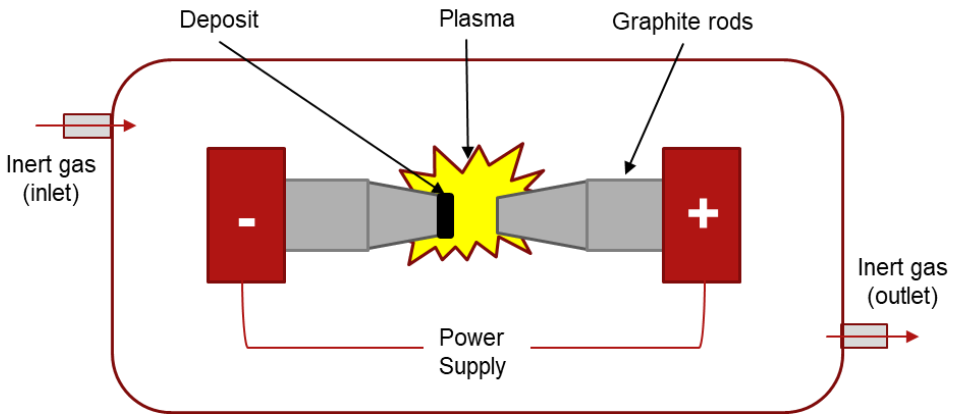


Figure 3.1: Schematic diagram showing the typical set up for an arc-discharge reaction.

Following on from the interest generated by CNTs and BNNTs during the early 1990's, the properties predicted for theoretical BC_2N tubules, *via* first principle calculations, were detailed in an attempt to encourage research into their synthesis.[151] As mentioned, the arc-discharge technique was used as template for the earliest examples of BCN-NTs within the literature. Stephan *et al.*[152] offer perhaps the earliest example of BCN-NT synthesis. They utilised a graphitic electrode packed with amorphous boron powder to act as the boron source, alongside a regular graphite electrode. The arc-discharge chamber was then filled with gaseous N_2 which behaved as the nitrogen source for the reaction. The incorporation of boron and nitrogen within the nanotubes was confirmed with energy loss spectra and the amounts, whilst varying, were always found to be in equal ratios. As has been mentioned, often with arc-discharge, refinement may be required and here the obtained reaction products were not uniform. The tubules varied significantly and were split into two categories,

nanotubes (*i.e.* a diameter up to 100 nm) and graphitic fibres (*i.e.* a diameter up to 500 nm). The presence of graphitic sheets, glassy carbon and nanoparticle impurities were also noted in the reaction product. In addition to the variable morphology of the tubules, the composition was found to vary with the authors suggesting that the thicker fibres had lower levels of boron and nitrogen (akin to doping) while the nanotubes could contain up to 50% of heteroatom content. It is also important to note that most of the compositional analysis provided in the paper was conducted on the BCN platelet morphologies as opposed to the tubes and fibres.

Following on from this work, Weng-Sieh *et al.*[153] also proposed the synthesis of MWBCN-NT tubules *via* arc-discharge methods. One of the pure graphite electrodes was replaced with a graphite electrode packed with boron nitride to promote the incorporation of boron and nitrogen within the tube structures. Interestingly, the previous study into this work noted the unsuccessful attempt to synthesise BCN-NTs using electrodes with this composition.[152] The composition of these nanotubes were similar to those predicted in the earlier theoretical study (*i.e*. 0.5 B :C: 0.5 N) by Miyamoto *et al.*[151] As well as BCN nanotubes, the authors also discovered the presence of boron carbide nanotubes in the electrode deposit. Additionally, the purity of the sample was not uniform as the presence of platelets and sheets were observed in the TEM analysis of the product. The resulting properties of the nanotubes are not explored in great detail, but this report offered another example of how the electrode composition within the arc-discharge set-up could be tuned to produce BCN-NTs.

Suenaga *et al.*[154] produced layered MW BCN-NT structures, *i.e.* a core of carbon surrounded by outer layers of boron nitride. This was achieved by arcing hafnium boride in the presence of nitrogen. Similar to the earlier examples however, the reaction product contained many impurities such as BCN coated hafnium nanoparticles. Due to the preference for phase separation, as observed between BN and C layers, the authors suggested it may be difficult to

control the homogeneity of boron and nitrogen incorporation across the CNT structure *via* the arc-discharge technique. Gourari *et al*. included nickel and yttrium as potential catalysts for the nanotube growth, in addition to packing the electrodes with boron nitride.[142] The incorporation of these catalysts allowed for the production of single walled BCN-NTs. Like previous examples, the products displayed a large number of impurities according to TEM analysis. The study also detailed how the amount of boron and nitrogen present in the precursors was detrimental to the yield of the final product. Whilst arc-discharge offered the first insight into the production of BCN-NTs, the high levels of impurity and high energy requirements associated with the procedure may have limited this technique as a means for mass production.

3.1.1.2. Chemical Vapour Deposition

Following on from the research conducted into arc-discharge techniques, chemical vapour deposition (CVD) became an area of exploration for the production of CNTs and ultimately BCN-NTs. It had previously been used within the thin film community and is now one the most prevalent techniques within the literature for nanotube production. CVD procedures are usually conducted at much lower temperatures (800 – 1000 ^{o}C) than those required for arc-discharge (3500 – 5500 ^{o}C). The apparatus for a standard CVD set-up is shown schematically in Figure 3.2. Typically, a CVD procedure involves flowing a carbon feedstock through a catalyst-containing reaction vessel, which is heated by an encasing furnace. The decomposition of the hydrocarbon source in the presence of a metal catalyst, under an inert atmosphere, promotes the growth of CNTs. As the carbon source decomposes, the carbon atoms generated dissolve into catalyst particles before reaching a saturation-point, where precipitation (*i.e.* CNT growth) occurs. The reaction product can then be collected after cooling the system to room temperature. The CVD procedure affords flexibility when it

comes to the precursor as it can be in either a gaseous, liquid or solid state; these each require slightly different introduction procedures into the reaction vessel.[155] Like the feedstock, there are alternative ways to introduce the catalyst into the reaction furnace, *e.g.* coating a substrate or loading into a reaction boat.[156] There are a number of variations to the CVD procedure, such as water assisted, microwave, low pressure and laser-assisted CVD techniques *etc.* which each allow fine tuning of the reaction environment.[157-160] Like the arc-discharge technique, there are a number of reaction parameters that have been studied for each CVD type, in order to refine the production of CNTs. These typically include the carbon feedstock, catalyst type, substrate, carrier gas flow rates and reaction temperatures, amongst others.[161-165] This highlights how diverse the CVD procedure can be for selective CNT production. Given the use of a catalyst material to promote growth, the nanotubes grown *via* CVD will typically contain metal catalyst impurities in the base or tip (depending on the growth mechanism) as well as the nanotube exterior. In addition to impurities, another potential drawback with CVD procedures, in particular for doped nanotubes, is the use of pyrophoric, flammable and corrosive gases, which can be difficult to handle and pose obvious health risks.[166] Despite this, CVD is seen as a more economical approach to the production of CNTs when compared to arc-discharge and laser ablation methods.[167]

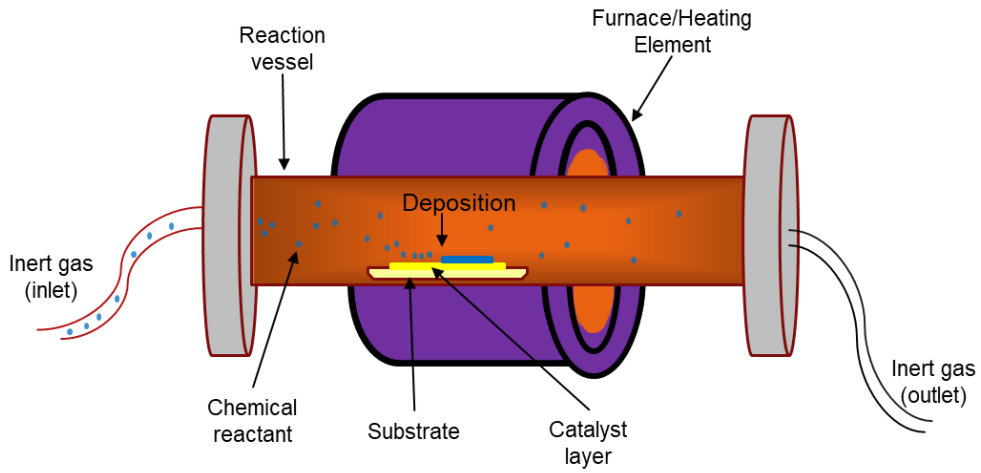


Figure 3.2: Schematic diagram showing the typical set up for a chemical vapour deposition reaction.

CVD procedures have been explored for the production of BCN-NTs. For example, Wang *et al.*[168] used bias-assisted hot-filament CVD to produce SWBCN-NTs. This varies slightly from regular CVD and involves a metal filament acting as the heat source for the reaction as opposed to an electric furnace; potential is applied to the filament which generates a glow-discharge and in this case, a temperature of *ca*. 1750 ^{o}C. The SWBCN-NTs were produced by flowing a mixture of diborane, methane, argon and ethylenediamine vapours over a synthesised catalyst that contained iron, molybdenum and magnesium oxide. This yielded single and double walled nanotubes doped with boron and nitrogen homogenously across the sample. The boron and nitrogen was found to vary across the sample with the nitrogen content typically being much larger. SEM imaging revealed that a large amount of catalyst remained after the synthesis, with the synthesised nanotubes appearing randomly oriented and embedded into the spent catalyst. The authors also noted that this procedure yielded multi-wall graphitic onion impurities, alongside the BCN-NTs. These experiments were performed on a *ca.* 10 mg scale and due to the gas selections, may not be suitable for scaling up. Each of the reactive gases used are flammable, with both ethylenediamine and diborane also being corrosive and toxic. That being said, this work still provided an early example of how BCN-NTs could be grown *via* CVD procedures.

A more standard approach was detailed by Kim *et al.*[169] who produced MWBCN-NTs *via* CVD. A mixture of boron, boron nitride and iron phthalocyanine powder were combined to act as boron, nitrogen and carbon sources respectively. This mixture was annealed under an ammonia atmosphere in the presence of iron nanoparticle coated substrates. The reaction successfully yielded MWBCN-NTs with a bamboo like morphology. Unlike a typical black CNT, here the reaction product was white. As well as visual appearance, the elemental composition further suggests that instead of CNTs doped with boron and nitrogen, the composition of these nanotubes were more akin to BNNTs doped with carbon. The BCN-NTs

had a combined nitrogen and boron content of 90 at.%, with a carbon content of 10 at.%. The authors found that through altering the amount of carbon containing precursor, the reaction product varied significantly. Lower carbon quantities in the precursor mix yielded BNNTs coated in outer layers of carbon instead of doping. Once again, the use of corrosive and toxic gases, in this case ammonia, is not ideal due to the risk they pose to metallic gas manifolds and general health. Whilst technically a BCN-NT, this procedure is more relevant to the boron nitride side of studies. It does however highlight the importance of precursor composition in reaction product during a CVD procedure.

Previous work conducted within our group attempted to produce MWBCN-NTs. Aerosol assisted CVD (AACVD) was utilised during the synthesis.[121] Here, instead of preparing a catalyst prior to the reaction and coating substrates that line the reaction vessel, the catalyst nanoparticles are generated *in-situ*. The catalyst precursor is dissolved in the carbon feedstock, which is then converted into an aerosol mist *via* a piezo-generator before being introduced into a heated reaction tube. Here the catalyst precursor, ferrocene, was dissolved in a mixture of toluene, benzylamine and triethyl-borane which acted as the carbon, nitrogen and boron sources respectively. The generated aerosols were then reacted at *ca*. 1000 ^{o}C which yielded the nanotube product. Upon analysis, it was found that unlike nitrogen doped CNTs grown using an analogous technique, the synthesised nanotubes were not vertically aligned and randomly oriented making it difficult to determine their length. The nanotubes can be difficult to observe due to a sooty impurity layer that coats the deposit, The use of triethyl-borane is not ideal given that it is pyrophoric and therefore difficult to handle in an everyday lab. The presence of nitrogen and boron within the nanotubes was confirmed with XPS and found to be 0.1 at.% each. Whilst a combined doping level of 0.2 at.% is relatively low, the AACVD procedure has the added benefit of producing large quantities during short

reaction times. Comparatively, the analogously produced nitrogen uni-doped CNTs were found to have significantly more nitrogen doping at 2.2 at.%.

3.1.1.3. Pyrolytic Techniques

An alternative to both arc-discharge and CVD procedures come in the form of pyrolytic techniques. Pyrolysis is essentially a derivative of CVD. Typically it involves the thermal treatment of one or more materials, in an inert atmosphere, to change the properties of said material. The reaction set-up is similar to that of CVD and usually involves a crucible, containing a reaction mixture, being centred inside a reaction tube which itself is surrounded by a furnace, see Figure 3.3 for reference. Where CNTs are concerned, and more specifically BCN-NTs, pyrolytic techniques can be classified into two subsections. The first typically involves taking a mixture of materials and sealing them inside a reaction vessel before heating to high temperatures under gas flow. A catalyst will typically be included in the mixture to catalyse the formation of the desired product.[170, 171] The gaseous environment can also be tuned (*i.e.* through the introduction of nitrogen or boron containing gases) to alter the composition of the desired product. Due to the nature of the synthesis, impurities within the product are common and control over the product is not as well defined as for other CNT synthesis techniques. That being said, the use of this route for the production of BCN-NTs is becoming increasingly prevalent within the literature given the relative ease of synthesis.

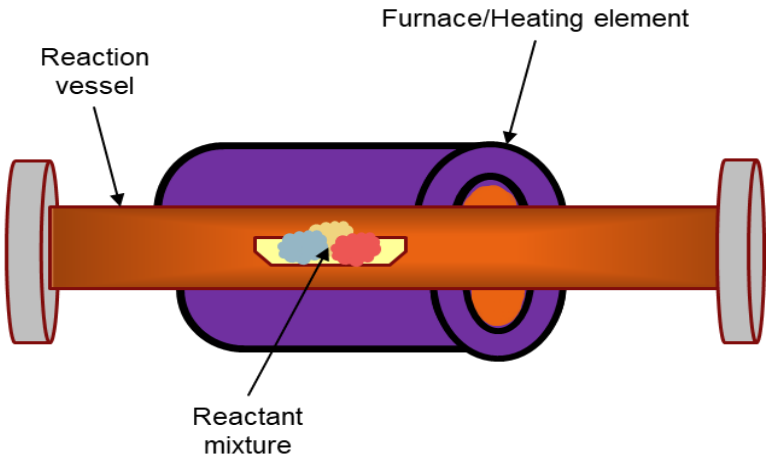


Figure 3.3: Schematic diagram showing the typical set up for pyrolytic synthesis.

The second reaction type takes pre-prepared carbon nanotubes and reacts them with either a solid reactant or a reactive gas, whilst heating. This is often used to introduce dopants into the nanotube but, depending on the reactants used, can also create a coating on the nanotube.[172] Often, when this solid-state route is explored for introducing dopants, harsh oxidative pre-treatments are used in order to introduce reactive defect sites where doping is thought to be more feasible.[173, 174] Alternatively, corrosive gases or oxidising agents are used to etch the nanotube starting material *in-situ*. These treatments can be detrimental to the nanotubes structure and properties and in some cases, lead to unzipping.[175]

Early examples of producing BCN-NTs *via* pyrolytic routes were based on work which involved reacting CNTs in the presence of B_2O_3 vapours at elevated temperatures to introduce boron dopants.[176] These substitution reactions consisted of introducing a nitrogen containing gas simultaneously with B_2O_3 to react with MWCNTs; the temperatures required for these reactions are high and typically range from *ca.*1500 – 1800 ^{o}C.[177, 178] In some cases, metal oxide additives were used to act as oxidising agents. However, this can etch away the nanotube during the reaction and can also lead to the formation of impurities.[179] Upon analysis of these products, it became apparent that the BCN-NTs were closer to BNNTs as

opposed to a CNT doped with heteroatoms. Depending on the reaction conditions, the CNTs could be completely converted to BNNTs, and oxidation of the product yielded BNNTs.[180] This is likely due to the fact that the simultaneous introduction of B_2O_3 and N_2/NH_3 has a preference for the formation of a BN coating. Chiang *et al.*[181] have recently detailed how the introduction of B_2O_3 and NH_3 together led to the formation of a segregated boron nitride coating which encased their carbon nanotubes. However, these works highlight how effective the post-synthesis treatment of CNTs with reactive vapours can be.

One-pot pyrolytic routes towards BCN-NTs have been recently explored. For example, BCN-NTs have been grown through annealing polyethylene glycol, boric acid and urea together in an inert atmosphere.[182] The randomly oriented nanotubes had a diameter of *ca*. 0.1 μm and a variable B, N and C content. Thermal analysis revealed that after oxidation, a residual weight of around 65 wt.% was observed. The authors suggested that this was attributed to boron nitride species meaning that the nanotubes were mainly composed of boron nitride. This report suggested that the nanotubes are akin to turbostratic carbon, but similar studies have proposed the product yielded is amorphous.[144] Given the discrepancies, this approach may therefore lead to non-uniform reaction products. Further to this, whilst this work utilises readily available precursors, very similar techniques have also been used to produce other carbon nanomaterials. Jin *et al*.[183] used the same combination of precursors to produce BCN graphite flakes. This report suggest there is the potential for impurities or side-products forming when following this one-pot synthesis for BCN-NTs. Despite this, the method allows BCN-NTs to be produced with relative ease which has encouraged application testing which in turn has stimulated further interest. This highlights the significance of being able to produce BCN-NTs readily in order to facilitate further research.

3.2. Materials and Methods

3.2.1. Chemicals

Benzylamine (ReagentPlus, 99 %) solution and boric acid (≥ 99.5 %) powders along with ethanol (puriss, ≥ 99.8 %) were purchased from Sigma-Aldrich and used without further treatment. Ferrocene (99 %) was also purchased from Sigma-Aldrich but was further purified *via* sublimation. The deionised water used was type 2 (0.45 µS/cm). Benzylamine was selected for the CNT growth process as it (i) acts as a carbon feedstock during the AACVD process and (ii) the amine group can donate nitrogen atoms during the growth, which incorporates nitrogen dopants into the nanotubes. Boric acid was chosen as a low-cost and readily available boron source for the second doping step. Ferrocene acts as a precursor which thermally decomposes to iron nanoparticles which catalyse the carbon nanotube growth. As noted, the ferrocene was sublimed in order to remove residual impurities.

3.2.2. Characterisation

Scanning electron microscopy (SEM) micrographs were obtained on a JEOL-840F with a 4 kV accelerating voltage. Energy dispersive X-ray (EDX) data was recorded on a Zeiss-Merlin microscope fitted with an in-lens SE detector. For the SEM and EDX measurements each of the materials in powder form were loaded onto conductive carbon films which were attached to aluminium stubs. Transmission electron microscopy (TEM) was performed on a JEOL-3000F microscope with an accelerating voltage of 200 kV. Samples were prepared by dispersing 1 mg of nanotubes in 10 ml of ethanol. The solutions were then drop-cast onto lacey carbon copper grids (400 mesh). The LabRam Aramis Raman confocal microscope (λ = 532 nm, 56 mW output, Si-wafer reference) was used to record spectra. Samples were

prepared by drop casting the same solution onto glass microscope slides and allowing the solvent to evaporate. UV-Vis absorption spectra were recorded with a Cary 5000 UV-Vis spectrophotometer by placing this solution in a transparent quartz cuvette (10 mm x 10 mm). X-ray photon electron spectroscopy was performed on each of the powdered products using a Thermo Scientific K-Alpha X-ray photoelectron spectrometer, fitted with a monochromated Al X-ray irradiation source. The source was operated at 12 keV and a 400 μm spot size was used. The analyser operates at a constant analyser energy of 200 eV for survey scans and 50 eV for detailed scans. Charge neutralization was applied using a combined low energy/ion flood source. Normalised atomic percentages were determined from peak areas of the elemental peaks detected on the survey scan following background subtraction and application of thermo sensitivity factors. These spectra were acquired by the Oxford Materials Characterisation Service and each of the spectra were deconvoluted using the CasaXPS software by myself. The thermogravimetric analysis was performed on a Perkin Elmer Pyris 1 TGA. The oxidation profiles recorded involved heating the CNT samples to 100 ^{o}C and holding for 10 minutes to ensure solvent removal; the sample temperature was then ramped up to 900 ^{o}C and held for an additional 15 minutes before cooling. The oxidation profile was recorded under an air flow (0.02 SLM).

3.2.3. Synthesis of Nitrogen-Doped Carbon Nanotubes

Multiwalled nitrogen doped carbon nanotubes (N-CNTs) were synthesised using an AACVD technique previously utilised by our group.[146] The aerosol precursor solution consisted of ferrocene (5% wt.) dissolved in benzylamine, with the latter acting as both a carbon and nitrogen source. Prior to synthesis, the furnace was mapped, and afterwards the product was collected from the central zone (+/- 60 mm) of the reactor. The selected carrier gas for the aerosol was argon (1.4 SLM) and the system was purged for 30 minutes prior to the reaction.

The aerosol was generated using a piezoelectric-fitted unit. The precursors were heated inside the quartz tube (B19/26 socket and cone, 24 mm diameter), at a temperature of 800 ^{o}C, for 20 minutes. The initial reaction product that was utilised for the co-doping procedure will be referred to as N-CNT.

3.2.4. Synthesis of Carbon Nanotubes

MWCNTs were synthesised using an AACVD technique previously utilised by our group.[184] The aerosol precursor solution consisted of ferrocene (5% wt.) dissolved in toluene, with the latter acting as the carbon feedstock. The selected carrier gas for the aerosol was argon (1.4 SLM) and the system was purged for 30 minutes prior to the reaction. The precursors were heated inside the quartz tube (B19/26 socket and cone, 24 mm diameter), at a temperature of 850 ^{o}C, for 75 minutes. This reaction product will be referred to as CNT.

3.2.5. Synthesis of Borocarbonitride Nanotubes

The synthesis of multiwalled borocarbonitride nanotubes (BCN-NTs) involved thermal treatment of the product from the initial reaction in 3.2.3. The standard procedure is as follows. The as-synthesised N-CNTs were ground with boric acid (1:1) using an agate pestle and mortar for 30 minutes, until a fine powder was obtained. The mixture was then placed inside an alumina boat centred in an alumina tube furnace (38 mm diameter). Before the reaction, the whole system was purged with argon (0.5 SLM). The solid mixture was then heated to 1000 ^{o}C and annealed for a duration of 4 hours under argon flow (0.35 SLM). In order to remove any residual boron reagents, the obtained product was collected, dispersed and boiled in ethanol (1000 ml), for 1 hour, before separating via vacuum filtration through a

PTFE membrane (pore size 0.2 μm). The powder was then re-collected and boiled in distilled water (1000 ml), for a further hour, before separating once again *via* vacuum filtration and finally rinsing with near boiling water (2000 mL). The final product was then dried overnight in a vacuum oven at 70 ^{o}C before further analysis. Henceforth the reaction products after the co-doping procedure will be referred to as BCN-NT.

3.2.6. Synthesis of Boron-Doped Carbon Nanotubes

In order to determine the influence of intrinsic defects on the co-doping procedure, B-CNTs were synthesised using a similar procedure detailed in 3.2.5. The standard procedure is as follows. The as-synthesised CNTs were ground with boric acid (1:1) using an agate pestle and mortar for 30 minutes, until a fine grey powder was obtained. The mixture was then placed inside an alumina boat centred in a tube furnace. Before the reaction, the whole system was purged with argon (0.5 SLM). The solid mixture was then heated to 1000 ^{o}C and annealed for a duration of 4 hours under argon flow (0.35 SLM). In order to remove any residual boron reagents, the obtained product was collected and washed using the same procedure detailed in section 3.2.5. Henceforth the reaction products from this section will be referred to as B-CNT.

3.3. Results and Discussion

3.3.1 Synthesis of BCN-NTs

3.3.1.1 SEM and TEM Analysis

BCN-NTs were produced using a two-step synthesis route which involved both CVD and substitutional techniques, this is shown schematically in Figure 3.4. The N-CNTs, that were used as the template material for the substitutional doping, were grown through the aerosol assisted CVD of a benzylamine-ferrocene mixture. The use of benzylamine as the reaction feedstock allows the incorporation of dopants atoms within the nanotubes, due to the presence of the nitrogen containing amine group that is attached to the benzyl ring.

The N-CNTs were used as the precursor for the synthesis of BCN-NTs as they are structurally uniform and can be produced in relatively large yields.[146] Additionally, due to the incorporation of nitrogen dopant atoms within the N-CNTs, they possess uniformly distributed defective sites across the nanotube. This is because the introduction of heteroatoms into CNTs leads to the formation of structural defects within the graphitic structure. Previous work has suggested that substitutional doping will occur more readily at defect sites and hence, we envisaged that the intrinsic defective nature of the N-CNTs would aid the substitutional incorporation of boron dopants across the nanotube to produce BCN-NTs.[173, 185]

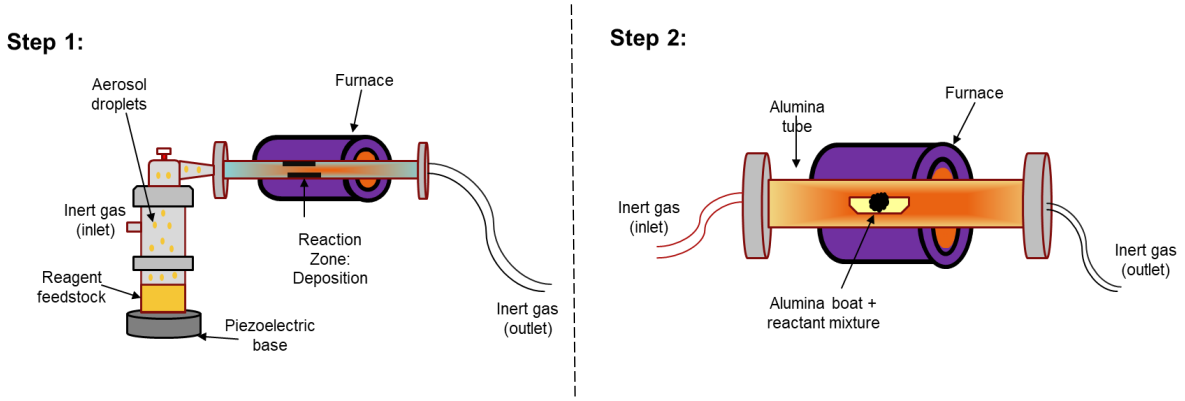


Figure 3.4: Schematic diagram for the apparatus employed here for the synthesis of BCN-NTs. Step (1) shows the aerosol assisted chemical vapour deposition of N-CNTs whilst Step (2) demonstrates the conversion to BCN-NTs through a substitutional reaction.

SEM was used to image the morphology of the as-synthesised starting material. As can be seen in Figure 3.5, the N-CNTs which are grown in a uniform and vertically aligned arrangement of flake-like nanotube bundles. The average length of the N-CNTs was measured to be *ca.* 34 μm, as highlighted in the statistical profile of measured lengths across the sample, shown in the appendix.

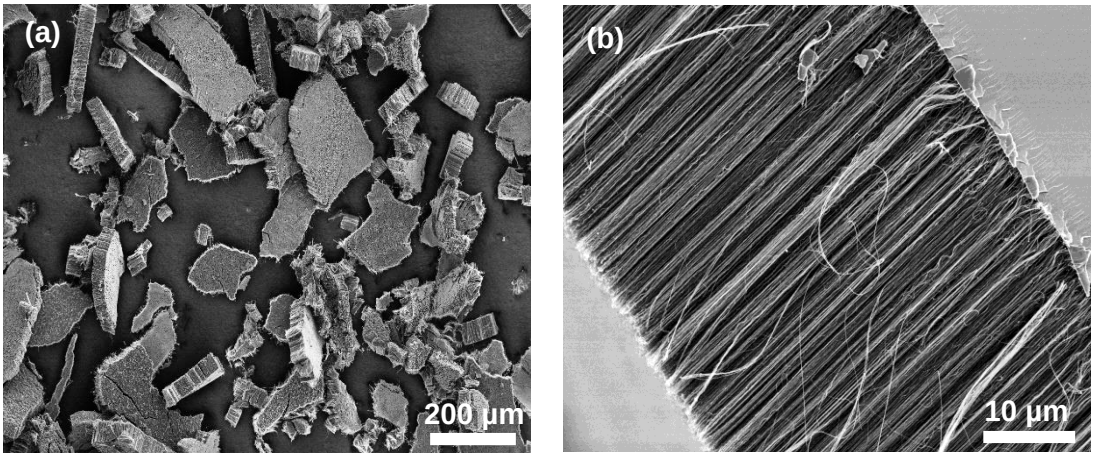


Figure 3.5: SEM micrographs that show an overview of vertically aligned N-CNT flakes (a) and a magnified cross-section of one of the nanotube bundles that allowed length measurements to be determined.

After the initial synthesis, the N-CNTs were subject to a substitutional doping reaction. For this second step, boric acid was selected as the boron precursor as on heating, it decomposes

to produce boron oxide vapour, as can be seen in equations 3.1-3; it has previously been demonstrated that boron vapours react with CNTs at elevated temperatures and hence here it was used as the reactive agent.[176, 186-188] The standard conditions for the boron doping step involved grinding the powder precursors together before then annealing at 1000 ^{o}C for 4 hours; as we will see later in the chapter, alterations were made to these standard conditions.

$$(\mathbf{3.1}) \quad H_3BO_{3\,(s)} \rightarrow HBO_{2\,(l)} + H_2O_{\,(g)}$$

$$(\mathbf{3.2}) \quad 4{\cdot}HBO_{2\,(l)} \rightarrow H_2B_4O_{7\,(l)} + H_2O_{\,(g)}$$

$$(\mathbf{3.3}) \quad H_2B_4O_{7\,(l)} \rightarrow 2{\cdot}B_2O_{3\,(l/g)} + H_2O_{\,(g)}$$

Nanotubes for the precursor material and subsequent BCN-NTs were imaged through TEM, as shown in Figure 3.6, to gain further insight into individual nanotube morphology. An individual N-CNT micrograph is shown in Figure 3.6(a). The most striking observation is that the N-CNTs possess a ‘bamboo’ like inner tube morphology which is characteristic of doped CNTs. It has been suggested that during the growth of doped nanotubes, dopant atoms substitute for carbon atoms within the hexagonal lattice leading to disruptions in the nanotube wall formation.[189] As this growth and dopant incorporation proceeds, wall curvatures occur which leads to compartmentalisation that can be observed within the inner tube morphology of the nanotubes.

Previous post-synthesis treatments of CNTs have reported the formation of boron-nitride coatings when nitrogen and boron sources are introduced simultaneously.[190] Here, therefore, the doping was performed in two isolated stages, to promote heteroatom substitution as opposed to forming a h-BN coating on the exterior of the nanotube. Through analysis of TEM micrographs, the overall diameter of the nanotubes were measured; the sample size for this

analysis was based on 250 nanotubes for both the N-CNT precursor and the BCN-NTs. The starting N-CNTs were measured to be *ca*. 30 nm as can be seen in Figure 3.6. The respective size distributions shown in Figure 3.6(c/d), demonstrates that the co-doping procedure did not affect the measured nanotube diameter of the BCN-NTs, when compared to the starting material. Due to there being no observable increase in the diameter of the BCN-NTs, it was confirmed that isolating the doping into two separate steps does not create a coating on the nanotube exterior which we would expect to increase the measured diameter noticeably.

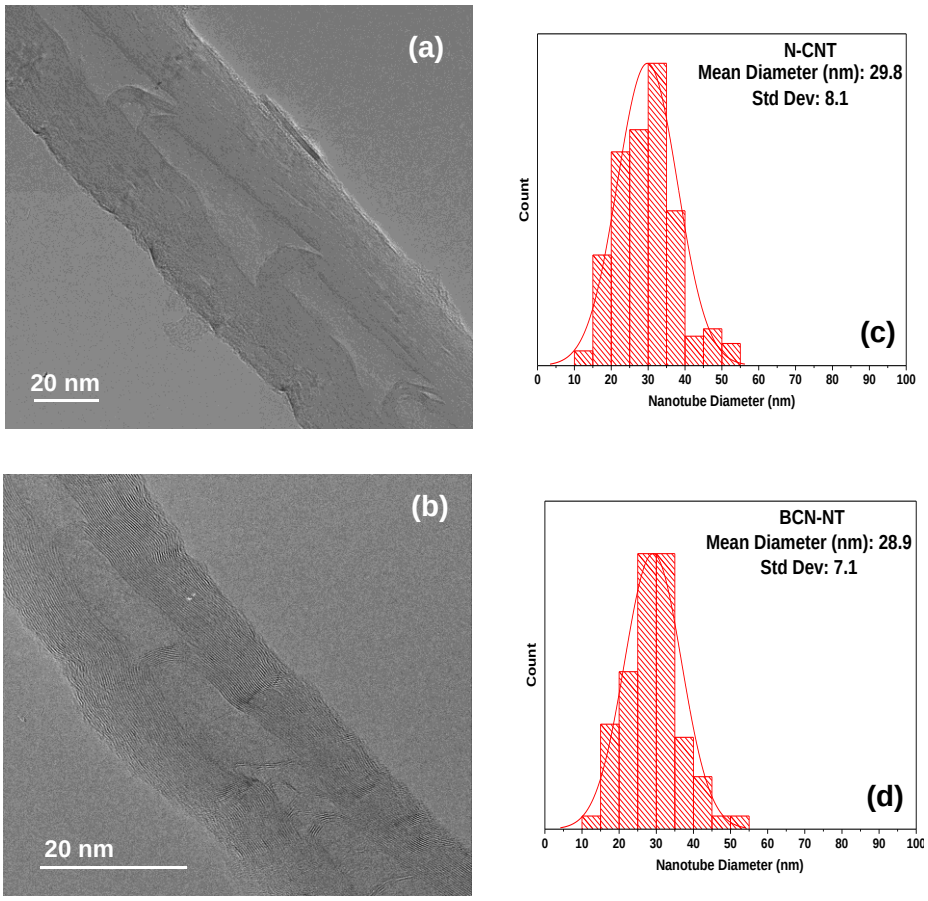


Figure 3.6: TEM micrographs revealing the inner-tube morphology of the N-CNT precursor (a) and the BCN-NTs (b) along with histograms for their respective diameter measurements (c/d).

As we can see in Figure 3.6(b), the BCN-NTs topography remains almost unchanged when compared to that of the N-CNTs shown Figure 3.6(a). TEM imaging also observed that after the co-doping procedure, the 'bamboo' inner tube morphology is maintained and there have

been no obvious deformations on the nanotubes. These observations demonstrate that this synthesis technique is non-destructive and effective at maintaining the integrity of the starting nanotube morphology. The use of the intrinsically defective N-CNTs circumvents any need for nanotube pre-treatments, such as acid etching, which are often employed as a pre-requisite to boron doping and, in some cases, have led to the unzipping of nanotubes.[175]

3.3.1.2 Elemental Analysis of BCN-NTs

Energy dispersive X-ray (EDX) analysis was used to probe the elemental distributions across the nanotube samples. Elemental mapping for the N-CNT precursor revealed that there is even coverage of nitrogen across the whole sample; this is highlighted in the appendix. The observation that nitrogen is uniformly distributed across individual nanotubes is in line with previous observations made by our group that showed nitrogen dopants are homogenously distributed across the nanotubes produced using this method.[146] It was envisaged that the even distribution of nitrogen dopants in the template N-CNTs would assist uniform boron doping across the sample, as opposed to forming segregated layers and domains of hexagonal boron nitride and graphitic carbon. The latter would be more akin to a hybrid BN/CNT material, as opposed to CNTs co-doped with nitrogen and boron heteroatoms, and is typically encountered when both nitrogen and boron precursors are introduced simultaneously together during the synthesis.[190, 191] Previous studies have suggested that the substitution of heteroatoms into graphitic carbon occurs more readily at preferential defects.[173, 185] It was therefore expected that the intrinsically defective composition of the N-CNTs would aid further uniform doping across the sample. Due to the nitrogen atoms essentially acting as surface defect sites, boron doping was anticipated to occur in the surrounding vicinity.

Figure 3.7 shows the EDX maps obtained for the BCN-NTs, revealing the distribution of dopants across the prepared sample.

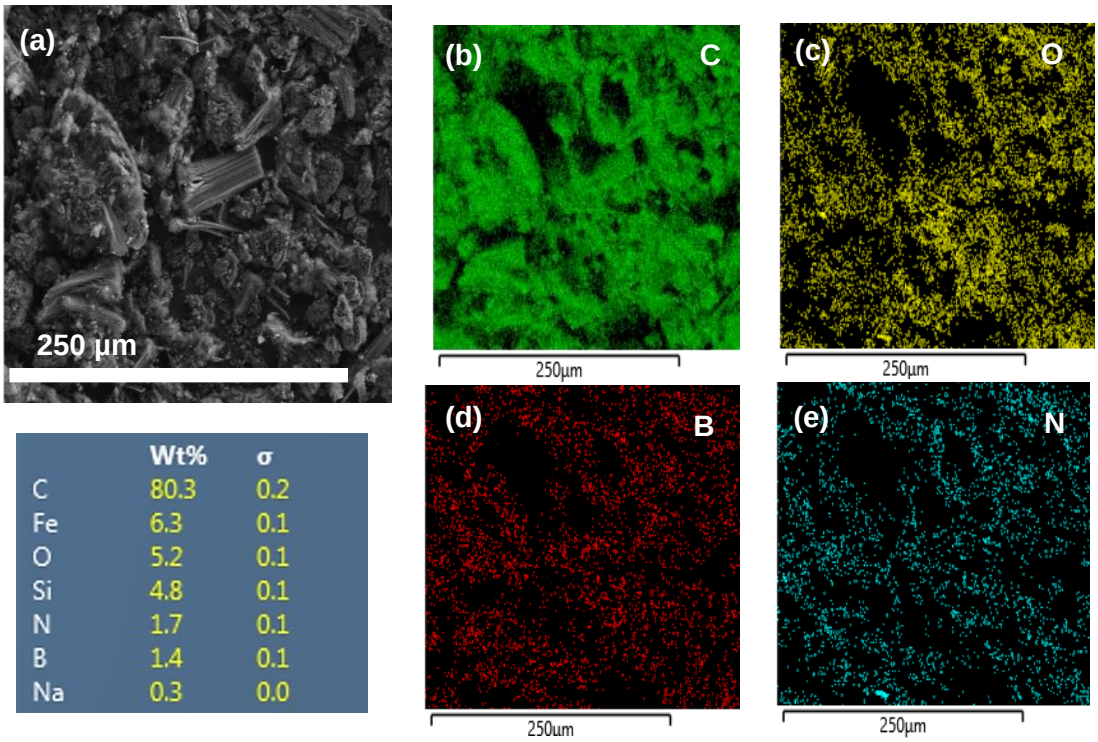


Figure 3.7: An SEM micrograph of the BCN-NTs (a) along with the respective elemental maps for carbon (b), oxygen (c), boron (d) and nitrogen (e) highlighting the uniform distribution of dopant atoms along with the mini-quant table obtained during the scan.

As can be seen in Figure 3.7, after the co-doping step, boron appears homogenously distributed across the BCN-NT sample as evinced by the EDX mapping. This indicates the incorporation of boron into the nanotubes and the successful formation of BCN-NTs. The map shows that, like nitrogen doping in the template, there is uniform boron coverage across the nanotubes. Due to the even distribution of nitrogen sites across the initial starting material, both boron and nitrogen heteroatoms are uniformly spread in the resulting BCN-NT product. This supports our prediction that the boron doping would occur in surrounding vicinity of nitrogen defects, as it has it has previously been established that substitutional doping can occur more readily at defect sites.

The presence and quantification of dopant atoms within the nanotubes were further confirmed with X-ray photoelectron spectroscopy (XPS). The compositions for the BCN-NTs were probed using these spectra in order to further understand the co-doping procedure. Initially the N-CNT precursor was analysed to act as a reference point for the BCN-NTs. As shown in Figure 3.8, the survey spectra displayed three prominent peaks at ca. 285 eV, 531 eV and 400 eV which correspond to the C1s, O1s and N1s peaks respectively.[192-194] After being subject to the co-doping step, for the BCN-NTs, it is apparent that an additional peak arises in the survey spectra Figure 3.8(b) at ca. 191 eV, which corresponds to the B1s binding energy.[195]

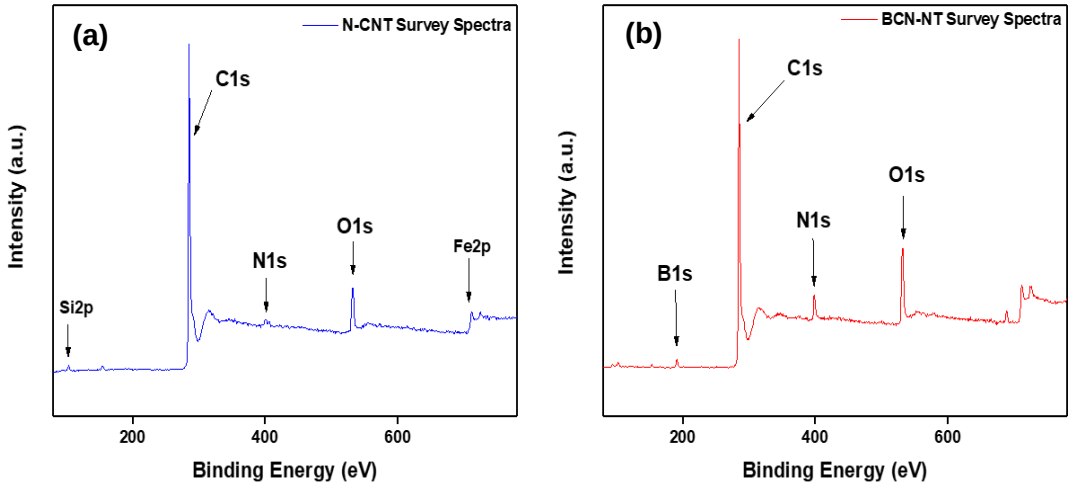


Figure 3.8: XPS survey spectra obtained for the N-CNTs (a) and for the BCN-NTs after the co-doping procedure (b) which reveal the elemental components of the synthesised materials.

This observation confirms the presence of boron dopant atoms within the nanotube sample. The B1s peak is downshifted significantly when compared to that recorded for the boric acid precursor reagent (see appendix). The shift, as well as further deconvolution, demonstrated that boron has been successfully incorporated into the graphitic carbon nanotube structure. It also shows that any unreacted reagent has been removed with the cleaning process, which involved boiling the sample in multiple solvents that boric acid is highly soluble in for a

prolonged period. The overall boron content measured within the nanotubes was 3.4 at.% and a nitrogen content of 3.5 at.%. This boron content is significantly higher than previous procedures used within our group that have solely-utilised AACVD.[121] The aforementioned technique is limited by the amount of boron containing reagent that can be dissolved into the feedstock. Additionally, the boron reagent that was used for that work is pyrophoric, making it difficult to handle, and yields a non-vertically aligned product coated in a carbonaceous impurity layer.

Deconvolution of the peaks displayed within the XPS spectra gives further insight into the chemical bonding present in the BCN-NTs. Figure 3.9 shows the B1s spectrum recorded for the BCN-NTs. The B1s peak can be broken down into four major components; these appear at ca. 188.7 eV, 190.8 eV, 191.7 eV and 192.7 eV, which can be assigned to B-C, B-N, B-C_X-O_Y and B-O bonding species, respectively.[196-200]

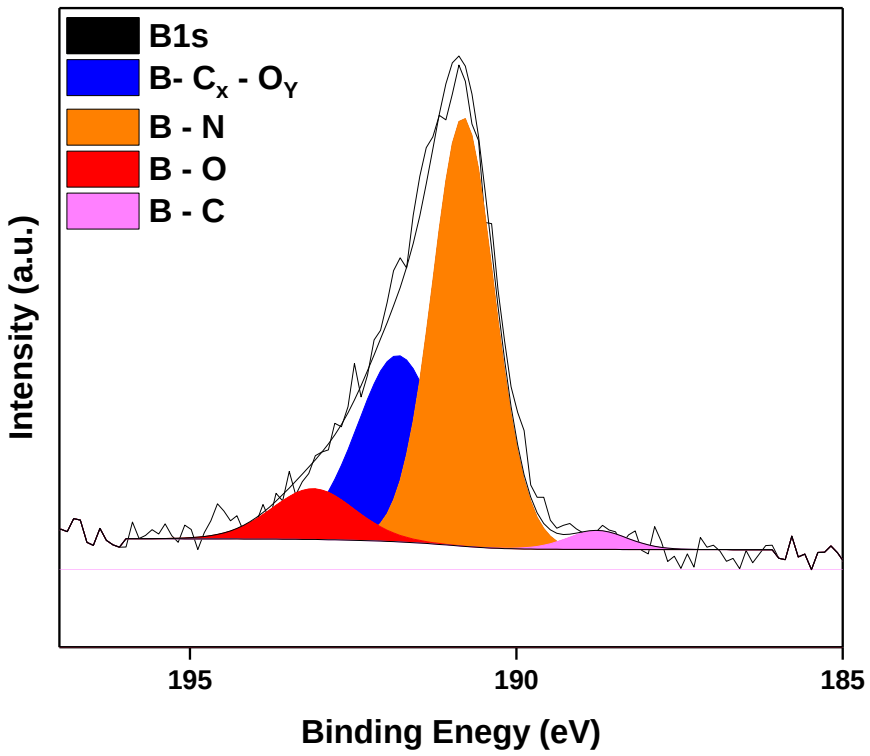


Figure 3.9: High resolution XPS spectra showing a typical signal recorded for B1s electrons within the BCN-NT sample prepared under standard conditions. The spectrum has been fitted with curves, using CasaXPS, that represent various bonding types within BCN systems.

These bonding configurations are expected for a typical borocarbonitride system. The B-O peak recorded in the BCN-NTs is downshifted by *ca*. 1.1 eV when compared to the boric acid precursor, suggesting these bonds are incorporated within the nanotube as opposed to being present as unreacted precursor. Due to the electron accepting nature of boron, incorporation into the graphitic lattice would reduce the polarity of B-O bonds and hence offers an explanation for the observed shift to a lower binding energy when incorporated within the nanotube structure.

Figure 3.10 shows the N1s spectra recorded for the N-CNT precursor material while the spectrum recorded for the as-synthesised BCN-NT can be seen in Figure 3.11.

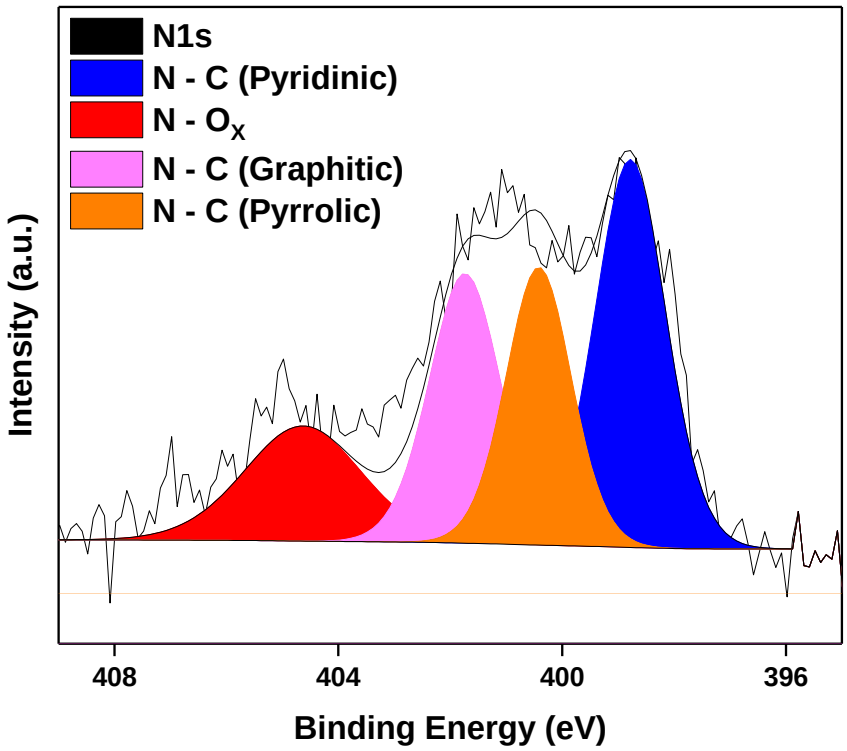


Figure 3.10: High resolution XPS spectra showing a typical signal recorded for N1s electrons within the N-CNT sample prior to being subject to the co-doping step. The spectrum has been fitted with curves, using CasaXPS, that represent various bonding types within nitrogen-doped graphitic systems.

The N1s peak displayed within the BCN-NTs can be broken down into four component parts. The peaks ca. 398.4 eV, 399.0 eV, 400.1 eV and 401.6 eV correspond to N-B, N-C (pyridinic), N-C (pyrrolic) and N-C (graphitic) respectively.[201-204] The N1s spectra for the BCN-NTs differ slightly when compared to the N-CNT precursor which does not display a N-B peak. Instead, when we examine the N1s for the N-CNTs, in addition to seeing the pyridinic, pyrrolic and graphitic peaks, we also observe a peak at *ca*. 404 eV which corresponds to adsorbed nitrogen-oxide species at pyridinic sites on the nanotube surface.[205]

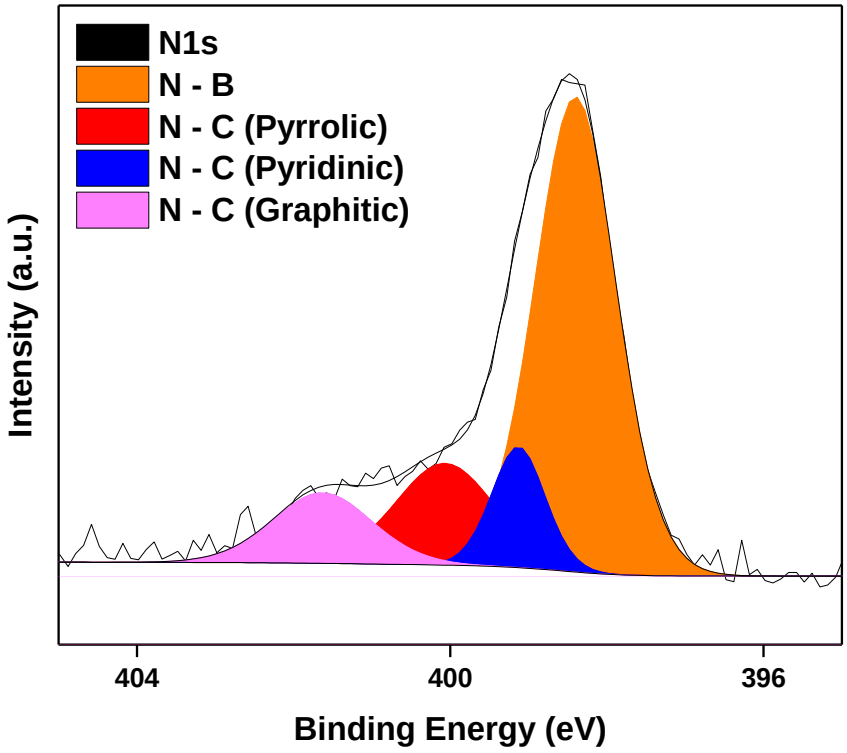


Figure 3.11: High resolution XPS spectra showing a typical signal recorded for N1s electrons within the BCN-NT sample prepared under standard conditions. The spectrum has been fitted with curves, using CasaXPS, that represent various bonding types within BCN systems.

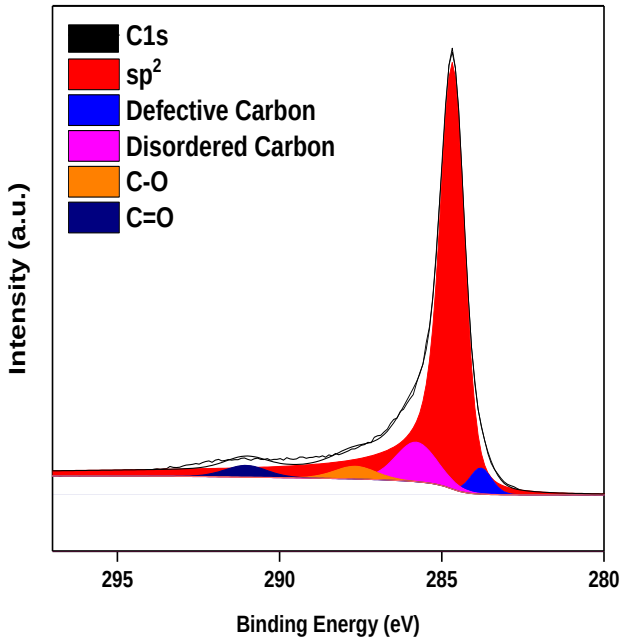
Upon the introduction of boron into the nanotube, the proportion of N-C bonding decreases, in particular for the pyridinic species. This suggests that during the co-doping step, pyridinic sites are sacrificed to form N-B bonds in addition to other boron bonding species. Interestingly, this result is similar to those obtained by both Fujisawa and Liu *et al*.[206, 207]

They each detail that during the thermal treatment of N-CNTs, it is the pyridinic sites that are subject to losses first. Upon annealing, the measured pyridinic contribution to the measured N1s doping peak decreases. It has been suggested that due to the relative energy of pyridinic sites being lower than other bonding types, that they are found to rearrange quicker than other dopant sites.[207, 208] The observation made in this work was further probed in section 3.3.5 *via* computational analysis and will be discussed at greater length there.

In addition, the results further support the prediction that the incorporation of boron within the nanotube would occur in the vicinity of nitrogen dopants due to their defective nature. The preference for doping to occur at defective sites was further supported by repeating the synthesis procedure using undoped MWCNTs to produce B-CNTs. The MWCNT precursor is intrinsically less defective than the N-CNTs. The B-CNTs produced via this route contained 0.8 at.% boron compared to 3.4 at.% in the BCN-NTs. The significant increase confirms the importance of the intrinsic defect sites within the N-CNTs in assisting the substitutional doping process across the nanotubes. This suggests that by modifying the nitrogen content of the precursor material we would be able to tune the boron content of BCN-NTs, which could be an avenue to explore in future.

The C1s peak recorded for BCN-NTs is shown in Figure 3.12 along with a comparative breakdown of the constituent components in Table 3.1. The C1s peak was fitted with a model based on that proposed by Blume *et al.*[192] which accounts for defective and disordered carbon contributions to the nanotube. Due to the dominance of the sp^2 graphitic peak, that is centred at 284.7 eV, and the small dopant contents, it is difficult to infer much from the C1s spectra. The combined defective and disordered contributions to the C1s peak remain almost the same for each of the N-CNT and BCN-NT, with an overall 0.3% increase for the latter. We do note however that the peak distribution ratio alters after the co-doping step. The defective peak contribution, at lower binding energies, is increased for the BCN-NT when compared to

the N-CNT precursor. This could be due to the incorporation of boron into the graphitic network, which typically appears as a peak at a lower binding energy to that of the sp^2 peak and nitrogen bound species.[209] Additionally, we also not that the sp^2 peak contribution to the C1s is slightly larger for the BCN-NTs (0.6% greater) as opposed to the precursor material. This is indicative of improved graphitisation after the co-doping procedure.



Sample	sp^2	Defective Carbon	Disordered Carbon	C-O	C=O
N-CNT	83.9%	1.9%	8.6%	2.8%	2.8%
BCN-NT	84.5%	3.0%	7.8%	2.5%	2.2%

Figure 3.12: High resolution XPS spectra showing a signal recorded for C1s electrons within the BCN-NT sample prepared under standard conditions that has been deconvoluted and Table 3.1: a comparison of the constituent peak contributions to the C1s peak recorded for N-CNTs and BCN-NTs.

3.3.2. Computational Study of BCN Bonding Sites

In section 3.3.1.2. the XPS analysis of the N-CNT precursor material and resulting BCN-NTs was detailed. It was revealed through analysis of the XPS data that the incorporation of boron into the nanotubes led to a reduction in the nitrogen-carbon bonding in place of boron bonding species. In particular the amount of pyridinic species, displayed within the N1s spectra, were reduced in the final BCN-NT product. To further investigate this phenomenon,

simulations were performed in order to understand the stability of various doping sites within the nanotube when compared to the sacrificial pyridinic site.

Ab-initio calculations were performed in order to gauge the relative stability of various boron bonding sites with respect to the pyridinic nitrogen sites. This work was undertaken with the assistance of Eoin O'Sullivan who performed the calculations. Due to time and computational access constraints, the work was modelled using a graphene sheet as opposed to MWCNTs in order to give a representation of the bonding stabilities within a graphitic network. A suitable slab model was established, which compromised between slab size, basis set, and Monkhorst-Pack k-space grid. A large slab size (120 atoms) is employed to accommodate the pyridinic structure. The stability of various structures were estimated from formation energies using equation 3.4:

$$E_f = E_{slab} - \sum_i N_i . \mu_i \quad (3.4)$$

Here, E_f denotes the formation energy, E_{slab} the total energy calculated for the structure, and N_i and μ_i represent the total number and chemical potential of each atom, respectively. The chemical potential of carbon (μ_C), nitrogen (μ_N) and boron (μ_B) are calculated via DFT. E_f of the graphene and pyridinic sites were set to zero and taken as the reference for each set of calculations.

In order to form an understanding of the various nitrogen dopant types for the N-CNT precursor material, potential nitrogen site stabilities were compared to an undoped graphitic carbon system. These results are summarised in Table 3.2, along with a representation of the sites that were modelled, as shown in Figure 3.13.

Table 3.2: A table summarising the simulated energy of formation values for various nitrogen bonding sites in relation to a pristine graphene binding species.

Dopant Site	Relative Energy of Formation (eV)
C-C$_{graphene}$	N/A
C – N$_{pyridinic}$	+7.00
C – N$_{pyridinic\ 4}$	+3.05
C – (N-O$_{pyridinic}$)	+5.80
C – (N-O$_{pyridinic\ 4}$)	+2.92
C – N$_{pyrrolic}$	+2.17
C - N$_{graphitic}$	+1.55

Our results showed that when compared to a pure graphene sheet, the graphitic nitrogen type dopant had the lowest enthalpy of formation and therefore, it can be suggested that it is the most stable out of those modelled. After that, the pyrrolic site was the next most stable site. A variety of pyridinic configurations exist and as such, a selection of dopant sites were probed. Out of all of the pyridine sites, and nitrogen dopants in general, the single nitrogen atom pyridinic site had the highest enthalpy of formation and was therefore the least stable. The four membered pyridine counterpart was found to be more stable in comparison. Previous computational studies by Ayiania *et al.*[210] support this observation and have suggested that the four membered pyridinic site is the most thermally stable pyridinic configuration. In general, the stability of the various nitrogen dopant types here can be summarised as

graphitic > *pyrrolic* > *pyridinic-oxide* > *pyridinic*. These calculations explain the pyridinic and oxide peak loss that were observed in the XPS spectra after the co-doping step.

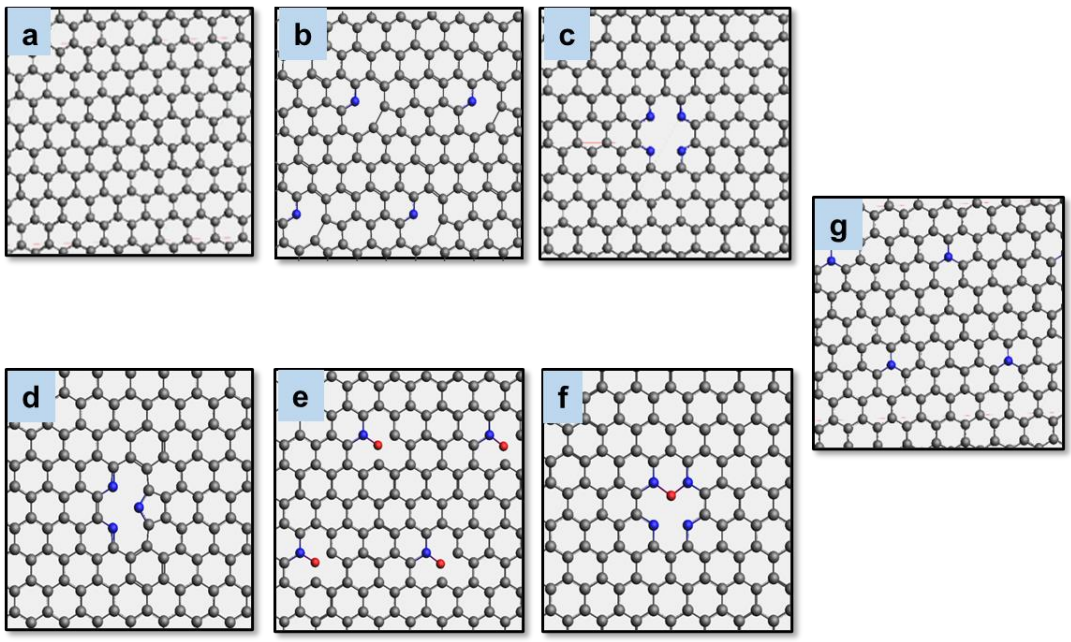


Figure 3.13: Structures used to determine relative stability of nitrogen dopant sites in comparison to a pristine graphene sheet; (a) graphene: C – Cgraphene), (b) pyridine site: C – Npyridinic), (c) four membered pyridine site: C – Npyridinic 4 (d) pyrrolic site: C - Npyrrolic, (e) pyridine oxide site: C-(N-Opyridinic), (f) four membered pyridine oxide site: C-(N-Opyridinic 4) and (g) a graphitic nitrogen site: C-Ngraphitic.

We then looked to further our understanding of the system after the boron introduction. XPS analysis had previously revealed the successful incorporation of various boron bonding types within the nanotubes; therefore these structures were compared to nitrogen dopant sites. Given that the single pyridinic site had the highest enthalpy of formation, and thus lowest stability, we used this configuration for the latter part of this computational study. Pyridine oxide was also included due to the peak loss observed in the XPS. The relative energies of formations for a variety of boron binding sites, when compared to the pyridinic sites, are summarised in Table 3.3. Model structures for the various dopant configurations are found in Figure 3.14. As can be seen, in each case, the relative energy for each of the sites upon boron introduction are energetically favourable in relation to each of the pyridinic sites, given the

negative energy of formation values we observe. This reaffirms the observations made through XPS analysis which showed a reduction in pyridinic species upon the incorporation of boron and supports our hypothesis that the pyridinic sites act as preferential sites for boron substitution to occur during the co-doping procedure, in order to form more stable configurations.

Table 3.3: A table summarising the simulated energy of formation values for various boron bonding sites in relation to pyridinic binding species.

Dopant Site	Relative Energy of Formation (eV)
C – ($N_{pyridinic}$)	N/A
C – ($N\text{-}O_{pyridinic}$)	-1.20
C – (N-B)	-5.50
C – (N-B-O)	-6.78
C – B-O-C	-4.21
C – (B-O)-C	-7.44

It had previously been observed within the literature how under thermal treatments, pyridinic content of N-CNTs can be subject to losses.[206, 207] Sharifi *et al*.[211] have detailed how the pyridinic site can undergo conversions to form more stable graphitic sites during thermal treatments which mirrors what has been seen here. These results demonstrate not only the importance of the intrinsic nitrogen content, but the type of nitrogen doping, in allowing the successful production of BCN-NTs through this synthesis. Given this, it would suggest that

we are able to fine tune the compositions of these nanotubes upon altering the nitrogen content in the starting material. This could act as a potential avenue of research in the future.

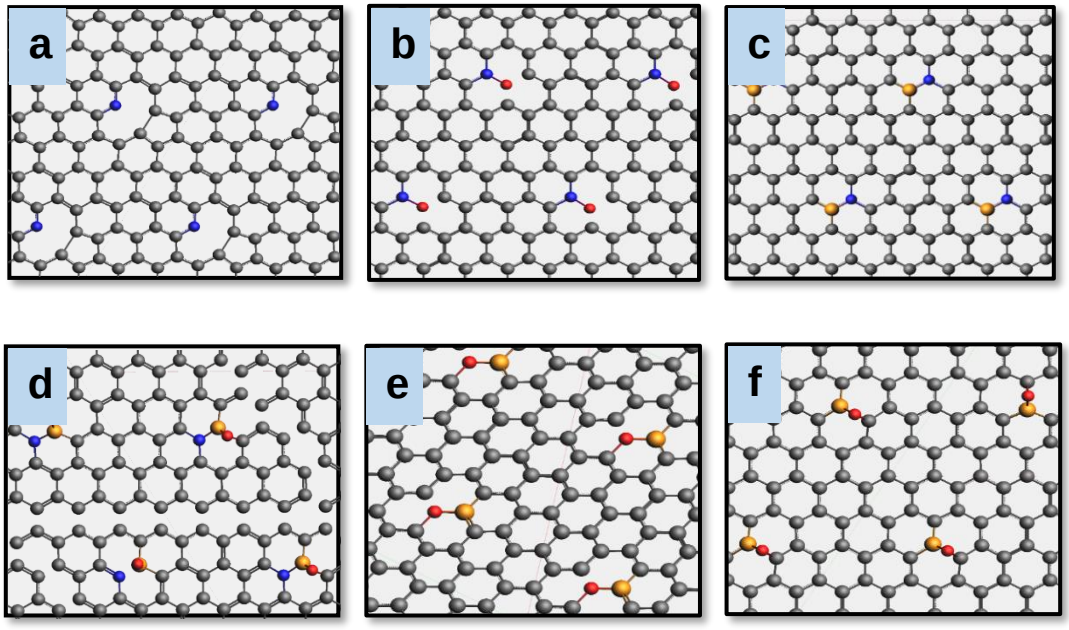


Figure 3.14: Structures used to determine relative stability of potential boron and nitrogen co-dopant sites in comparison to pyridinic sites; (a) pyridine site: C – (Npyridinic), (b) pyridine oxide site: C – (N-Opyridinic), (c) BN doped site: C - (N-B) (d) BNO doped site: C - (N-B-O), (e) boron carboxy doped site: C-B-O-C, (f) boron carboxy doped site: C-(B-O)-C.

3.3.3. Effect of Co-Doping on Crystal Structure

Raman spectroscopy was used to examine how co-doping influences the structural and chemical properties of the BCN-NTs synthesised here. Figure 3.15 shows the region of interest for the Raman spectra recorded for both the N-CNTs and BCN-NTs, which each represent an average over several spots. As can be seen, each of the materials display prominent features that are characteristic of graphitic carbon materials. The two distinct peaks that are highlighted at *ca.* 1345 cm^{-1} and 1580 cm^{-1} can be ascribed to the D and G bands respectively.[133] Through analysis of each of these peaks, information regarding the crystal structure and composition of the nanotube samples can be inferred.

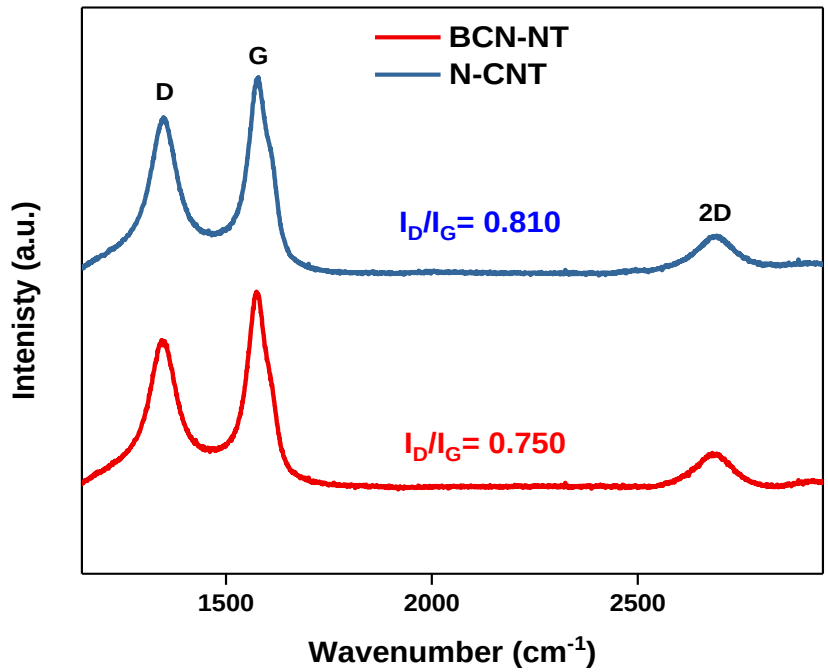


Figure 3.15: Raman spectra obtained for the N-CNTs (blue) and the BCN-NTs (red), which were obtained using a 532 nm laser, highlighting the prominent D and G bands displayed, along with calculated defect densities.

The D band arises due to structural defects that are present within the nanotubes, whereas the G band essentially corresponds to the level of graphitization present within the sample.[133, 212] The I_D/I_G ratio can be quantified through comparison of the D and G peak intensities, and is typically used as a measurement of the defect density present within the nanotubes. The defect density for the N-CNTs, as we can see in Figure 3.15, is relatively high when compared to regular CNTs produced by AACVD (0.44) due to the incorporation of nitrogen atoms.[213] This is because the nitrogen atoms can essentially cause surface defect points within the carbon lattice. It was this intrinsic defective nature of the N-CNTs that made them an attractive candidate for the boron doping procedure. This negated the need for any acid pre-treatments; these have previously been used to etch the nanotube and activate the surface prior to substitutional doping, but they can be destructive to the nanotube structure.[174, 214] When compared to the N-CNTs, the measured I_D/I_G value for the BCN-NTs is lower. We can see therefore, that the BCN-NTs possess a smaller defect density when compared to the starting material. This provides indication that the incorporation of boron into the graphitic

network has modified the microstructure within the nanotubes. This reduction in defect density, mirrors the observation that the graphitic peak in the C1s XPS spectra increased in magnitude for the BCN-NTs. At first these results may seem counterintuitive as the dopant level is increasing. As has been established, dopant sites can essentially be viewed as surface defects and hence, one might expect the incorporation of boron to increase this value. This suggests that there are competing factors that influence the measured defect density of these nanotubes.

The XPS analysis suggested that substitutional doping occurs preferentially at pre-existing nitrogen defect sites, which would mean that the generation of new defects within the co-doped BCN-NTs is less likely to occur, than for other reports of substitutionally doped CNTs such as those by Shan *et al*.[215] They detailed that a substitutional treatment of CNTs led to an increased defect density upon the incorporation of nitrogen heteroatoms. The nanotubes they used, however, had a lower defect density than the N-CNTs used here and were utilised without any further treatment. This reduced density of defects would provide a more difficult reaction pathway when compared to the defective N-CNTs that have been used here and could encourage the formation of new defect sites. Additionally, their reactions were conducted at lower temperatures than utilised here. Previous work has shown that prolonged heat treatments and the incorporation of boron atoms into carbon lattices can enhance graphitisation within CNTs, thus reducing the influence of any new defect sites that may be generated during the co-doping step performed here.[216, 217] It has also been demonstrated by Zheng *et al*.[218] how boron doping of CNTs can reduce the measured defect density. The reactive boron vapours were shown to assist the chemical reduction of defect sites within CNTs.

The G peak itself, in addition to the defect density, can give us further insight into the co-doping procedure. As we can see in Table 3.4, the position of the G peak shifts slightly for

the BCN-NTs. This shifting of the G peak has previously been encountered upon the introduction of boron dopants into the nanotube structure and has also been attributed to enhanced graphitisation within CNTs.[92] Finally, the full width half maximum (FWHM) of the G peak has previously been used as an indicator of the crystalline disorder within carbonaceous materials.

Table 3.4: Summary of the details inferred from the Raman spectra that are displayed in Figure 3.15 for N-CNT and BCN-NTs

Sample	I_D/I_G	G Position (cm^{-1})	G FWHM (cm^{-1})
N-CNT	0.81 (+/- 0.02)	1579.3	66.86 ($^{+}/_{-}$ 0.5)
BCN-NT	0.75 (+/- 0.01)	1576.3	64.58 ($^{+}/_{-}$ 0.4)

The narrowing of the G peak FWHM observed after the co-doping procedure is further indication that the incorporation of boron into the final product has enhanced the overall graphitisation of the BCN-NT when compared to the N-CNTs.[219] The improvement of graphitisation demonstrated in this may be of interest for potential electronic applications, as it has previously been illustrated that reduced defect densities can improve electrical conductivities.[220]

3.3.4. Effect of Co-Doping on Optical Properties

Through UV-Vis analysis, the optical properties of each nanotube sample were probed in order to determine the effect of boron doping. A typical UV-Vis spectra recorded for the

nanotubes is shown below in Figure 3.16, and as can be seen, displays a peak absorbance at a wavelength between 250 and 300 nm.

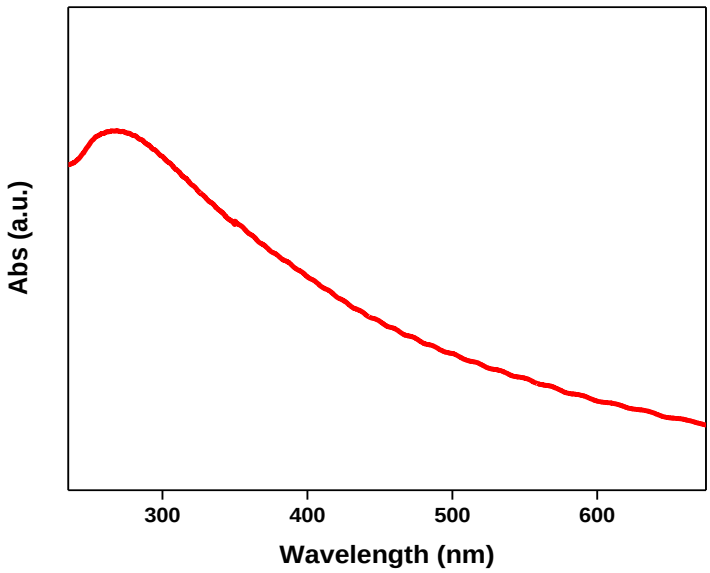


Figure 3.16: A typical UV-Vis absorption spectra for carbonaceous nanomaterials, in this case recorded for the BCN-NTs prepared under standard conditions.

This peak is characteristic of a CNT dispersion and can be ascribed to π-π transitions within the nanotubes.[134] Through further analysis of the UV-Vis spectra we can gain a greater insight into the nanotubes optical properties. Optical band gap energy estimations, which can range from *ca*. 2.9 – 4.4 eV for CNT and CNT composites, have previously been calculated through use of the Tauc formula, which involves plotting $(\alpha h\nu)^2$ against the photon energy.[221, 222] Figure 3.17 shows the Tauc plots obtained for the N-CNTs and BCN-NTs. These plots, which are derived from the recorded UV-Vis absorption spectra, were then used to determine the band gap of each material. This was done by extrapolating from the linear region of the plot and measuring the intercept which gave the optical band gap value. As we can see, the band gap for the BCN-NTs (2.34 eV) is lowered noticeably when compared to the N-CNTs (2.69 eV) starting material. This band gap closing can be attributed to the incorporation of

boron into the nanotubes. It has been shown that the introduction of boron dopants into CNTs can lead to the formation of additional electronic bands and can lead to a shift of the Fermi-level towards the valence band, resulting in a reduction in the band gap .[223, 224] Computational work by Talla *et al.*[120] had predicted that the dual incorporation of both boron and nitrogen co-dopants could decrease the band gap when compared to nanotubes that were uni-doped. Additionally, they suggested that this band gap reduction could alter the electrical conductivity of the co-doped nanotubes when compared to the uni-doped counterpart. Finally, unlike CNTs, BNNTs displays a broad band gap of *ca.* 6.1 eV, as has been demonstrated elsewhere, due to their insulating nature.[225] The absence of a band gap absorption expected for hexagonal boron nitride, further indicates the successful production of heteroatom doped BCN-NTs as opposed to a BN/CNT hybrid using this co-doping procedure. A singular band gap suggests a heterogenous material as opposed to a BN coated hybrid. The ability to tune the band gap through the introduction of boron dopants, to yield BCN-NT, could be an attractive trait for potential optical applications of the nanotubes such as photocatalysis or in the development of optoelectronics.[226, 227]

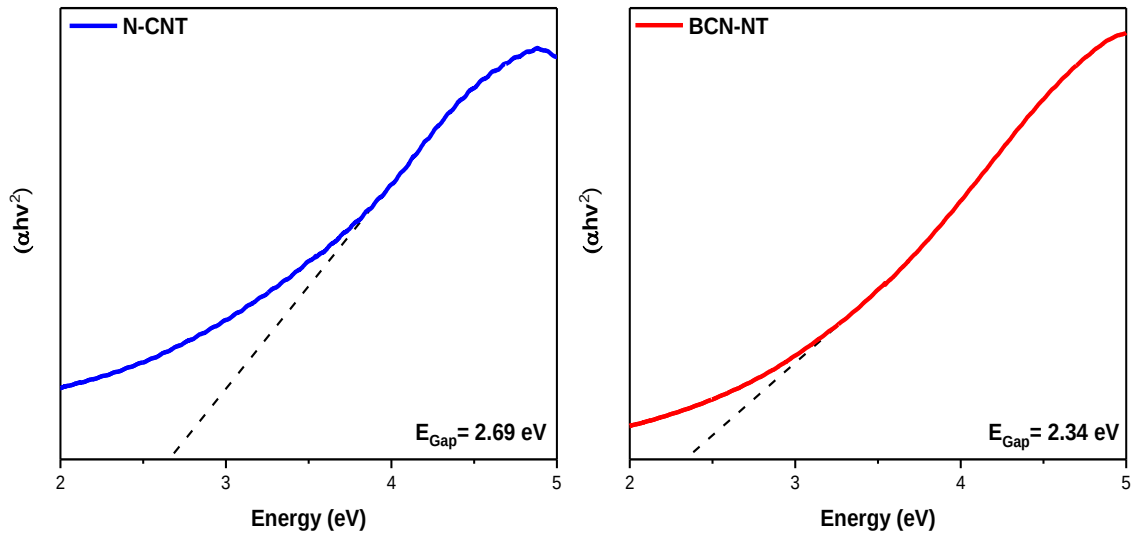


Figure 3.17: Tauc plots, derived from UV-Vis absorption spectra, are shown here for the N-CNTs (blue) and BCN-NTs (red) and used to determine the change in optical properties upon the introduction of boron.

3.3.5. Effect of Co-Doping on Oxidation Resistance

The thermal properties of the BCN-NTs, in comparison to the precursor material, were assessed using thermogravimetric analysis. The nanotube samples were subject to oxidation at a fixed rate, with the recorded oxidation profiles for the N-CNTs and BCN-NT being shown in Figure 3.18. The profiles displayed by each material are typical of graphitic carbons which show little activity before 400 ^{o}C at which point oxidation steadily occurs. The oxidation of material causes the sample weight to decrease as the temperature continues to increase, until complete consumption. Any residual weight typically represents impurities remaining from the synthesis. We note here that residual weight for each sample is similar and there is no significant increase after the co-doping step. This provides further confirmation of heteroatom co-doping as opposed to the formation of a boron nitride coating on the nanotubes, which would increase the residual weight significantly, owing to boron nitrides substantial oxidation resistance.[190]

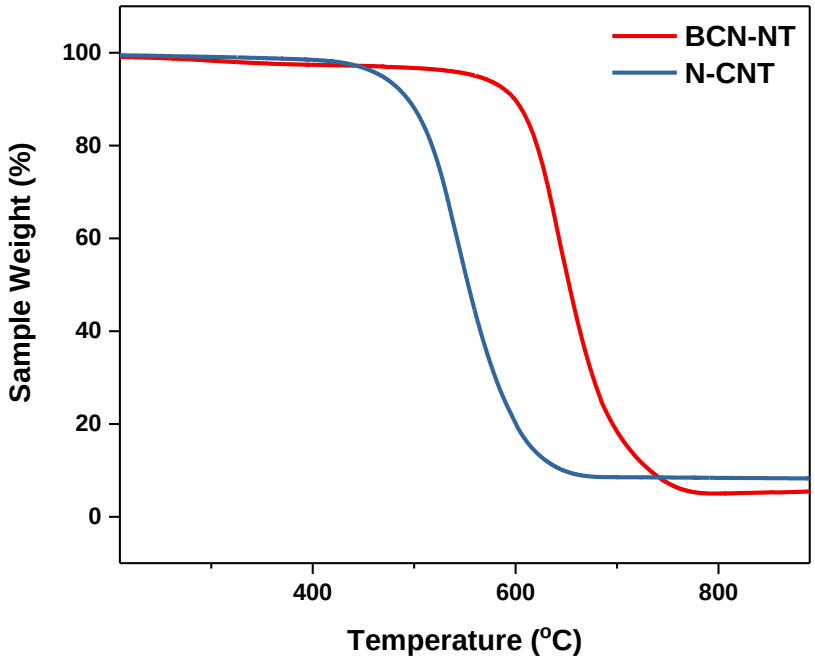


Figure 3.18: Thermogravimetric analysis profiles , recorded in air, for each of the N-CNT (blue) and B-CNTs (red) which reveals a distinct alteration in oxidation resistance after co-doping.

The oxidation profile displayed by carbonaceous nanomaterials can be strongly influenced by the crystallinity of the nanotubes.[228] The 50 *wt*.% loss temperature, *i.e.* the temperature at which half the starting material has been consumed, can be used here as indicator of thermal and oxidation resistance. This feature was recorded for the N-CNTs at *ca.* 550 ^{o}C. This temperature is downshifted when compared to undoped carbon nanotubes, *ca.* 625 ^{o}C, that have been grown *via* AACVD within our group.[121] This can be ascribed to the relatively high defect density on N-CNTs. Oxidation occurs more readily at the defect sites on a nanotube and hence, with more sites to attack due to their intrinsic disorder, the thermal degradation of the doped nanotubes is more pronounced.[121] When boron is incorporated into the structure, after the co-doping procedure, we can see that the measured oxidation resistance improves markedly. Previous work has shown how thermal treatments of CNTs can improve oxidation resistance, supporting the observation that has been made here.[228] Additionally, there is further literature regarding the use of substitutional boron to promote or enhance this graphitisation effect within carbonaceous materials, which again can result in enhanced oxidation resistance.[217, 229] The temperatures typically employed for this boron promoted graphitisation often exceed those that were used in this thesis (by *ca.* 1000 ^{o}C). That being said, prior studies have reported that the exploitation of defective sites and high surface areas associated with certain CNTs can enable boron-promoted graphitisation at lower temperatures than typically encountered.[218, 230] Given the high concentration of defects in the N-CNT precursor, it is feasible that that this low-temperature graphitisation effect could have been achieved here. As has been shown previously within this chapter, according to the I_D/I_G ratio, the level of graphitisation has improved for the BCN-NTs when compared to the N-CNTs. This reduction of defect density for the BCN-NTs, therefore, means there are fewer active sites for oxidation to occur at, resulting in improved thermal resistance.

Further to the 50 wt.% loss temperature, additional information regarding the thermal properties can be inferred from the TGA curves obtained for the N-CNTs and BCN-NTs. Figure 3.19 displays the derivate weight loss curves for both samples. These first derivative weight loss plots can be used to determine the temperature at which weight loss rate (*i.e.* oxidation) is at a maximum. This point is often referred to as the oxidation temperature. We can see that this peak temperature is 548 ^{o}C for the N-CNTs and 646 ^{o}C for the BCN-NTs. The upshift in the inflection point displayed by the BCN-NTs clearly shows that the thermal resistance has been enhanced, as a greater temperature is required to achieve the maximum oxidation rate when compared to the precursor. This once again highlights the impact of the co-doping procedure to produce BCN-NTs, as we can significantly improve the thermal resistance of these nanotubes. Applications such as thermal management or ones that may require high operating temperatures may benefit from these enhanced thermal properties displayed by the BCN-NTs produced here.

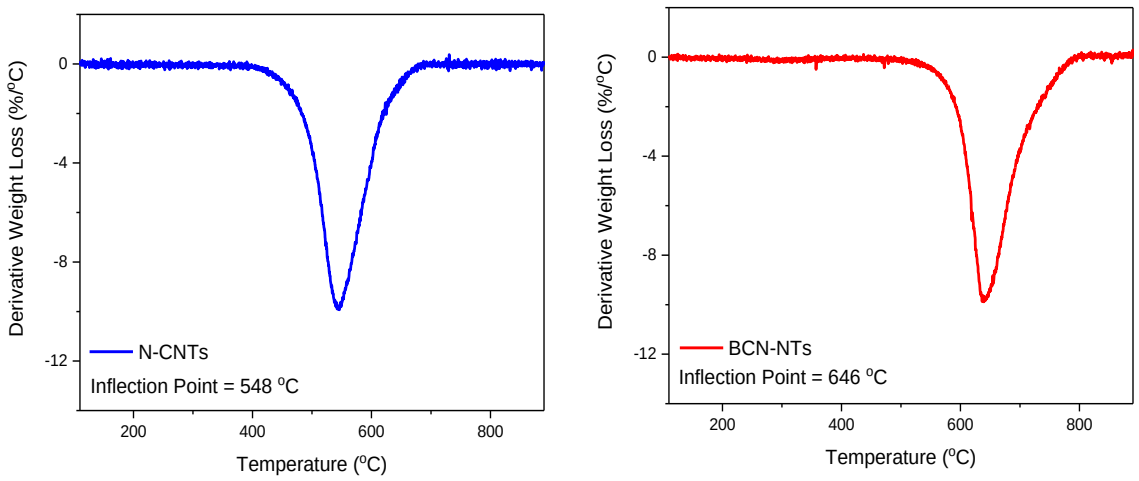


Figure 3.19: First derivative weight loss curves recorded for the N-CNTs (blue) and B-CNTs (red) which reveals the alteration in inflection point temperature between samples.

3.3.6. Effect of Reaction Variables on Boron Doping

As we have demonstrated in this chapter, computationally and experimentally, the subsequent doping of pre-formed N-CNTs with boron occurs readily and is a feasible process. After establishing this, we wished to gain further insight into the doping process and determine how the boron doping is influenced by various reaction parameters that can readily be varied in this type of system which include: reaction temperature, the heating rate and the crystallinity of the starting material. XPS analysis was used to determine the amount of boron present under each reaction condition and to assess, qualitatively, how the composition alters. For each reaction variable studied, standard condition experiments were performed using the same batch of N-CNTs for consistency and comparison.

3.3.6.1. Reaction Temperature

Given that the procedure used here is a solid-state reaction, perhaps the most apparent reaction condition to alter in this type of procedure, was the reaction temperature. Higher temperatures can increase the energy of the system which ultimately affects the diffusion of reactants and the reaction thermodynamics. For this set of experiments, the only thing that was varied from the regular standard conditions, therefore, was the reaction temperature. Experiments were performed at lower temperatures, of 800 and 900 ^{o}C, than those conducted under standard conditions (1000 ^{o}C). These lower temperature experiments were conducted using N-CNTs from the same batch and compared against products obtained under standard conditions. In Figure 3.20, we see a plot of the boron doping level against the reaction temperature; as we can see, there is a clear relationship observed between the two. For the standard conditions, the doping level is atypical for the work we had conducted thus far, *i.e.* around 3 at.%.

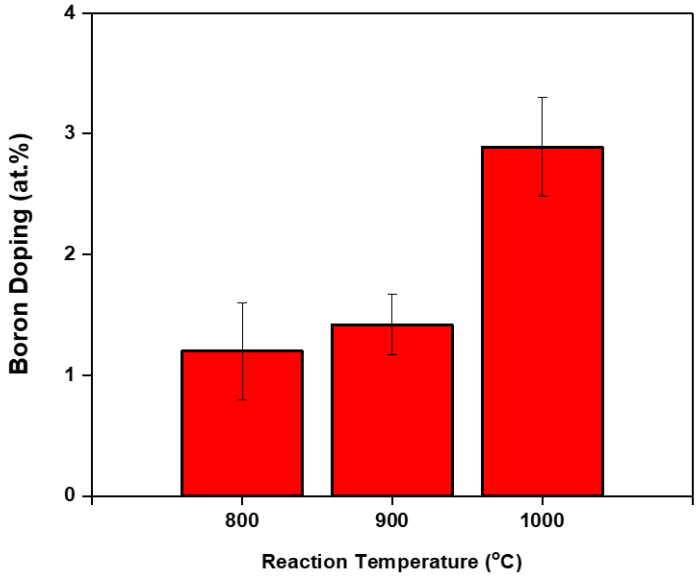


Figure 3.20: A plot demonstrating how the boron content of the BCN-NTs varies when the reaction temperature is reduced. The boron content incorporated displays a positive correlation with reaction temperature.

As the reaction temperature lowers however, the boron doping level steadily decreases also, with the experiments performed at 800 ^{o}C yielding the lowest boron content overall. Despite the dopant level decreasing, this work still reveals the successful incorporation of boron and demonstrates that the synthesis of BCN-NTs using this technique is achievable at relatively low reaction temperatures.

It has previously been shown by researchers that the level of nitrogen incorporation in N-CNTs can be affected by the reaction temperature. Liu *et al*.[89] demonstrated that the nitrogen content decreases with increasing reaction temperature. They attribute this to the increased bond energy of C – C when compared to C – N bonds.[231, 232] Higher temperatures would therefore favour the formation of the stronger bonding energies. By that deduction, we can offer explanation for the increasing boron content with reaction temperature. As the C – B bond has a greater energy than that of C – C, we would expect to see an increase in boron doping content as the reaction temperature is increased, as was observed here.[233]

3.3.6.2. Precursor Crystallinity

As we have demonstrated theoretically and experimentally in this chapter, the nitrogen dopant sites on the precursor material assist the incorporation of boron dopants into the nanotube to produce BCN-NTs. These nitrogen sites can be considered as defects and therefore, it can be suggested that the presence of defects assist with the boron doping. To further clarify this, we conducted the boron doping procedure using undoped multi-walled CNTs, synthesised *via* AACVD, which have a higher crystalline structure when compared to N-CNTs. The resulting product is referred to as B-CNTs.

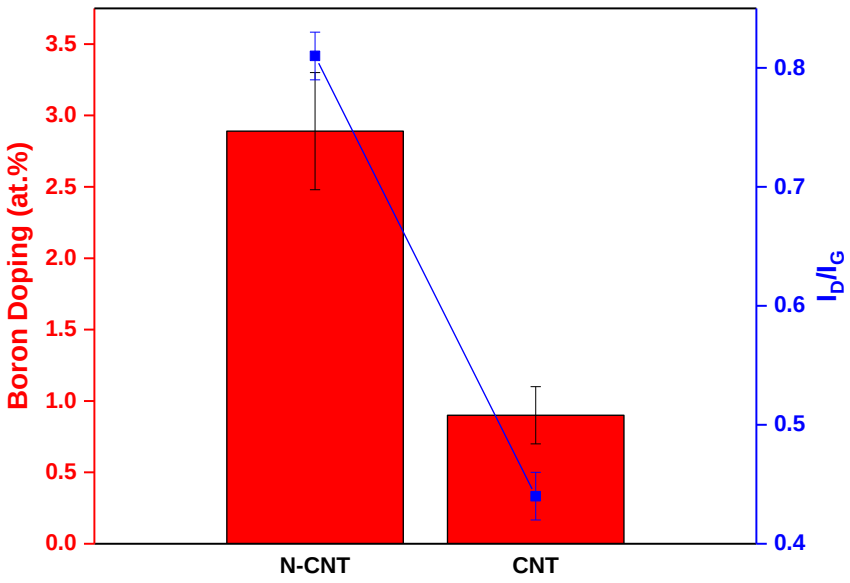


Figure 3.21: A plot demonstrating how the boron content of the reaction product varies when the precursor crystallinity, represented by the defect density ratio, is altered. The blue line acts as guide for the eye.

In Figure 3.21 we see a comparison of the boron doping level achieved when using N-CNTs and regular CNTs, produced *via* AACVD, as precursor materials. As we can see, the overall boron content within the B-CNTs is significantly less than what was achieved in the BCN-NTs. The measured defect density for the N-CNTs was shown earlier in Figure 3.15; the

CNTs used for the synthesis of the B-CNTs have a considerably lower I_D/I_G ratio (0.44) when compared to the N-CNTs (0.81). It is clear from this that by reducing the number of defects, the number of accessible active sites for boron doping to occur at also decrease. As such, these results reaffirm the importance of the nitrogen dopant or defect sites in the incorporation of boron dopants into the nanotubes produced *via* AACVD, which allows the fabrication of BCN-NTs. This observation offers a potential route to fine tuning the boron content. As we have demonstrated, the amount of boron that can be introduced is closely linked to the defect density of the nanotube. Through altering the nitrogen content, therefore, we could tune the crystallinity of the precursor and theoretically tune the boron content.

3.3.6.3. Heating Procedure

After confirming the importance of the intrinsic defective nature of N-CNTs for the boron doping procedure, we looked to explore the effect of the heating procedure. It has previously been shown that heat treatments can reduce defects in nanotubes, and as such, the heating process employed under standard conditions may be reducing the number of defects available for substitution. As the temperature ramps up, the defect sites may begin 'healing' before there is sufficient energy to react with the generated boron oxide vapours. To address this, we employed what we have termed as a 'burst heating' procedure. This involves the furnace being heated to temperature, away from the sample boat, then being moved into position for the reaction. This means that the reactants are heated rapidly, as opposed to the gradual ramp under standard conditions. This, in theory, should lead to the defect sites remaining more accessible during the co-doping step. In Figure 3.22 we see a plot of the boron doping levels obtained under standard conditions and burst heating. The results show that, although small, the boron doping level is affected by the heating procedure employed.

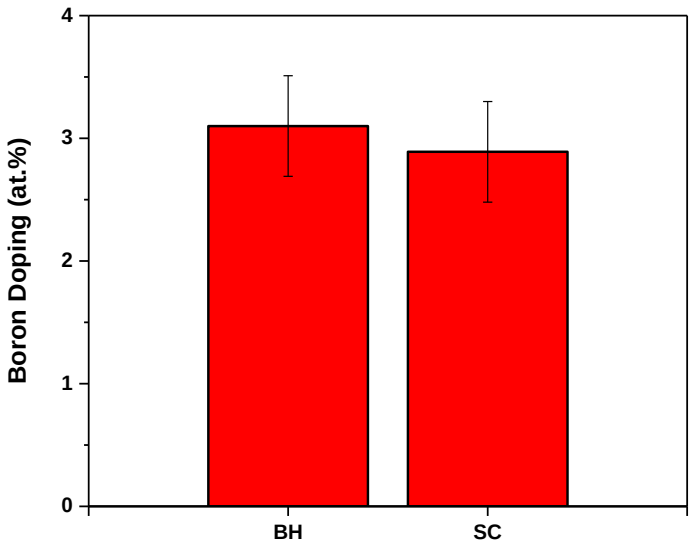


Figure 3.22: A plot demonstrating how the boron content of the BCN-NTs varies when the reaction heating procedure is changed between gradual and 'burst' heating.

On average, the boron doping levels obtained under burst heating are greater than that under standard conditions. There have not been many investigations into the effect of heating rate of the substitutional doping of CNTs, and as such, the hypothesis we designed these experiments with are the best explanation that can be reasoned, thus far. Whilst we observe that the doping increases under burst heating conditions, the magnitude of increase is not enormous. A possible explanation for this is that as the furnace is moved into position, at temperature, the boron reagent boils rapidly meaning some is potentially lost from the reaction vessel before it is able to react. It would therefore be interesting to generate the boron vapours separately and introduce them simultaneously as the furnace is moved into position to determine if the boron doping can be increased further. Alternatively, this observation may mean that the thermally assisted 'healing' of the nitrogen defect sites is not that pronounced during the temperature ramping stage. It is an area for further research to be conducted in exploring fine tuning of the boron content within these BCN-NTs.

3.4. Conclusions

The main objectives of this chapter were to overcome some of the traditional limitations associated with the synthesis of BCN-NT nanotubes in order to lay the foundations for further processing that would be explored later on in the thesis. Here we have presented a two-step synthesis procedure, that combines AACVD and a solid-state chemical route, that allows the production of structurally uniform BCN-NTs at relatively large yields. The successful incorporation of boron into the N-CNT precursor was confirmed using a variety of characterisation techniques. Computational studies were used to compliment some of the observations made through characterisation of the BCN-NTs. We found that the pyridinic sites are sacrificial and make way for the incorporation of boron dopants which was supported through computational calculations. Further to this, we evaluated how the conversion of N-CNTs to BCN-NT impacted the properties of the nanotubes. It was found that the graphitic nature, as well as the thermal resistance of the BCN-NTs was improved when compared to the precursor material. Additionally, the optical properties were altered. We have also explored the effect that various reaction parameters had on the level of boron introduced, to understand this reaction further. Through these studies we have found that the reaction temperature, heating rate and defect density of the precursor each have an impact on the amount of boron that could be introduced into the product. In turn, we are able to tune the degree of boron doping through alteration of these reaction parameters. This allows the production of BCN-NTs with variable composition.

This work has allowed the production of nanotube co-doped with nitrogen and boron heteroatoms and has laid the foundation for this thesis. By being able to produce these BCN-NTs on relatively large scales, we can now explore the methods for their functionalisation and conversion into macroscopic assemblies which we will detail subsequently.

Chapter 4

Developing Methods for the Synthesis of Doped CNT – Nanoparticle Hybrids: The Effect of Solvent Medium

4.1. Introduction

Since their advent, carbon nanotubes (CNTs) have displayed enormous promise with regard to a number of applications including energy storage, thermal management, catalysis, biomedical and electronics owing to their unique properties.[7, 226, 234-236] Due to the rate at which the world is developing however, it is becoming increasingly important to design 'next-generation' materials with unique and tailorable properties. The natural progression of CNTs therefore, much like their 2D counterparts, has involved further processing of the raw material to alter their functionality.[237] By processing the CNTs and enhancing functionality, we are able to change their properties to suit a desired application. A prominent area of research related to the processing of next-generation CNT materials involves the attachment of nanoparticles to create CNT – nanoparticle hybrids. The aforementioned properties of CNTs such as high surface area, mechanical robustness and excellent conductivity make them ideal scaffold candidates which, in turn, has led to these hybrids being utilised in optoelectronics, electrocatalysis and environmental remediation.[109, 111, 112] Through the attachment of nanoparticles we can further tune the functionality of CNTs for specific applications and potentially couple properties of the component parts, synergistically. Further tailoring of a hybrids properties may be afforded through the use of heteroatom doped CNTs as a starting scaffold.

Thus far within this thesis, we have presented a procedure for the synthesis of BCN-NTs. This approach allows the production of the co-doped nanotubes on a relatively large scale (gram/day). In turn, this now allows us to explore further processing of these BCN-NTs, more specifically their *ex-situ* functionalisation with metal oxide nanoparticles. In general, there have only been a few attempts to functionalise BCN-NTs with additive nanoparticles, and to my best knowledge *ex-situ* methods have not yet been explored for BCN-NTs. Given

the nature of the BCN-NTs, *i.e.* nanotubes doped with boron and nitrogen heteroatoms, avoiding the use of covalent procedures is preferred. Covalent procedures, as we will see, typically require an acid etching step to introduce surface functionality; this can damage the structure of the nanotube, and in the case of doped nanotubes, remove dopant atoms.[238, 239] Therefore, the BCN-NTs were used here, as produced, without an oxidative acid etching step. We looked to determine the effect that solvent, and thus non-covalent interactions, had on the composition of the BCN-NT hybrids. This was done by justifying the results obtained here with existing predictive models based on surface energy differences and dielectric effects, as will be discussed later in this section. The aim here being that we can use this work to rationally produce nanoparticle – BCN-NT hybrid materials, for the first time.

Given the field of BCN-NT functionalisation is at an infant stage and that we are aiming to develop an understanding of the factors that govern the functionalisation procedure, it is important to consider the nanoparticle within the hybrid. Developing an appropriate reference system and methodology will help facilitate better design and synthesis of hybrids in the future. Given these aims, we selected iron oxide nanoparticles as a suitable candidate for hybrid production. Oleylamine-capped iron oxide nanoparticles can be produced with controllable dimensions at relatively low cost. The surface chemistry of these nanoparticles allows them to be dispersed in various solvent media and negatively interact with others, which makes them highly suited to the studies detailed in this thesis. The physical properties of the iron oxide nanoparticles that differ from CNTs, such as oxidation resistance and mass contrast, allow us to quantify and visualise the degree of functionalisation achieved which is of importance when conducting studies such as these. Finally, whilst not explored within this thesis, CNT/iron oxide nanoparticle hybrids are a growing research area for various applications such as energy storage devices, electrocatalysis and biomedical technologies

which makes the work to be detailed here, a stepping stone for application testing giving the promising potential of both BCN-NTs and CNT/iron oxide nanoparticle hybrids.[240, 241]

Before investigating this process for BCN-NTs however, we first looked at producing N-CNT hybrids. Once again, the literature is sparse when it comes to the rational design and production of N-CNT – nanoparticle hybrids. Additionally, we attempted to further understand some discrepancies from predicted hybrid compositions, which have been reported previously within the literature and our group. This was done by studying the impact a de-stabilising agent had on the composition of these hybrids materials. The work here investigates the suitability of these predictive models towards doped nanotubes and proposes a simple approach toward the production of these next generation, hierarchical nanoparticle – nanotube hybrids.

Prior to detailing the experimental results that have been recorded as part of this work, I will first provide the reader with an introduction into techniques used for the production of these hierarchical hybrid materials. Given that there are few examples detailed for BCN-NTs, I will here present an overview of methods used for CNTs, and less so N-CNTs, to give the reader a grasp on the techniques used within the field. I will also touch upon the few methodologies that do exist for BCN-NTs, briefly, at the end of this introductory section.

4.1.1. Synthesis of Hierarchical Nanotube-Nanoparticle Composites

4.1.1.1. *In-Situ* Synthesis Techniques

As will be discussed here, there have been many research efforts to produce hierarchical nanostructures composed of nanotubes and nanoparticles. These can be broadly categorised into two separate types of synthesis procedure: *ex-situ* and *in-situ*. The work presented in this experimental section focusses on an *ex-situ* synthesis technique and for this reason, we will pay greater attention when reviewing that section of the field. Nevertheless, here we will briefly provide the reader with an overview of *in-situ* techniques that are employed for the production of these nanocomposite materials.

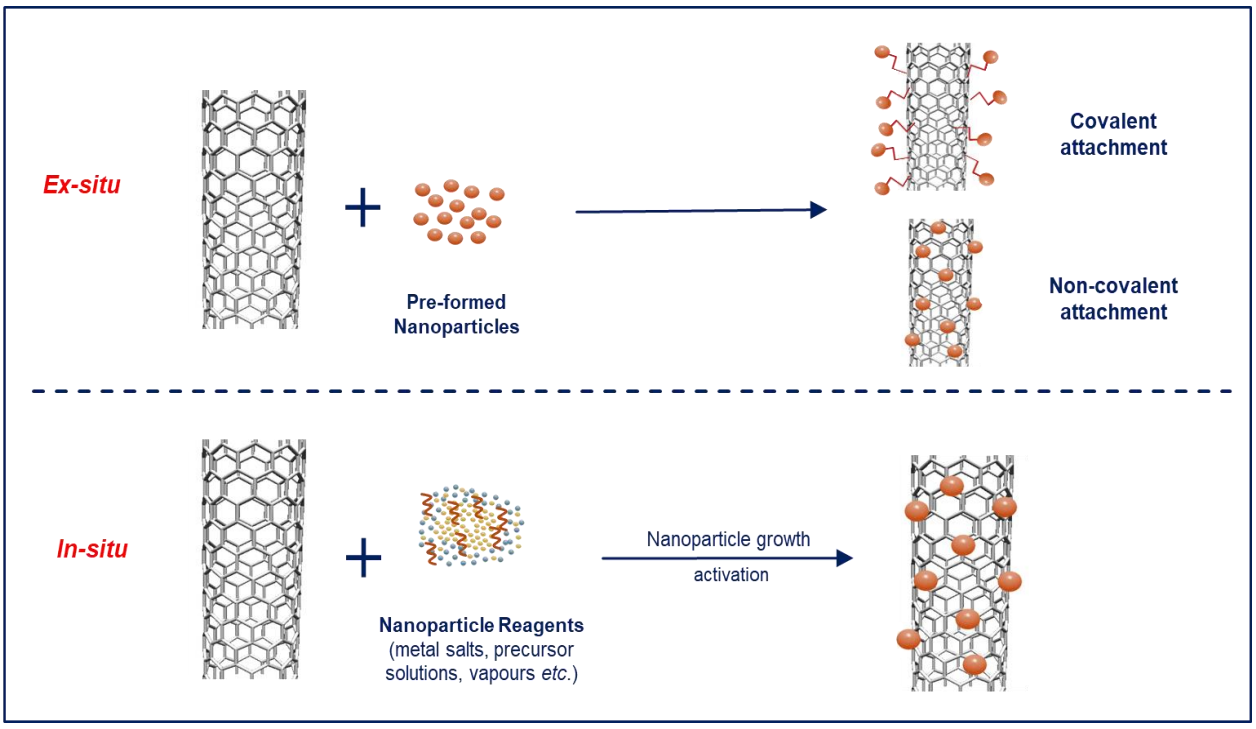


Figure 4.1: A schematic diagram summarising the two main approaches encountered in the literature that are employed for the production of nanoparticle - nanotube hybrid materials: ex-situ and in-situ techniques.

The category of *in-situ* synthesis techniques refers to how the nanoparticles, which functionalise the CNTs, are produced. Essentially, the nanoparticles are produced in the presence of the nanotube as opposed to being prepared separately. This is shown schematically in Figure 4.1. These strategies can further be categorised into two sub-sections which include deposition techniques or growth-related approaches. The former may involve

CVD coating of the nanoparticles onto nanotubes whilst the latter involve the direct growth of nanoparticles on the nanotube surface.

As has been mentioned, where 'deposition' approaches are concerned, CVD is a commonly employed technique to introduce nanoparticles onto the surfaces of nanotubes. For example, metal organic CVD approaches have been used to produce cobalt – MWCNT hybrids.[242] By using dicobalt octacarbonly, as the organometallic precursor material, cobalt nanoparticles were successfully dispersed across the nanotube substrates during an annealing process. This procedure yielded a maximum cobalt loading of *ca.* 11 wt.% onto the exterior of the nanotubes. Liu *et al*.[243] used an atomic layer deposition technique, which is a variant of traditional CVD, to functionalise CNTs. Through this procedure, they were able to deposit varying levels of platinum nanoparticles onto the surface of CNTs. These CVD processes offer efficient synthesis techniques for these CNT – nanoparticle hybrids, however they typically require an acid etching pre-treatment to introduce surface functionality, which can hinder the intrinsic properties of the CNTs, such as electrical conductivity.[244]

In addition to CVD, there are also electrochemical based functionalisation procedures. Typically this involves casting the nanotubes on an electrode that is suspended in an active solution, from which the metal nanoparticles can be grown. For example, Guo *et al*.[245] successfully cast platinum nanoparticles, from solution, onto a MWCNT electrode. Whilst there are some examples of this technique being explored for transition metal oxide nanoparticle deposition, the majority of examples are focused on the production of noble metal hybrids.[246] As with CVD methodologies, some form of acid-etching or pre-treatment step precedes the electrochemical deposition of nanoparticles onto the CNTs.[245, 247] In addition to this, the electrochemical strategy as of yet is not scalable and is normally performed on a small level.[248]

The final, and most prominent, sub-category of *in-situ* techniques involves growing the nanoparticles directly on the surface of nanotubes. This is sometimes referred to as the reductive technique as it often involves the adsorption of precursor reagent onto the surface of the CNTs before being subjected to a reduction step. For example, Liang *et al*.[249] synthesised cobalt – CNT hybrids using this reductive approach. Oxidised MWCNTs were soaked in a cobalt containing solution which was dried before annealing under an ammonia atmosphere to promote the nucleation of cobalt nanoparticles on the nanotube surface. This reductive approach has been used to coat CNTs with a host of nanoparticles such as Sn, Ag and Pt.[250-252] An example of a hybrid material produced through this approach is highlighted in Figure 4.2.[252] Once again, these procedures will often require an oxidative treatment to activate the surface of the nanotubes, which can be detrimental to the nanotubes graphitic structure. Additionally, this approach can lead to aggregated formation of nanoparticles, as opposed to uniform nanoparticle coverage. This section was included to give the reader an introduction into the field of *in-situ* functionalisation techniques for the production of nanohybrids. If of interest, other reviews cover this area of research in greater detail.[248]

4.1.1.2. *Ex-Situ* Synthesis Techniques

The *ex-situ* category of functionalisation involves preparing the nanoparticles and CNTs separately, before then coupling the two materials in a further step to yield the hybrid. This is exemplified in Figure 4.1. When compared to *in-situ* techniques, it is generally accepted that *ex-situ* procedures allow the production of nanoparticles with greater control, as they are synthesised away from the nanotube. This allows us to tune parameters such as the dispersant (*i.e.* solvent), nanoparticle size and surface functionality. Additionally, the absence of the nanotubes during the synthesis means they cannot impede the nanoparticle growth process. In

particular here, the variable solvent selection is important as we are investigating solvophobic effects on the level of nanotube functionalisation. *Ex-situ* synthesis techniques can themselves be sub-categorised into covalent and non-covalent strategies, which refers to the interactions that dictate the functionalisation. Here we will provide a summary of existing techniques for both covalent and non-covalent *ex-situ* techniques, with an emphasis on the latter given the relevance to the work conducted throughout this experimental chapter. It should be noted here that there are often no attempts in the literature to discern between covalent bonding and non-covalent interactions that facilitate the nanotubes and nanoparticles attachment. Instead, the methodology is typically categorised according to how the nanotubes are treated before use *i.e.* intentional introduction of oxygen containing groups through acid treatment or no treatment at all.

To begin with, we will discuss covalent methodologies to attach nanoparticles to the surface of nanotubes. Covalent techniques refer to the covalent linkage that is formed within the nanoparticle – nanotube hybrid. This can be between the nanoparticle and the nanotube itself or between an intermediary species, such as a polymer, which is located between the two. The covalent linkage is a robust and less reversible technique for coating nanoparticles onto nanotubes.[113] That being said, as will be discussed later, non-covalent methodologies provide sufficient interaction to form a lasting nanoparticle coating.

Most covalent synthesis techniques detailed within the literature require activation of the nanotube surface. This allows the introduction of surface functional groups that are capable of forming these covalent connections. Perhaps the simplest example of this methodology involves taking oxidised CNTs and mixing them with pre-prepared nanoparticles. An early example, of this comes from Unger *et al*.[253] who detailed a simple procedure that involved the oxidation of MWCNTs followed by the attachment of various metal oxide nanoparticles. This included the attachment of iron, cobalt and nickel nano-clusters. The authors attribute

this coupling to interactions between the oxidised nanotubes and the oleic acid capping agent. However, they do not express explicitly how the covalent linkage was formed. Additionally, they also detailed a control experiment where pristine nanotubes were used. The level of functionalisation achieved was similar to that of the oxidised nanotubes, which suggests that oxidative procedures, are not always necessary. It also highlights that when covalent procedures are used, non-covalent interactions will also be present during the synthesis. Variations to these approaches involve the conversion of the introduced oxy-surface groups into other functionalities. For example, Marsh *et al*.[254] converted carboxylic groups to amides before then converting to thiol functionalities. They utilised the introduction of these thiol groups to attach gold nanoparticles to the surface of the MWCNTs. Similarly, it was reported that amine terminated FeNPs could be used to form covalent linkages with CNTs.[255] Oxidised CNTs underwent a conversion to introduce acyl chloride groups on the surface of the nanotube. These were then subject to a reaction with the amine terminal group, which allowed covalent bond formation between the nanoparticle and nanotube. An issue with these procedures however is that the initial surface functionalisation process can yield uneven coverage across the nanotube.[256] This deviation in surface functionality across the nanotube, in turn, can lead to variations in the uniformity of nanoparticle coverage. The final covalent approach that we will briefly discuss involves an intermediary molecule assisting the functionalisation process. Typically this will involve a polymer. For example, Zhou *et al*.[257] detailed the grafting of polyacrylic acid to the surface of MW nanotubes to assist in nanoparticle attachment. Initially the MWCNTs were oxidised through acid treatment, followed by the covalent attachment of the polymer. This polyacrylic acid layer then allowed sufficient interactions with iron nanoparticles to attach to the nanotubes. Despite the polymer layer however, the attached nanoparticles were randomly distributed across the surface, possibly owing to an uneven distribution of polyacrylic acid across the sample. This can be

seen in Figure 4.2. A similar approach was used to attach noble metal nanoparticles to the exterior of nitrogen doped MWCNTs.[258] An acid etching step preceded the attachment of polyelectrolyte before finally attaching gold nanoparticles. Pyrene moieties have also been used as an alternative to polymer molecules in an effort to assist with magnetic nanoparticle attachment.[259]

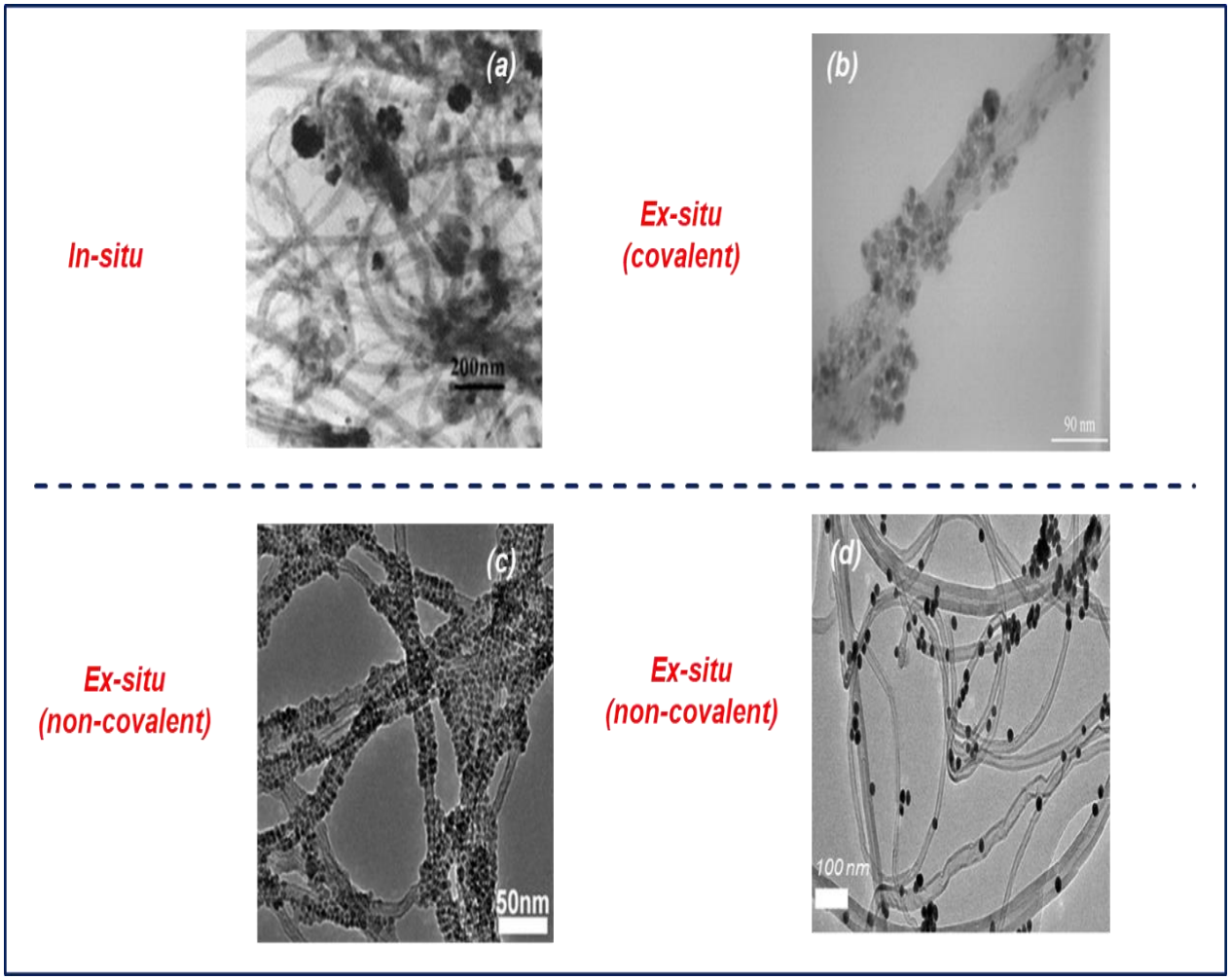


Figure 4.2: TEM micrographs adapted from the literature highlighting hierarchical nanostructures that have been produced through a variety of techniques. These coatings can range from uniform to sparse. (a) in-situ synthesis techniques, from reference 252 with permission from Elsevier. (b) covalent, ex-situ techniques, from reference 257 with permission from John Wiley and Sons. (c) non-covalent, ex-situ techniques with the assistance of an additive molecule, from reference 262 with permission from The Royal Society of Chemistry. (d) non-covalent, ex-situ techniques, without additive molecules, from reference 264 with permission from the American Chemical Society.

Whilst covalent routes offer a host of techniques for the production of nanoparticle – nanotube hybrids, there are some drawbacks within the methodologies. In particular, the damage that can be introduced into nanotube structure during the initial activation steps may be detrimental for certain starting materials and applications. The use of non-covalent options may circumvent some of these drawbacks and could be more suitable for different types of materials *i.e.* heteroatom doped nanotubes.

Non-covalent methodologies differ from covalent techniques in that there is no bond formed between the nanotube and the nanoparticle or intermediary molecule. Instead, non-covalent procedures are dictated by intermolecular interactions experienced between the materials that can include Van der Waals, hydrophobic interactions, electrostatics and π-π interactions.[113, 253] Some accounts offer little detail regarding the non-covalent interactions that dictate the attachment of nanoparticles, whilst other attempt to explain the process with greater reasoning. Here we will review examples of non-covalent functionalisation techniques and describe how various intermolecular forces might drive the reaction.

Small molecules can be used to promote non-covalent interactions between the nanotubes and nanoparticles. A good example of this comes from Ellis *et al.*[260] who detail the production of precious metal – nanotube composites through the attachment of gold nanoparticles to the surface of MWCNTs. The MWCNTs were first soaked with acetone and dried, in order to remove any excess solvent. They then successfully attached gold nanoclusters *via* a brief sonication procedure. This non-covalent pre-treatment left acetone molecules adsorbed on the surface of the nanotubes. Control experiments, performed with untreated nanotubes, did not yield nanoparticles attached to the MWCNT surface. They detail that the driving force for this functionalisation is hydrophobic interactions. When compared to the untreated CNTs, the acetone-adsorbed species provided sufficient interaction to entangle with the capping ligands on the gold nanoparticles. The use of a silane coating on CNTs has also been exploited to

promote this hydrophobic driving force.[261] A similar approach that utilised small molecules, by Li *et al*.[262], was vaguer in comparison to their description of the non-covalent functionalisation. MWCNTs were first pre-treated with an amine molecule before uniformly attaching FeNPs to the CNTs, as can be seen in Figure 4.2. However, without the presence of the pre-treatment, the nanoparticles were found to aggregate instead of uniformly coating the nanotube surface. They do not offer a real explanation for this discrepancy, however, and attribute the successful functionalisation to the presence of the adsorbed amine that facilitated the attachment.

It has been demonstrated that pre-treatments with small molecules is not a pre-requisite to the successful non-covalent functionalisation of CNTs with nanoparticles. Rance *et al*.[263-265] are prominent in exploring non-covalent methodologies for the attachment of nanoparticles to CNTs. Typically, their approach involves attaching citrate capped gold nanoparticles to unmodified MWCNTs through a simple sonication assisted mixing process. In each case, the samples were analysed with TEM which revealed attachment of the gold nanoparticles on the surface of the nanotubes, as exemplified in Figure 4.2. They have investigated the non-covalent functionalisation further by trying to gain insight into what dictates the attachment of nanoparticles. They initially demonstrated that the electrostatic interactions were the driving force for the functionalisation.[263] They found that by altering the pH and ionic strength of the aqueous nanoparticle solution, the level of functionalisation was altered. This they attributed to electrostatic repulsion experienced between the nanoparticles and CNTs. Following on from this, they detailed how another intermolecular force, Van der Waals, could control the functionalisation procedure.[264] This was deduced by altering the geometries of the various nanomaterials, and ultimately the surface area, to observe how this affected the functionalisation. They concluded that the nanotube diameter was the most significant contributor to the experienced Van der Waals between the nanoparticle and MWCNTs, and

ultimately, the level of functionalisation. Finally, they once again explored the effect of electrostatics on the functionalisation, but this time through alteration of the solvent medium.[265] This was the first account detailed for how different solvent media can influence the *ex-situ* functionalisation of CNTs with NPs. By altering the dielectric constant of the solvent, they were able to tune non-covalent interactions within the system. More specifically, the electrostatics experienced between the nanoparticle and nanotube, like their initial study, were altered. This led to variation in the degree of nanoparticle functionalisation achieved. However, in a previous study conducted within our research group by Quijano-Velasco *et al.*,[115] this relationship was not observed. Their study used a surface energy-based approach to explain the functionalisation of MWCNTs with FeO_xNPs. This approach was derived from existing methodologies developed by Bergin *et al.*[266] for determining the solubility of nanotubes in various solvent media and is based on solubility parameters. Using this method, they found good agreement between predictions made through this predictive model and experimental observations for the extent of functionalisation achieved in various solvents. Their results however did not follow the same trend when plotted against dielectric constant, as observed by Rance *et al.*[265]. It is interesting to note that the nanoparticles used in each of these studies differed which may have an effect on the observed trends. Given these discrepancies however, investigating the role of solvent further would be an interesting topic to explore in order to compare the trends displayed in each of these studies. By altering the solvent, the non-covalent interactions can be varied which can impact the nanoparticle loading. For doped nanotubes, in particular, the effect of solvent has not been explored in the rational design and production of these nanocomposite materials.

4.1.1.3. Synthesis Techniques for BCN-NT Hierarchical Structures

As has been mentioned, the field surrounding the production of BCN-NT – nanoparticle hybrids is relatively new, with only a few examples existing in the literature. Despite this, a brief overview of these strategies will be given here to familiarise the reader with the current state of this emerging field.

The existing accounts of BCN-NT functionalisation are predominantly achieved during the initial growth of the nanotube themselves. These are often based on polymeric pyrolysis routes that were mentioned in section 3.1.2.3. For example, by including a cobalt precursor in the polymeric starting solution, a BCN-NT/graphene oxide support was loaded with cobalt nanoparticles that grew during the nanotube synthesis.[267] The product displayed a non-uniform coating of nanoparticles on the surface of the nanotubes, with only a few particles being detected. The authors also note that the cobalt particles are detectable as aggregates within the sample as opposed to monodisperse particles. There is no detail given about the actual loading quantity achieved in this hybrid material either. Similar approaches have been used to introduce ruthenium, iridium and titanium carbides onto BCN-NTs, which again are grown through the polymeric route.[268, 269] The *in-situ* approaches detailed earlier in the section, have been used to hydrothermally grow nickel nanoparticles on BCN-NTs, that were again produced through the polymer-based route.[270] Additionally, *in-situ* CVD deposition has been used to deposit tungsten disulphide flakes on MWBCN-NTs.[271]

Despite their promise as a next-generation hierarchical support material, when compared to regular CNTs, the field of BCN-NT functionalisation remains in its infancy. Given that it would be desirable for control over the composition of these hybrids, and that there has been little, if any, investigation into the *ex-situ* production of BCN-NT – nanoparticle hybrids it

would be interesting to explore this approach. Further to this, exploring the role of solvent on the functionalisation would be an important parameter to consider, given the significance discussed in the previous section. To the best of our knowledge, no study has been conducted to elucidate the effect of solvent on the functionalisation of BCN-NTs, or N-CNTs for that matter. Given this, in the subsequent section we will look to address these research gaps.

4.2. Materials and Methods

4.2.1. Chemicals

For the synthesis of nanotubes, benzylamine (ReagentPlus, 99 %) solution and boric acid (≥ 99.5 %) powder along with ethanol (puriss, ≥ 99.8 %) were purchased from Sigma-Aldrich and used without further treatment. Hydrochloric acid (32%) was purchased from Sigma-Aldrich and diluted before use. Ferrocene (99 %) was also purchased from Sigma-Aldrich but was further purified *via* sublimation. The deionised water used was type 2 (0.45 μS/cm).

For the nanoparticle synthesis and nanotube functionalisation, oleylamine (technical grade, 70 %), ethanol (puriss, ≥ 99.8 %), toluene (anhydrous, 99.8%), tetrahydrofuran (anhydrous, ≥ 99.9 %), dimethylformamide (anhydrous, 99.8%) and iron acetylacetonate (≥ 99.9 %, trace metal basis) were purchased from Sigma-Aldrich and used without further treatment. Cyclohexane (analytical grade, ≥ 99.8%) was purchased from Fisher Scientific and used without further treatment. Poly-4-vinylpyridine (mw – 160,000) was also purchased from Sigma-Aldrich but was further purified before use.

4.2.2. Characterisation

TEM images were obtained on a JEOL-3000F microscope operating at an accelerating voltage of 200 kV. Samples were prepared by diluting nanoparticle solutions in their dispersing solvent and drop-casting onto lacey carbon copper grids (400 mesh). Similarly, nanoparticle-nanotube hybrids were diluted in the reaction solvent and drop-cast onto grids. X-ray diffraction spectra were obtained on a Bruker D8 ADVANCE eco powder diffractometer employing copper kα radiation (λ = 0.15406 nm) and a LYNXEYE XE detector. Thermogravimetric analysis was performed on a Perkin Elmer Pyris 1 TGA machine. Typically, the nanoparticle-nanotube composites were heated to a temperature of 100 ^{o}C and holding for 10 minutes before increasing to 340 ^{o}C and holding for 10 minutes before finally heating to 900 ^{o}C and holding for a further 20 minutes. This was performed under flowing air (0.02 SLM). To determine the loading of the polymer wrapped nanotubes, the samples were initially heated to 100 ^{o}C and held for 10 minutes before heating to 900 ^{o}C and holding for 20 minutes under a N_2 atmosphere. Dynamic light scattering measurements for were recorded using a Malvern Zetasizer Nano ZS. X-ray diffraction (XRD) analysis was carried out using a Bruker D8 Advance eco powder diffractometer employing copper kα radiation (λ = 0.15406 nm) and a LYNXEYE XE detector. The sample was continuously spun during data collection. XRD measurements were conducted by the Oxford Materials Characterisation Service.

4.2.3. Synthesis of Nitrogen-Doped & $B_xC_YN_Z$ Nanotubes

The same synthesis procedures, as detailed in sections 3.2.3 and 3.2.5. were employed here for the synthesis of the N-CNT, CNTs and BCN-NTs, respectively. Briefly, AACVD was

used to grow CNTs from a benzylamine carbon feedstock, which utilised ferrocene as the catalyst precursor. These N-CNTs were treated with a non-oxidative procedure to remove surface impurities. HCl acid was used as the catalyst removal agent. After purification through HCl treatment, the N-CNTs were subject to an additional co-doping procedure to yield the BCN-NTs. For further details, please see Chapter 3.

4.2.4. Synthesis of Iron Oxide Nanoparticles

In order to vary the nanoparticle size, two synthesis strategies were employed, both involving the thermal degradation of a metal organic complex. One set of nanoparticles were used for functionalisation studies whilst the other was used for stabilisation experiments. These methodologies were adapted from previous synthesis routes developed within the Nanomaterials by Design research group.[115, 272]

To a three-neck round bottomed flask (100 ml) which was attached with a glass condensing unit, a thermocouple, a glass stopper and a PTFE magnetic stir bar, iron (III) acetylacetonate (1060 mg) and oleylamine (28 cm^3) were added. The reagent flask was fitted to a Schlenk line which is used for inert atmosphere chemistry. The set-up was mounted on top of a stir plate whilst the flask was surrounded by a heating mantle which was controlled by the thermocouple. Whilst stirring, the system was placed under vacuum for 5 minutes before flushing with nitrogen gas for a further 5 minutes. This procedure was repeated an additional two times. The system was then heated to 100 ^oC and held under vacuum for 30 minutes. The reaction mixture was heated to 300 ^oC and held for 60 minutes. In order to quench the reaction, the heating mantle was removed immediately, and the flask was allowed to cool to

room temperature. Once at room temperature, the reaction mixture was added to ethanol (50 cm^3) before splitting between three centrifuge tubes. The mixture was then centrifuged (4250 rpm) for 20 minutes until the nanoparticles separated out. The transparent supernatant was discarded before adding further ethanol (10 cm^3) to the centrifuge tubes and sonicating for 10 minutes. The mixtures were then re-centrifuged (4250 rpm) for an additional 10 minutes before once again discarding the supernatant. The nanoparticles were then collected in solvent (cyclohexane, toluene or tetrahydrofuran) and stored in a fridge. This synthesis procedure is referred to as Method 1. The nanoparticles prepared using this technique were used for the functionalisation studies.

Analogous nanoparticles of a smaller size were also produced here. In order to alter the size of the nanoparticles, the reaction was performed at a lower temperature (225 ^oC) and for a shorter duration (15 minutes). The same collection and washing procedure was employed here. This synthesis procedure is referred to as Method 2. The nanoparticles prepared using this technique were utilised in the stability experiments.

4.2.5. Synthesis of Polymer/N-CNT Hybrids

Typically, polyvinyl pyridine (40 mg) was dissolved in an organic solvent (4 ml) before adding nanotubes (4 mg) to the polymer solution. The mixture was then sonicated for 1 hour. After sonicating, the nanotubes were separated *via* vacuum filtration (PTFE membrane, 0.2 μm) and rinsed with solvent (30 ml). The product was collected and added to a clean vial along with solvent (10 ml) before sonicating for a further 15 minutes. The nanotubes were again collected *via* vacuum filtration and rinsed with solvent (30 ml). The product was then dried in a vacuum oven overnight at 75 ^oC before further analysis.

4.2.6. Synthesis of Iron Oxide NP/BCN & N-CNT Hybrids

The standard conditions employed for the production of BCN-NT and N-CNTs coated in iron oxide nanoparticles is as follows. The approaches used for functionalising the nanotubes were adapted from procedures developed within our research group.[115] Nanotubes (4 mg) were added to a glass vial along with iron oxide nanoparticles dispersed in solvent (1 ml of 8 mg/ml solution) as well as additional dispersing solvent (4 ml). The mixture was then sonicated for 1 hour. The nanotubes were collected *via* vacuum filtration (PTFE membrane, 0.2 µm). They were then rinsed with solvent (30 cm^3) until the filtrate ran clear to ensure the removal of any weakly bound nanoparticles. The product was recollected in solvent (10 cm^3) and sonicated for 15 minutes before filtering once more and rinsing with solvent (30 cm^3). The collected products were dried in a vacuum oven overnight at a temperature of 75 ^oC.

4.2.7. Effect of Solvent on Iron Oxide NP/BCN-NT & N-CNT Hybrids

In order to determine if the solvent, that the nanoparticles were dispersed in, influenced the functionalisation procedure, the nanoparticle stock solution was varied. Similar procedures to those detailed in 4.2.7 were employed here. Separate solutions of iron nanoparticles dispersed in either cyclohexane, toluene or tetrahydrofuran were added to separate glass vials. For each experiment, the overall volume of the mixture was maintained at 5 ml by adding 4 ml of the dispersing solvent (*i.e.* cyclohexane, toluene or tetrahydrofuran) to the respective reaction vial. In each case, the same weight of BCN-NT/N-CNTs (4 mg) was used. The mixture was sonicated for 1 hour before collecting and washing using the procedure detailed in 4.2.7.

4.2.8. Effect of Destabilising Agent on Iron Oxide NP/N-CNT Hybrids

The effect of nanoparticle stability on the functionalisation procedure was studied by altering the solvent composition in the reaction mixture. Similar procedures to those detailed in 4.2.7 were employed here. To begin with, N-CNTs (4 mg) and iron oxide nanoparticles dispersed in solvent (1 ml of 8 mg/ml solution) were added to separate glass vials. To each vial, differing amounts of ethanol were added (1 and 2 ml) before then making up the final volume to 5 ml using the NP dispersing solvent (3 and 2 ml respectively). In this case the dispersant was cyclohexane. The mixture was sonicated for 1 hour before the collection and washing.

4.2.9. Effect of Polymer Coating on Iron Oxide NP/N-CNT Hybrids

The influence of a polymer coating on the functionalisation procedure was investigated. Similar procedures to those detailed in 4.2.7 were employed here. To begin with, iron oxide nanoparticles dispersed in solvent (1 ml of 8 mg/ml solution) as well as additional dispersing solvent (4 ml) were added to a glass vial. To the vial, polymer-wrapped N-CNTs (4 mg, see 4.2.6) were then added. The reaction mixture was then sonicated for 1 hour before the collection and washing procedure.

4.3. Results and Discussion

4.3.1. Synthesis of Iron Oxide Nanoparticles

Prior to the functionalisation experiments, iron oxide nanoparticles (FeO_xNPs) of varying sizes were synthesised through the controlled degradation of iron acetylacetonate using a wet-chemical approach. This procedure has been modified from a methodology developed within the Nanomaterials by Design group, prior to this work.[115, 272] The synthesis involves heating the metal acetylacetonate in the presence of a capping agent under an inert atmosphere, which was achieved using a Schlenk set-up. Upon heating the reagents together, it is widely accepted that the reaction proceeds *via* LaMer's theory.[273] Thermal breakdown of the precursor initiates the formation of iron oxide nuclei. As the reaction proceeds, the nuclei begin to aggregate and form the nanoparticle core.[274] The oleylamine, which also acts as a high boiling point solvent for the reaction, attaches to the nanoparticle core *via* the amine terminal group. The alkyl chain on the oleylamine ligand facilitates suitable repulsion between the individual nanoparticles, preventing clustering and sedimentation. The alkyl chain of the oleylamine, that coats the nucleus, dictates the properties of the nanoparticle's exterior and thus, allows them to be dispersed in the range of organic solvents that are used throughout this chapter.

X-ray diffraction (XRD) was used to probe the crystalline structure of the as-prepared nanoparticles. Iron oxide displays a number of potential crystal structures which include maghemite, hematite and magnetite. Each of these iron oxide phases display different properties and this can therefore influence the intrinsic properties of the FeO_xNPs.[275] The XRD pattern recorded for the FeO_xNPs is shown in Figure 4.3. The recorded spectrum displays several peaks at various angles, these can be attributed to the 111, 220, 311, 222, 400, 331, 422, 511, 440, 620 and 533 crystal planes.[276, 277] These diffraction peaks correspond

well with a pattern expected for iron oxide nanoparticles with a spinel structure. In relation to the theoretical diffractions expected, we can infer from the XRD diffractogram that the FeO_xNPs synthesised, possess a mixture of magnetite and maghemite crystal phases. The sharp, well-defined nature of these peaks show that the synthesised nanoparticles are crystalline which could be an important consideration for future applications. The XRD spectrum is indicative of a face centred cubic lattice structure.[276, 278]

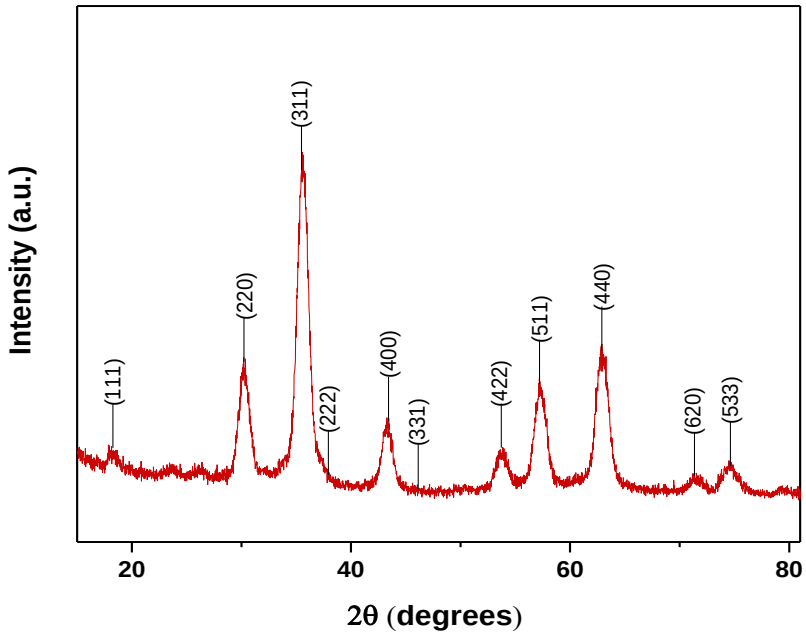


Figure 4.3: XRD pattern displayed by as-synthesised FeO_xNPs with corresponding peak labels.

Transmission electron microscopy (TEM) was used to image the synthesised FeO_xNPs. Figure 4.4 shows micrographs of the nanoparticles in non-polar solvents which include, cyclohexane, toluene and tetrahydrofuran (THF) . The FeO_xNPs are spherical, with no visible aggregates present, and appear monodisperse. The dispersed nanoparticles were measured to have a typical diameter of *ca.* 7.6 nm, regardless of solvent. In each case, the nanoparticles were well dispersed. These nanoparticles were used for the functionalisation experiments in subsequent sections.

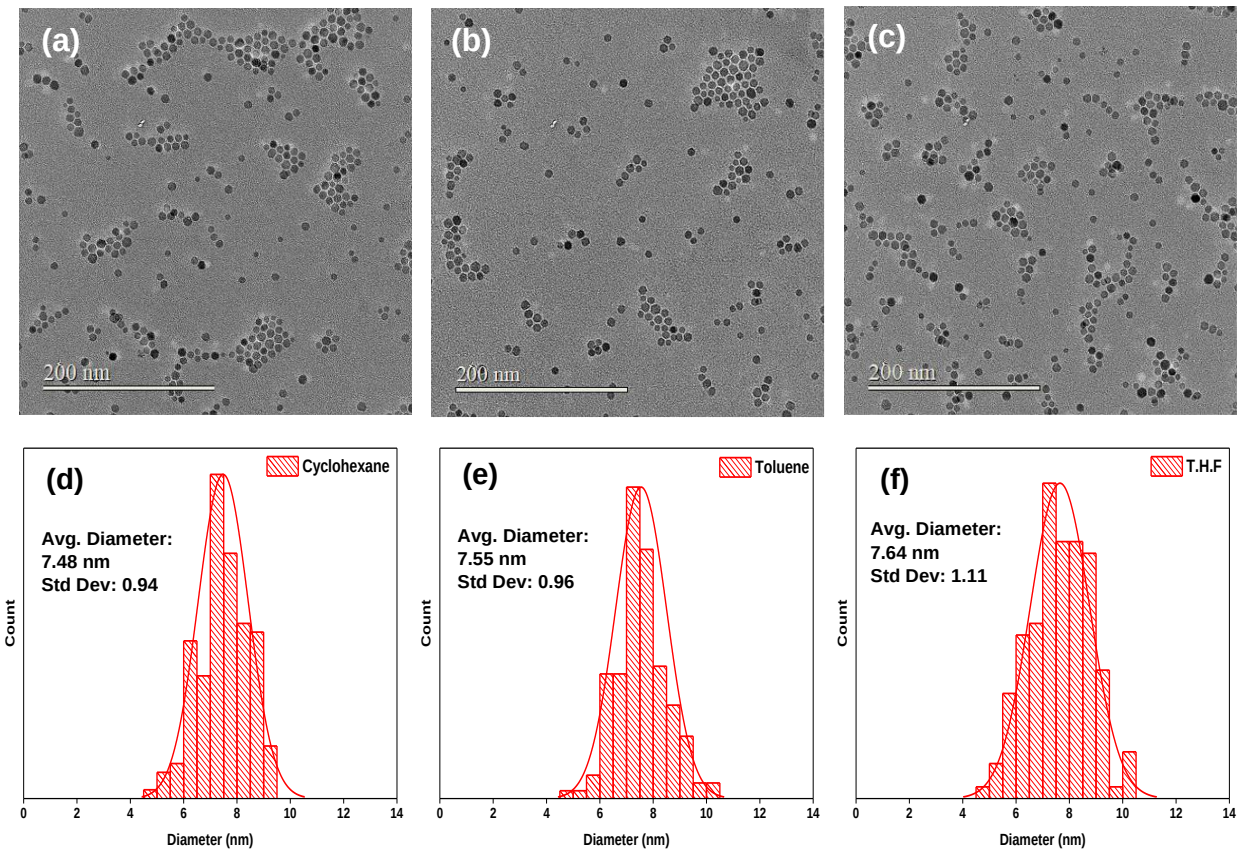


Figure 4.4: TEM micrographs showing iron oxide nanoparticles dipsersed in (a) cyclohexane, (b) toluene and (c) tetrahydrofuran along with the respective size distributions recorded in each solvent (d, e, f).

Dynamic light scattering (DLS) was used to complement the measurements made *via* TEM analysis. The nanoparticles dispersed in cyclohexane were examined through DLS measurements. As can be seen in Figure 4.5, the nanoparticle size distribution for the nanoparticle verify the initial observations made *via* TEM analysis *i.e.* uniform distributions that lack the significant presence of aggregates. The average size of the nanoparticles synthesised *via* Method 1 was measured at *ca*. 8.9 nm. This recorded distribution is slightly larger than TEM analysis which is to be expected as the DLS measurement accounts for the contribution of attached oleylamine ligands, whereas TEM only images and allows measurement for the core of the nanoparticle. In the appendix we can see that by decreasing the reaction time and temperature, we were able to reduce the size of the nanoparticles. The average measured size of the nanoparticles synthesised *via* Method 2 were found to be 3.7 nm

according to TEM analysis and 5.6 nm though DLS; these nanoparticles were employed for stability testing.

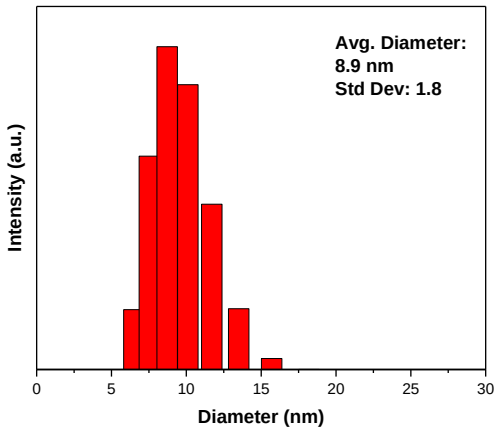


Figure 4.5: Size distribution plot of the recorded hydrodynamic diameters for the iron oxide nanoparticles produced via Method 1, dispersed in cylohexane, through DLS analysis.

4.3.2 Synthesis of Iron Oxide NP/N-CNT Hybrids

4.3.2.1 Standard Conditions

Here we will briefly establish the standard conditions employed for the doped-nanotube hybrids and detail their characterisation, to act as a baseline for further exploration. Prior to functionalisation, the nanotubes were treated with hydrochloric acid to remove any potential residual catalyst particles from the surface of the nanotube. The treatments resulted in a colour change of the acid from clear to orange, signifying the dissolution of the exterior catalyst (see appendix). The purified nanotubes are shown in Figure 4.6. As we can see, the surface of the nanotubes is, on the whole, clear of external catalyst impurities that have been removed with the acid treatment. From the TEM micrographs we can see from the areas encircled in red, that a small number of impurities remain in the sample. These are embedded into the nanotube itself as opposed to being attached to the exterior walls. Hydrochloric acid was selected as the purifying agent as it is non-oxidative in the treatment of carbonaceous species. As a result of this, the acid does not penetrate the nanotubes and thus leaves a small

amount of embedded catalyst. The standard deviation in residual mass across the sample after purification was 0.53 wt.% which highlights the effectiveness of this purification technique and uniformity of the sample prior to functionalisation .

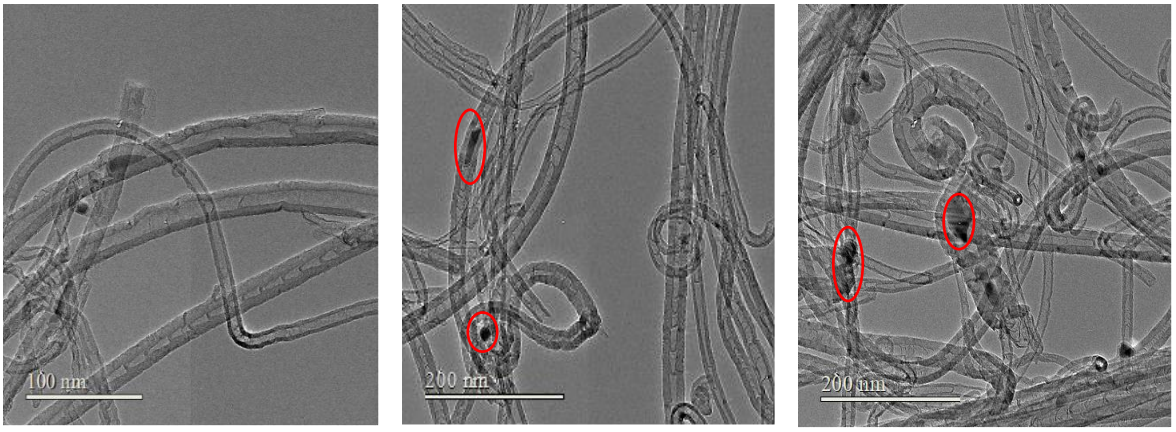


Figure 4.6: TEM micrograhs highlighting the removal of any potential external catalyst residue, through non-oxidative washing, from the surface of starting nanotubes. The areas circled in red highlight embedded and ecapsulated catalyst material which are not removed through non-oxidative procedures.

After purification, for a typical functionalisation procedure, either the N-CNTs or BCN-NTs were added to a vial containing FeO_xNPs along with a dispersing solvent. The mixture was sonicated for a fixed period and then thoroughly washed, to remove any unbound nanoparticles from the nanotube surface, before drying. These procedures were adapted from work on undoped CNTs, previously conducted within our research group.[115] The main characterisation techniques used to analyse the composition of the produced materials were thermogravimetric analysis (TGA) and TEM. TGA allows us to quantify the loading of the nanoparticles onto the nanotubes, whilst TEM allows visualisation of the nanoparticle distribution across the nanotube. A typical TGA profile for one of the nanotube-nanoparticle hybrids, obtained under an air atmosphere, is shown in Figure 4.7; these oxidation profiles can be split into three sections. Initially the sample is held at 100 ^{o}C to ensure any moisture was removed from the sample. The first weight loss, occurring at temperatures below 400 ^{o}C, corresponds well with that observed in the oxidation profile of isolated FeO_xNPs, which is

shown in the appendix of this thesis. This weight loss can be assigned to the degradation of the oleylamine ligands which are removed as a gas.[279] This weight loss is complete at 340 ^{o}C and for this reason, the oxidation procedure is held at this temperature for 15 minutes to ensure complete burning off when conducting the analysis. Depending on the sample, the second weight loss appears between the temperatures of 400 and 850 ^{o}C and can be assigned to the oxidation of the graphitic N-CNT or BCN-NTs. The final section of the profile corresponds to the residual mass which represents the loading of FeO_xNPs onto the doped nanotubes. The oxidation profile displayed by FeO_xNPs on their own, shown in the appendix, reveal that the bulk mass of isolated FeO_xNPs remain after oxidation to 900 ^{o}C, owing to the iron content of the sample. Iron oxide is thermally stable under these operating conditions. TGA analysis of the nanotube-nanoparticle hybrids therefore allows us to probe the ligand, nanotube and nanoparticle composition of the sample.

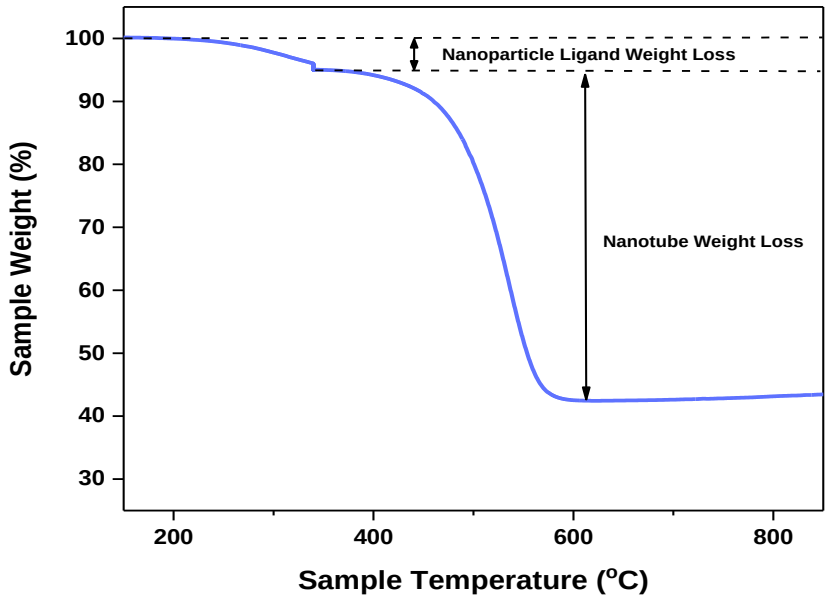


Figure 4.7: A typical TGA profile, obtained in air, displayed by the hierarchical nanoparticle – nanotube hybrids produced in this study, which highlight the breakdown in composition of the hybrid material.

A typical TEM micrograph obtained for one of the as-synthesised hierarchical hybrids is shown in Figure 4.8. As can be clearly seen, when compared to the purified starting material, the functionalisation procedure has succeeded in attaching nanoparticles to the surface of the

nanotube. The monodisperse nanoparticles have retained their uniform size when coating the nanotubes and can be distinguished from residual catalyst impurities, which are significantly larger than the attached nanoparticles. A magnified image of the hybrid, shown in the appendix, highlights the crystalline nature of the FeO_xNP attached to the nanotube wall. The TEM analysis also revealed that the FeO_xNPs present in the sample are only attached to the nanotubes, and no phase separation has been detected. This highlights that the washing procedure was effective in removing any unbound FeO_xNPs from the sample. The effect of various parameters on the nanoparticles distribution across the nanotubes will be discussed in subsequent sections.

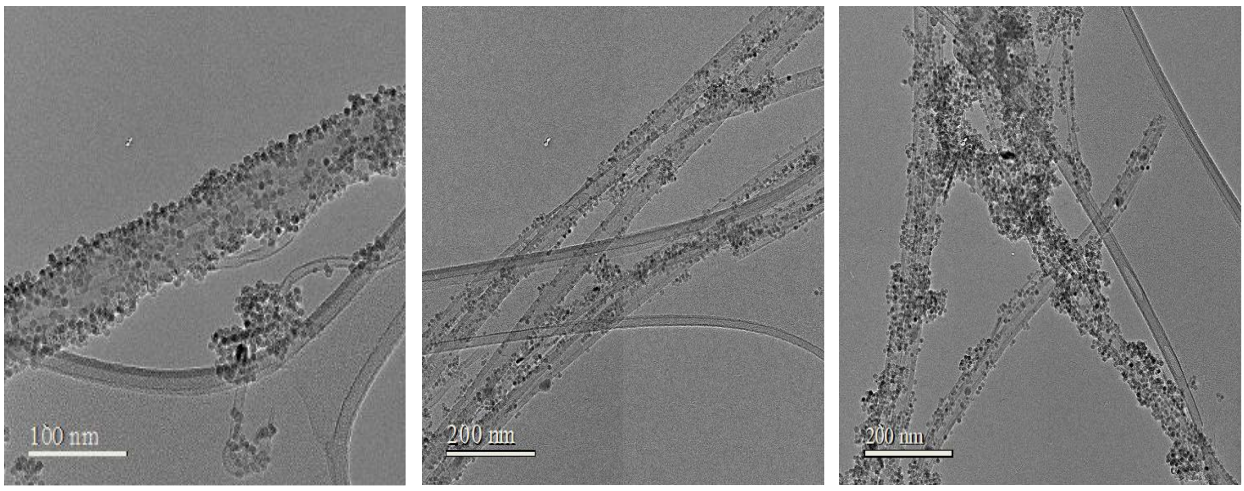


Figure 4.8: Typical TEM micrographs obtained for the as-produced hierarchical nanoparticle – nanotube hybrids which demonstrate the successful attachment of iron oxide nanoparticles to the nanotube surface and highlight the lack of separate phases detected through this analysis technique.

4.3.2.2 Effect of Solvent on Functionalisation

After establishing that the *ex-situ* decoration techniques translated to doped nanotubes, we wanted to investigate the functionalisation further in order to gain control over the process. The selection of solvent has previously been shown to impact non-covalent interactions and thus the functionalisation of nanotubes where polymer attachment is concerned.[280] For the

production of nanoparticle-nanotube hybrid materials, two previous studies showed that the selection of solvent was a contributing factor in the level of nanoparticle functionalisation achieved on undoped CNTs.[115, 265] Here therefore, we looked to extend these studies and investigate the effect of solvent selection on the functionalisation of N-CNTs with FeO_xNPs. Whilst doped nanotubes offer the potential for alternative interactions (*e.g.* coordination) through heteroatoms and defects, this study was primarily focused on the effect of non-covalent interactions through altering the solvent medium.

As has been mentioned, the functionalisation experiments involved sonicating nanotubes and nanoparticles together in a solvent medium. The experiments were conducted in either cyclohexane, toluene or THF, to determine how solvents with varying chemical properties impacted the functionalisation procedure. This was followed by a thorough washing procedure, in each respective solvent, to remove any loosely bound FeO_xNPs from the sample, which could be observed through the resulting clear filtrate. The cleaning procedure was controlled for each experiment to ensure each batch had the same treatment. The characterisation techniques established in section 4.3.2.1 were employed here to evaluate and compare the composition of the hybrids produced in each solvent medium.

The compositions of the N-CNT/FeO_xNP hybrids produced in various solvents are summarised in Table 4.1, while Figure 4.9 highlights the iron nanoparticle loading in the respective solvents. As we can clearly see, the composition of the hybrid materials are strongly affected by the choice of solvent used during the fabrication process. The results from this study show that by altering the solvent, the nanoparticle loading on the nanotubes can be tuned. From the tabulated compositions, we can see that the ligand content within the hybrid material remains relatively uniform, regardless of the solvent selection.

Table 4.1: A breakdown of compositions for the N-CNT/FeO_xNP hybrids produced in various solvents.

Solvent	Sample Name	Oleylamine Content (average wt.%)	Iron Oxide Content (average wt.%)
Cyclohexane	N-CNT + FeO_xNP Hybrid (C-Hex)	6.6 ± 1.5	42.5 ± 2.3
Tetrahydrofuran	N-CNT + FeO_xNP Hybrid (THF)	5.4 ± 0.9	24.4 ± 1.7
Toluene	N-CNT +FeO_xNP Hybrid (Tol)	5.0 ± 1.4	33.6 ± 1.3

For example, the oleylamine-ligand composition obtained using toluene is lower than that of THF despite having a larger nanoparticle loading overall. This demonstrates that the functionalisation of the nanotubes with FeO_xNPs is not determined by the amount of oleylamine present within the sample; or at least that the solvent choice is more significant towards the level of functionalisation achieved. It has previously been suggested that the presence of oleylamine is a significant factor in the functionalisation of nanotubes but that does not seem to be the case here, with solvent effects being more pronounced.[262]

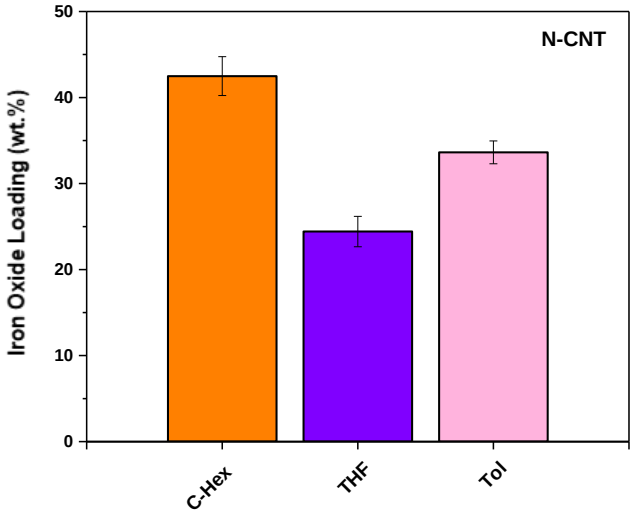


Figure 4.9: A comparison the iron loading present within each of the N-CNT/FeO_xNP hybrids produced in various solvents.

Figure 4.9 shows that the FeO_xNP loading varies when the functionalisation is conducted in different solvent media. Experiments conducted in THF gave the lowest loading, whilst

toluene showed an increase, and finally, cyclohexane displayed the highest nanoparticle content overall. This observation highlights the impact that a trivial reaction parameter, solvent selection, can have on the result of these functionalisation experiments. The loadings achieved for each experiment-set is fairly consistent across each solvent-type, which reaffirms the significance of solvent selection on the functionalisation process.

Figure 4.10 compares the results obtained from the TEM analysis of the hybrid materials synthesised in the various solvents.

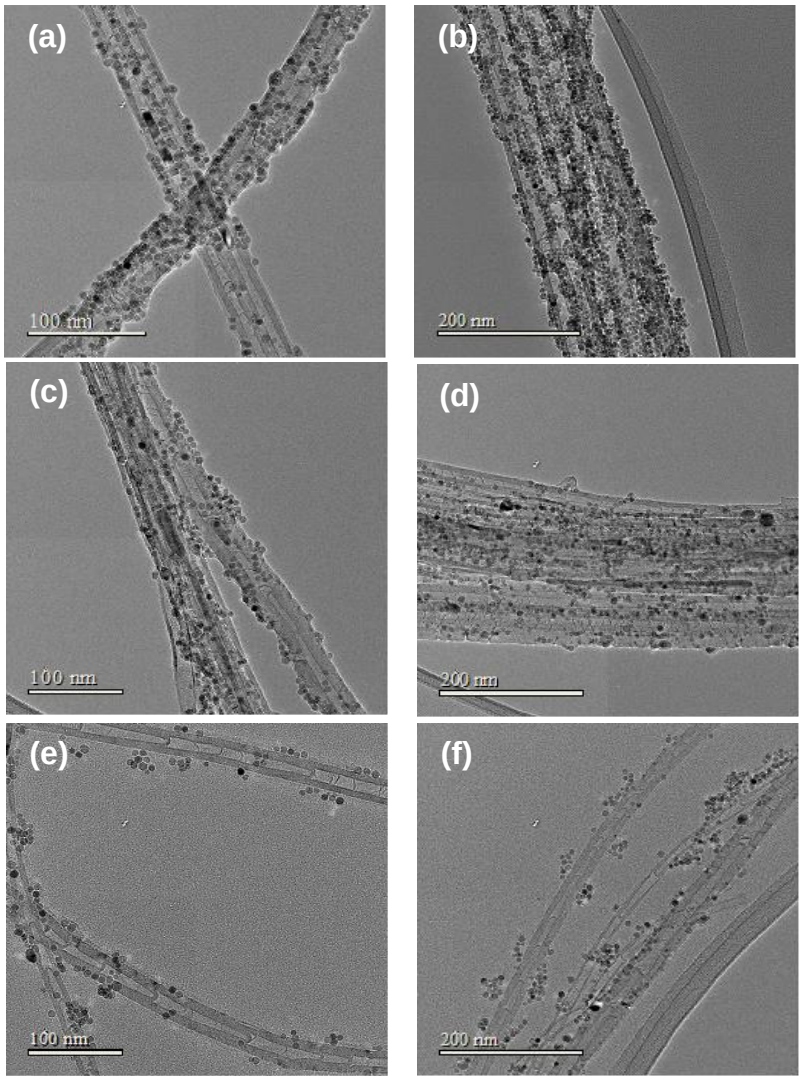


Figure 4.10: TEM micrographs obtained for the N-CNT/FeO_xNP hybrid materials produced under standard conditions in (a/b) cyclohexane, (c/d) toluene and (e/f) tetrahydrofuran. The images highlight how the coverage across the nanotube alters with solvent selection.

In each case we can clearly observe the presence and successful anchoring of the FeO_xNPs onto the nanotubes. Additionally, no separate phases of free nanoparticles were detected. This highlights that the nanoparticles present in the sample were indeed partaking exclusively in nanotube attachment. As can be seen, the solvent impacts the distribution of nanoparticles over the surface of the nanotubes. The hybrids produced in cyclohexane shown in Fig 9 (a), are found to possess a uniform coating of FeO_xNPs on the exterior surface of the nanotubes. Some sections of the exterior remain uncoated after the functionalisation, but images at lower magnifications highlight that the majority of sample is coated in FeO_xNPs. There were no large areas of aggregated FeO_xNPs clusters identified within the coating. The use of toluene during the synthesis altered the observed FeO_xNP distribution on the nanotubes. Whilst still clearly identifiable, the FeO_xNP coating is less continuous across the nanotube exterior. Once again, no significant clustering is observed amongst the coating. Further to this, the FeO_xNP coating becomes more sporadic when THF was used when compared to the toluene. In Figure 4.9 we demonstrated that the FeO_xNP loading on the nanotubes, determined through TGA analysis, was of the order cyclohexane>toluene>THF. This trend can clearly be visualised through the TEM analysis conducted here.

As has been demonstrated thus far, the solvent choice has a significant impact on the level of FeO_xNP functionalisation achieved. Hitherto, there have been two studies that looked to understand the influence solvent had on the non-covalent functionalisation of CNTs with nanoparticles. The latter study found discrepancies between their findings and the original trend observed. The first study by Rance *et al.*[265] suggested that there was correlation between the dielectric constant of the solvent medium and the level of functionalisation achieved. This, however, was not observed by Quijano-Velasco *et al*.[115] who used a surface energy model to explain their results. Neither of these studies were conducted with the doped nanotubes used here, that typically possess different surface properties to their undoped

counterparts. Here we looked to evaluate the observations made thus far in this study by comparing them to the existing models that have been used to rationalise how non-covalent interactions impact the attachment of nanoparticles.

Figure 4.11 (a) presents a plot of the nanoparticle loadings obtained in various solvents against the dielectric constant of the respective solvent. From the figure we can see an inversely proportional relationship; as the magnitude of the dielectric constant increases, the level of FeO_xNP functionalisation achieved decreases. Given that the dielectric constant is an indicator of polarity, it is no surprise to see that this relationship is mirrored for relative polarity, in Figure 4.11(b). The relationship with solvent polarity appears linear with respect to the loading achieved. The solvent with the lowest dielectric constant used here, cyclohexane gave the highest loading, with the opposite being observed for THF.

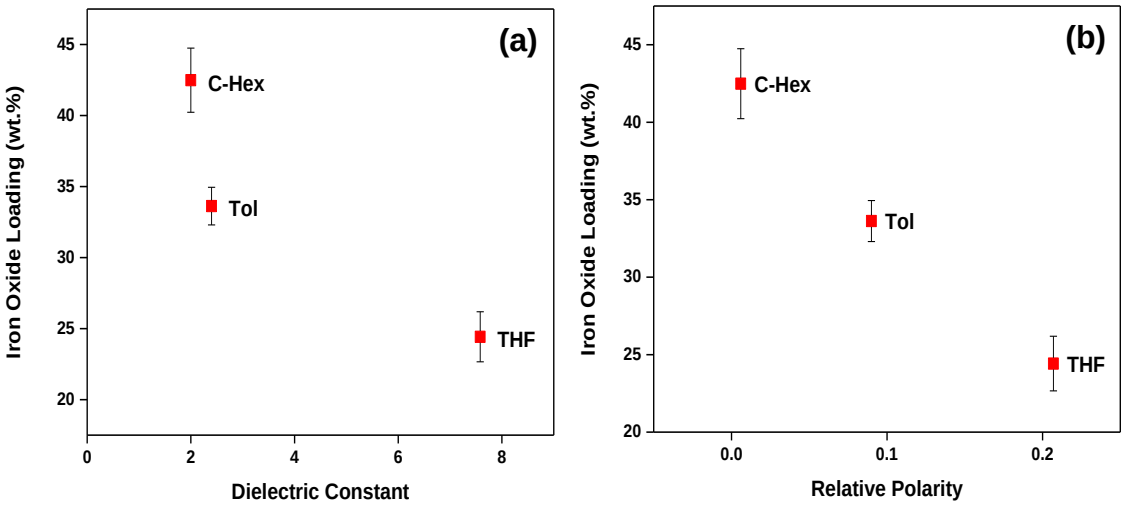


Figure 4.11: Plots of iron nanoparticle loading for each of the N-CNT/FeO_xNP hybrids produced in cylohexane, toluene and tetrahydrofuran, against the respective solvents (a) dielectric constant and (b) relative polarity.

This result demonstrates that Coulombic interactions experienced between the nanoparticles, nanotube and solvent are impacting the degree of functionalisation achieved. It has been proposed in a previously that this observation is related to increased repulsion between the

nanotubes and nanoparticles. As the dielectric constant of the solvent increases, the magnitude of negative charge located on the surface of the nanoparticles also increases. This effect then increases the electrostatic repulsion experienced between the nanoparticles and nanotubes, in turn reducing the immobilisation of the former onto the surface of the latter material. However, previous work within our group did not follow this trend. The original study by Rance *et al.*[265] used AuNPs to functionalise undoped CNTs, whilst the previous work conducted within our group functionalised undoped CNTs with FeO_xNPs.[115] Under these altered conditions, the dielectric effect may be less pronounced for FeO_xNPs, due to the difference in surface properties, which offers an explanation for the deviation from the trend demonstrated in the original study. Given that the results presented here showed good correlation with the dielectric effect, however, it could be suggested that the use of doped nanotubes may impact the observed result. According to other reports, dopant sites within N-CNTs can introduce concentrated areas of surface charge.[281-283] If the surface charges on the N-CNTs are negative, the repulsive interactions would be more pronounced for this combination of materials when compared to undoped CNTs under the same conditions. The use of N-CNTs therefore offers explanation for the dielectric effect observed here *i.e.* increased FeO_xNP loading as the solvent polarity decreases. The study by Rance *et al*.[265] varied the solvent medium to confirm this effect throughout their study and three of those solvent choices were used here. This further highlights the correlation between the original study and the work presented in this chapter.

Instead of just considering electrostatics, surface energy based predictive models look to account for additional interactions experienced between material sets. Surface energy-based solubility parameter (SESP) theory has been developed from Hansen solubility theory, as well as work from Bergin and Quijano-Velasco *et al.* on the solubility and functionalisation of nanotubes in solvent.[115, 266, 284, 285] Where the dielectric effect considers how solvent affects

the interaction between nanoparticles and nanotubes, the surface energy approach considers the interactions between solvent and the nanotubes. SESP accounts for multiple intermolecular interactions which contribute to the total surface energy of a material ($E_{S,\ Total}$). These contributions include, dispersive interactions ($E_{S,\ Dispersive}$), polar interactions ($E_{S,\ Polar}$) and hydrogen bonding ($E_{S,\ H\text{-}Bonding}$) which each relate to Van der Waal forces, electrostatic forces and electronic exchanges, respectively. This relationship between surface energy and its component parts is expressed by equation 4.1.

$$(4.1) \quad E_{S,\ Total} = E_{S,\ Dispersive} + E_{S,\ Polar} + E_{S,\ H-Bonding}$$

The approach of Bergin *et al*.[266] states that the SESP values for a substance can be determined using equation 4.2; where δ_i represents the Hansen solubility value for the material in $MPa^{0.5}$ and α_i signifies constants relating to either, dispersive, polar or H-bonding contributions. $E_{S,\ Total}$ denotes the total surface energy and itself can be calculated using equation 3. Here, γ is the surface tension of a given solvent, T is the temperature and $\Delta S_{Solvent}$ is a constant relating to the entropy of the solvent.[256]

$$(4.2) \quad E_{S,\ i(D,P,H)} = \frac{\alpha_i \delta_i}{\alpha_D \delta_D^2 + \alpha_P \delta_P^2 + \alpha_H \delta_H^2} E_{S,\ Total}$$

$$(4.3) \quad E_{S,\ Total} = \gamma + T\Delta S_{Solvent}$$

From these values, we are then able to calculate the solubility parameter for each of the dispersive, polar and H-Bonding components, represented by $\partial_{i(D,P,H)}$), using equation 4.4.[256]

$$(4.4) \quad \partial_{i(D,P,H)} = \sqrt{E_{S,\ i(D,P,H)}}$$

Finally, using the calculated solubility parameters for each component of the solvent, we can compare them to those of the nanotubes. This allows us to determine the Hansen SESP distance (R) using equation 4.5, which is related to the enthalpy of mixing in a given solvent. This distance, in Hansen space, has been used to predict the dispersibility of a nanotube in solvent. The smaller the distance, the smaller the enthalpy of mixing and the increased likelihood of dispersing.[256]

$$(4.5) \quad R = \sqrt{(\partial_D^{CNT} - \partial_D^{Solvent})^2 + (\partial_P^{CNT} - \partial_P^{Solvent})^2 + (\partial_H^{CNT} - \partial_H^{Solvent})^2}$$

In Figure 4.12, a plot of iron loading onto the N-CNTs, in various solvents, against the calculated SESP distance (R) is presented. A summary of the values used for the calculation of these Hansen space distances is tabulated in the appendix.[115, 286, 287] From this plot we can see that there is a clear trend displayed between the SESP distance and level of nanoparticle functionalisation achieved. As the measured solvent-nanotube SESP distance is increased, we see that the iron loading also increases in a linear fashion. This highlights that the solvent selection has a significant impact on the degree of functionalisation. In prior studies, the

relationship between solvent medium and the level of functionalisation has been investigated for the functionalisation of nanotubes with polymer.

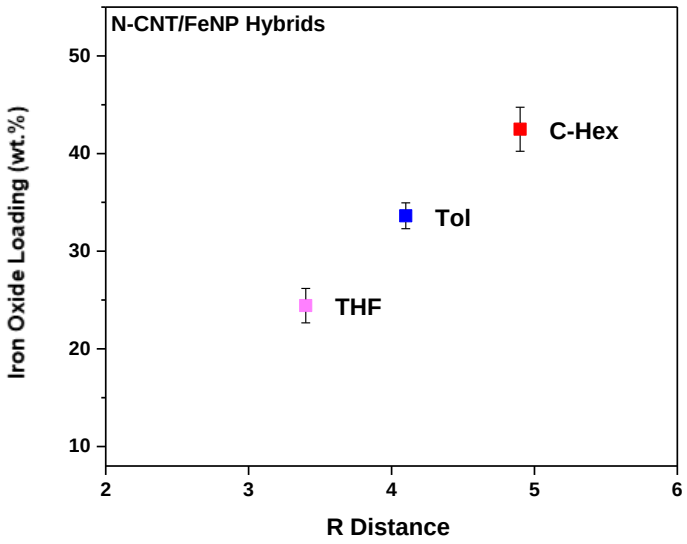


Figure 4.12: A plot of iron oxide loading for each of the N-CNT/FeO_xNP hybrids produced in cylohexane, toluene and tetrahydrofuran, against the calculated SESP distance, R.

According to O'Connell *et al*.[288] the functionalisation procedure is driven by the interactions between the solvent and nanotube. If these are unfavourable, the polymer wraps itself around the nanotube in an effort to minimise these unfavourable interactions. This could be extended for materials other than polymer. As has been mentioned, Bergin *et al*.[266] suggested that the solvent-nanotube SESP distance (R) is an indicator of dispersibility, with larger distances being unfavourable. Given this, we would expect that as the value of R increases, the level of nanoparticle attachment to the N-CNTs would increase as a means for coating the nanotube and reducing unfavourable interactions experienced with the solvent. This reasoning provides a good fit with the results that are presented here and strongly suggest that the solvent choice and non-covalent interactions are key considerations when planning functionalisation experiments. This result highlights that the SESP based approach, for predicting functionalisation, can be applied to doped nanotubes. It is important to note, due to

unforeseen complications arising and time constraints, we were unable to perform the characterisation required to determine the exact surface energy values for the nanotubes used in this study; this would require external collaboration. Therefore, the Hansen distances were calculated using values that have been utilised in prior studies within our group. We do not anticipate that this would have a drastic effect on the trends that have been observed here given the defect densities are fairly consistent. Furthermore, in future this could be a topic for further exploration to provide additional validity to the results presented here.

4.3.2.3 Effect of Destabilising Agent on Functionalisation

Due to the long alkyl chain section of the oleylamine ligands, the as-prepared FeO_xNPs can be dispersed in non-polar solvents. The surface chemistry of the nanoparticles makes them unsuitable for dispersion in polar solvents and the addition of excess polar solvent is often used to precipitate the nanoparticles out of solution through aggregation.[289] The stability of a nanoparticle solution has been shown to have influence over the level of functionalisation achieved on nanotubes.[115] Unstable nanoparticle solutions, that have a tendency to aggregate, have shown higher levels of functionalisation than had been predicted for a stable dispersion. It was proposed that this is because, in an attempt to minimise their unfavourable interaction with 'poor' solvent, the nanoparticles are driven to coat the nanotubes. Here, we explored this destabilisation effect further. Through the addition of ethanol to the starting reaction mixture (of nanotubes, nanoparticles and solvent) we attempted to intentionally de-stabilise the nanoparticles *in-situ* and determine the effect it had on the nanotube functionalisation.

The effect of ethanol addition to the nanoparticle solutions is exemplified in Figure 4.13. Each of the vials contain the same amount of FeO_xNPs in cyclohexane, with different dilution components added to them. Each of the vials contain FeO_xNPs in cyclohexane (1 ml). Vial A

was diluted with cyclohexane (3 ml), Vial B with cyclohexane (2 ml) and ethanol (1 ml) and Vial C again with cyclohexane (1ml) and ethanol (2 ml). The vials were left for 24 hours after dilution. As can be seen, the sample in Vial A represents a typical iron oxide nanoparticle solution which is deep brown in colour. When inverted, it is clear there is no precipitate at the bottom of the vial due to the FeO_xNPs being well dispersed. Vial B does not show any significant visual differences when compared to Vial A.

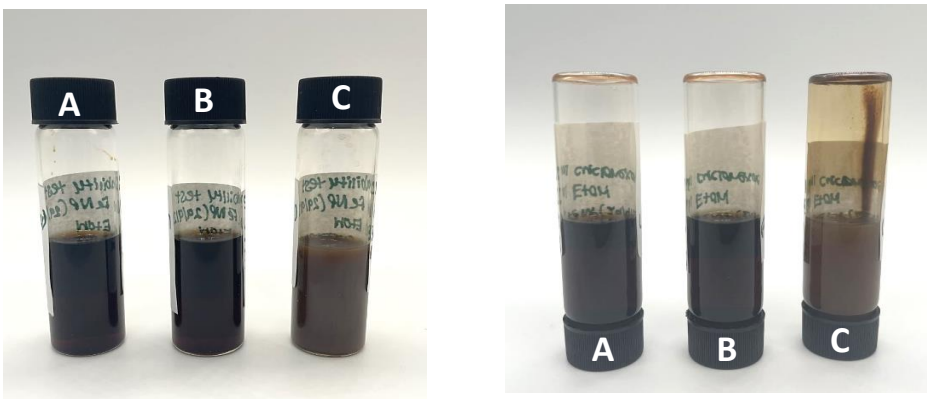


Figure 4.13: Optical images showing iron oxide nanoaparticle solutions with varying levels of ethanol added to each vial. (a) contains no ethanol, (b) contains 1 ml ethanol and (c) contains 2 ml of ethanol. Increasing addition of ethanol leads to a colour change and noticeable aggreagtion upon inversion of the vials.

Vial C however shows a clear visual difference, with a cloudy colour being noted. On inversion, it is clear that the nanoparticles have begun to sediment in Vial C. This shows that the gradual addition of ethanol to the FeO_xNP starting solution is sufficient to destabilise the nanoparticles due to unfavourable interactions with the added polar solvent.

The destabilisation effect was further probed by TEM analysis. As we can see for Vial A in Figure 4.14, the NP solution diluted with just cyclohexane is typical of a FeO_xNP solution as visualised in section 4.3.1. The nanoparticles are uniform in size and are well dispersed with no aggregate clusters detected. Upon addition of ethanol to the vials however, the presence of

aggregates can be observed. For Vial B, despite visually looking similar to Vial A macroscopically, the addition of ethanol had an impact on the stability of the NPs in solution. As we can see in Figure 4.14 (b), the addition of just 1 ml of ethanol was sufficient in destabilising the nanoparticles as visible aggregates begin to form. Further ethanol addition in Vial C led to more significant aggregation, as shown in Figure 4.14 (c). These observations show that through the addition of small amounts of ethanol to a starting NP solution, the nanoparticles can be sufficiently de-stabilised.

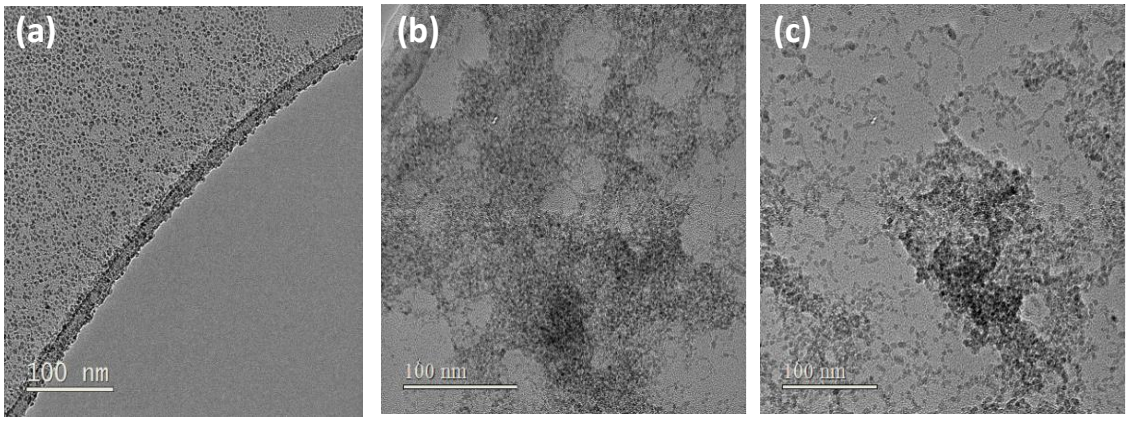


Figure 4.14: TEM micrographs showing the effect that the addition of ethanol has on the stability of iron oxide nanoparticle dispersions produced using Method 2. In (a) no ethanol is added whilst in (b) 1 ml of ethanol has been added and (c) 2 ml of ethanol.

Quijano-Velasco *et al.*[115] proposed that the stability of a nanoparticle solution had an impact on the level of nanoparticle attachment on to nanotubes during the functionalisation. Experiments conducted in dichloromethane showed unprecedent levels of NP loading, which the authors attributed to the poor stability of the nanoparticles in this solvent, when compared to other solvents used in the study. However, this was not explored in detail. Here we attempted to mimic and investigate this effect through the intentional destabilisation of the starting nanoparticles, to gain further insight into this phenomena. Table 4.2 summarises the data derived from TGA and gives us an insight into the NP loadings on to the N-CNTs under

varying degrees of destabilisation.

Table 4.2: A breakdown of compositions for the N-CNT/FeO_xNP hybrids produced under standard conditions with varying degrees of ethanol added to the mixture.

Solvent	Sample Name	Oleylamine Content (average wt.%)	Iron Oxide Content (average wt.%)
Cyclohexane	N-CNT + FeO_xNP Hybrid (C-Hex)	6.6 ± 1.5	42.5 ± 2.3
Cyclohexane + 1 ml EtOH	N-CNT + FeO_xNP Hybrid (1 ml EtOH)	6.0 ± 1.0	43.5 ± 1.2
Cyclohexane + 2 ml EtOH	N-CNT +FeO_xNP Hybrid (2 ml EtOH)	6.5 ± 0.5	63.2 ± 0.6

As we can see, for the first two results *i.e.* standard conditions and the lowest level of destabilising agent, the composition of both hybrids remains almost unchanged despite the altered synthesis conditions. Upon further addition of ethanol however, we see a significant deviation in the composition of the FeO_xNP/N-CNT material. In each of the experiments we see that the ligand composition of the hybrids is consistent, regardless of the amount of destabilising agent. The iron loading can be starkly different however, as exemplified in Figure 4.15 and Table 4.2.

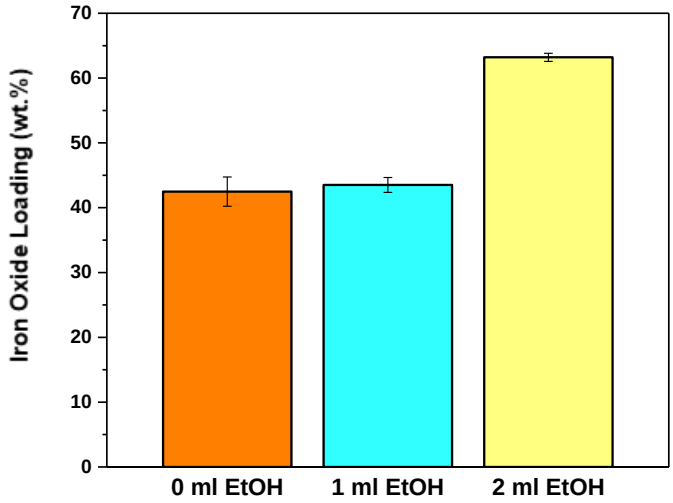


Figure 4.15: A comparison the iron loading present within each of the N-CNT/FeO_xNP hybrids produced with varying degrees of ethanol added to the reaction mixture.

When 2 ml of destabilising agent is added during the functionalisation, the loading of nanoparticles onto the hybrid increases to an average of 63 wt.% in total. This finding supports the explanation provided for the deviation, noted by Quijano-Velasco *et al.*,[115] in their study. The unstable nanoparticles are essentially driven towards coating the nanotubes in an attempt to reduce unfavourable interactions they are experiencing within the solvent mixture that contains ethanol. This provides a reasonable description for the significant increases noted upon the addition of destabilising agent (2 ml), as we have shown in Figure 4.14 (c) that this quantity of ethanol promotes significant aggregation. It is interesting to note that the initial addition of ethanol (1 ml) did not alter the composition significantly. An explanation for this may be that there are competing factors influencing the functionalisation process. As we have demonstrated in section 4.3.2.2, the level of functionalisation that could be achieved on the nanotubes showed correlation with the dielectric constant of the solvent. The higher the dielectric constant, the lower the level of nanoparticle functionalisation that can be attained. Given this, as we introduce ethanol, we have increased the dielectric constant of the system which would be expected to hinder functionalisation, according to our previous observations. Simultaneously however, we are promoting aggregation of the nanoparticles, which favours attachment to the nanotubes. With 1 ml of ethanol added, these driving forces are balanced, which leads to a composition similar to that obtained under standard conditions. Upon the addition of 2 ml however, a critical aggregation point may have been achieved which shifts the balance in favour of functionalising the nanotubes. Alternatively, given that on visual inspection the addition of ethanol (1 ml) does not cause significant aggregation or precipitation, there may be a threshold of nanoparticle solution ‘instability’ that translates to promoting loading of the nanoparticles onto the nanotube surface. Considering that, moving forward this would be an interesting area of research to explore further.

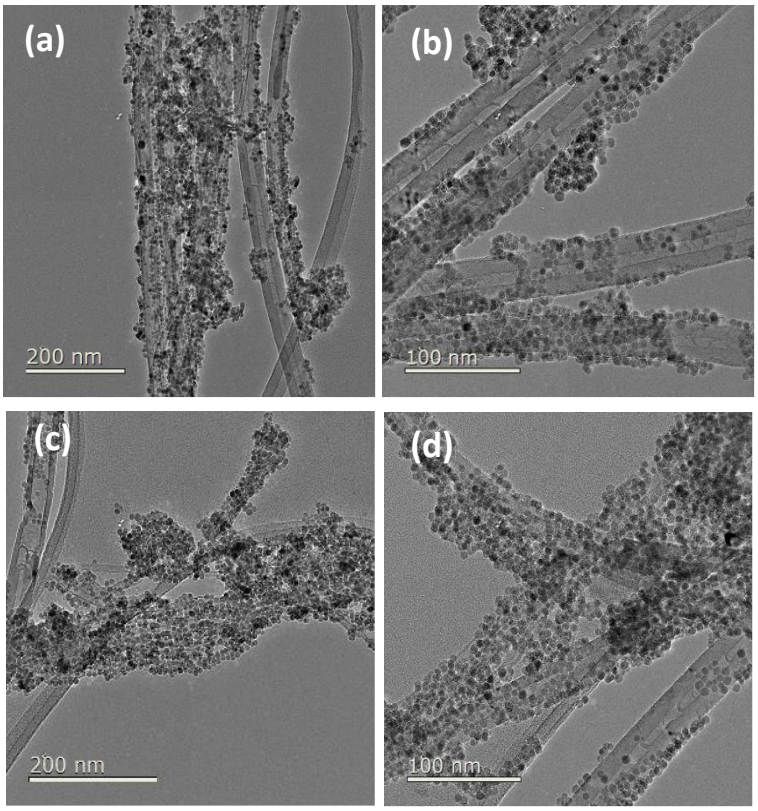


Figure 4.16: TEM micrographs obtained for the N-CNT/FeO_xNP hybrid materials produced with varying degrees of ethanol added to reaction mixture; in (a/b) 1 ml of ethanol and (c/d) 2 ml of ethanol. The images highlight how the coverage across the nanotube, in comparison to standard conditions, when ethanol is added. These images are representaive of each sample on the whole after scanning various areas of the grid, each image representing a different sample section.

In Figure 4.16, we see TEM images obtained for the hybrids produced with varying levels of destabilising agent added. When compared to standard conditions, shown in Figure 4.10 (a and b), the morphology of hybrids produced in the presence of ethanol is altered. The addition of 1 ml of ethanol did not drastically impact the visual appearance. The regularity of the coating is slightly disrupted however, with the presence of bundles being noted on the side of the nanotubes. The hybrids produced in the presence of 2 ml of ethanol are significantly different. As we can see, there is increased aggregation of the nanoparticles in between the nanotubes and the coating around the nanotubes appears much thicker, owing to

the greater FeO_xNP loading recorded for these samples. In each case, no phase separation is detected as with sample prepared under standard conditions.

4.3.2.4 Effect of Polymer Additive on Functionalisation

It was envisaged that non-covalent interactions between the nanotube and nanoparticle would be enhanced through the addition of a polymer layer. Functional groups contained within the polymer backbone can facilitate additional interactions with nanoparticles, which could increase loading.[290] Therefore, in order to study the influence pre-coating had on the attachment of nanoparticles to the N-CNTs, polymer wrapped N-CNTs were first prepared. For this work, polyvinylpyridine (PVP) was selected as the polymer to wrap the nanotubes in. PVP displays a similar structure to polystyrene (PS), which has commonly been used to coat carbon nanotubes.[49] This can be achieved through covalent pre-treatment of the nanotubes, followed by attachment of the PS.[291] Recent efforts have demonstrated the effectiveness of non-covalent PS attachment which negates the need for a harsh treatment of the nanotubes, however.[292] The non-covalent functionalisation is driven by interactions that are experienced between solvent, nanotube and PS within the system. The main difference between PS and PVP is the presence of a pyridine ring in place of a phenyl group within the polymeric chain. We anticipated that the aromatic pyridine group would mimic the interactions attributed to the phenyl group and allow functionalisation of N-CNTs with PVP. Additionally, as well as the aromatic pyridine ring, the nitrogen atoms contained within the PVP have previously been shown to adsorb metal ions.[290] This could be a desirable property for the production of NP coated N-CNTs, as it could enhance the loading and distribution of NPs by offering additional interactions when compared to an aromatic ring alone. Initially the PVP was purified, as the starting product contained residual solvent from the synthesis that was only

detected when passing through the glass transition temperature; this led to erratic TGA profiles which are shown in the appendix. The purification therefore involved heating the polymer in a vacuum oven to past its glass transition temperature, which released the trapped solvent. After purification, we attempted to attach the PVP to the N-CNTs using a procedure which involved sonicating the nanotubes in a PVP solution. After washing thoroughly, the product was probed *via* TGA analysis. We were able to determine the polymer loading as the PVP is completely degraded under inert atmospheres whilst the nanotube component remains in-tact at the same operating temperatures owing to the thermal resistance.

Table 4.3 compares the breakdown of the hybrid compositions under standard conditions and with the addition of PVP to the starting nanotube. It can be seen from the results displayed in the table that the ligand composition is different for the two samples. The FeO_xNP + N-CNT/PVP hybrid has a significantly larger amount of ligand present within the sample. This increase is not related to the presence of nanoparticles but due to the successful attachment of PVP onto the starting nanotubes, however.

Table 4.3: A comparison of the composition for each of the nano – hybrids produced under standard conditions and with the addition of a polymer coating.

Solvent	Sample Name	Ligand + Polymer Content (average wt.%)	Iron Oxide Content (average wt.%)
Cyclohexane	N-CNT + FeO_xNP Hybrid (SC)	6.6 ± 1.5	42.5 ± 2.3
Cyclohexane	N-CNT/PVP + FeO_xNP Hybrid (PVP)	11.6 ± 1.4	40.9 ± 1.1

In Figure 4.17, the composition is compared in a bar chart format. From this we can see that despite the introduction of an attached polymer to the N-CNT, there is no increase observed

for the iron loading within the sample. We anticipated that the presence of polymer may enhance interactions with the FeO_xNPs and thus increase the attachment of nanoparticles, but this was not the case. Instead, this result further highlights the significance of the solvent media. Attempting to increase interactions between the nanoparticle and nanotube through an intermediary molecule were unsuccessful. Instead, the solvent – nanotube non-covalent interactions are the predominant factors we have observed concerning functionalisation.

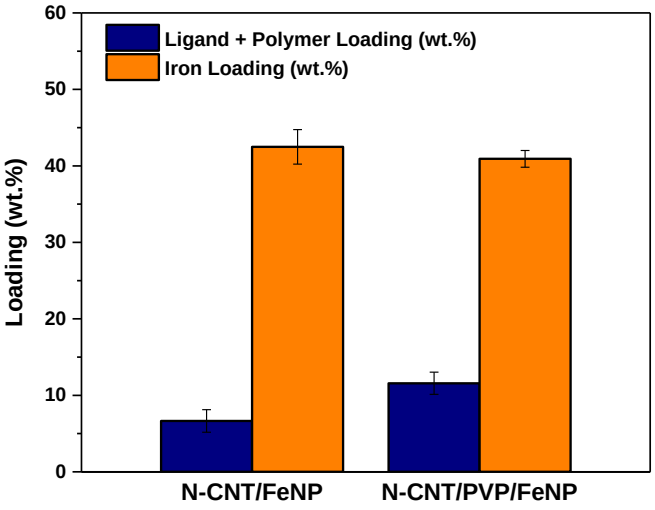


Figure 4.17: A comparison the iron oxide loading present within the nano – hybrids produced under standard conditions and with the addition of a polymer coating.

Figure 4.18 shows the TEM images obtained for the FeO_xNP + N-CNT/PVP hybrid to provide comparison to the nanocomposite obtained under 'standard conditions.' As we can see, when compared to the standard conditions, shown in Figure 4.10 (a and b), there is no significant difference with the addition of the polymer coating to the nanotube. The coverage across the nanotube appears fairly uniform as observed within the polymer free hybrid materials, produced under the same conditions. This suggests that enhancing non-covalent interactions by altering the solvent is sufficient in producing uniform nanoparticle coatings, negating the need for an additional coating step. Additionally, it reaffirms the significance of solvent medium in controlling the nanoparticle coating across the nanotubes. The level of

polymer being low may explain its negligible effect and thus it may be interesting to explore the influence of greater polymer loadings onto the nanotubes and the effect this may have on nanoparticle attachment.

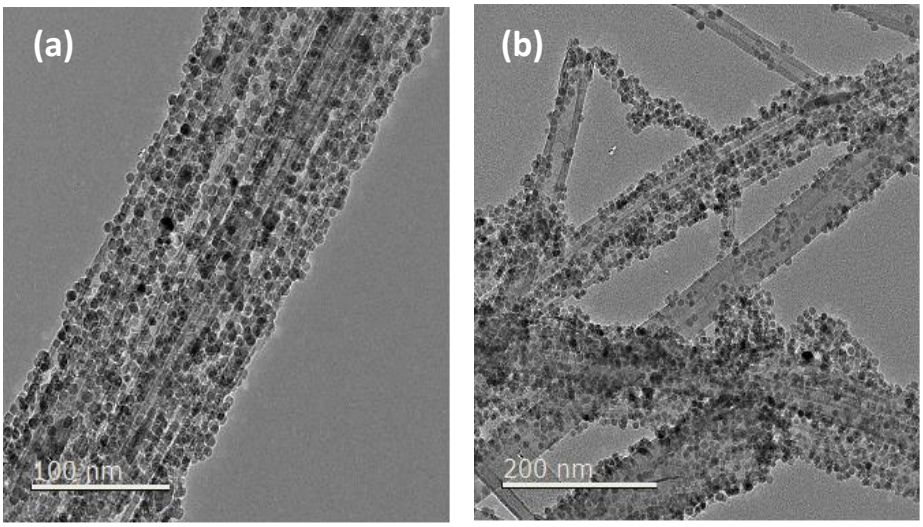


Figure 4.18: TEM micrographs obtained for the (a/b) N-CNT/PVP/FeO_xNP hybrid material.

4.3.3 Synthesis of Iron Oxide NP/BCN-NT Hybrids

Following on from the work established for the N-CNTs in section 4.3.2.2, we wanted to continue this work for BCN-NTs. These nanotubes have displayed promising performance within a number of applications and as a result, are seen ideal candidates for supports in next generation hierarchical nanostructures. Despite this, there have been very few attempts to functionalise BCN-NTs with other nanomaterials. To the best of my knowledge, *ex-situ* methods that looked to vary non-covalent interactions have not been investigated yet and hence the work presented here is the first report of this. The BCN-NTs were produced using the same batch of N-CNTs used for the respective set of functionalisation experiments. As was established in an earlier chapter, the boron incorporation technique does not cause any distinct damage to the nanotube surface or alter the diameter of the nanotubes. For this study,

an analogous experiment set was performed which included sonicating the same quantities of nanotubes and nanoparticles together in various solvents. The only difference being that BCN-NTs were used, as opposed to N-CNTs. After synthesising and cleaning the FeO_xNP – BCN-NT hybrids, they were once more characterised using TGA and TEM analysis.

In Table 4.4 we see a summary of the FeO_xNP – BCN-NT hybrids' composition, whilst Figure 4.19 provides a comparison of the iron nanoparticle loading variation attributed to the different solvents used here.

Table 4.4: A breakdown of compositions for the BCN-NT/FeO_xNP hybrids produced in various solvents.

Solvent	Sample Name	Oleylamine Content (average wt.%)	Iron Oxide Content (average wt.%)
Cyclohexane	BCN-NT + FeO_xNP Hybrid (C-Hex)	6.8 ± 0.9	40.9 ± 1.3
Tetrahydrofuran	BCN-NT + FeO_xNP Hybrid (THF)	7.4 ± 0.6	20.4 ± 1.2
Toluene	BCN-NT +FeO_xNP Hybrid (Tol)	6.8 ± 1.2	33.5 ± 2.0

It is observed that the ligand content is fairly consistent for each of the samples, regardless of the solvent used. This suggests that like the N-CNTs, the functionalisation of BCN-NTs with the FeO_xNPs is not dependent on the ligand coating the nanoparticles. What is striking about the data presented in Figure 4.19, is that once more, the iron loadings of the BCN-NT hybrids are impacted by the solvent selection and are similar to that of the N-CNT hybrids. Again, this reasserts the significance of solvent selection on the functionalisation procedure for doped CNTs. The results presented here for each hybrid are similar to that of the N-CNT analogues; THF gave the lowest level of nanoparticle attachment loading whilst toluene showed an increase and finally, cyclohexane displayed the highest nanoparticle attachment overall. This is the same trend that was observed for the N-CNTs. Interestingly, for the FeO_xNP – BCN-NT hybrids, whilst the composition is broadly the same, the iron loadings are

slightly lower than the N-CNT hybrids in general. It had previously been suggested that the presence of dual boron and nitrogen dopants may improve interactions with metal heteroatoms.[293] Despite this we did not see an increase in the nanoparticle loading.

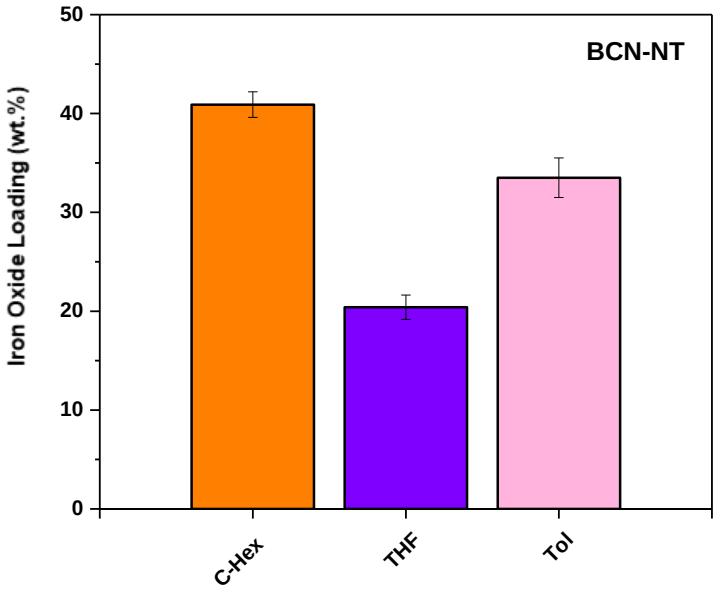


Figure 4.19: A comparison the iron loading present within each of the BCN-NT/FeO_xNP hybrids produced in various solvents.

As was mentioned in Chapter 3, the boron doping procedure used here reduced the defect density measured on the nanotubes. This defect reduction may offer an explanation for the slight reduction in nanoparticle loading because, as has been indicated elsewhere, these defects have the potential to act as preferential bonding sites for metal nanoparticles.[294, 295]

TEM micrographs for the hybrids prepared in each of THF, toluene and cyclohexane are shown in Figure 4.20. In each case, we can clearly observe the attachment of nanoparticles to the exterior walls of the BCN-NTs. To the best of our knowledge, this is the first account of *ex-situ* anchoring of transition metal nanoparticles onto the surface of BCN-NTs. The recorded micrographs reveal that the compositions of the hybrids are generally the same for the BCN-NTs as the N-CNTs. In each case there are no significant aggregates detected. As we change the solvent, and thus the iron nanoparticle loading, the homogeneity of the

nanoparticle coating alters correspondingly. The samples prepared in cyclohexane, which have the highest overall loading, have the most uniform coating, with the samples prepared in THF having a more sporadic coating due to the lowest loadings overall.

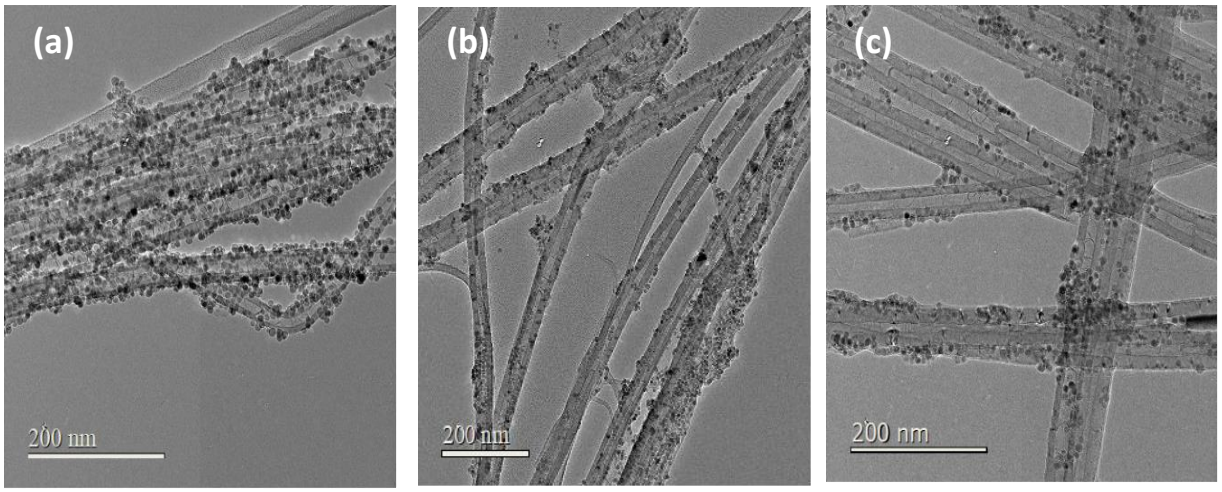


Figure 4.20: TEM micrographs obtained for the BCN-NT/FeO_xNP hybrid materials produced under standard conditions in (a) cyclohexane, (b) toluene and (c) tetrahydrofuran. The images highlight how the coverage across the nanotube alters with solvent selection.

The iron nanoparticle loadings for each of the hybrids were plotted against the dielectric constants of the respective solvents, as can be seen in Figure 4.21 (a). Additionally, using the SESP based approach to rationalising the obtained results, Figure 4.21 (c) shows a plot of iron loading against the Hansen distance between various solvents and the nanotubes. In each case, the BCN-NTs follow the same trends that were exhibited by the N-CNTs. This is highlighted in Figure 4.22 where both sets of data are plotted together. As the dielectric constant increases, the level of nanoparticle attachment decreases. Once again, this is likely because the solvent has the ability to induce negative surface charges on the nanoparticles which increases repulsive interactions between the nanoparticle and nanotube.

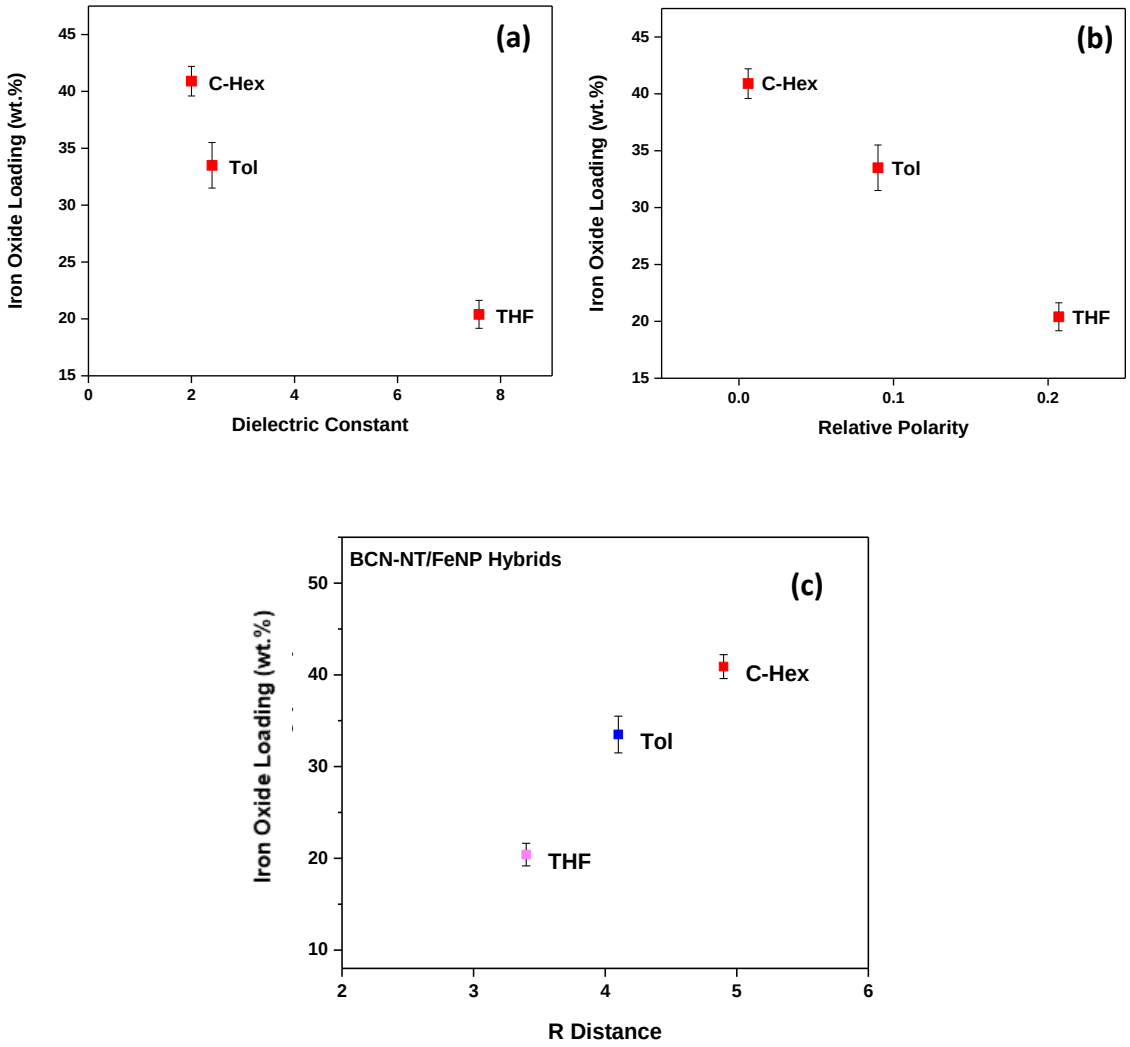


Figure 4.21: Plots of iron oxide nanoparticle loading for each of the BCN-NT/FeO_xNP hybrids produced in cylohexane, toluene and tetrahydrofuran, against the (a) dielectric constant and (b) relative polarity for each solvent and the calculated SESP distance, R.

The results also show good agreement with the predictions made through the SESP approach. As the solvent-nanotube SESP distance increases, the level of nanoparticle loading increases also. As has been noted for N-CNTs, this inverse relationship is driven by the model of functionalisation suggested by O'Connell *et al*.[288] that proposes in an effort to minimise unfavourable interactions with a solvent, a nanotube will coat itself in an active material to reduce these interactions.

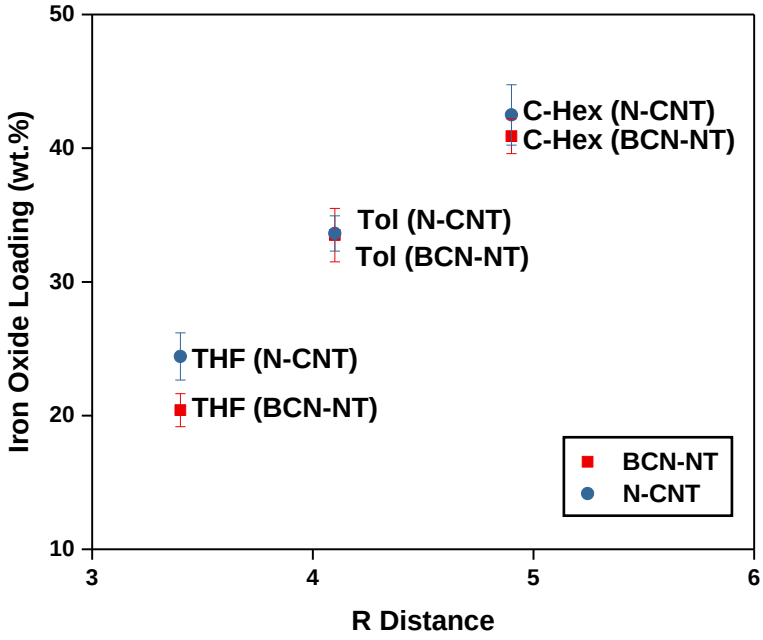


Figure 4.22: A plot of iron oxide nanoparticle loading obtained for the BCN-NT/FeO_xNP and N-CNT/FeO_xNP hybrids produced in cylohexane, toluene and tetrahydrofuran, against the calculated SESP distance, R for each of the solvents. This emphasises the similarities between the functionalisation mechanism and the subtle differences between the use of BCN-NTs and N-CNTs.

The work presented here reaffirms the importance of both these models in predicting the level of functionalisation which will allow the rational production of nanoparticle – doped nanotube hybrids. Additionally, it highlights how the co-doping procedure used in this work does not cause any deviations from these predictions as both the BCN-NTs and N-CNTs follow the same trends. Finally, it stresses the significance of non-covalent interactions in dictating the attachment of nanoparticles to BCN-NTs; this will allow further progression in the construction of desired hierarchical structures in future.

4.4. Conclusions

In this chapter, we aimed to further the processing of BCN-NTs by creating hybrid materials through the attachment of nanoparticles. We have explored the use of *ex situ* functionalisation

techniques for the synthesis of nanoparticle-nanotube hybrids using N-CNTs and BCN-NTs. More specifically we have investigated the role that non-covalent interactions have on the production of these doped nanotube hybrids by varying the solvent medium. Further to this, we have attempted to rationalise our observations within the context of the literature surrounding undoped CNTs.

For N-CNTs, we have found that the solvent selection has a significant impact on the level of iron loading that can be achieved during the functionalisation experiments, with cyclohexane offering the highest loadings and THF the lowest. The observations presented here were consistent with models presented by Rance and Quijano-Velasco *et al*.[115, 265] that attempt to explain nanotube functionalisation in terms of dielectric effects and through a SESP approach, respectively. These dielectric and SESP models provide a good insight into the non-covalent interactions experienced between solvent medium and nanomaterials. Whilst these models distil the complex interactions experience between solvent and nanomaterial, they provide good rationale for the level of nanoparticle loading achieved here according to non-covalent interactions. Quijano-Velasco *et al*.[115]'s work did not follow the trend detailed by Rance *et al*.[265] and we suggest that the use of doped nanotubes, which possess different surface chemistry, may offer an explanation for why the dielectric effect was more pronounced here. The impact of non-covalent interactions were again observed during the production of BCN-NT hybrids. Further to the work on solvent, we also detailed how the stability of the nanoparticle solution could alter the level of functionalisation achieved on the surface of the N-CNTs. By destabilising the nanoparticles, we were able to increase the FeO_xNP loading by *ca*. 20 wt.% when compared to standard conditions.

To the best of our knowledge, the work detailed in this chapter is one of the first attempts to successfully produce BCN-NT/FeO_xNP hybrids of variable composition, in particular through the use of *ex-situ*, methodologies. Above all, it is the first to demonstrate the

influence solvent media has on the resulting composition of these nanotube-nanoparticle hybrids when doped nanotubes are used as the support material. This work can act as a blueprint for the production of various hierarchical BCN-NT composites in the future which will open-up a plethora of avenues for application testing.

Chapter 5

Macroscopic Assemblies of $B_XC_YN_Z$ Nanotubes

5.1. Introduction

Up to now, the experimental work presented in this thesis has focused on the production of nanotubes and converting them into hierarchical – nanostructures. In Chapter 3, we proposed a two-step synthesis technique for BCN-NTs and in Chapter 4 we explored the suitability of, *ex-situ,* non-covalent methodologies for the production of BCN-NT – nanoparticle hybrids. This work was very much concentrated on the nanoscale. In this chapter however, our attention turns towards the macroscale. For carbon nanomaterials to be implemented within a wide range of technologies, their ease of handling needs to be addressed. Typically they are produced and encountered in powder form, and as a result, macroscopic assemblies have been sought-after to combat processing issues. There are a variety of assemblies that have been explored in the literature thus far, such as interconnected nanotube foams and fibres.[296, 297] One of the most prominent areas of research, however, is the production of macroscopic CNT films. These film assemblies possess a number of desirable properties such as porous microstructures, low densities, flexibility and electrical conductivity, amongst others.[298] This has made them a material of interest for a number of applications including, electrocatalysis, energy storage, flexible electronics and thermal management.[60, 234, 299, 300] Throughout this chapter, we explore two techniques for the production of BCN-NT films and thus, the chapter is separated into two sub-sections. The strategies investigated include electrophoretic and vacuum assisted techniques.

Prior to detailing the results, I will first provide a background introduction for both of the strategies, used here. Within the literature there are very few, if any, examples detailed for BCN-NT film production. Given this, here we will focus on the methodologies that exist for the production of CNT films using electrophoretic deposition and vacuum filtration. As there are a host of methodologies for producing CNT films, the reader's attention can be drawn

elsewhere to reviews that detail dry-techniques such as spinning that will not be covered in this section .[298, 301]

5.1.1 Electrophoretic Deposition for CNT Films

As-synthesised, undoped, carbon nanotubes are notoriously difficult to disperse in a variety of common laboratory solvents. Pristine CNTs are typically unreactive due to the surface chemistry they possess. The bonding present within these pristine CNTs consists mainly of a strong sp^2 hybridised carbon network and as a result, the nanotubes lack the required surface functional groups to interact with solvents.[70] Additionally, during the synthesis, CNTs are prone bundling, which is driven by the high aspect ratios and attractive Van der Waal forces experienced between individual nanotubes.[71] The high surface areas associated with the nanotubes and intermolecular forces promote the attraction of these bundles in solution, which leads to aggregation.[72] This renders many CNT dispersions as quasi-stable solutions due to their tendency to agglomerate.

Given this, carbon nanotubes usually require a chemical pre-treatment to enhance their dispersion for further processing. Typically these treatments are either non-covalent or covalent. The former involves wrapping the nanotubes in an organic molecule or polymer to provide surface functionality.[302] In order to attach, the polymer or molecule itself must possess an active moiety that can interact with the surface of the nanotubes (*i.e.* through pi-pi interactions). The adsorbed species can then facilitate interactions with solvents to enhance dispersion. The latter, covalent strategy, involves treating the nanotubes chemically in order to deteriorate the nanotube structure and establish functional groups on their surface, that aid dispersion in solvent.[73]

Where EPD is concerned, covalent treatments are overwhelmingly preferred within the literature. This is because for deposition to occur, the depositing particle requires sufficient surface charge that can be attracted to an electrode when a potential is applied across the set-up. Therefore, the simplest means of achieving this with CNTs is through disrupting the sp^2 network and introducing surface functionality (such as -OH and =O groups) that can provide adequate negative charge for electrophoretic motion.[303] A schematic of the EPD procedure is shown in Figure 5.1.

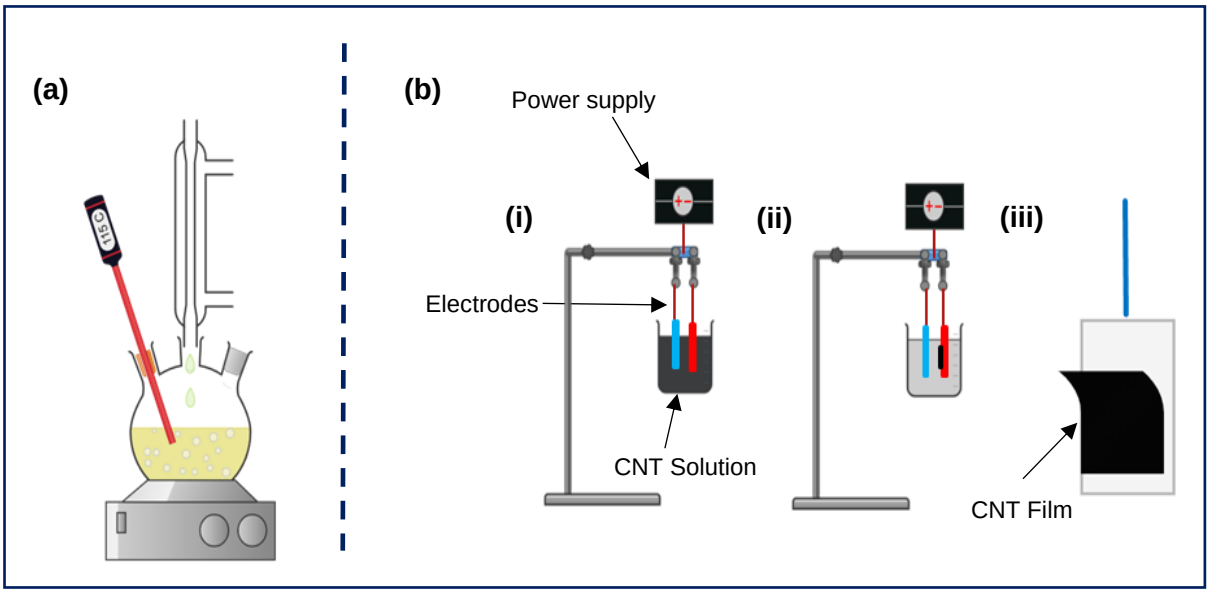


Figure 5.1: A schematic diagram of the EPD procedure for CNTs. CNTs are chemically functionalised (a) before depositing (b). For the deposition, electrodes are submerged in a CNT dispersion before the application of voltage which promotes deposition of the CNTs at the electrode(ii), at which point the film is allowed to dry (iii).

One of the earliest examples of this being used for the electrophoretic deposition of CNTs came from Choi *et al.*[304] who detailed the production of patterned thin-film coatings from SWCNTs. By employing a harsh acid treatment, involving a mixture of sulphuric and nitric acid, they were able to introduce charge onto the nanotubes that allowed deposition when a potential was applied across the system. This process was aided by the addition of magnesium salts to provide sufficient surface charge for deposition. This suggests that the

initial procedure did not prove adequate surface charge to undergo electrophoresis without the supplement of additives. The films produced in this study were also patterned thin-film coatings as opposed to a free-standing CNT film. In many cases acid etching is seemingly necessary for the introduction of charge onto the nanotube surface but can also be detrimental to desirable surface properties. These harsh acid treatments may be unsuitable for doped-nanotubes, however, due to the previously demonstrated capability of acid treatments in attacking and removing dopant-sites.[238, 239] Following on from this work, Gao *et al.*[305] showed how the EPD process could be used to vary the thin-film thickness. The functionalisation procedure was similar to the one used by Choi *et al.*[304] and was reported to cut the length of nanotubes, however. Through varying the deposition time and the applied voltage, the thickness of the deposited films could be varied. Whilst still not free-standing, this technique showed that the film dimensions could be controlled. Additionally, the authors detailed how the density of the films could be improved by annealing under vacuum. This could be an interesting technique for improving the properties of CNT films in the future by increasing the inter-CNT contact within the films.

In addition to SWCNTs, research into the electrophoretic deposition of MWCNTs soon followed. Using the same nitric/sulphuric mixture noted earlier, Thomas *et al.*[306] were able to fabricate thin film coatings with MWCNTs. They reported that by changing dispersion concentrations and deposition times, films of variable thickness could be produced. Like with the work established for SWCNTs, the thickness of thin film MWCNT coatings can be varied by altering deposition times.[307] Cho *et al*.[308] also furthered our understanding of the nanotube deposition process using MWCNTs. Thin-film coatings on stainless steel were produced by depositing acid-treated nanotubes. They probed the deposition process further by comparing experimental results to a mathematical model, for which they found good agreement. The model was based on Hamaker's law, which describes the relationship between rate of

deposition and field strength, providing an explanation for the kinetics of MWCNT deposition. In each of these examples, the CNT films did not delaminate from the substrate which would limit application to the field of thin-film coatings.

The aforementioned examples of CNT-EPD, reviewed here, have all yielded thin coatings of CNTs onto a host medium such as stainless-steel. As a result of the strong adhesion between the deposit and the depositing electrode, the coatings remain bound to the substrate after drying. Whilst the deposition of coatings is useful, for many applications a free-standing CNT film of controllable thickness is desirable. There have been efforts by researchers to liberate the CNT films from the depositing electrodes. For example, mechanical cleavage has been used to remove deposited MWCNT films from substrates.[309] After depositing dispersed CNTs from a commercially produced solution, the deposited film was submerged in water to aid removal and was mechanically cleaved using a razor blade. The MWCNT film's thickness was controlled by successive depositions, *i.e.* deposition followed by drying followed by deposition once more, before cleaving.

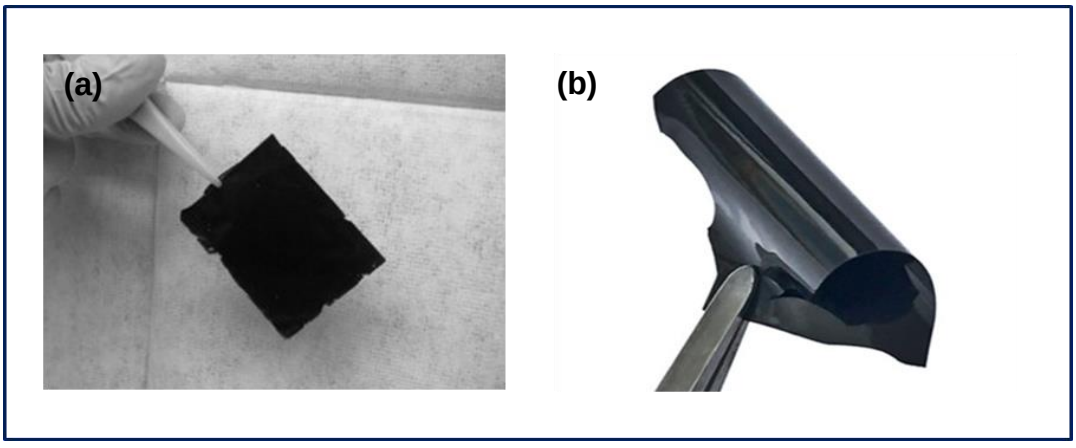


Figure 5.2: Optical images, adapted from the literature, showing freestanding CNT films produced via electrophoretic deposition. (a) MWCNT film produced through the mechanical cleavage of a deposit, from reference 309 with permission from Elsevier. (b) MWCNT film produced from spontaneous delamination, reprinted with permission from reference 312. ©2019, American Chemical Society.

The resulting film can be seen in Figure 5.2. This work demonstrated a unique procedure for the liberation of MWCNT films after EPD which could be useful in cases where adhesion is

strong between the deposition electrode and CNTs. It would have been interesting to explore if similar results could be achieved through starting with a higher initial concentration rather than the repetitive deposition procedure which is time consuming. Biswas *et al.*[310], who employed an almost identical EPD process as the previous example, used two techniques to liberate the MWCNT films. The first procedure once again utilised mechanical detachment, but the second involved electrochemical cleavage of the CNT film. By re-submerging the coated substrate in the parallel electrode set-up and reversing the bias, at a higher electric field strength, the CNT film was released from the surface of the electrode, yielding a freestanding CNT buckypaper. Further research could be conducted to determine the effectiveness of this technique for some of the aforementioned thin film coatings. The minimum thickness of deposit required to produce a free-standing CNT film may be determined by exploring the technique further. Whilst these detaching techniques are useful for the production of freestanding films, the addition of an extra processing step is undesirable when compared to potential auto-delamination. Work conducted within our research group, by Ballentine *et al.*,[311] have looked to address this and successfully produced freestanding SWCNT films using EPD. The SWCNTs were chemically reduced using sodium naphthalide which afforded charged and well dispersed nanotubes. Solutions of these reduced SWCNTs were then deposited on a variety of substrates. Depending on the thickness of the deposit, the films varied from thin-coatings to freestanding and required no removal-step. This reductive technique also affords no structural damage to the nanotube which would be ideal for doped-nanotubes. That being said, initial work conducted by the authors for MWCNTs was unsuccessful with this technique which, to this point, makes it unsuitable for the materials used within this thesis. Additionally, this procedure had to be conducted in a glovebox environment, whereas the other reviewed examples are all conducted in a regular atmosphere. This inert atmosphere requirement could be viewed as a handling issue. Other

work conducted within our group by Xiao *et al*.[312] reported the first example of spontaneously freestanding MWCNT films *via* EPD, which they named ‘buckyfilms’. An example of these films can be seen in Figure 5.2. Commercially bought MWCNTs were refluxed in nitric acid to aid dispersion in water. The diluted stock solution was deposited onto FTO electrodes, after applying a voltage of 30 V, which led to a thick film forming. Upon drying, the films thickness reduced, and the authors note that the deposit began to peel away from the electrode leaving a freestanding film. This technique offers promise with regard to the production of freestanding CNT films, as it utilises EPD which is scalable and doesn’t require any additional liberation steps. This work also utilised, intrinsically defective, commercially produced MWCNTs; as such, it would be interesting to see how this method translate to MWCNTs of a better starting crystallinity. Once again, the long oxidation times required in concentrated acids could be detrimental to dopant sites within the nanotube and to the nanotube structure. That being said, this work will act as foundation for the work detailed in this chapter that utilises EPD produced films.

5.1.2 Vacuum Filtration for CNT Films

Like with EPD, due to the aforementioned properties of CNTs, vacuum filtration experiences similar difficulties with material dispersion. Vacuum filtration is one of the earliest and most commonly employed techniques for the production of free-standing CNT films. This procedure typically involves filtering a solution of dispersed CNTs through a fine membrane, under vacuum, which ultimately results in the formation of an entangled CNT film, commonly known as a ‘buckypaper’.[313] This procedure is shown schematically in Figure 5.3. Several variations to this procedure can be made. How the dispersion is generated, through mechanical or chemical means, is one of the most commonly tuned variables. These

alterations ultimately have impacts on the films properties. Additionally, the incorporation of other materials within these dispersions has allowed the production of composites in the form of freestanding films.[314] In this section, we will detail examples of CNT film production *via* vacuum filtration and discuss how variations to the standard procedure have been developed.

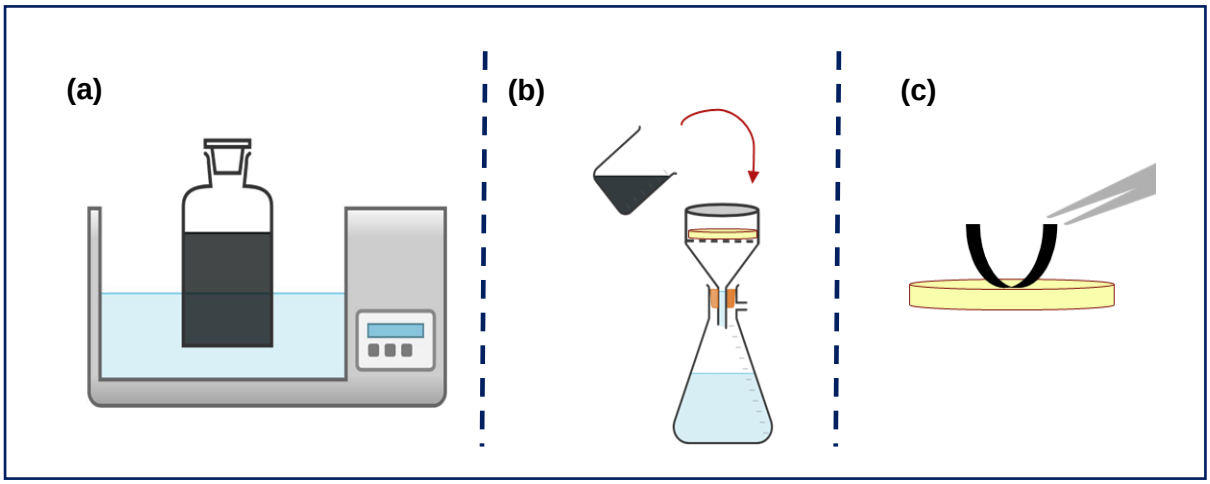


Figure 5.3: A schematic representation of the production of CNT films via vacuum filtration. Initially CNTs are dispersed, in this case through sonication (a) which is followed by filtration through a membrane with the assistance of vacuum (b) before the film is dried and peeled away from the membrane (c)

The earliest mention of buckypapers comes from Liu *et al*.[315, 316] who were the first to detail a method for their production, which arose from purifying SWCNTs. The SWCNTs were first oxidised for two days *via* a nitric acid reflux treatment. The etched nanotubes were then dispersed, with the assistance of a common surfactant, before subjecting to vacuum filtration through a filter. After filtering, a freestanding buckypaper could then be peeled away from the filter membrane. Their investigation revealed that these films were made up of interconnected SWCNTs with a porous topography. The produced buckypapers enabled the CNTs to be readily handled on a macroscopic scale and were suitable for testing. Whilst this work demonstrated an effective technique for the integration of CNTs into macroscopic assemblies, there are downsides to the processing techniques employed here. The lengthy acid reflux times used here destroyed the raw material and reduced CNT yields by *ca.* 80%

making the upscaling of this procedure unfeasible. Additionally, it has been shown that oxidative procedures can detrimentally affect the unique properties of CNTs which is undesirable for specific applications. Cooper *et al.*[317] used an extensive oxidation procedure which involved refluxing SWCNTs in nitric acid for *ca*. 144 hours followed by a 24-hour sonication period in a mixture of sulphuric and nitric acid. The final dispersion yielded was passed through a cellulose nitrate filter and dried to produce a buckypaper. Despite this procedure yielding freestanding films, analysis revealed that the morphology was non-uniform and had several aggregate sites, as opposed to a smooth uniform film. Even with the excessive acid treatments, the authors attribute the lack of uniformity to the presence of amorphous carbon and other impurities, that should have been removed during the purification. This suggests that the acid-treatments employed here were not vigorous enough, regardless of the extensive time required. Additionally, sonication time of 24 hours can cause significant shortening of CNTs which can inhibit CNT entanglement. These sonication parameters may offer an alternative explanation for the film quality and highlight a drawback to excessive sonication times. Where buckypaper properties were concerned, Galiotis *et al.*[318] investigated the effect of various acids and oxidising agents. They found that increasing the level of functionalisation on the MWCNTs affected the dispersions, and ultimately the properties of the films. Mild oxidation procedures were found to display better properties, such as electrical conductivity, overall. This highlights that where possible, harsh oxidation procedures should be avoided. The correlation between film properties and the quality of initial dispersion has been supported elsewhere.[319] An example of a SWCNT 'buckypaper' prepared through oxidative treatment and subsequent vacuum filtration is shown in Figure 5.4.[320] As can be seen, a freestanding film can be peeled away from the filter paper. It is interesting to note, however, the shrivelling observed around the film edge.

As the field progressed, the necessity for an oxidative pre-step diminished. For example, Wang *et al*.[321] produced dispersions using a procedure that required no oxidation of the nanotubes. A slurry was prepared by grinding and sonicating SWCNTs with a small amount of water which was then diluted and sonicated after the addition of surfactant. Following vacuum filtration, the CNT film that had formed was washed with water to remove residual surfactant with the resulting freestanding film being highlighted in Figure 5.4.

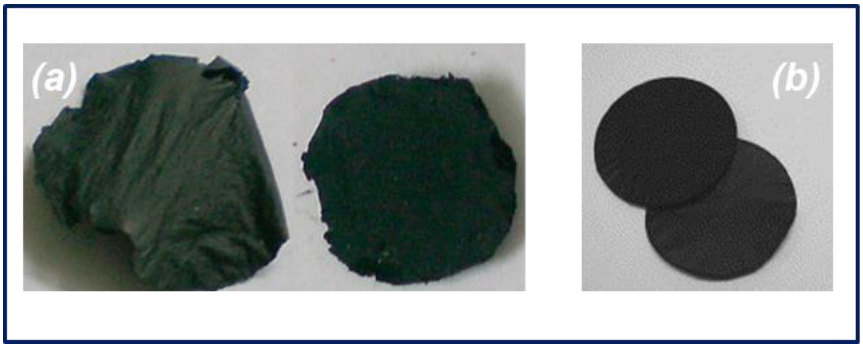


Figure 5.4: Optical images, adapted from the literature, showing freestanding CNT films produced via vacuum filtration. (a) SWCNT films produced with acid-treated carbon nanotubes, reprinted with permission from reference 320. ©2012, American Chemical Society. (b) SWCNT film produced through, non-covalent, surfactant assisted dispersion, from reference 321 with permission from Elsevier.

A similar procedure to this was translated to the production of MWCNT buckypapers.[322] These works highlight how a simple sonication strategy can be used to provide a dispersion of CNTs suitable for macroscopic assembly. They do fail to detail how effective this washing procedure was in removing surfactant from the buckypapers which could pose an issue for certain applications. Where possible, it would be advantageous to avoid the use of surfactants to disperse the nanotubes. Work conducted within our research group developed this strategy further for the production of N-CNT buckypapers.[323] By employing a prolonged sonication time of 15-hours, no surfactant was required to disperse the nanotubes. Whilst this procedure yielded freestanding buckypapers of N-CNTs, extensive sonication procedures have previously been shown to affect nanotube structure, and ultimately, this may impact film

properties.[324-326] The latter technique, however, will act as foundation for the production of BCN-NT films that will be explored later on in this chapter.

5.2. Materials and Methods

5.2.1. Chemicals

For the synthesis of nanotubes, benzylamine (ReagentPlus, 99 %) solution and boric acid (≥ 99.5 %) powder along with ethanol (puriss, ≥ 99.8 %) were purchased from Sigma-Aldrich and used without further treatment. Ferrocene (99 %) purchased from Sigma-Aldrich was purified *via* sublimation.

Nitric acid (concentrated, 70 %), borane ammonia complex (97 %), methanol (puriss, ≥ 99.8 %), iso-propanol (puriss, ≥ 99.8 %) and fluorine doped tin-oxide coated glass were all purchased from Sigma-Aldrich and were used without any further treatment. The deionised water used was type 2 (0.45 μS/cm).

5.2.2. Characterisation

Scanning electron microscopy (SEM) micrographs were obtained on a JEOL-840F with a 4 kV accelerating voltage; samples were loaded onto a carbon tab mounted on an aluminium stub. TEM images were obtained on a JEOL-3000F microscope operating at an accelerating voltage of 200 kV. Samples were prepared by dispersing materials in solvent and drop-casting onto lacey carbon copper grids (400 mesh). The LabRam Aramis Raman confocal microscope (λ = 532 nm) was used to record spectra. Samples were prepared by drop casting the same solution onto glass microscope slides and allowing the solvent to evaporate. In the

case of buckypapers, the as produced film was analysed. UV-Vis absorption spectra were recorded with a Cary 5000 UV-Vis spectrophotometer by placing this solution in a transparent quartz cuvette (10 mm x 10 mm). X-ray photon electron spectroscopy was performed on each of the powdered products using a K-Alpha X-ray photoelectron spectrometer with a monochromated Al K irradiation source. Each of the spectra were deconvoluted using the CasaXPS software. Thermogravimetric analysis was performed on a Perkin Elmer Pyris 1 TGA machine. Typically, the materials were heated to a temperature of 100 ^{o}C and holding for 10 minutes before increasing to 900 ^{o}C and holding for a further 20 minutes. This was performed under flowing air (0.02 SLM). Brunauer–Emmett–Teller and Barrett-Joyner-Halenda analysis were conducted on a Micromeritics Gemini VII surface area analyser for the macroscopic assemblies. N_2 gas was used as the adsorbate and liquid N_2 to cool the sample. The films were degassed at 160 ˚C until a constant weight was achieved prior to analysis being conducted. Isotherms were recorded by the Oxford Materials Characterisation Service. Sheet resistances were recorded using an Osilla four – point probe that was fitted with four non-destructive soft contact probes.

5.2.3. Synthesis of Nanotubes

The same synthesis procedures, as detailed in sections 3.2.3, 3.2.4 and 3.2.5. were employed here for the synthesis of the N-CNT, CNTs and BCN-NTs, respectively. Briefly, AACVD was used to grow CNTs from various carbon feedstocks which utilised ferrocene as the catalyst precursor. The as-synthesised N-CNTs were subject to an additional co-doping procedure to yield the BCN-NTs.

5.2.4. Oxidation of CNTs

A three-neck round bottomed flask (250 cm^3) was equipped with a stirring bar, glass-coated thermocouple and a water-cooled condensing unit. To the flask, CNTs (1000 mg) and nitric acid (100 ml) were added before refluxing at 118 ^oC for up to 24 hours. The oxidised CNTs (Ox-CNT) were separated from the acid *via* centrifugation (4600 rpm). Distilled water was then added to the Ox-CNTs and was vigorously shook before centrifuging (4000 rpm) again and discarding the supernatant. In order to remove amorphous carbon, trace metal impurities and residual acid, this cleaning procedure of washing separation was repeated until a pH of ≥ 7 was obtained. The Ox-CNTs were then collected in DI water as a stock solution with a concentration of *ca*. 4 mg/ml. The oxidation and deposition procedure were adapted from previous work conducted within our research group.[312]

5.2.5. Electrophoretic Deposition of Oxidised CNTs

The Ox-CNT solution was diluted with methanol (using a dilution factor of 10) prior to the EPD process. Before use, the fluorine-doped tin oxide (FTO) coated glass (2 cm x 2 cm) and silicon (2.5 cm x 2.5 cm) electrodes were washed in a soap solution followed by subsequent rinses in DI water, ethanol and iso-propanol before drying in a box oven at 80 ^oC overnight. The electrodes were arranged parallel to each other, with a spacing of 2 cm, and submerged into a beaker containing the diluted Ox-CNT solution. A Genvolt 73030 power source was used to supply a voltage of *ca.* 35 V. After the reaction was complete, a gelatinous deposit remained adhered to the FTO electrode. This electrode was transferred to a PTFE stage where it was left to dry, deposit side down. After drying, the deposit had transferred and could be peeled away from the PTFE surface revealing a free-standing CNT film.

5.2.6. CVD Functionalisation of Oxidised CNT Films

To convert the electrophoretically deposited CNT films to BCN films, a CVD procedure was utilised. This was adapted from procedures previously utilised within the group.[312, 327] The CNT films produced in 5.2.5 were mounted on top of a quartz slide which itself was placed inside a quartz tube. The sealed quartz tube was attached to a separate precursor vessel and a vacuum line. The reaction vessel tube was surrounded by a tube-furnace that was mounted to wheels. A mixture of ammonia borane and BN powder (1:10) was held within the precursor chamber, which was wrapped in a heating jacket and held at 60 ^{o}C. Prior to the reaction, the whole system was purged with Ar/H2 (0.40 SLM) for 10 minutes before then evacuating under vacuum for a duration of 15 minutes. The vacuum tap was then closed, before the Ar/H2 mix (0.40 SLM) was reintroduced for an additional 10 minutes. After purging, the furnace was heated to 1100 ^{o}C and moved into position, where the centre of the furnace was directly positioned over the CNT film, once the set-temperature was reached. At this point, precursor vessel's temperature was increased to 85 ^{o}C which enabled ammonia borane vapours to be introduced into the reaction chamber. The reaction was held for 2 hours and quenched by removing the precursor vessels heating jacket and by moving the furnace away from the film before allowing it to cool.

5.2.7. Dispersion of BCN-NTs in Common Laboratory Solvents

In order to determine the best common lab-solvent to utilise for the production of buckypapers from BCN-NTs, a variety of solvents which included water, ethanol and iso-propanol (IPA) were screened for their dispersion. BCN-NTs (4 mg) were placed in a centrifuge tube along with solvent (40 ml) before being suspended in an ultrasonication water bath and subjecting to sonication (5 hours). After sonication, the dispersions were centrifuged

at three various speeds. Initially, the solutions were rotated at 1500 rpm for 10 minutes and 3 ml aliquots of the supernatant were collected. This procedure was then repeated at centrifugation speeds of 2500 and 3500 rpm.

5.2.8. Production of Nanotube Dispersions & Buckypaper

Nanotubes (30 mg) were ground in an agate pestle and mortar with a small amount of solvent (IPA) until a thick paste was formed. This paste was transferred to a reagent bottle and diluted with more solvent (300 ml) before vigorously stirring for 2 hours prior to sonication. The mixture was then sonicated at 25 ^{o}C for 4 hours. For the buckypaper fabrication, 100 ml of the nanotube dispersion was slowly filtered through a polycarbonate membrane (25 mm, 0.4μm pore) using vacuum filtration, liquid N_2 assisted by a cold-trap. The buckypaper was held under vacuum for 1 hour after fabrication. The buckypapers were then dried in a vacuum oven at 70 ^{o}C overnight. These procedures were adapted and modified from methods previously developed within our research group for undoped and uni-doped CNTs that used more extensive sonication procedures.[323]

5.2.9. Production of $B_xC_YN_Z$-FeO_xNP Hybrid Buckypaper

Here we looked to replicate the experimental conditions used in section 4.2.9, where 2 ml of ethanol was added to the reaction mixture; this involved scaling the procedure by a magnitude of 3 and combining with the strategies used in section 5.2.8. BCN-NTs (12 mg) were ground in an agate pestle and mortar with a small amount of solvent until a thick paste was formed. This paste was transferred to a reagent bottle and diluted with more solvent before vigorously stirring for 2 hours prior to sonication. The mixture was then sonicated at 25 ^{o}C for 4 hours. Before the final hour of sonication, FeO_xNPs in cyclohexane (3 ml) were

added to the vessel. For the buckypaper fabrication, the nanotube/nanoparticle dispersion was slowly filtered through a membrane using vacuum filtration, assisted by a cold-trap. The buckypaper was rinsed with solvent after fabrication to remove any loose nanoparticles and was then held under vacuum for 1 hour. The buckypapers were then dried in a vacuum oven at 70 ^{o}C overnight.

5.3. Results and Discussion

5.3.1. Part I: Electrophoretic Assisted Production of Macroscopic BCN-NT Films

5.3.1.1 Oxidation of CNTs

As has been established, CNTs are notoriously difficult to disperse due to the surface chemistry they possess. Pristine nanotubes lack the required surface functional groups to interact with solvents.[328] During their synthesis, nanotubes are prone to bundling which is driven by the Van der Waal forces between them.[71] High surface areas promote attraction between bundles, resulting in aggregation.[72] As we have mentioned, CNTs therefore typically require a pre-treatment to aid dispersion. Non-covalent procedures involve wrapping the nanotubes in organic molecules or polymers, whilst covalent methodologies involve the chemical introduction of surface functional groups that improve dispersion.[73, 329] For EPD, covalent treatments are often preferred. This is because for electrophoretic motion to occur, a surface charge is required.[303] The most common way to achieve this is through a vigorous acid treatment that introduces oxy-containing groups onto the nanotube surface. Where doped nanotubes are concerned, however, oxidative treatments face limitations. Previous research has shown that these acid treatments can remove the heteroatom dopants from the nanotubes during the oxidation procedure.[238, 330] Additionally, due to the comparatively high number of defects (which act as active sites for oxidation) within doped nanotubes, there is a risk of excessive structural damage.[330, 331] Therefore, undoped CNTs were utilised before then attempting to co-dope at a later stage, after the oxidation procedure was complete.

Undoped CNTs were grown through an AACVD procedure, similar to those detailed for the N-CNTs, that has previously been established within our research group.[184] Here, a feedstock

of toluene and ferrocene (5 wt.%) was utilised for the synthesis.. The as produced CNTs are not dispersible in water, even with the assistance of ultrasonication. To overcome this, a mild oxidation procedure was employed to aid their dispersion. The nanotubes were refluxed in concentrated nitric acid for a reaction time that varied between 18 and 24 hours. After this, the now oxidised nanotubes were collected in DI water at a concentration of *ca*. 4 mg/ml. As can be seen in Figure 5.5, the oxidised nanotubes were dispersed much easier in water when compared to the raw material.

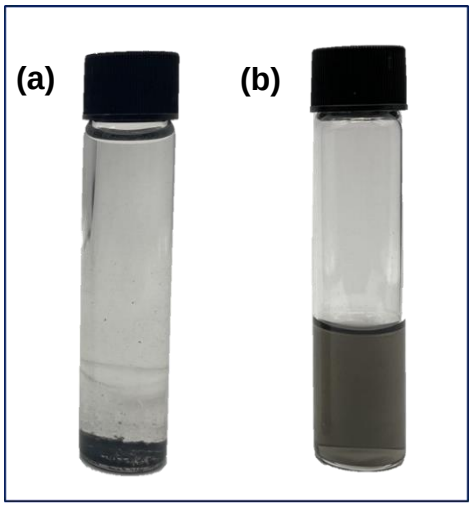


Figure 5.5: Optical images of two vials containing CNTs in water. This highlights how untreated, as-synthesised, CNTs sediment in solvent (a) whilst acid modified CNTs disperse well (b)

XPS spectra were recorded before and after the oxidation procedure in order to quantify the change in oxygen containing species within the nanotubes. Table 5.1 shows a typical elemental composition after the oxidation procedure. As can be seen the oxygen content showed an appreciable increase after the oxidation. This demonstrates that the acid treatment has successfully introduced oxygen-containing species onto the carbon nanotubes. The increased presence of oxygen containing groups provides an explanation for the enhanced dispersion of nanotubes in aqueous solution as demonstrated in Figure 5.5.[332, 333]

Table 5.1: A summary of the carbon and oxygen content of CNTs before and after acid treatment recorded via XPS.

Sample Name	Carbon Content	Oxygen Content
As-Synthesised CNTs	98.6 (at. %)	1.4 (at. %)
Acid Treated CNTs	91.7 (at. %)	8.3 (at. %)

As the Raman spectroscopy offers an insight into the crystalline nature of the CNTs, spectra were recorded for each of the acid-treated CNTs that were oxidised for durations of 18, 20 and 24 hours. In each case, the defect density when compared to the starting material (0.44) has increased as a result of the introduction of oxy-containing species onto the nanotube surface structure. The magnitude of change may be offset by removal of amorphous carbon from the sample during the washing procedure and work-up.

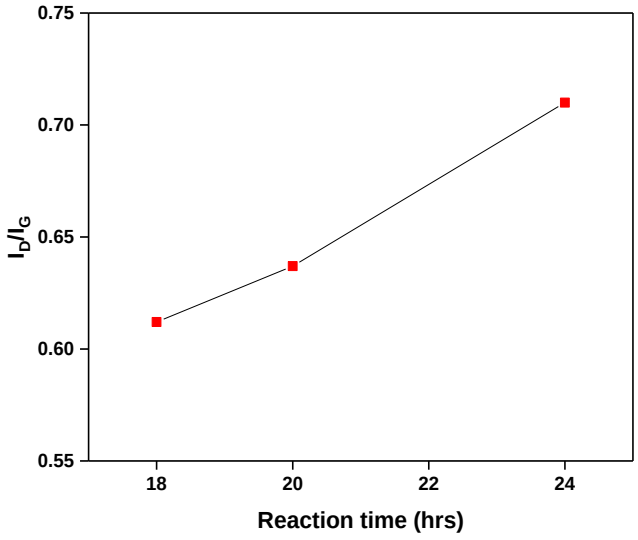


Figure 5.6: A plot of the average defect densities recorded for CNTs treated under increasing acid - reflux durations.

As can be seen in Figure 5.6, as the oxidation reaction time increases, the defect density recorded for the oxidised CNTs grows linearly also. This result is in good agreement with previous findings that have shown that as the oxidation conditions harshen, the number of defects introduced into the nanotube structure increase.[334]

5.3.1.2 Electrophoretic Deposition of CNTs

After successfully oxidising the CNT nanotubes in 5.3.1.1, electrophoretic deposition was performed in an attempt to produce CNT films. The oxidised CNTs were dispersed in a mixture of water and methanol before suspending FTO and silicon electrodes in the solution. Upon applying a potential across the set-up, nanotubes were deposited at the FTO electrode. As the reaction progresses, the black starting solution begins converting to a transparent liquid as the CNTs deposit and begin to agglomerate at the electrode – solvent interface. The extent of this colour change depended on the oxidation time utilised in the preparation of stock solution, with the longer oxidations having a starker change. Upon completion, the electrode was removed from the solution and allowed to dry overnight.

Figure 5.7 shows the macroscopic results obtained for depositions of various oxidation times. As can be seen in the appendix, for a typical film, the wet deposit immediately appears as a gel-like coating on the electrode with a varied thickness which depends on the oxidation time used to produce the stock solution. Subject to the oxidation time utilised, the appearance of the dried product also varied. The electrodes were placed deposit side down on a PTFE platform whilst drying. As we can see in Figure 5.7(a), the nanotubes that were oxidised for a duration of 18 hours deposited on the electrode and when dried formed a thin film. This film was akin to a thin film coating and could not be removed from the surface of the electrode, suggesting the nanotubes were strongly bound to the FTO glass. This suggest that 18 hours is an insufficient reflux time for creating a dispersion suitable for deposition of freestanding films. By increasing the oxidation time to 20-hours, the thickness of the CNT deposit increased appreciably as shown in Figure 5.7(b). Whilst thicker than the 18-hour oxidation times, the dried product for the CNTs that had been oxidised for 20 hours also remained adhered to the electrode. Portions of this could be removed through mechanical cleaving using a scalpel but the centre of the film remained intact with the substrate. The initial deposit

for the CNTs that had been oxidised for 24 hours was significantly thicker than the shorter oxidation times. After drying, the collapsed film had transferred to the PTFE platform from which it then delaminated, leaving a freestanding CNT film. This observation suggests that there is a minimum mass of deposit required for the films to overcome the adhesive forces with the electrode and form a freestanding film spontaneously. It has been suggested that increasing film thickness, and thus the mass of deposit, is related to microstructural changes in a film that reduces adhesion and eases the requirements for delamination to occur.[312, 335]

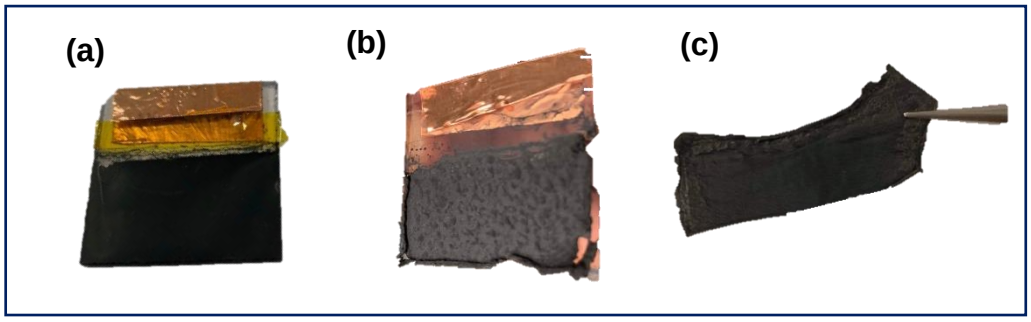


Figure 5.7: (a) thin film coating produced from dispersion of CNTs that had been refluxed in nitric acid for 18 hours, (b) thicker coating produced from dispersion of CNTs that had been refluxed for 20 hours and (c) a freestanding film that was afforded by a dispersion of CNTs that had been refluxed for 24 hours.

Interestingly, work previously conducted within our group achieved free-standing CNT films as opposed to thin film coatings using the shorter oxidation time of 18 hours. An explanation for the formation of these thin film coatings likely lies with the starting material used. Here, we have utilised homegrown AACVD CNTs whilst Xiao *et al.*[312] used commercially sourced Nanocyl. The average diameter for the Nanocyl nanotubes is *ca*. 10 nm, whereas the nanotubes produced *via* AACVD were measured to be *ca*. 65 nm. This disparity in diameter is likely to have an effect on the chemical oxidation procedure. This is because as a particle's diameter decreases, the specific surface area increases. Given this, the enhanced specific area associated with the smaller diameter Nanocyl CNTs enhances the likelihood of successful acid-etching when compared to the thicker AACVD nanotubes. Researchers have

demonstrated that the nanotube diameter affects the functionalisation of CNTs, with smaller diameter tubes undergoing oxidation more readily.[336, 337] In addition to possessing a narrower diameter, the Nanocyl tubes that they used have a lower quality of starting crystallinity when compared to the AACVD nanotubes. The defect density, which is an indicator of nanotube crystallinity, measured for the AACVD nanotubes (0.44) was significantly lower to that of the Nanocyl (*ca*.1).[338] This demonstrates that the graphitic content of the Nanocyl tubes is more disordered than those produced *via* AACVD. It has previously been shown that an intrinsically higher defect density eases the oxidation procedure as existing defect sites are attacked first.[337] As a result of this, it can be expected that oxidation will occur more readily, under the same conditions, for the Nanocyl tubes due to the defects providing a greater number of active sites for the oxidation procedure to occur. Given this, longer oxidation times (*i.e.* 24 hours) are therefore required for the AACVD product to replicate the deposition of nanotubes needed for freestanding CNT films.

Figure 5.8 shows SEM images of the as-produced freestanding CNT films. As can be seen, the film consists of a network of CNTs that have been entangled during the deposition process. The nanotubes have formed a randomly oriented packing arrangement during the deposition process which has afforded the presence of pores within the microstructure of the freestanding films.

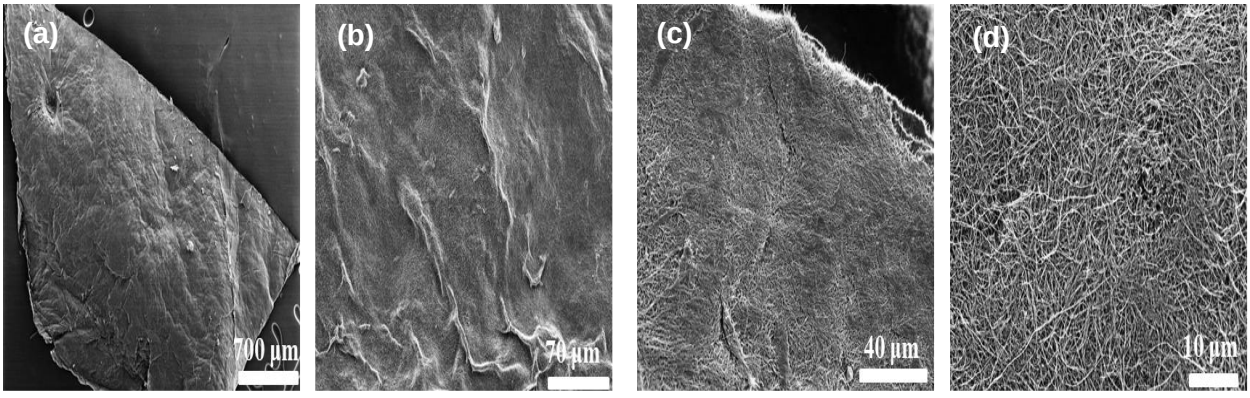


Figure 5.8: SEM micrographs of the CNT films produced via EPD with varying degrees of magnification.

5.3.1.3 Attempted Conversion of CNT to BCN-NT Film *via* CVD

Upon the successful production of freestanding CNT films *via* EPD, we attempted to convert them to BCN-NT films. This involved a CVD procedure where ammonia borane was utilised as a single-source precursor for both the nitrogen and boron sources. This procedure is shown schematically in Figure 5.9.

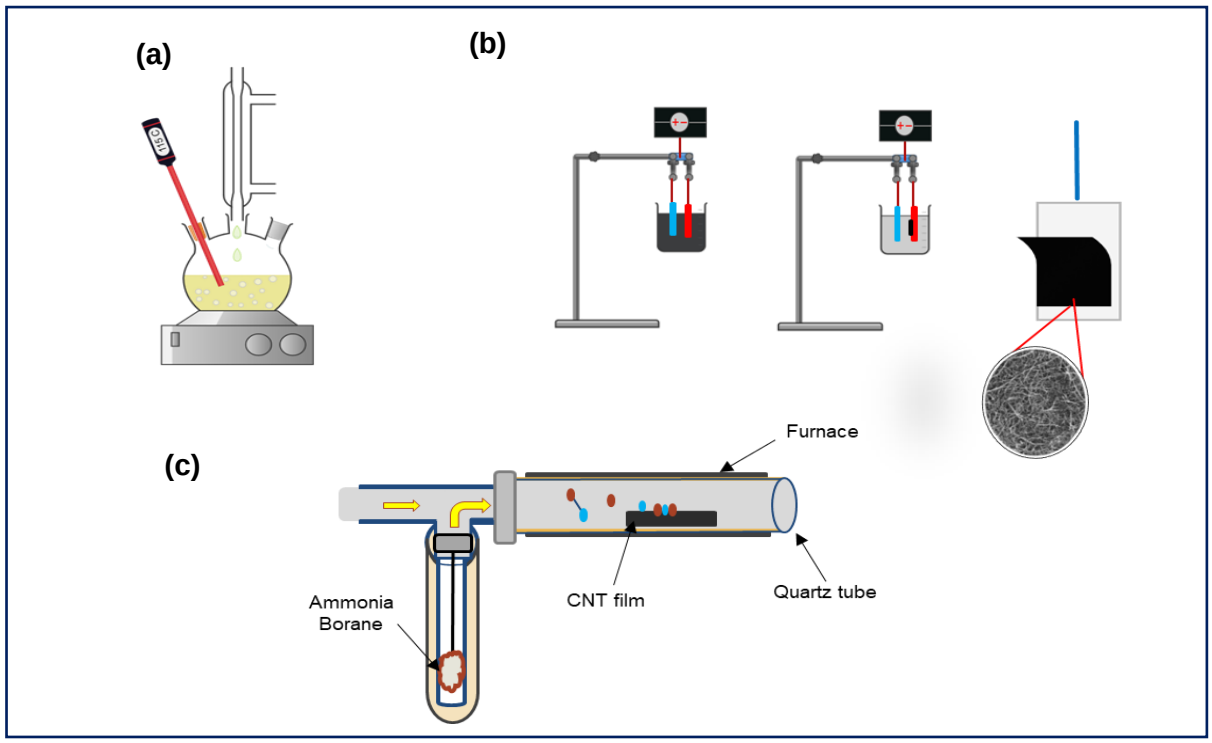


Figure 5.9: A schematic diagram highlighting each step in the attempted fabrication of BCN-NT films. (a) shows the chemical treatment of undoped CNTs which is followed by the deposition process (b) to produce freestanding films. Co-doping is then attempted through CVD, using a single-source boron and nitrogen precursor (c).

The ammonia borane was pre-heated in a separate section from the main reaction zone, in order to produce reactive vapours. At the same time, the tube furnace was heated to 1100 ^{o}C away from the main reaction zone. Once at temperature, the furnace was moved into position over the CNT film that was located inside a quartz tube. At this point, the ammonia borane vapour was introduced using a mixture of argon and hydrogen as a carrier gas. The vapours were allowed to react with the film for a duration of two hours at which point the product was then allowed to cool.

The introduction of boron and nitrogen within the CNT films was confirmed *via* XPS. Upon inspection of the recorded spectra, clear peaks at *ca*. 190 eV and 398 eV were detected which correspond to the B1s and N1s spectra, respectively.[194, 195] As we can see, a significant amount of boron and nitrogen have been introduced into the CNT with contents of 25.95 and 21.7 at.%, respectively. Given that the carbon content is 48.3 at.%, the relative boron and nitrogen contribution to the film is nearly 50%. Deconvolution of the B1s and N1s spectra gave further insight into the composition of the boron and nitrogen content within the film. As can be seen in Figure 5.10, deconvolution using the same model utilised in Chapter 3 revealed that for each of the B1s and N1s spectra, there were multiple contributions.

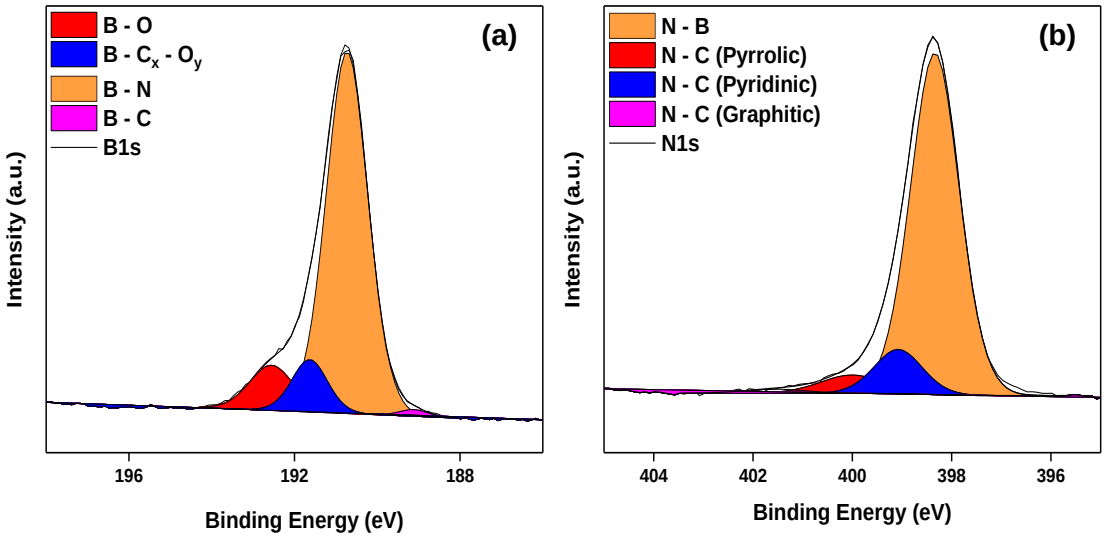


Figure 5.10: XPS spectra showing a typical signal recorded for B1s electrons (a) and N1s electrons within the electrophoretically deposited CNTs film after CVD treatment. The spectra have been fitted with curves, that represent various types of bonding present.

The B1s peak can be split into four peaks which are attributed to contributions from B-C, B-N, B-C_xO_y and B-O bonding present within the system.[196-199] The N1s peak can be split into contributions from N-B and three types of N-C bonding.[201-204] As we can see, the deconvolution of each of the B1s and N1s peak revealed the presence of a dominant peak at *ca*. 190.8 and 398 eV. These peaks correspond to B-N and N-B bonding, respectively. The large quantity of boron and nitrogen (*ca.* 50 at.%) detected by XPS and the dominance of the

B-N/N-B peaks suggest that segregated formation of boron nitride has occurred as opposed to heteroatom doping during this CVD procedure. Simulations have demonstrated that there is a thermodynamic favourability for the formation of segregated BN and carbon domains within nanotubes, due to bonding preferences.[118] Further to this, experimental work has corroborated these studies and shown that the introduction of both boron and nitrogen precursors simultaneously can lead to the formation of boron nitride coatings on CNTs.[172, 190] Upon heating, ammonia borane degrades to produce boron and nitrogen containing vapours that can undergo reactions to form BN at elevated temperatures and these have previously been used for the formation of BN-graphene layered structures.[327, 339] Given this, the XPS suggests that it is likely that the CNT structures here have acted as a template for BN growth instead of direct incorporation into the CNT structure as dopants. It was thought the oxidation defects may facilitate heteroatom doping as achieved in chapter 3, but this doesn't seem to be the case. It has been suggested by researchers that disordered/defective structures can facilitate and enhance boron nitride nucleation on carbon templates; the nanotube film used here is composed of oxidised CNTs and the defects may have promoted the formation of a boron nitride coating.[340] Considering that the oxidised nanotubes are a pre-formed crystal structure, the tendency to form segregated domains reported in the literature, and the noted ability of defects to catalyse BN nucleation, it is not unsurprising that we have seen BN/C formation here. Recently, work within our group has detailed how boron nitride coatings of CNTs can be achieved using ammonia borane before eventual conversion to BNNTs; it is likely a similar heterostructure has formed here.[341] Henceforth, we will refer to this product as BN/CNT film.

TGA analysis was used to further probe and deduce the composition of the film. A comparison of the raw CNT film and the treated film are shown in Figure 5.11 where we can observe the effect of the CVD procedure. As we can see, the BN/CNT film shows enhanced

thermal resistance when compared to the oxidised CNT film. The 50 wt.% temperature is greater for the BN/CNT film when compared to the precursor film. We also see that for the CNT film, the onset of oxidation begins at a lower temperature when compared to the BN/CNT film. A boron nitride coating on the CNT film would explain this observation due to the superior thermal resistance of the boron nitride. This effect was previously observed by Wang *et al.*[342] who reported enhanced oxidation resistance for BN coated CNTs when compared to uncoated. In addition to thermal properties, we can see from the TGA profiles that the residual weights of the samples are significantly different. After oxidation of the CNT film, only a small residual weight is observed; for the BN/CNT hybrid, however, the residual weight is *ca*. 25 wt.%. This is a characteristic of BN coated carbon nanotubes, as boron nitride is resistant to temperatures greater than 900 °C that is the maximum oxidation temperature used here. This provides further indication that the CVD procedure has produced a BN/CNT hybrid film as opposed to a heteroatom doped CNT film.

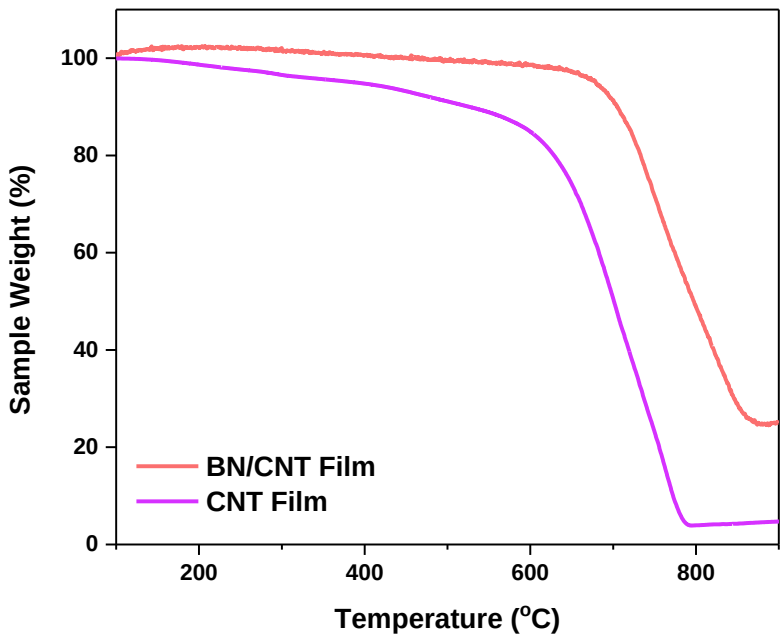


Figure 5.11: Thermogravimetric analysis profiles, in air, for each of the CNT (blue) and BN/CNT (red) films which reveals a distinct alteration in oxidation resistance after the CVD treatment.

Given that the main focus of this thesis is on heteroatom doped BCN-NTs, I turned my attention to exploring different avenues for the production of macroscopic films due to this method yielding BN/CNT hybrids. Despite this, the two-step technique that has been developed within this sub-section provides an interesting and promising route toward the production of BN coated CNT films on the macro scale. The benefits of the EPD process such as the potential for scalability and controllable film thickness make it an attractive technique for producing CNT films. The ability to coat these films with boron nitride, through a simple CVD procedure, may be desirable for applications that are looking to utilise these hybrid materials on the macroscale. For example, previous work has investigated BN/CNT aerogels and foams for desulphurisation and as thermal management materials.[343, 344]

5.3.2. Part II: Vacuum Assisted Production of Macroscopic BCN-NT Films

5.3.2.1 Optimisation of Nanotube Dispersion in Green Solvent

The production of buckypapers using vacuum filtration involves passing CNTs, suspended in solution, through a membrane which results in their entanglement and ultimately thin film formation. The quality of the starting solution has been shown to impact the success of this technique and dictate the properties of the resulting CNT films.[345] As was detailed earlier, CNTs are particularly difficult to disperse in solvent media, owing to surface properties. As a consequence, pre-treatment of the nanotubes is usually employed to enhance dispersion. This can disrupt the properties of the CNTs and/or lead to unwanted impurities in the final product, however. Where possible therefore, it is preferable to avoid the use of these pre-treatments. For this work, the dopant atoms and intrinsic defects within were anticipated to

aid dispersion in solvent. Additionally, the use of mild ultrasonication has previously been used to enhance the dispersion of CNTs whilst retaining the nanotube properties.[323, 346] Therefore, we begun by attempting to determine the best common laboratory solvent that could produce dispersions of BCN-NTs suitable for buckypaper fabrication.

For this study, BCN-NTs were suspended in three solvents which included water, iso-propanol (IPA) and ethanol. These solvents are common in most laboratories and each display different properties. The mixtures were then ultrasonicated for a fixed period to aid their dispersion. This was followed by centrifugation at which point aliquots were taken in order to investigate *via* UV-Vis analysis. This would allow us to determine the optimal 'common' laboratory solvent for the production of BCN-NTs buckypapers.

Figure 5.12 shows aliquots of each solutions after the sonication period had finished. As we can see, the nanotubes formed grey suspensions in two of the solvents, IPA and ethanol, whilst in water they remained predominantly undispersed. After centrifugation, some aggregation was observed at the bottom of the centrifuge tube, completely in the case of water, but for IPA and ethanol, the supernatant retained a grey colour due to the dispersion of nanotubes.

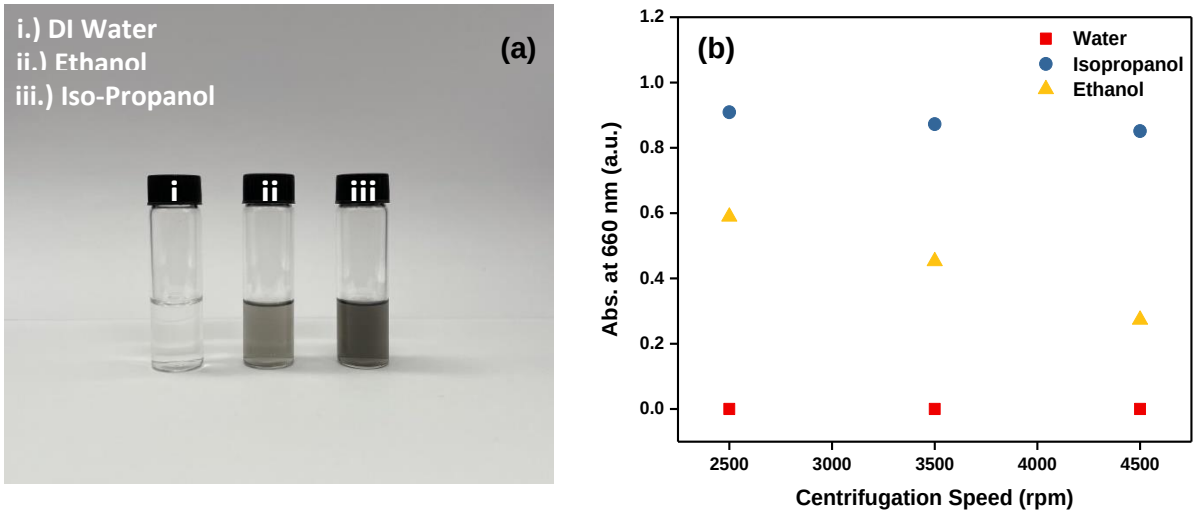


Figure 5.12: Optical images showing BCN-NTs dispersed in various solvents (a). A plot of absorbance (at 660 nm) for aliquots of each dispersion recorded after various centrifugations.

Figure 5.12 also shows a plot of UV-Vis absorption at 660 nm recorded for each of the different nanotube dispersions at a variety of centrifugation speeds. In previous works, the absorption recorded at $\lambda = 660$ nm has been used to assess the quality of CNT dispersions in solution.[347, 348] For example, Castel *et al*.[349] demonstrated through use of the Beer-Lambert law, that absorbance of MWCNT dispersions at 660 nm displayed a linear relationship with concentration. This was used to ultimately determine absorption coefficients. Given that the same starting mass of nanotubes was used for each dispersion, the absorbance at 660 nm was then recorded to qualitatively evaluate the concentration of the dispersions. As we can see in Figure 5.12, for each solvent, increasing the centrifugation speed decreases the absorbance and therefore the concentration of nanotubes suspended in solution, given their linear nature. This observation is consistent with previous studies that measured absorbance before and after dispersion.[350] This decrease is to be expected as the ultrasonication dispersion employed here is relatively mild when compared to other examples. The application of increasing centrifugal force will promote the flocculation of larger aggregates and bundles, resulting in the observed lower absorbance. The most interesting feature, however, is the variation with solvent. As we can see, in each case, IPA has the largest absorbance recorded at 660 nm when compared to the other solvents. The correlation between the absorbance at 660 nm and nanotube concentration therefore suggests that IPA is the most effective 'common' laboratory solvent for dispersing BCN-NTs out of the solvents screened, under mild sonication.

When considering the work presented in the previous chapter, it was shown that Hansen-distance can be used as predictor for the level of nanoparticle loading achieved. It was suggested that as the distance increases, the level of loading also does in an attempt to minimise unfavourable interactions with the solvent. Solvents with a small distance therefore would have favourable interactions when compared to solvents with a large distance. By

applying that logic here, we would expect solvents with a lower distance to disperse the nanotubes better. Solvents with large Hansen distances would likely aggregate in order to minimise surface area and interactions with the solvent. The calculated Hansen distances for the solvents used here decrease in the order of water (8.5), ethanol (5.7) and IPA (5.2). This decrease in Hansen distance is inversely proportional with the observations made *via* UV-Vis analysis, *i.e.* as the distance decreases, the magnitude of dispersion increases. Given the large Hansen distance for water, it makes sense to see both visually and through UV-Vis analysis that there has been poor dispersion in this solvent. The IPA and ethanol are more comparable in magnitude, with the IPA being slightly lower. This Hansen-distance description of nanotube-solvent interactions offers one explanation for superior dispersion in IPA out of the solvents screened here. The dispersion of nanotubes in solvent is a complex process dictated by many factors; previous studies have been conducted for explaining the dispersibility of doped nanotubes in common laboratory solvents.[351] It would be of interest to develop this type of extensive study to the BCN-NTs used here. This potential future work would allow greater evaluation of the BCN-NT dispersions but at present is beyond the scope of this thesis. For this work, given the wide-spread compatibility and availability of IPA, it is a suitable solvent to proceed with for further processing of these nanotubes into buckypapers.

5.3.2.2 Production of BCN-NT Film *via* Vacuum Filtration

5.3.2.2.1 Overview of BCN-NT Films

After determining the most suitable, common laboratory solvent for dispersing the BCN-NTs in 5.3.2.1, we looked to produce free-standing films using iso-propanol as the dispersant. The BCN-NTs were initially ground into a paste which was then diluted with solvent before sonicating. After dispersing the nanotubes in solvent, they were slowly filtered through a

polycarbonate membrane which was assisted by a vacuum pump. This process is shown schematically in the introduction. Upon completion of the filtering, the membrane was dried in a vacuum oven overnight. A film could then be peeled away from the PC membrane which revealed a free-standing BCN-NT 'buckypaper'. For comparison, films were also produced using N-CNTs and undoped CNTs.

Figure 5.13 displays optical images of the BCN-NT films obtained using this vacuum filtration method. As can be seen, this technique has allowed the successful production of a matt black, macroscopic BCN-NT film which can be easily manipulated with tweezers on the macro-scale. This can further be seen in appendix where the BCN-NT films are grasped by hand. To the best of our knowledge, this is one of the first reports for processing BCN-NTs into a thin film assembly. This method negates the need for surfactant assistance, which has previously been shown to leave residual coatings that can be difficult to remove; or acid etching, which may damage the CNT structure.[352, 353] The solvent used in this procedure can also be fully recovered after filtration and recycled for use in further dispersion/film fabrication. Additionally, the adapted technique used here required less than a third of the sonication time to that which has previously been used within our group.

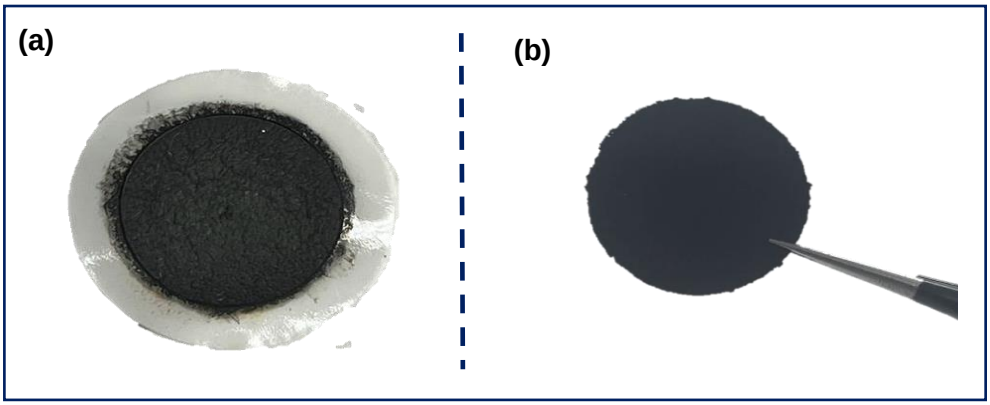


Figure 5.13: Optical images of the BCN-NT buckypaper produced via vacuum filtration, before (a) and after (b) removal from the polycarbonate membrane.

The typical mass for one of these buckypapers is 10 mg and the average thickness was recorded at 208 μm ± 9. This small thickness variation highlights the uniformity of the vacuum filtration procedure in producing BCN-NT films. When compared to the BCN-NTs, there were no obvious differences observed for the macroscopic films produced using the N-CNTs, with the thicknesses being approximately the same. It is interesting to note that attempts to lower the nanotube concentration by more than half (from 1 mg/10 ml) did not afford successful delamination of the BCN-NT film from the membrane. This suggests there is a minimum mass of filtrate required to provide sufficient entanglement for buckypaper formation. This had previously been observed by Dalina *et al*.[354] who found that for a 90 mm membrane, a minimum mass of 150 mg was required for the successful peeling off of their CNT film. It would be interesting in future, to investigate this further and determine the limit in order to gain better control over the production of films with variable thickness.

5.3.2.2.2 Properties of BCN-NT Films

Considering that we altered the ultrasonication times that were previously used within our group by more than two thirds, we wanted to examine the effect this shortened sonication procedure had on the buckypapers graphitisation, given that it can be affected by sonication. Figure 5.14 shows the average Raman spectra recorded, over several points, for the N-CNTs, the BCN-NTs and the BCN-NT buckypaper. Additionally, we can see the I_D/I_G ratios calculated for the respective materials. These I_D/I_G ratios give an indication of crystal disorder and defect density within the nanotubes, and ultimately allow us to compare the relative graphitisation. As can be seen, as was previously reported in Chapter 3, the recorded I_D/I_G ratio for the raw BCN-NTs is lower than the N-CNTs, which we attributed to the introduction of the boron dual-dopant and the heat treatment performed. We then compared

the raw BCN-NTs to those in the BCN-NT buckypaper, which had been subjected to 4 hours of bath sonication. The findings, which are displayed in Figure 5.14, show that there was no discernible difference in the defect densities after the sonication procedure. This finding is in contrast to some previous works that have detailed how similar sonication procedures can introduce defects into CNTs.[355, 356] For example, Song et al.[355] reported an increased in measured I_D/I_G ratio after a period of just two hours. This difference in results may be explained by the dispersing medium they utilised, however. They used concentrated nitric acid during the sonication procedure which is known to oxidise CNTs. Additionally, no details are provided about the sonicator they used during the study. These observations would suggest that the ultrasonication procedure used here, is relatively mild as there has been no significant surface damage introduced during this step. Despite being a relatively mild sonication procedure, as had been shown, it still allows sufficient dispersion of the BCN-NTs required for the production of free-standing buckypapers.

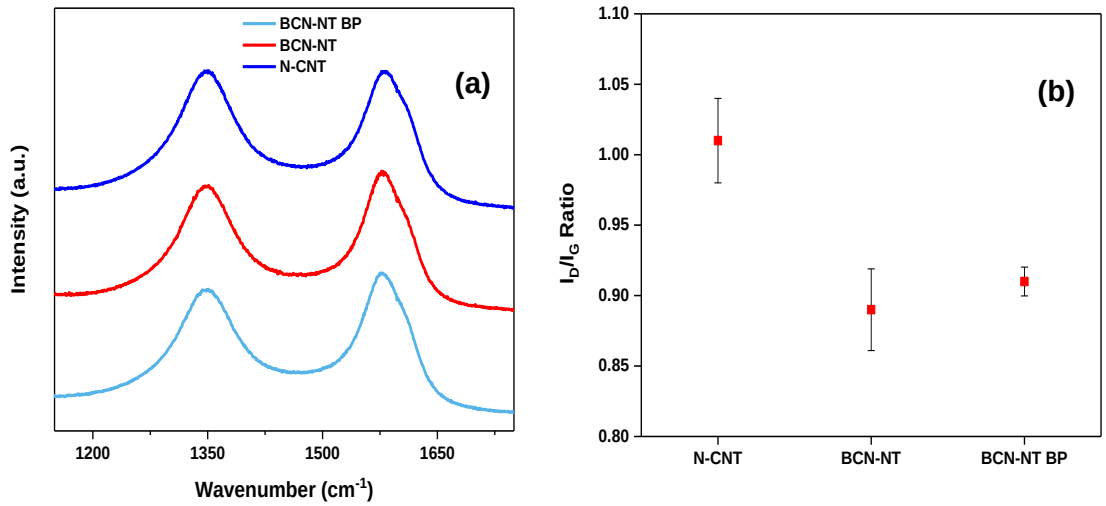


Figure 5.14: Raman spectra highlighting the D and G peaks for precursor materials and the BCN-NT paper (a). A plot of the recorded I_D/I_G ratios for each of the respective materials (b)

In Figure 5.15(a), a low-magnification SEM micrograph of a BCN-NT buckypaper is displayed, giving an overview of the film morphology. As can be seen, the topography of the

BCN-NT film lacks any distinct surface roughness and is fairly even across the entire sample. This shows that during the filtration process, the BCN-NT dispersion passed uniformly through the filter, which allowed an even distribution of material. A magnified edge profile, where an incision on the BCN-NT buckypaper had been made, is shown in Figure 5.15(b). This highlights the layered structure that has formed. It has been suggested that these layered structures arise as a result of the vacuum assistance.[354] After an initial layer of CNTs forms on top of the membrane, the applied vacuum causes additional layers of CNTs to compress. This then results in the 'stacking' formation which can be observed at the edges of the CNT film. This filtration process is thought to be 'self-regulating' which allows the formation of even deposits on the PC membranes.[357]

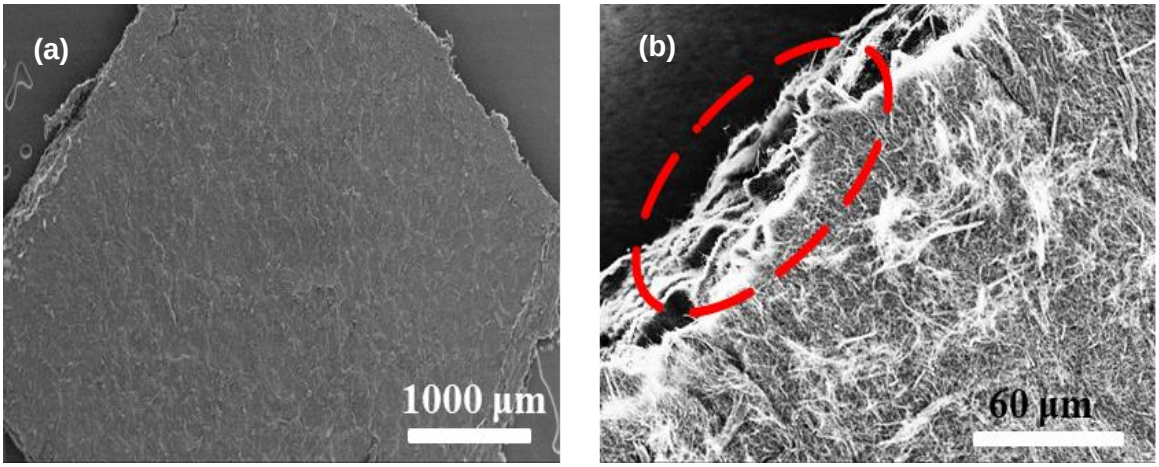


Figure 5.15: SEM micrographs showing an overview of the uniform BCN-NT buckypaper surface (a) and a magnified view of the film edge highlighting the layered structure, encircled in red (b).

In Figure 5.16 we see magnified SEM images of the BCN-NT buckypaper surface which gives us further insight into the film morphology. As we can see in Figure 5.16, a magnified view of the film's topography reveals the small presence of some bundles that remain after sonication and filtration. This is likely due to the fact that the mild sonication procedure employed here was insufficient in overcoming the Van der Waal forces, that hold the nanotube bundles together, to individualise the BCN-NTs in solution. Despite this, the level of dispersion achieved was clearly sufficient to allow adequate intertwining and a free-

standing film to form. Further magnification of the buckypaper showed that the film is composed of entangled nanotubes in a random order, as shown in Figure 5.16(c). These entangled networks arise due to self-assembly resulting from the Van der Waal interactions experienced between the nanotubes.[358] We also note the presence of pores within film structure which form between the overlapping nanotubes. This porous, entangled web of nanotubes, displayed by the BCN-NT film is a commonly encountered structure in the fabrication of CNT buckypapers, within the literature.[359]

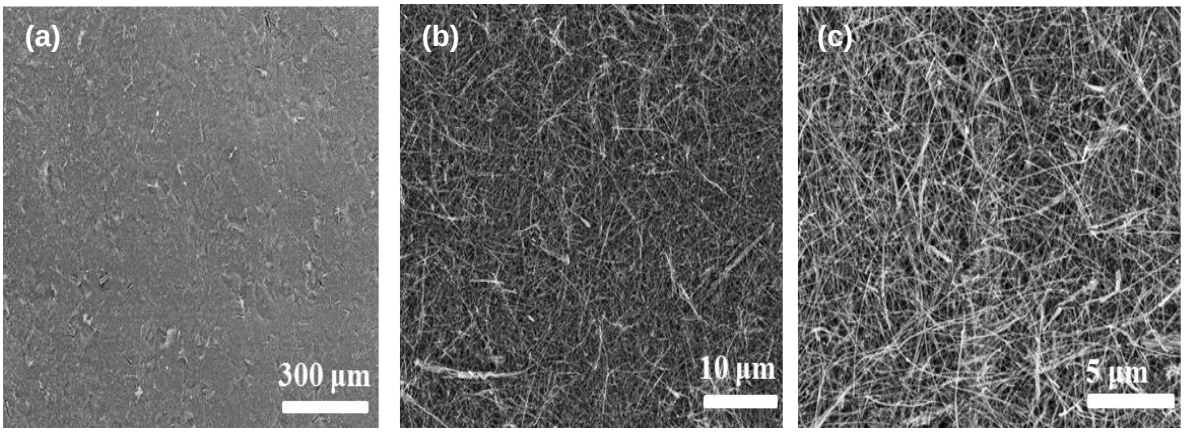


Figure 5.16: SEM micrographs of the BCN-NT buckypaper surface with increasing magnification which highlight the presence of some remaining bundles (a), but generally a uniformly entangled carbon nanotube web (b/c).

The porosity and pore size displayed by a CNT film is of particular interest for a number of applications. More recent examples of these include, water treatment, potential as filtration materials and in electrocatalysis.[360-362] For these prospective applications, it is therefore important to gauge an understanding of the porous nature of the BCN-NT films. The porosity of buckypapers was further probed through analysis of SEM micrographs of the buckypaper surface. In Figure 5.17 we see histograms relating to the measured pore sizes for each of the BCN-NT and N-CNT films. For the pore size analysis, we used the minimum Feret diameter to signify the diameter of the pores on the surface of the nanotube films. Before the measurement of pore diameters, SEM micrographs were first treated using a thresholding

adjustment, in order to highlight the surface pores on the films. An example of this thresholding treatment is displayed in the appendix of this thesis. This processing was conducted on several points of different films to determine the average pore size distribution for each nanotube type. As we can see from the measured pore distributions in Figure 5.17, the diameters are wide ranging in size. On the surface, both of the BCN-NT and N-CNT films display a mixture of mesoporous (2 -50 nm) and macroporous (>50 nm) microstructure, according to pore size definitions.[363] The pore size distribution highlights a predominance for mesoporous contribution, however.

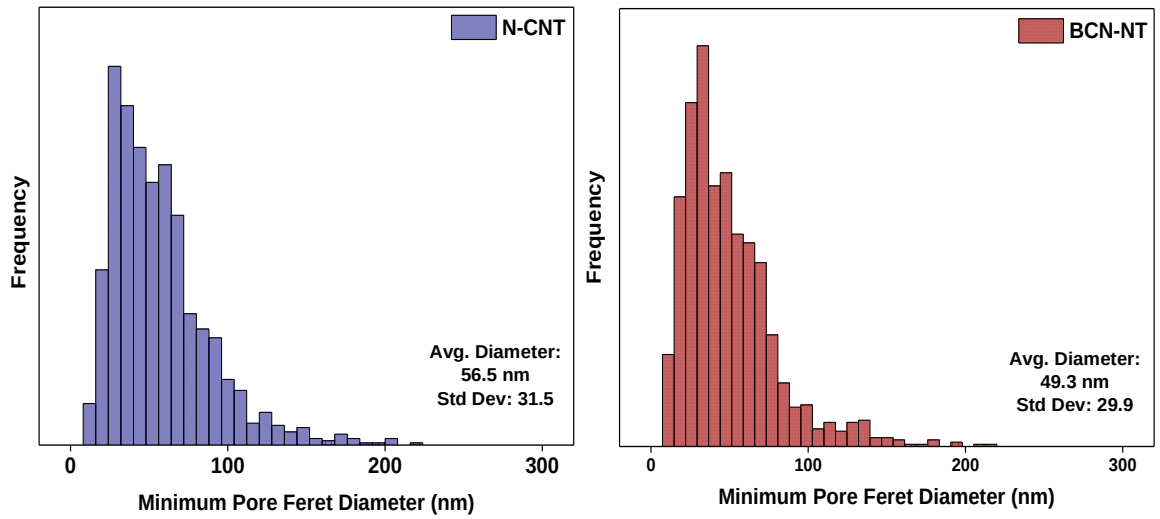


Figure 5.17: Pore size distribution curves recorded for each of the N-CNT (blue) and BCN-NT buckypapers (red). Pore sizes were recorded according to the minimum Feret diameter.

In addition to measuring pore size distribution from SEM micrographs, the microstructure of the BCN-NT and N-CNT films were probed through nitrogen sorption measurements. The surface area was determined using the Brunauer–Emmett–Teller (BET) method whilst the Barrett-Joyner-Halenda (BJH) technique was used to determine the average pore size within the films.[364, 365] Figure 5.18 shows the N_2 adsorption and desorption isotherms recorded for the BCN-NT and N-CNT buckypapers. In each case, the buckypapers display a profile that resembles a H3 isotherm according to IUPAC classification.[363] The H3 type hysteresis loop is

characteristic of a mesoporous microstructure, according to previous reports for CNT films.[366] The average pore width measured for the BCN-NT film using the BJH method was 6.5 nm. Interestingly, this is lower than average diameter recorded using SEM analysis of the buckypapers topography. The reason for this discrepancy may be explained by limitations of the SEM approach. With the SEM approach, the pore size measurement is limited to a particular surface of the film. The BJH approach allows measurement of all accessible pores on the film which gives a more uniform representation of the films pore composition. Applying both these techniques is a complementary approach to probing the surface and inner-structure of the BCN-NT film. The surface areas recorded *via* the BET method, for the BCN-NT and N-CNT films were 181.2 ± 1.2 and 110.5 ± 0.5 m^2/g, respectively.

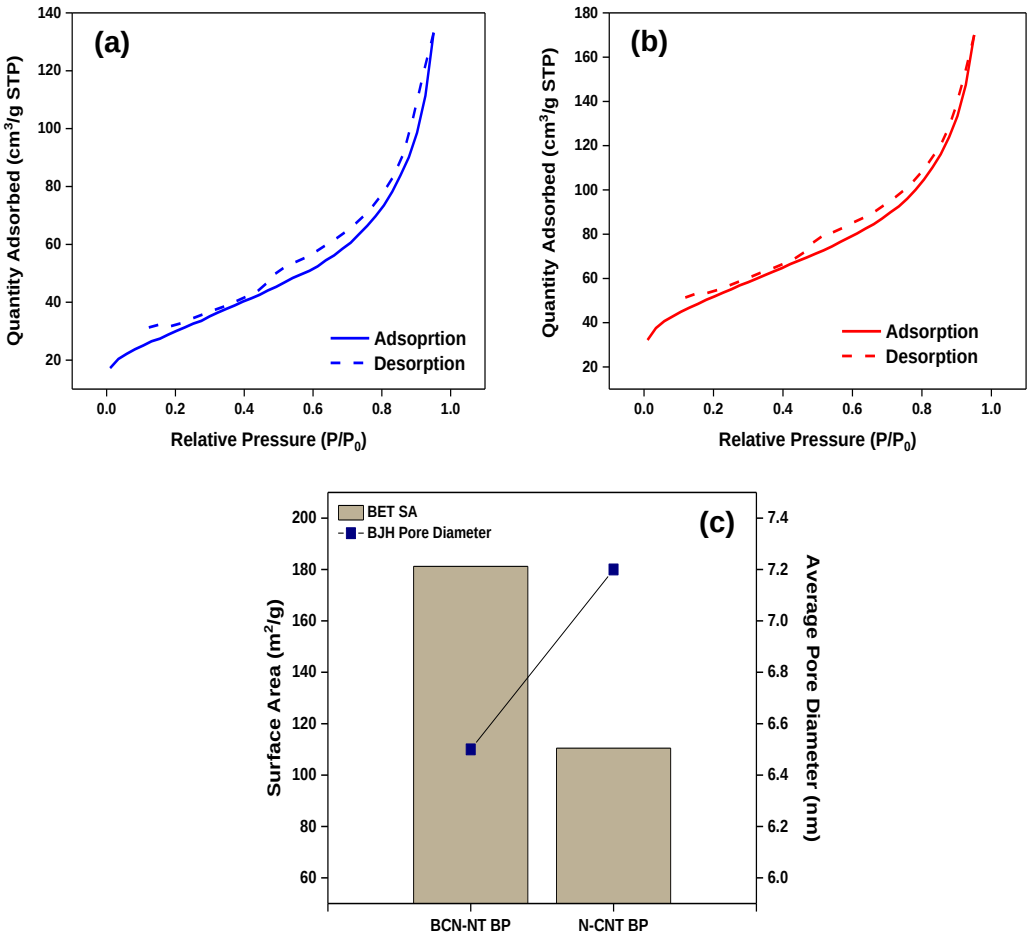


Figure 5.18: BET adsorption and desorption plots obtained for the N-CNT (a) and BCN-NT (b) buckypapers along with a plot of the buckypaper surface areas and BJH pore analysis (c)

Despite the exact same procedure being employed for the fabrication of these films, the BCN-NT film clearly has a higher surface area. Taking into account that N_2 adsorption is a physisorption process, the increased surface area cannot be simply described by the presence of boron dopants sites enhancing this. Similarly, we noted in chapter 3 that the co-doping process does not significantly impact the nanotube structure. Given this, it is likely that the boron doping has instead impacted the final macroscopic structure which in turn has afforded a greater number of active sites for nitrogen adsorption to occur at. The presence of boron dopants within the BCN-NTs aids the dispersion process and thus would minimise the presence of bundles and aggregates in the macroscopic film, when compared to N-CNTs. The increased presence of bundling and aggregates within the N-CNT films would reduce accessibility during the BET measurements resulting in an apparent decrease in film surface area. We also note that the measured BJH pore diameter is slightly smaller for the BCN-NTs when compared to the N-CNT film; the smaller pores would offer more surface area per unit volume. Nevertheless, the enhanced surface area noted here could be useful for applications such as electrocatalysis in the future, especially considering the film porosity.[367]

The porous nature observed here can influence the density of the as-prepared nanotube films. Given that the volume of a disc can be expressed by equation 5.1, shown below, we were able to calculate the average bulk density for the BCN-NT buckypapers using equation 5.2. The average estimated value was found to be 0.25 g/cm^3. Whilst this value is lower than densities achieved by electrophoretic deposition, it is still on the order that would be expected for other CNT films produced by vacuum filtration that have been reported in the literature.[312, 338, 368]

$$V = \pi r^2 h \quad (5.1)$$

$$(5.2) \quad \rho = \frac{m}{V}$$

Due to the size of the PC membrane utilised in the fabrication of the BCN-NT buckypapers, we were unable to quantitatively assess the mechanical properties of the film. This is due to the minimum length requirement for mechanical testing being 30 mm, and the films we produced possessing a diameter of 17 mm. Despite this, the films were shown to be fairly robust and could be held and moved with tweezers without breaking. The films were flexible and did not break when bent, as can be seen in the appendix. Clamping the films between two pairs of tweezers and pulling did lead to film fracturing and mechanical failure however, showing that there is an obvious limit to the extent they can be handled. It would be interesting to quantitate the mechanical properties of the BCN-NT film and compare them to the uni-doped N-CNT films; this would require scaling the buckypaper fabrication appropriately to produce a film with a minimum diameter of 30 mm.

The final property of the films to be investigated was their electrical conductivities. The conductivity for each film was determined using the 4-point probe method. Briefly, the four probes are contacted with the CNT films, at which point a current is applied to the external probes and the voltage response for the inner probes is measured. These known values can then be applied to equation 5.3, where σ = conductivity and ρ = resistivity, which yields the measured conductivity of the buckypapers. For each type of buckypaper conductivities were measured for three separate samples.

$$(5.3) \quad \sigma = \frac{1}{\rho} \text{ where } \rho = t \times 4.532 \frac{\Delta V}{I}$$

Figure 5.19 displays the measured conductivities for both the BCN-NT and N-CNT films, in addition to an undoped CNT sample. When compared to values reported in the literature, the conductivities reported here are comparable to what we would expect for nanotube films prepared *via* vacuum filtration.[369, 370] As well as the porosity demonstrated and increased surface area, the conductivity measured here makes the BCN-NT film suitable for potential applications such as a free-standing electrode for electrocatalytic applications, in accordance with conductivities recorded in previous reports.[371] In Chapter 3 we detailed that the optical band gap for the BCN-NTs was reduced when compared to the N-CNT starting material, according to the Tauc analysis performed.

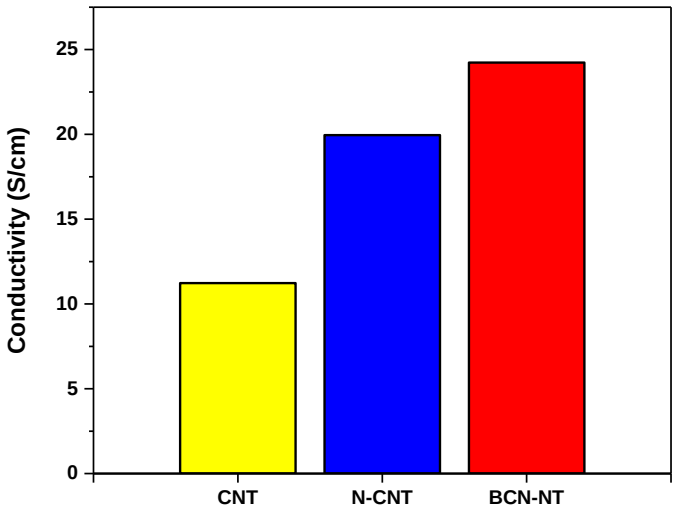


Figure 5.19: 4 point-probe conductivity measurements for each of the buckypapers which revealed the highest conductivity for the BCN-NT buckypaper.

In their computational study, Talla *et al.*[120] also detailed this band gap closing upon the introduction of both boron and nitrogen dopants into CNTs. They expected this to cause alterations to the electrical conductivities of the nanotubes. Here therefore, we anticipated that our dual doping procedure would have an impact on the electrical properties of the nanotubes. It is apparent from Figure 5.19, that the conductivity measured for the BCN-NT is

greater than the N-CNT buckypaper. There has been an enhancement in electrical conductivity upon the introduction of boron into the sample, which confirmed our predictions. The substitutional introduction of boron has previously been shown to enhance the conductivity of nanotubes in other reports.[218] As such, the improvement in electrical conductivity could be ascribed to the shifting of the Fermi level towards the valence band caused by the introduction of boron into the nanotubes. The boron induced improvement in electronic properties may also be due to the greater number of charge carriers that have been introduced into the nanotube. Additionally, the quality of starting dispersion has been shown to correlate to the conductivity of buckypapers, which could display influence here.[318] The additional boron doping sites may have assisted with dispersing the nanotubes and improved the films overall quality by increasing entanglement and reducing contact resistance experienced between nanotubes. Further to this, these observations provide additional support to successful heteroatom doping as opposed to the formation of BN coating. As we have seen, for the BCN-NT buckypapers an improvement in conductivity was measured; this would not be expected if a BN coating had been formed on the nanotubes. Due to the insulating nature of BN, we would expect BN coated CNTs to display increased resistivity and thus, a reduced electrical conductivity, in accordance with previous investigations into BN coated CNTs. Through producing macroscopic assemblies of the BCN-NTs we can see that alterations made to individual nanotubes have therefore been translated and observed on the macroscopic scale when measuring the conductivity of the films.

5.3.2.3 Production of BCN/FeO_xNP Film *via* Vacuum Filtration

In this final experimental section, we looked to tie the thesis together by combining work detailed in Chapters 3 and 4 as well as section 5.3.2.2. As a proof-of-concept experiment, we looked to produce a macroscopic hybrid BCN-NT/FeO_xNP film. As was shown in Chapter 4,

the *ex-situ* functionalisation of BCN-NTs with FeO_xNPs could be achieved through a non-covalent procedure. Therefore, here we introduced FeO_xNPs into the reagent bottle during the sonication procedure and adjusted the solvent composition to combine these works. This is shown schematically in Figure 5.20.

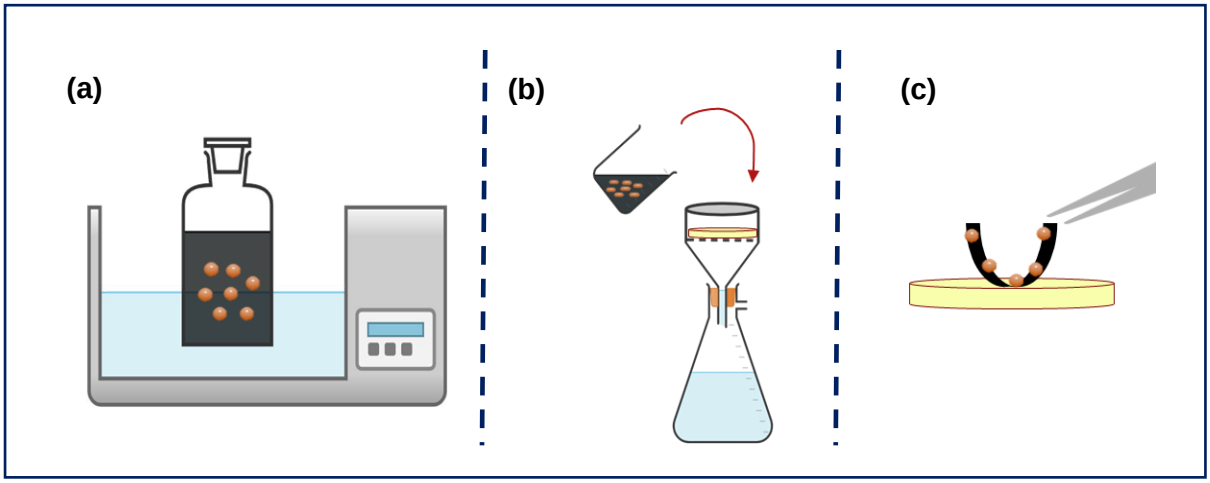


Figure 5.20: Schematic diagram showing the fabrication procedure used for the production of BCN-NT/FeO_xNP hybrid films. Initially BCN-NT were dispersed in solvent before the addition of NPs for the final hour of sonication (a). The mixture then underwent vacuum filtration (b) and was allowed to dry before peeling to yield a freestanding film (c).

Like a regular buckypaper produced in section 5.2.3.2, the sonicated mixture was then filtered through a PC membrane. In an attempt to replicate previous loadings we used the solvent composition that gave the highest loading of FeO_xNPs onto the nanotubes, that was detailed in Chapter 4. In Figure 5.21 we see the TGA profile obtained for the as-prepared BCN-NT film. The profile shows a residual of 66 wt.% which confirms that there has been significant loading of FeO_xNPs onto the BCN-NTs and that a hybrid BCN-NT/FeO_xNP film has been successfully produced. To the best of our knowledge, this is the first time a hierarchical BCN-NT/NP hybrid film has been prepared.

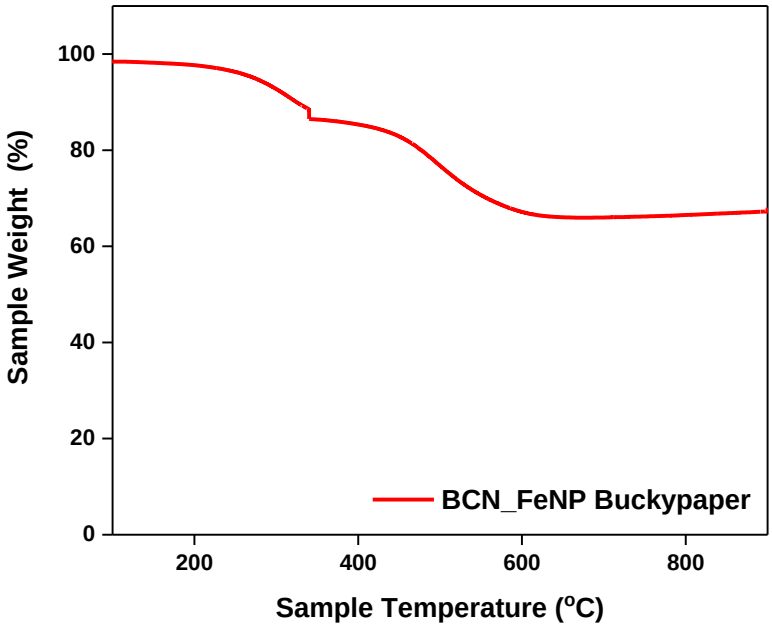


Figure 5.21: TGA profile recorded, in air, for the BCN/FeO_xNP hybrid buckypaper revealing a significant loading of iron oxide NPs into the film.

Figure 5.22 shows an image of the as prepared BCN-NT/FeO_xNP film. As is illustrated, after drying, the film could be mechanically peeled from the membrane and held with tweezers. Immediately, one of the most obvious differences we notice from optical view is the difference in appearance between the as produced BCN-NT/FeO_xNP film and a regular BCN-NT buckypaper. The former has a shiny surface as opposed to the matt surface of a regular BCN-NT film. This alteration is likely due to the introduction of FeO_xNPs during the fabrication of BCN-NT films.

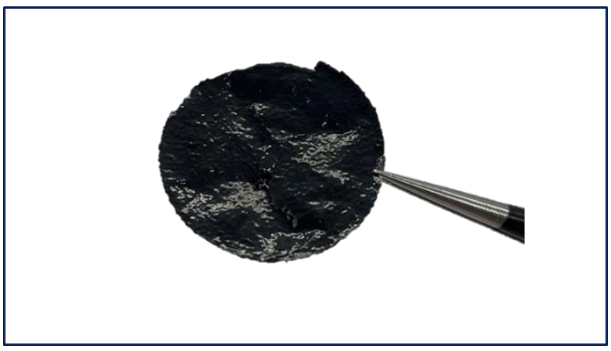


Figure 5.22: An optical image of the as obtained BCN-NT/FeO_xNP hybrid buckypaper which shows a shiny surface as opposed to a matt-surface obtained with just nanotubes.

The morphology of the hybrid film was further probed through SEM imaging; Figure 5.23 displays micrographs obtained. The first thing of note for these hybrid buckypapers is that the micrographs appear brighter (whilst keeping SEM contrast and brightness levels constant).

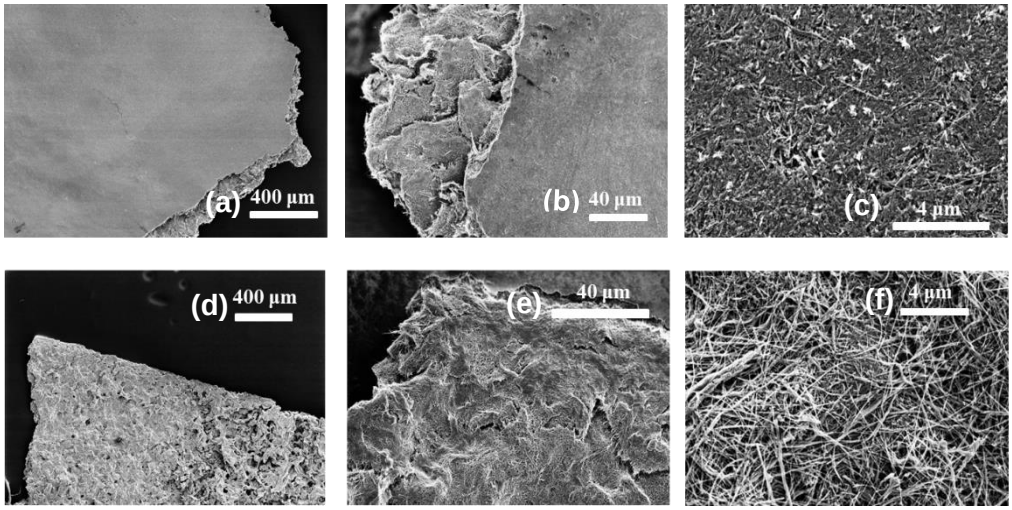


Figure 5.23: SEM micrographs at varying degrees of magnification for the side of the film that formed in contact with the membrane (a-c) and the side that was exposed to air on drying (d-f) which are both distinct from each other.

Due to the high loading of nanoparticles and the insulating properties of iron oxide, the sample may be undergoing charging. In Figure 5.23(a-c) we see the surface of the BCN-NT/FeO_xNP film that formed in contact with the PC membrane. As with the regular BCN-NT and N-CNT buckypapers, the overall surface of the film appears smooth. Upon magnification, the morphology differs slightly however as the pores of the film are not as apparent. This is likely due to the presence of the nanoparticles that block the channels formed by overlapping nanotubes. In section 4.3.2.4 we noted that the introduction of ethanol into the functionalisation solvent media led to an increase in the thickness of the nanoparticle coating and aggregation of nanoparticles between nanotubes. It would appear that this effect is mimicked on the macroscale through the SEM imaging. From recorded micrographs, we can see that side of the buckypaper exposed to air on drying differs from the side in contact with the filter. In contrast to the smooth surface, the morphology displayed by other side of

the film appears more textured and porous. As has been mentioned, in order to produce these composite films, the solvent medium was altered from that of a typical buckypaper detailed in section 5.3.2.2. As such, the drying of the film will have been affected by this change in solvent which ultimately impacted the topography of the surface exposed to air on drying.

When compared to the regular BCN-NT film, it was found that the mechanical properties were significantly different. Whilst the BCN-NT film could be readily handled and bent, the BCN-NT/FeO_xNP film was a lot more brittle which can be attributed to the high loading of FeO_xNPs which have interrupted the entangled network of nanotubes. This high loading of FeO_xNPs also offers explanation for the reduction in electrical conductivity observed for the hybrid films. Given the poor conductivity of iron oxide, the coating of the BCN-NTs with the nanoparticles has hindered the conductivity of the film, overall. As a result of the controllable nature of the functionalisation detailed in Chapter 4, however, it is likely that we would be able to tune the loading of FeO_xNPs within the buckypaper and ultimately the electrical conductivity if this was desirable for specific applications.

5.4 Conclusions

In this final experimental chapter we turned our attention to the macroscale and attempted to develop strategies for the production of freestanding BCN-NT films. This involved the exploration of two strategies; electrophoretically assisted and vacuum filtration techniques, which resulted in the chapter being divided into two-sub-sections.

The electrophoretic based approach began by chemically treating homegrown, un-doped CNTs with acid to create dispersion capable of undergoing electrophoretic deposition. This allowed the fabrication of freestanding CNT films. The films were flexible and upon analysis

with SEM, composed of randomly oriented entangled CNTs. We then attempted to convert these films to BCN-NT films though the use of a single-step, CVD co-doping procedure which utilised ammonia borane as boron and nitrogen precursor. XPS analysis revealed significant incorporation of boron and nitrogen into the film after the CVD treatment. Upon further inspection, and with the addition of complementary TGA analysis, it became clear that the boron and nitrogen had been incorporated as a separate boron nitride phase, as opposed to heteroatom doping. The boron nitride coating resulted in greater thermal resistance for the BN/CNT hybrid films which might be of interest for high temperature applications. The combination of electrophoretic deposition with a CVD treatment offers a promising route towards these BN/CNT composite films for the future.

After establishing a technique for the production of BN/CNT hybrids, we looked to producing BCN-NT films through a vacuum filtration-based route. This was done by first determining the best 'common' laboratory solvent for the as-synthesised BCN-NTs. Through UV-Vis analysis of various dispersions, we found iso-propanol was the most suitable solvent. We used this information to produce BCN-NT dispersions *via* sonication that were converted into films through the assistance of vacuum filtration. This yielded free-standing, flexible, BCN-NT films. Raman analysis revealed that no significant structural damage was introduced on the nanotubes; the sonication procedure utilised was deemed mild whilst still allowing the production of BCN-NT dispersions. Further to this, film properties were probed and compared to N-CNT films. SEM pore analysis revealed a porous structure for each of the BCN and N-CNT buckypapers. As highlighted, this may be of interest to research areas including electrocatalysis and filtration.[361, 362] The structure of the buckypapers were further probed with BET and BJH analysis. The former showed that the BCN-NT buckypaper had a higher surface area than the N-CNT counterpart, which is likely due to the presence of boron dopants which improve the dispersion process and enhance the final surface area of the

nanotube films. The BJH analysis corroborated the pore analysis conducted though SEM imaging. The conductivity of the BCN-NT film was shown to be improved when compared to both the N-CNT and CNT counterparts. We finally looked to tie the thesis together by combining aspects from each experimental chapter of this thesis. To the best of our knowledge, for this first time we have reported a freestanding BCN-NT/FeO_xNP hybrid film.

Chapter 6

Summary and Potential Future Work

The study set out in this thesis aimed to further progression within the field of BCN-NTs by developing methods for their processing, an area of research which had remained in its relative infancy despite the promise they possess. More specifically, we looked to establish a means for the production of hierarchical nanostructures, with BCN-NTs at the foundation; and also arranging BCN-NTs in macroscopic assemblies. Before attempting this, we looked to overcome some traditional synthesis limitations and produce the BCN-NTs on a scale suitable for development of the aforementioned processing. The thesis was divided into three experimental chapters that each looked to address one of these research topics.

In the first experimental chapter, we detailed a two-step synthesis procedure for BCN-NTs. A solid-state chemical process was applied to N-CNTs that had been produced, initially, by AACVD. Through the combination of these synthesis techniques we were able to successfully incorporate both boron and nitrogen dopants into the nanotubes, yielding BCN-NTs. We subsequently explored how reaction parameters such as temperature, heating rate and precursor crystallinity influenced the boron incorporation and the resulting product composition. It was found that the level of boron doping achieved showed correlation with increased reaction temperature, heating rate and defective nature of the precursor. In this chapter it was also demonstrated that the presence of nitrogen – dopant sites, within the precursor, are key to the success of the co-doping reaction and production of BCN-NTs. Experimental results revealed the sacrificial nature of nitrogen – carbon bonding, in particular for pyridinic species, that allowed the incorporation of boron dopants into the nanotubes. Computational simulations were performed to verify and elucidate these experimental observations. These calculations revealed that several potential boron bonding sites were energetically favourable when compared to various pyridinic nitrogen sites.

After producing the BCN-NTs using this two-step procedure, we probed nanotube properties through a number of characterisation techniques. We found that the crystallinity of the BCN-

NTs were improved when compared to N-CNTs through Raman analysis. In comparison to the starting material, optical properties of the BCN-NTs were also altered after the co-doping procedure, as well showing improved oxidation resistance. These findings could be of interest within research fields such as nano-sensors and microwave absorption, where the crystal order and thermal resistance are of importance for the application.[372, 373] The reduction in defect density and increased oxidation displayed could make the BCN-NTs produced here suitable candidates for exploration within these applications.

Given the significance of the nitrogen dopant sites in the success of the co-doping procedure that we have demonstrated, an area of research I would investigate further is attempting to tune the BCN-NT elemental composition through varying the initial composition of the N-CNT precursor. There have been several reports that detail the production of N-CNTs with adjustable nitrogen contents.[213, 374] It would therefore be of interest to synthesise various batches of N-CNTs, with different nitrogen doping levels, and subject them to the standard conditions detailed here for BCN-NT production. In particular, producing pyridine-rich nanotubes has been reported within the literature which would make them an interesting material to explore for the co-doping process.[375] A domain along the same lines that could also be probed further is the nanotube dimensions. As with nitrogen dopant concentrations, there are accounts that exist for controlling the morphology of N-CNTs, such as diameter and length.[376, 377] Additional research into the aforementioned reaction variables would therefore be useful in developing our understanding of the two-step BCN-NT synthesis procedure.

Further to investigating the two-step process in greater detail, it would be interesting in the future to modify the process for enhanced ease. There are various potential routes that could be explored to achieve this, with the ultimate aim to condense the process into a single-step procedure. The first involves the incorporation of the boron reagent into the AACVD feedstock which would render the procedure to a singular growth step. As part of this project,

preliminary work has been conducted to achieve this by dissolving boric acid into the benzylamine and ferrocene solution then performing a standard AACVD synthesis. The initial results showed that using this reagent mixture in an AACVD synthesis allowed the production of vertically aligned nanotubes. Upon further investigation with XPS analysis, the presence of both boron and nitrogen was detected in the product, albeit on a much lower level than the two-step procedure yielded. In addition to the lower doping levels, some issues regarding the boron reagent solubility in the benzylamine solvent were noted during these primary experiments. More research would therefore be required to explore this single-step route. An alternative single-step route involves the same basic concepts as the two-step procedure, but is housed under one experimental set-up, shown in Figure 6.1. Boron oxide vapours would be generated away from the main reaction vessel, then introduced immediately after the synthesis of the N-CNTs. This would negate need for dismantling of reaction kit in-between doping steps. Whilst strictly still a two-step process, removing the need for reaction apparatus disassembly would be desirable for processing simplification. The manual incorporation of boron reactant in the vicinity of the N-CNTs may prove to be integral for a successful reaction. Given the equipment that is available in the Nanomaterials by Design laboratory, this alternative reaction set-up could offer a basis for future studies.

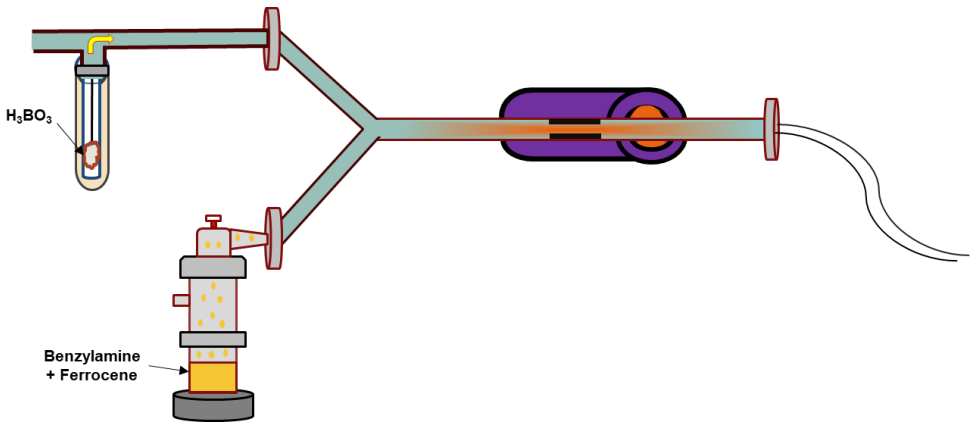


Figure 6.1: A schematic diagram highlighting a potential apparatus set-up that could condense the two-step BCN-NT synthesis into a single reaction manifold.

The second experimental chapter turned towards developing processing techniques and focused on the design and synthesis of novel hierarchical BCN-NT composites. This involved the *ex-situ* attachment of FeO_xNPs to the surface of BCN-NTs, for the first time, through modification of non-covalent interactions. To begin with, we began by establishing a baseline using the N-CNTs prior to the co-doping process. We investigated the effect that the solvent media had on the functionalisation process and used previously established models to rationalise the results we obtained here. In this study, we observed that the choice of solvent had a major influence on the level of iron nanoparticles that could be attached to the N-CNTs. Through altering the solvent, a variable nanohybrid composition could be achieved. This observation was once again observed for the BCN-NTs. By using the dielectric effect and SESP approaches that have been detailed by Rance and Quijano-Velasco *et al*.[265, 378] for undoped CNTs, we were able to offer reasoned explanations for the functionalisation results obtained here as we found good agreement with both experimental models. The use of doped nanotubes in this thesis offers a potential explanation as to why the discrepancies that were previously observed between these two explanatory models, within our group, were not seen here. We also probed the influence that nanoparticle stability had on the level of functionalisation that could be achieved on doped nanotubes. By intentionally de-stabilising the starting nanoparticle solution, through the increasing addition of ethanol, we were able to enhance the level of nanoparticles attached to the nanotubes. The work that was presented in this chapter offers potential routes to follow up with future research. Where the functionalisation itself is concerned, there is room to explore this further. As was noted, the values used for the surface energy calculations were based on commercial samples previously used within this group. To further corroborate the findings here, surface energy values could be determined for the BCN-NT and N-CNTs. These values can be determined through inverse gas chromatography measurements.[285] The study performed here could be extended

further by keeping the same experimental conditions but increasing the number of solvents screened.

Given the novel nature and variability of these nanohybrids; a natural progression would be to investigate their suitability within a range of applications. CNT – nanoparticle hybrids have thus far found potential applications in optoelectronics, electrocatalysis and environmental remediation, amongst others.[109, 111, 112] As BCN-NTs have also been explored for a number of these applications, it would be an interesting and logical next step to evaluate the performance of the BCN-NT – hybrids produced here against existing material candidates. Previously BCN-NT hybrids that have been produced through *in-situ* methodologies have been explored for next-generation batteries.[267] This may be an interesting area to begin with, to see how the materials produced here compare. A final suggestion for further work would involve altering the type of nanoparticle used to functionalise the BCN-NTs. Given the understanding of the non-covalent interactions on the nanoparticle decoration procedure that we have developed in this thesis, future work could extend this to attaching other material types, in particular if a specific application was in mind.

Most research into carbonaceous nanomaterials aims for eventual industrial application to tackle modern day societal issues. The considerations including ease of handling, safety and intrinsic properties make arranging these nanomaterials in suitable macroscale arrangements an important research avenue to consider. The final experimental chapter of this thesis dealt with the assembly of BCN-NTs on the macroscopic scale and was split into two sub-sections that explored different routes towards BCN-NT films. The first sub-section detailed the electrophoretic deposition of CNT films that were subject to a CVD conversion, in attempt to produce BCN-NT films. Analysis revealed that there was significant boron and nitrogen incorporation, but the resulting films were more akin to BN/CNT hybrid materials, as opposed to heteroatom doped BCN-NT films. According to previous research, these

heterogenous films may be of interest for further study in areas such as electrocatalysis, high temperature applications and thermal interface materials.[190, 341, 379] The second section detailed the production of freestanding BCN-NT films through vacuum filtration. The suitability of some common laboratory solvents for dispersing the BCN-NTs were first screened and it was concluded that iso-propanol was the most suitable. It would be interesting to explore the dispersibility in greater detail after measuring the surface energy values for the as-produced BCN-NTs which would allow greater reasoning to the observations we have made here. A relatively mild ultrasonication procedure was used to produce BCN-NT dispersions that were suitable for vacuum filtration. After vacuum filtration, pliable freestanding BCN-NT films were obtained. This technique was employed to N-CNTs to act as a comparator. Raman analysis revealed that the sonication procedure produced minimal structural damage within the BCN-NT films. The BCN-NT and N-CNT film properties were then analysed and compared. It was shown through nitrogen sorption measurements that the BCN-NT film had a higher surface area which is likely due to the introduced boron dopants aiding the dispersion and improving accessibility for nitrogen adsorption in the macroscopic film. Electrical conductivity measurements were improved for the BCN-NT films which we ascribed to introduction of boron which altered the properties of the nanotube when compared to the uni-doped N-CNTs. The enhanced electrical conductivity and surface area demonstrated here offer an encouragement for these films to be explored as potential electrocatalytic and water remediation materials that could be explored further in future. Further to this we also detailed the novel production of a BCN-NT/FeO_xNP hybrid films. This work offered a preliminary route towards the assembly of hierarchical BCN-NT hybrids on the macroscopic scale which again would be of interest for a number of applications to explore in the future. As detailed, the hybrid film was more brittle than the BCN-NTs on their own; through investigating and altering the nanoparticle loading, it may be feasible to create

a more flexible film. Given that the results in the second experimental chapter highlighted the impact that solvent selection has on the nanoparticle loading, this could act as a starting point for varying the composition of these hybrid films. The iron nanoparticles loaded onto the BCN-NTs could act as potential sites for CNT growth and as such, an area of research we would have liked to explore would have been subjecting these BCN-NT/FeO_xNP films to a CVD process. By flowing a reactive gas over such as acetylene over these films, there is the potential to infiltrate and reinforce the films with CNTs, which could be a novel area of research to explore for BCN-NT hybrids and macroscopic CNT assemblies in general. Further to the film production methods detailed in this chapter, further routes to macroscopic assemblies are arising. A procedure for electrophoretically deposited SWCNT films has been developed within the Nanomaterials by Design that utilises a non-destructive, reductive charging technique.[311] This non-destructive charging would be ideal for doped nanotubes as it avoids acid etching. Initial work is being conducted to determine if this method translates to MWCNTs and in future this could be explored for the BCN-NTs used here.

To conclude, this thesis has presented contributions within the field of borocarbonitride nanomaterials. A two-step synthesis route for the production of BCN-NTs has been detailed. In doing so, we have been able to develop and understand processing methods that allowed the fabrication of BCN-NT – nanoparticle hybrids and macroscopic films. Given the results that have been presented here, there is scope for further exploration into these materials and studies; it is intended that this work can act as a foundation for future research.

Bibliography

1. S. F. Hansen, M. B. Nielsen, O. F. H. Hansen, L. P. W. Clausen, L. M. Skjolding, A. Baun and R. Arvidsson, *J. Nanopart. Res.*, 2022, **24**, 8.
2. S. Bayda, M. Adeel, T. Tuccinardi, M. Cordani and F. Rizzolio, *Molecules*, 2020, **25**, 15.
3. M. Monthioux and V. L. Kuznetsov, *Carbon*, 2006, **44**, 1621-1623.
4. M. Kokarneswaran, P. Selvaraj, T. Ashokan, S. Perumal, P. Sellappan, K. D. Murugan, S. Ramalingam, N. Mohan and V. Chandrasekaran, *Sci Rep*, 2020, **10**, 6.
5. S. Iijima, *Nature*, 1991, **354**, 56-58.
6. W. Yu, C. H. Liu and S. S. Fan, *Nano Res.*, 2021, **14**, 2471-2490.
7. L. M. Sun, X. H. Wang, Y. R. Wang and Q. Zhang, *Carbon*, 2017, **122**, 462-474.
8. P. Serp, M. Corrias and P. Kalck, *Appl. Catal. A-Gen.*, 2003, **253**, 337-358.
9. C. Wang, K. Takei, T. Takahashi and A. Javey, *Chem. Soc. Rev.*, 2013, **42**, 2592-2609.
10. H. He, L. A. Pham-Huy, P. Dramou, D. L. Xiao, P. L. Zuo and C. Pham-Huy, *Biomed Res. Int.*, 2013, **2013**, 12.
11. U. N. Maiti, W. J. Lee, J. M. Lee, Y. Oh, J. Y. Kim, J. E. Kim, J. Shim, T. H. Han and S. O. Kim, *Adv. Mater.*, 2014, **26**, 40-67.
12. B. H. Wu, Y. J. Kuang, X. H. Zhang and J. H. Chen, *Nano Today*, 2011, **6**, 75-90.
13. L. Q. Liu, W. J. Ma and Z. Zhang, *Small*, 2011, **7**, 1504-1520.
14. X. Blase, J. C. Charlier, A. DeVita and R. Car, *Appl. Phys. Lett.*, 1997, **70**, 197-199.
15. C. N. R. Rao and K. Gopalakrishnan, *ACS Appl. Mater. Interfaces*, 2017, **9**, 19478-19494.
16. E. Iyyamperumal, S. Y. Wang and L. M. Dai, *ACS Nano*, 2012, **6**, 5259-5265.
17. N. Karousis, N. Tagmatarchis and D. Tasis, *Chem. Rev.*, 2010, **110**, 5366-5397.
18. N. Saifuddin, A. Z. Raziah and A. R. Junizah, *J. Chem.*, 2013, **2013**, 18.
19. T. A. Saleh, *Environ. Technol. Innov.*, 2020, **20**, 16.
20. B. C. Satishkumar, A. Govindaraj, J. Mofokeng, G. N. Subbanna and C. N. R. Rao, *J. Phys. B-At. Mol. Opt. Phys.*, 1996, **29**, 4925-4934.
21. N. Arora and N. N. Sharma, *Diam. Relat. Mat.*, 2014, **50**, 135-150.
22. M. L. Terranova, V. Sessa and M. Rossi, *Chem. Vapor Depos.*, 2006, **12**, 315-325.
23. C. T. Kingston and B. Simard, *J. Nanosci. Nanotechnol.*, 2006, **6**, 1225-1232.
24. Y. Wang, J. Wu and F. Wei, *Carbon*, 2003, **41**, 2939-2948.
25. J. C. Charlier, *Accounts Chem. Res.*, 2002, **35**, 1063-1069.
26. H. F. Bettinger, *J. Phys. Chem. B*, 2005, **109**, 6922-6924.
27. V. Lordi, S. X. C. Ma and N. Yao, *Surf. Sci.*, 1999, **421**, L150-L155.
28. I. Zsoldos, *Nanotechnol Sci Appl*, 2010, **3**, 101-106.
29. D. Walgraef, *Eur. Phys. J.-Spec. Top.*, 2007, **146**, 443-457.
30. P. G. Collins, in *Oxford Handbook of Nanoscience and Technology*, Oxford University Press, 2009, vol. 1, ch. 2 - Defects and Disorder in Carbon Nanotubes.
31. B. Ben Doudou, J. Chen, A. Vivet and C. PoiLane, *J. Nanosci. Nanotechnol.*, 2012, **12**, 8635-8639.
32. R. M. Kumar, S. K. Sharma, B. V. M. Kumar and D. Lahiri, *Compos. Pt. A-Appl. Sci. Manuf.*, 2015, **76**, 62-72.
33. D. Janas, *Mat. Chem. Front.*, 2018, **2**, 36-63.
34. N. Gupta, S. M. Gupta and S. K. Sharma, *Carbon Lett.*, 2019, **29**, 419-447.
35. Z. H. Gao, L. Oudjedi, R. Faes, F. Morote, C. Jaillet, P. Poulin, B. Lounis and L. Cognet, *Sci Rep*, 2015, **5**, 10.
36. H. W. Zhu, C. L. Xu, D. H. Wu, B. Q. Wei, R. Vajtai and P. M. Ajayan, *Science*, 2002, **296**, 884-886.

37. Y. Qiang, X. L. Wang, Z. M. Ying, Y. Y. Zhou, R. D. Liu, S. Y. Gao and L. Yan, *Nanomaterials*, 2022, **12**, 13.
38. S. S. Meysami, P. Dallas, J. Britton, J. G. Lozano, A. T. Murdock, C. Ferraro, E. S. Gutierrez, N. Rijnveld, P. Holdway, K. Porfyrakis and N. Grobert, *Nanoscale*, 2016, **8**, 11993-12001.
39. A. Takakura, K. Beppu, T. Nishihara, A. Fukui, T. Kozeki, T. Namazu, Y. Miyauchi and K. Itami, *Nat. Commun.*, 2019, **10**, 7.
40. M. F. Yu, O. Lourie, M. J. Dyer, K. Moloni, T. F. Kelly and R. S. Ruoff, *Science*, 2000, **287**, 637-640.
41. M. Terrones, *Int. Mater. Rev.*, 2004, **49**, 325-377.
42. E. Pop, D. Mann, Q. Wang, K. E. Goodson and H. J. Dai, *Nano Lett.*, 2006, **6**, 96-100.
43. P. Kim, L. Shi, A. Majumdar and P. L. McEuen, *Phys. Rev. Lett.*, 2001, **87**, 4.
44. J. P. Salvetat, J. M. Bonard, N. H. Thomson, A. J. Kulik, L. Forro, W. Benoit and L. Zuppiroli, *Appl. Phys. A-Mater. Sci. Process.*, 1999, **69**, 255-260.
45. O. Lourie and H. D. Wagner, *J. Mater. Res.*, 1998, **13**, 2418-2422.
46. G. Overney, W. Zhong and D. Tomanek, *Z. Phys. D-Atoms Mol. Clusters*, 1993, **27**, 93-96.
47. M. M. J. Treacy, T. W. Ebbesen and J. M. Gibson, *Nature*, 1996, **381**, 678-680.
48. C. S. Choi, B. J. Park and H. J. Choi, *Diam. Relat. Mat.*, 2007, **16**, 1170-1173.
49. D. E. Hill, Y. Lin, A. M. Rao, L. F. Allard and Y. P. Sun, *Macromolecules*, 2002, **35**, 9466-9471.
50. Z. J. Jia, Z. Y. Wang, C. L. Xu, J. Liang, B. Q. Wei, D. H. Wu and S. W. Zhu, *Mater. Sci. Eng. A-Struct. Mater. Prop. Microstruct. Process.*, 1999, **271**, 395-400.
51. S. Bal and S. S. Samal, *Bull. Mat. Sci.*, 2007, **30**, 379-386.
52. J. N. Coleman, U. Khan, W. J. Blau and Y. K. Gun'ko, *Carbon*, 2006, **44**, 1624-1652.
53. Z. Spitalsky, D. Tasis, K. Papagelis and C. Galiotis, *Prog. Polym. Sci.*, 2010, **35**, 357-401.
54. Y. Wang and G. J. Weng, *Micromechanics and nanomechanics of composite solids*, 2018, 123-156.
55. A. Abdulhameed, N. Z. Abd Wahab, M. N. Mohtar, M. N. Hamidon, S. Shafie and I. A. Halin, *J. Electron. Mater.*, 2021, **50**, 3207-3221.
56. X. M. Liu, Z. D. Huang, S. W. Oh, B. Zhang, P. C. Ma, M. M. F. Yuen and J. K. Kim, *Compos. Sci. Technol.*, 2012, **72**, 121-144.
57. B. J. Landi, M. J. Ganter, C. D. Cress, R. A. DiLeo and R. P. Raffaelle, *Energy Environ. Sci.*, 2009, **2**, 638-654.
58. H. Pan, J. Y. Li and Y. P. Feng, *Nanoscale Res. Lett.*, 2010, **5**, 654-668.
59. S. Kumar, M. Nehra, D. Kedia, N. Dilbaghi, K. Tankeshwar and K. H. Kim, *Prog. Energy Combust. Sci.*, 2018, **64**, 219-253.
60. S. Park, M. Vosguerichian and Z. A. Bao, *Nanoscale*, 2013, **5**, 1727-1752.
61. J. Sheng and Y. Li, *ACS Appl. Mater. Interfaces*, 2022, **14**, 20455-20462.
62. B. Kumanek and D. Janas, *J. Mater. Sci.*, 2019, **54**, 7397-7427.
63. D. J. Yang, Q. Zhang, G. Chen, S. F. Yoon, J. Ahn, S. G. Wang, Q. Zhou, Q. Wang and J. Q. Li, *Phys. Rev. B*, 2002, **66**, 6.
64. G. S. B. McKee and K. S. Vecchio, *J. Phys. Chem. B*, 2006, **110**, 1179-1186.
65. D. Bom, R. Andrews, D. Jacques, J. Anthony, B. L. Chen, M. S. Meier and J. P. Selegue, *Nano Lett.*, 2002, **2**, 615-619.
66. A. Mahajan, A. Kingon, A. Kukovecz, Z. Konya and P. M. Vilarinho, *Mater. Lett.*, 2013, **90**, 165-168.
67. Y. A. Kim, H. Muramatsu, T. Hayashi, M. Endo, M. Terrones and M. S. Dresselhaus, *Chem. Phys. Lett.*, 2004, **398**, 87-92.

68. K. Saeed and Ibrahim, *Carbon Lett.*, 2013, **14**, 131-144.
69. J. Hone, in *Dekker Encyclopedia of Nanoscience and Nanotechnology*, 2004, vol. 7, ch. Carbon Nanotubes: Thermal Properties, pp. 603-610.
70. A. Setaro, *J. Phys.-Condes. Matter*, 2017, **29**, 19.
71. O. V. Kharissova, B. I. Kharisov and E. G. D. Ortiz, *RSC Adv.*, 2013, **3**, 24812-24852.
72. L. Vaisman, H. D. Wagner and G. Marom, *Adv. Colloid Interface Sci.*, 2006, **128**, 37-46.
73. K. Balasubramanian and M. Burghard, *Small*, 2005, **1**, 180-192.
74. S. Z. Mortazavi, A. J. Novinrooz, A. Reyhani and S. Mirershadi, *Cent. Eur. J. Phys.*, 2010, **8**, 940-946.
75. Y. Peng and H. W. Liu, *Ind. Eng. Chem. Res.*, 2006, **45**, 6483-6488.
76. N. Sezer and M. Koc, *Surf. Interfaces*, 2019, **14**, 1-8.
77. S. H. Su, W. T. Chiang, C. C. Lin and M. Yokoyama, *Physica E*, 2008, **40**, 2322-2326.
78. S. Porro, S. Musso, M. Vinante, L. Vanzetti, M. Anderle, F. Trotta and A. Tagliaferro, *Physica E*, 2007, **37**, 58-61.
79. H. Hiura, T. W. Ebbesen and K. Tanigaki, *Adv. Mater.*, 1995, **7**, 275-276.
80. P. X. Hou, C. Liu and H. M. Cheng, *Carbon*, 2008, **46**, 2003-2025.
81. D. Tasis, N. Tagmatarchis, A. Bianco and M. Prato, *Chem. Rev.*, 2006, **106**, 1105-1136.
82. M. U. D. Naik, Y. S. Lee and A. Qurashi, *ACS Omega*, 2018, **3**, 10442-10448.
83. E. V. Basiuk, M. Monroy-Pelaez, I. Puente-Lee and V. A. Basiuk, *Nano Lett.*, 2004, **4**, 863-866.
84. A. Roy, K. K. Gupta, S. Naskar, T. Mukhopadhyay and S. Dey, *Mater. Today Commun.*, 2021, **26**, 16.
85. M. Glerup, J. Steinmetz, D. Samaille, O. Stephan, S. Enouz, A. Loiseau, S. Roth and P. Bernier, *Chem. Phys. Lett.*, 2004, **387**, 193-197.
86. R. Droppa, P. Hammer, A. C. M. Carvalho, M. C. dos Santos and F. Alvarez, *J. Non-Cryst. Solids*, 2002, **299**, 874-879.
87. T. Sharifi, F. Nitze, H. R. Barzegar, C. W. Tai, M. Mazurkiewicz, A. Malolepszy, L. Stobinski and T. Wagberg, *Carbon*, 2012, **50**, 3535-3541.
88. P. Ghosh, T. Soga, K. Ghosh, R. A. Afre, T. Jimbo and Y. Ando, *J. Non-Cryst. Solids*, 2008, **354**, 4101-4106.
89. J. W. Liu, S. Webster and D. L. Carroll, *J. Phys. Chem. B*, 2005, **109**, 15769-15774.
90. K. Yokoyama, Y. Sato, K. Hirano, H. Ohta, K. Motomiya, K. Tohji and Y. Sato, *Carbon*, 2015, **94**, 1052-1060.
91. D. P. Hashim, N. T. Narayanan, J. M. Romo-Herrera, D. A. Cullen, M. G. Hahm, P. Lezzi, J. R. Suttle, D. Kelkhoff, E. Munoz-Sandoval, S. Ganguli, A. K. Roy, D. J. Smith, R. Vajtai, B. G. Sumpter, V. Meunier, H. Terrones, M. Terrones and P. M. Ajayan, *Sci Rep*, 2012, **2**, 8.
92. C. Preston, D. Song, J. Taillon, J. Cumings and L. B. Hu, *Nanotechnology*, 2016, **27**, 9.
93. C. G. Hu and L. M. Dai, *Adv. Mater.*, 2019, **31**, 17.
94. S. H. Lee, D. H. Lee, W. J. Lee and S. O. Kim, *Adv. Funct. Mater.*, 2011, **21**, 1338-1354.
95. J. E. Riggs, Z. X. Guo, D. L. Carroll and Y. P. Sun, *J. Am. Chem. Soc.*, 2000, **122**, 5879-5880.
96. T. Xin, L. Chang, H. M. Cheng, H. C. Zhao, Y. Feng and X. Q. Zhang, *J. Appl. Polym. Sci.*, 2004, **92**, 3697-3700.

97. P. Bilalis, D. Katsigiannopoulos, A. Avgeropoulos and G. Sakellariou, *RSC Adv.*, 2014, **4**, 2911-2934.
98. V. Bavastrello, E. Stura, S. Carrara, V. Erokhin and C. Nicolini, *Sens. Actuator B-Chem.*, 2004, **98**, 247-253.
99. G. F. Cheng, J. Zhao, Y. H. Tu, P. A. He and Y. H. Fang, *Anal. Chim. Acta*, 2005, **533**, 11-16.
100. B. K. Kuila, S. Malik, S. K. Batabyal and A. K. Nandi, *Macromolecules*, 2007, **40**, 278-287.
101. K. S. Novoselov, A. K. Geim, S. V. Morozov, D. Jiang, Y. Zhang, S. V. Dubonos, I. V. Grigorieva and A. A. Firsov, *Science*, 2004, **306**, 666-669.
102. H. X. Kong, *Curr. Opin. Solid State Mat. Sci.*, 2013, **17**, 31-37.
103. M. Y. Yen, M. C. Hsiao, S. H. Liao, P. I. Liu, H. M. Tsai, C. C. M. Ma, N. W. Pu and M. D. Ger, *Carbon*, 2011, **49**, 3597-3606.
104. A. S. Patole, S. P. Patole, S. Y. Jung, J. B. Yoo, J. H. An and T. H. Kim, *Eur. Polym. J.*, 2012, **48**, 252-259.
105. D. S. Yu and L. M. Dai, *J. Phys. Chem. Lett.*, 2010, **1**, 467-470.
106. Y. Zhu, L. Li, C. G. Zhang, G. Casillas, Z. Z. Sun, Z. Yan, G. D. Ruan, Z. W. Peng, A. R. O. Raji, C. Kittrell, R. H. Hauge and J. M. Tour, *Nat. Commun.*, 2012, **3**, 7.
107. K. Y. Li, G. Eres, J. Howe, Y. J. Chuang, X. F. Li, Z. J. Gu, L. T. Zhang, S. S. Xie and Z. W. Pan, *Sci Rep*, 2013, **3**, 4.
108. I. Khan, K. Saeed and I. Khan, *Arab. J. Chem.*, 2019, **12**, 908-931.
109. X. L. Li, Y. Jia and A. Y. Cao, *ACS Nano*, 2010, **4**, 506-512.
110. P. P. Zhang, X. X. Zhang, H. X. Sun, R. H. Liu, B. Wang and Y. H. Lin, *Tetrahedron Lett.*, 2009, **50**, 4455-4458.
111. H. T. Chung, J. H. Won and P. Zelenay, *Nat. Commun.*, 2013, **4**, 5.
112. W. H. Lu, J. H. Li, Y. Q. Sheng, X. S. Zhang, J. M. You and L. X. Chen, *J. Colloid Interface Sci.*, 2017, **505**, 1134-1146.
113. X. H. Peng, J. Y. Chen, J. A. Misewich and S. S. Wong, *Chem. Soc. Rev.*, 2009, **38**, 1076-1098.
114. D. Eder, *Chem. Rev.*, 2010, **110**, 1348-1385.
115. P. Quijano Velasco, V. Karde, Y. Ito, J. Y. Y. Heng, K. Porfyrakis and N. Grobert, *Carbon Trends*, 2022, **6**, 100141.
116. T. Altalhi, A. Mezni, A. Aldalbahi, A. Alrooqi, Y. Attia, A. Santos and D. Losic, *Chem. Phys. Lett.*, 2016, **658**, 92-96.
117. C. Y. Zhi, J. D. Guo, X. D. Bai and E. G. Wang, *J. Appl. Phys.*, 2002, **91**, 5325-5333.
118. N. Saikia and R. C. Deka, *Comput. Theor. Chem.*, 2012, **996**, 11-20.
119. T. Schiros, D. Nordlund, L. Palova, L. Y. Zhao, M. Levendorf, C. Jaye, D. Reichman, J. Park, M. Hybertsen and A. Pasupathy, *ACS Nano*, 2016, **10**, 6574-6584.
120. J. A. Talla and A. A. Ghozlan, *Chin. J. Phys.*, 2018, **56**, 740-746.
121. A. A. Koos, F. Dillon, E. A. Obraztsova, A. Crossley and N. Grobert, *Carbon*, 2010, **48**, 3033-3041.
122. J. S. Zhou, N. Li, F. M. Gao, Y. F. Zhao, L. Hou and Z. M. Xu, *Sci Rep*, 2014, **4**, 6.
123. B. Liu, X. L. Sun, Z. Q. Liao, X. Y. Lu, L. Zhang and G. P. Hao, *Sci Rep*, 2021, **11**, 11.
124. S. Y. Wang, E. Iyyamperumal, A. Roy, Y. H. Xue, D. S. Yu and L. M. Dai, *Angew. Chem.-Int. Edit.*, 2011, **50**, 11756-11760.
125. S. V. Sawant, S. Banerjee, A. W. Patwardhan, J. B. Joshi and K. Dasgupta, *Int. J. Hydrog. Energy*, 2020, **45**, 13406-13413.
126. J. Garel, C. Zhao, R. Popovitz-Biro, D. Golberg, W. L. Wang and E. Joselevich, *Nano Lett.*, 2014, **14**, 6132-6137.

127. A. Einstein, *Annalen Der Physik*, 1905, **17**, 132-148.
128. H. Seyama, M. Soma and B. K. G. Theng, in *Handbook of Clay Science*, eds. F. Bergaya, B. K. G. Theng and G. Lagaly, Elsevier Science Bv, Amsterdam, 2006, vol. 1, pp. 865-878.
129. F. A. Stevie and C. L. Donley, *J. Vac. Sci. Technol. A*, 2020, **38**, 20.
130. G. Greczynski and L. Hultman, *Prog. Mater. Sci.*, 2020, **107**, 46.
131. H. G. J. Moseley, *Philos. Mag.*, 1913, **26**, 1024-1034.
132. S. Nasrazadani and S. Hassani, in *Handbook of Materials Failure Analysis with Case Studies from the Oil and Gas Industry*, eds. A. S. H. Makhlouf and M. Aliofkhazraei, Butterworth-Heinemann, 2016, DOI: https://doi.org/10.1016/B978-0-08-100117-2.00010-8, pp. 39-54.
133. M. S. Dresselhaus, G. Dresselhaus, R. Saito and A. Jorio, *Phys. Rep.-Rev. Sec. Phys. Lett.*, 2005, **409**, 47-99.
134. H. Z. Cui, X. T. Yan, M. Monasterio and F. Xing, *Nanomaterials*, 2017, **7**, 14.
135. A. K. Sharma, R. Sharma, R. Prajapati and S. Chaudhary, *Fuller. Nanotub. Carbon Nanostruct.*, 2016, **24**, 332-338.
136. X. M. Li, H. W. Zhu, J. Q. Wei, K. L. Wang, E. Y. Xu, Z. Li and D. H. Wu, *Appl. Phys. A-Mater. Sci. Process.*, 2009, **97**, 341-344.
137. M. Thommes, K. Kaneko, A. V. Neimark, J. P. Olivier, F. Rodriguez-Reinoso, J. Rouquerol and K. S. W. Sing, *Pure Appl. Chem.*, 2015, **87**, 1051-1069.
138. D. C. Binwal, K. Pramoda, A. Zak, M. Kaur, P. Chithaiah and C. N. R. Rao, *ACS Appl. Energ. Mater.*, 2021, **4**, 2339-2347.
139. T. Zhang, Y. P. Wang, J. Q. Yang, X. X. Huang and G. Wen, *Mater. Sci. Eng. B-Adv. Funct. Solid-State Mater.*, 2015, **199**, 9-14.
140. Y. Zhao, L. J. Yang, S. Chen, X. Z. Wang, Y. W. Ma, Q. Wu, Y. F. Jiang, W. J. Qian and Z. Hu, *J. Am. Chem. Soc.*, 2013, **135**, 1201-1204.
141. Y. H. Li, T. H. Hung and C. W. Chen, *Carbon*, 2009, **47**, 850-855.
142. D. E. Gourari, M. Razafinimanana, M. Monthioux, R. Arenal, F. Valensi, S. Joulie and V. Serin, *Plasma Sci. Technol.*, 2016, **18**, 465-468.
143. L. Liao, K. H. Liu, W. L. Wang, X. D. Bai, E. G. Wang, Y. L. Liu, J. C. Li and C. Liu, *J. Am. Chem. Soc.*, 2007, **129**, 9562-+.
144. H. Tabassum, C. Qu, K. T. Cai, W. Aftab, Z. B. Liang, T. J. Qiu, A. Mahmood, W. Meng and R. Q. Zou, *J. Mater. Chem. A*, 2018, **6**, 21225-21230.
145. N. Grobert, *Mater. Today*, 2006, **9**, 64-64.
146. A. A. Koos, M. Dowling, K. Jurkschat, A. Crossley and N. Grobert, *Carbon*, 2009, **47**, 30-37.
147. F. Liang, M. Tanaka, S. Choi and T. Watanabe, *Carbon*, 2017, **117**, 100-111.
148. S. Cui, P. Scharff, C. Siegmund, D. Schneider, K. Risch, S. Klotzer, L. Spiess, H. Romanus and J. Schawohl, *Carbon*, 2004, **42**, 931-939.
149. D. L. He, Y. N. Liu, T. K. Zhao, J. W. Zhu and G. Yu, *J. Nanopart. Res.*, 2008, **10**, 409-414.
150. Z. J. Li, L. M. Wei and Y. F. Zhang, *Appl. Surf. Sci.*, 2008, **254**, 5247-5251.
151. Y. Miyamoto, A. Rubio, M. L. Cohen and S. G. Louie, *Phys. Rev. B*, 1994, **50**, 4976-4979.
152. O. Stephan, P. M. Ajayan, C. Colliex, P. Redlich, J. M. Lambert, P. Bernier and P. Lefin, *Science*, 1994, **266**, 1683-1685.
153. Z. Wengsieh, K. Cherrey, N. G. Chopra, X. Blase, Y. Miyamoto, A. Rubio, M. L. Cohen, S. G. Louie, A. Zettl and R. Gronsky, *Phys. Rev. B*, 1995, **51**, 11229-11232.
154. K. Suenaga, C. Colliex, N. Demoncy, A. Loiseau, H. Pascard and F. Willaime, *Science*, 1997, **278**, 653-655.

155. M. Kumar and Y. Ando, *J. Nanosci. Nanotechnol.*, 2010, **10**, 3739-3758.
156. A. Szabo, C. Perri, A. Csato, G. Giordano, D. Vuono and J. B. Nagy, *Materials*, 2010, **3**, 3092-3140.
157. Y. H. Yun, V. Shanov, Y. Tu, S. Subramaniam and M. J. Schulz, *J. Phys. Chem. B*, 2006, **110**, 23920-23925.
158. W. L. Wang, X. D. Bai, Z. Xu, S. Liu and E. G. Wang, *Chem. Phys. Lett.*, 2006, **419**, 81-85.
159. B. B. Wang, S. Lee, X. Z. Xu, S. H. Choi, H. Yan, B. Zhang and W. Hao, *Appl. Surf. Sci.*, 2004, **236**, 6-12.
160. F. Le Normand, C. S. Cojocaru, O. Ersen, P. Legagneux, L. Gangloff, C. Fleaca, R. Alexandrescu, F. Dumitrache and I. Morjan, *Appl. Surf. Sci.*, 2007, **254**, 1058-1066.
161. C. Oncel and Y. Yurum, *Fuller. Nanotub. Carbon Nanostruct.*, 2006, **14**, 17-37.
162. A. Ansaldo, M. Haluska, J. Cech, J. C. Meyer, D. Ricci, F. Gatti, E. Di Zitti, S. Cincotti and S. Roth, *Physica E*, 2007, **37**, 6-10.
163. E. Terrado, M. Redrado, E. Munoz, W. K. Maser, A. M. Benito and M. T. Martinez, *Diam. Relat. Mat.*, 2006, **15**, 1059-1063.
164. G. F. Malgas, C. J. Arendse, N. P. Cele and F. R. Cummings, *J. Mater. Sci.*, 2008, **43**, 1020-1025.
165. A. A. Muataz, F. Ahmadun, C. Guan, E. Mahdi and A. Rinaldi, *Nano*, 2006, **1**, 251-257.
166. K. L. Choy, *Prog. Mater. Sci.*, 2003, **48**, 57-170.
167. C. H. See and A. T. Harris, *Ind. Eng. Chem. Res.*, 2007, **46**, 997-1012.
168. W. L. Wang, X. D. Bai, K. H. Liu, Z. Xu, D. Golberg, Y. Bando and E. G. Wang, *J. Am. Chem. Soc.*, 2006, **128**, 6530-6531.
169. S. Y. Kim, J. Park, H. C. Choi, J. P. Ahn, J. Q. Hou and H. S. Kang, *J. Am. Chem. Soc.*, 2007, **129**, 1705-1716.
170. M. G. S. Bernd, S. R. Braganca, N. Heck and L. C. P. da Silva, *J. Mater. Res. Technol-JMRT*, 2017, **6**, 171-177.
171. K. Z. Li, H. J. Zhang, Y. F. Zheng, G. Q. Yuan, Q. L. Jia and S. W. Zhang, *Nanomaterials*, 2020, **10**, 12.
172. P. Y. K. Wang, Y. J. Zheng, T. Inoue, R. Xiang, A. Shawky, M. Watanabe, A. Anisimov, E. I. Kauppinen, S. Chiashi and S. Maruyama, *ACS Nano*, 2020, **14**, 4298-4305.
173. Q. L. Wei, X. Tong, G. X. Zhang, J. L. Qiao, Q. J. Gong and S. H. Sun, *Catalysts*, 2015, **5**, 1574-1602.
174. M. Vikkisk, I. Kruusenberg, S. Ratso, U. Joost, E. Shulga, I. Kink, P. Rauwel and K. Tammeveski, *RSC Advances*, 2015, **5**, 59495-59505.
175. Q. Yang, Y. D. Chen, X. G. Duan, S. K. Zhou, Y. Niu, H. Q. Sun, L. J. Zhi and S. B. Wang, *Appl. Catal. B-Environ.*, 2020, **276**, 10.
176. D. Golberg, Y. Bando, K. Kurashima and T. Sato, *Chem. Phys. Lett.*, 2000, **323**, 185-191.
177. W. Q. Han, W. Mickelson, J. Cumings and A. Zettl, *Appl. Phys. Lett.*, 2002, **81**, 1110-1112.
178. D. Golberg and Y. Bando, *Appl. Phys. Lett.*, 2001, **79**, 415-417.
179. D. Golberg, Y. Bando, M. Mitome, K. Kurashima, T. Sato, N. Grobert, M. Reyes-Reyes, H. Terrones and M. Terrones, *Physica B*, 2002, **323**, 60-66.
180. C. W. Chang, W. Q. Han and A. Zettl, *Appl. Phys. Lett.*, 2005, **86**, 3.
181. W. H. Chiang, C. Y. Hsieh, S. C. Lo, Y. C. Chang, T. Kawai and Y. Nonoguchi, *Carbon*, 2016, **109**, 49-56.

182. X. F. Zhang, P. Q. Yan, J. K. Xu, F. Li, F. Herold, B. J. M. Etzold, P. Wang, D. S. Su, S. Lin, W. Qi and Z. L. Xie, *Sci. Adv.*, 2020, **6**, 9.
183. J. T. Jin, F. P. Pan, L. H. Jiang, X. G. Fu, A. M. Liang, Z. Y. Wei, J. Y. Zhang and G. Q. Sun, *ACS Nano*, 2014, **8**, 3313-3321.
184. S. S. Meysami, A. A. Koos, F. Dillon and N. Grobert, *Carbon*, 2013, **58**, 159-169.
185. J. Zhang, J. J. Zhang, F. He, Y. J. Chen, J. W. Zhu, D. L. Wang, S. C. Mu and H. Y. Yang, *Nano-Micro Lett.*, 2021, **13**, 30.
186. Y. Liu, V. Khavrus, T. Lehmann, H. L. Yang, L. Stepien, M. Greifzu, S. Oswald, T. Gemming, V. Bezugly and G. Cuniberti, *ACS Appl. Energ. Mater.*, 2020, **3**, 2556-2564.
187. C. Huber, S. S. Jahromy, F. Birkelbach, J. Weber, C. Jordan, M. Schreiner, M. Harasek and F. Winter, *Energy Sci. Eng.*, 2020, **8**, 1650-1666.
188. R. Vonburg, *J. Appl. Toxicol.*, 1992, **12**, 149-152.
189. B. G. Sumpter, V. Meunier, J. M. Romo-Herrera, E. Cruz-Silva, D. A. Cullen, H. Terrones, D. J. Smith and M. Terrones, *ACS Nano*, 2007, **1**, 369-375.
190. Y. J. Li, M. Yang, B. B. Xu, Q. L. Sun, W. Zhang, Y. J. Zhang and F. B. Meng, *Appl. Surf. Sci.*, 2018, **450**, 284-291.
191. W. Yan, Y. Zhang, H. W. Sun, S. W. Liu, Z. G. Chi, X. D. Chen and J. R. Xu, *J. Mater. Chem. A*, 2014, **2**, 20958-20965.
192. R. Blume, D. Rosenthal, J. P. Tessonnier, H. N. Li, A. Knop-Gericke and R. Schlogl, *ChemCatChem*, 2015, **7**, 2871-2881.
193. G. X. Zhang, S. H. Sun, D. Q. Yang, J. P. Dodelet and E. Sacher, *Carbon*, 2008, **46**, 196-205.
194. N. Hellgren, R. T. Haasch, S. Schmidt, L. Hultman and I. Petrov, *Carbon*, 2016, **108**, 242-252.
195. P. Ayala, J. Reppert, M. Grobosch, M. Knupfer, T. Pichler and A. M. Rao, *Appl. Phys. Lett.*, 2010, **96**, 3.
196. L. G. Jacobsohn, R. K. Schulze, M. da Costa and M. Nastasi, *Surf. Sci.*, 2004, **572**, 418-424.
197. S. H. Lee, H. Jeong, O. F. NgomeOkello, S. Y. Xiao, S. Moon, D. Kim, G. Y. Kim, J. L. Lo, Y. C. Peng, B. M. Cheng, H. Miyake, S. Y. Choi and J. K. Kim, *Sci Rep*, 2019, **9**, 8.
198. Z. H. Sheng, H. L. Gao, W. J. Bao, F. B. Wang and X. H. Xia, *J. Mater. Chem.*, 2012, **22**, 390-395.
199. M. Wang, Y. Yang, Z. Z. Yang, L. Gu, Q. W. Chen and Y. Yu, *Adv. Sci.*, 2017, **4**, 8.
200. O. Soares, R. P. Rocha, J. J. M. Orfao, M. F. R. Pereira and J. L. Figueiredo, *C-J. Carbon Res.*, 2019, **5**, 14.
201. A. F. Khan, M. P. Down, G. C. Smith, C. W. Foster and C. E. Banks, *J. Mater. Chem. A*, 2017, **5**, 4103-4113.
202. A. Ishitani, *Carbon*, 1981, **19**, 269-275.
203. R. Du, N. Zhang, J. H. Zhu, Y. Wang, C. Y. Xu, Y. Hu, N. N. Mao, H. Xu, W. J. Duan, L. Zhuang, L. T. Qu, Y. L. Hou and J. Zhang, *Small*, 2015, **11**, 3903-3908.
204. Y. J. Yao, H. Chen, J. C. Qin, G. D. Wu, C. Lian, J. Zhang and S. B. Wang, *Water Res.*, 2016, **101**, 281-291.
205. S. Kundu, T. C. Nagaiah, W. Xia, Y. M. Wang, S. Van Dommele, J. H. Bitter, M. Santa, G. Grundmeier, M. Bron, W. Schuhmann and M. Muhler, *J. Phys. Chem. C*, 2009, **113**, 14302-14310.
206. K. Fujisawa, T. Tojo, H. Muramatsu, A. L. Elias, S. M. Vega-Diaz, F. Tristan-Lopez, J. H. Kim, T. Hayashi, Y. A. Kim, M. Endo and M. Terrones, *Nanoscale*, 2011, **3**, 4359-4364.

207. H. Liu, Y. Zhang, R. Y. Li, X. L. Sun and H. Abou-Rachid, *J. Nanopart. Res.*, 2012, **14**, 8.
208. H. Chen, Y. Yang, Z. Hu, K. F. Huo, Y. W. Ma, Y. Chen, X. S. Wang and Y. N. Lu, *J. Phys. Chem. B*, 2006, **110**, 16422-16427.
209. K. Ranganathan, A. Morais, I. Nongwe, C. Longo, A. F. Nogueira and N. J. Coville, *J. Mol. Catal. A-Chem.*, 2016, **422**, 165-174.
210. M. Ayiania, A. J. R. Hensley, K. Groden, M. Garcia-Perez and J. S. McEwen, *Carbon*, 2019, **152**, 715-726.
211. T. Sharifi, G. Hu, X. E. Jia and T. Wagberg, *ACS Nano*, 2012, **6**, 8904-8912.
212. A. Ferrari, D. Basko !!! INVALID CITATION !!! 77.
213. H. Liu, Y. Zhang, R. Y. Li, X. L. Sun, S. Desilets, H. Abou-Rachid, M. Jaidann and L. S. Lussier, *Carbon*, 2010, **48**, 1498-1507.
214. E. A. Arkhipova, A. S. Ivanov, N. E. Strokova, S. A. Chernyak, A. V. Shumyantsev, K. I. Maslakov, S. V. Savilov and V. V. Lunin, *Carbon*, 2017, **125**, 20-31.
215. J. X. Shan, X. Q. Sun, S. Y. Zheng, T. D. Wang, X. W. Zhang and G. Z. Li, *Carbon*, 2019, **146**, 60-69.
216. J. Hansson, A. Nylander, M. Flygare, K. Svensson, L. L. Ye, T. Nilsson, Y. F. Fu and J. Liu, *Nanotechnology*, 2020, **31**, 11.
217. L. E. Jones and P. A. Thrower, *Carbon*, 1991, **29**, 251-269.
218. X. L. Zheng, H. N. Chen, Q. Li, Y. L. Yang, Z. H. Wei, Y. Bai, Y. C. Qiu, D. Zhou, K. S. Wong and S. H. Yang, *Nano Lett.*, 2017, **17**, 2496-2505.
219. A. Yoshida, Y. Kaburagi and Y. Hishiyama, *Carbon*, 2006, **44**, 2333-2335.
220. W. Lin, K. S. Moon, S. J. Zhang, Y. Ding, J. T. Shang, M. X. Chen and C. P. Wong, *ACS Nano*, 2010, **4**, 1716-1722.
221. I. Hasan, S. Walia, K. H. Alharbi, M. Abu Khanjer, A. Alsalme and R. A. Khan, *J. Mol. Liq.*, 2020, **317**, 11.
222. M. R. Johan and L. S. Moh, *Int. J. Electrochem. Sci.*, 2013, **8**, 1047-1056.
223. N. G. Tsierkezos, U. Ritter, Y. N. Thaha, A. Knauer, D. Fernandes, A. Kelarakis and E. K. McCarthy, *Chem. Phys. Lett.*, 2018, **710**, 157-167.
224. B. Anand, R. Podila, P. Ayala, L. Oliveira, R. Philip, S. S. S. Sai, A. A. Zakhidov and A. M. Rao, *Nanoscale*, 2013, **5**, 7271-7276.
225. C. A. de los Reyes, K. L. W. Mitra, A. D. Smith, S. Yazdi, A. Loredo, F. J. Frankovsky, E. Ringe, M. Pasquali and A. A. Marti, *ACS Appl. Nano Mater.*, 2018, **1**, 2421-2429.
226. Y. B. Yan, J. W. Miao, Z. H. Yang, F. X. Xiao, H. B. Yang, B. Liu and Y. H. Yang, *Chem. Soc. Rev.*, 2015, **44**, 3295-3346.
227. A. K. Sharma, A. K. Sharma and R. Sharma, *Bull. Mat. Sci.*, 2021, **44**, 8.
228. W. Huang, Y. Wang, G. H. Luo and F. Wei, *Carbon*, 2003, **41**, 2585-2590.
229. A. Ramos, I. Cameán and A. B. García, *Carbon*, 2013, **59**, 2-32.
230. W. Q. Han, Y. Bando, K. Kurashima and T. Sato, *Chem. Phys. Lett.*, 1999, **299**, 368-373.
231. Y. Zhang, H. Gu and S. Iijima, *Appl. Phys. Lett.*, 1998, **73**, 3827-3829.
232. H. O. Pierson, in *Handbook of Carbon, Graphite, Diamonds and Fullerenes*, William Andrew Publishing, Oxford, 1993, ch. 2 - The Element Carbon, pp. 11-42.
233. G. Rayner-Canham and T. Overton, in *Descriptive Inorganic Chemistry*, W. H. Freeman and Co., New York, 5th edn., 2010, ch. Appendix 3
234. H. Huang, C. H. Liu, Y. Wu and S. S. Fan, *Adv. Mater.*, 2005, **17**, 1652-+.
235. A. Bianco, R. Sainz, S. P. Li, H. Dumortier, L. Lacerda, K. Kostarelos, S. Giordani and M. Prato, *Biomedical Applications of Functionalised Carbon Nanotubes*, Springer, Dordrecht, 2008.

236. L. M. Peng, Z. Y. Zhang and S. Wang, *Mater. Today*, 2014, **17**, 433-442.
237. P. T. Yin, S. Shah, M. Chhowalla and K. B. Lee, *Chem. Rev.*, 2015, **115**, 2483-2531.
238. J. Wei, R. Lv, N. Guo, H. G. Wang, X. Bai, A. Mathkar, F. Y. Kang, H. W. Zhu, K. L. Wang, D. H. Wu, R. Vajtai and P. M. Ajayan, *Nanotechnology*, 2012, **23**, 5.
239. N. V. Perez-Aguilar, E. Munoz-Sandoval, P. E. Diaz-Flores and J. R. Rangel-Mendez, *J. Nanopart. Res.*, 2010, **12**, 467-480.
240. S. Mallakpour and E. Khadem, *Chem. Eng. J.*, 2016, **302**, 344-367.
241. X. J. Fan, G. Z. Jiao, L. Gao, P. F. Jin and X. Li, *J. Mat. Chem. B*, 2013, **1**, 2658-2664.
242. H. Z. Zhang, J. S. Qiu, C. H. Liang, Z. L. Li, X. N. Wang, Y. P. Wang, Z. C. Feng and C. Li, *Catal. Lett.*, 2005, **101**, 211-214.
243. C. Liu, C. C. Wang, C. C. Kei, Y. C. Hsueh and T. P. Perng, *Small*, 2009, **5**, 1535-1538.
244. S. Mallakpour and S. Soltanian, *RSC Adv.*, 2016, **6**, 109916-109935.
245. D. J. Guo and H. L. Li, *Electrochem. Commun.*, 2004, **6**, 999-1003.
246. Z. C. Meng, B. Liu, J. B. Zheng, Q. L. Sheng and H. F. Zhang, *Microchim. Acta*, 2011, **175**, 251-257.
247. R. Sharma and K. K. Kar, *Electrochim. Acta*, 2015, **156**, 199-206.
248. G. G. Wildgoose, C. E. Banks and R. G. Compton, *Small*, 2006, **2**, 182-193.
249. Y. Y. Liang, H. L. Wang, P. Diao, W. Chang, G. S. Hong, Y. G. Li, M. Gong, L. M. Xie, J. G. Zhou, J. Wang, T. Z. Regier, F. Wei and H. J. Dai, *J. Am. Chem. Soc.*, 2012, **134**, 15849-15857.
250. Y. D. Li, X. Lu, H. K. Wang, C. Xie, G. Yang and C. M. Niu, *Electrochim. Acta*, 2015, **178**, 778-785.
251. B. Xue, P. Chen, Q. Hong, J. Y. Lin and K. L. Tan, *J. Mater. Chem.*, 2001, **11**, 2378-2381.
252. H. Huang, W. K. Zhang, M. C. Li, Y. P. Gan, J. H. Chen and Y. F. Kuang, *J. Colloid Interface Sci.*, 2005, **284**, 593-599.
253. E. Unger, G. S. Duesberg, M. Liebau, A. P. Graham, R. Seidel, F. Kreupl and W. Hoenlein, *Appl. Phys. A-Mater. Sci. Process.*, 2003, **77**, 735-738.
254. D. H. Marsh, G. A. Rance, R. J. Whitby, F. Giustiniano and A. N. Khlobystov, *J. Mater. Chem.*, 2008, **18**, 2249-2256.
255. P. Xu, D. X. Cui, B. F. Pan, F. Gao, R. He, Q. Li, T. Huang, C. C. Bao and H. Yang, *Appl. Surf. Sci.*, 2008, **254**, 5236-5240.
256. H. Nakajima, T. Morimoto, Y. Zhou, K. Kobashi, S. Ata, T. Yamada and T. Okazaki, *Nanoscale*, 2019, **11**, 21487-21492.
257. H. F. Zhou, C. Zhang, H. Q. Li and Z. J. Du, *J. Polym. Sci. Pol. Chem.*, 2010, **48**, 4697-4703.
258. K. Y. Jiang, A. Eitan, L. S. Schadler, P. M. Ajayan, R. W. Siegel, N. Grobert, M. Mayne, M. Reyes-Reyes, H. Terrones and M. Terrones, *Nano Lett.*, 2003, **3**, 275-277.
259. V. Georgakilas, V. Tzitzios, D. Gournis and D. Petridis, *Chem. Mat.*, 2005, **17**, 1613-1617.
260. A. V. Ellis, K. Vjayamohanan, R. Goswaimi, N. Chakrapani, L. S. Ramanathan, P. M. Ajayan and G. Ramanath, *Nano Lett.*, 2003, **3**, 279-282.
261. T. Wang, X. G. Hu, X. H. Qu and S. J. Dong, *J. Phys. Chem. B*, 2006, **110**, 6631-6636.
262. X. L. Li, J. D. Thompson, Y. Y. Zhang, C. I. Brady, G. F. Zou, N. H. Mack, D. Williams, J. G. Duque, Q. X. Jia and S. K. Doorn, *Nanoscale*, 2011, **3**, 668-673.
263. G. A. Rance and A. N. Khlobystov, *Phys. Chem. Chem. Phys.*, 2010, **12**, 10775-10780.

264. G. A. Rance, D. H. Marsh, S. J. Bourne, T. J. Reade and A. N. Khlobystov, *ACS Nano*, 2010, **4**, 4920-4928.
265. G. A. Rance and A. N. Khlobystov, *Dalton Trans.*, 2014, **43**, 7400-7406.
266. S. D. Bergin, Z. Y. Sun, D. Rickard, P. V. Streich, J. P. Hamilton and J. N. Coleman, *ACS Nano*, 2009, **3**, 2340-2350.
267. L. Cao, Y. Wang, Q. Zhu, L. L. Fan, Y. Wu, Z. H. Li, S. X. Xiong and F. Gu, *ACS Appl. Mater. Interfaces*, 2022, **14**, 17249-17258.
268. T. J. Qiu, J. Q. Cheng, Z. B. Liang, H. Tabassum, J. M. Shi, Y. Q. Tang, W. H. Guo, L. R. Zheng, S. Gao, S. Z. Xu and R. Q. Zou, *Appl. Catal. B-Environ.*, 2022, **316**, 12.
269. Y. Wang, F. Gu, L. Cao, L. L. Fan, T. J. Hou, Q. Zhu, Y. Wu and S. X. Xiong, *Int. J. Hydrog. Energy*, 2022, **47**, 20894-20904.
270. X. F. Li, J. Y. Liu, J. Zhang, S. Wu, D. W. Zhang and J. L. Shui, *Chem. Eng. J.*, 2021, **411**, 8.
271. Y. O. Yesilbag, F. N. T. Yesilbag, A. Huseyin and M. Ertugrul, *J. Energy Storage*, 2022, **52**, 13.
272. K. Mandel, F. Dillon, A. A. Koos, Z. Aslam, F. Cullen, H. Bishop, A. Crossley and N. Grobert, *RSC Adv.*, 2012, **2**, 3748-3752.
273. V. K. Lamer and R. H. Dinegar, *J. Am. Chem. Soc.*, 1950, **72**, 4847-4854.
274. F. B. Effenberger, R. A. Couto, P. K. Kiyohara, G. Machado, S. H. Masunaga, R. F. Jardim and L. M. Rossi, *Nanotechnology*, 2017, **28**, 8.
275. A. S. Teja and P. Y. Koh, *Prog. Cryst. Growth Charact. Mater.*, 2009, **55**, 22-45.
276. W. Kim, C. Y. Suh, S. W. Cho, K. M. Roh, H. Kwon, K. Song and I. J. Shon, *Talanta*, 2012, **94**, 348-352.
277. S. P. Schwaminger, C. Syhr and S. Berensmeier, *Crystals*, 2020, **10**, 12.
278. S. J. Iyengar, M. Joy, C. K. Ghosh, S. Dey, R. K. Kotnala and S. Ghosh, *RSC Adv.*, 2014, **4**, 64919-64929.
279. V. Patsula, E. Petrovsky, J. Kovarova, R. Konefal and D. Horak, *Colloid Polym. Sci.*, 2014, **292**, 2097-2110.
280. A. Di Crescenzo, V. Ettorre and A. Fontana, *Beilstein J. Nanotechnol.*, 2014, **5**, 1675-1690.
281. R. Sanchez-Salas, S. Kashina, R. Galindo, A. K. Cuentas-Gallegos, N. Rayon-Lopez, M. Miranda-Hernandez, R. Fuentes-Ramirez, F. Lopez-Urias and E. Munoz-Sandoval, *Carbon*, 2021, **183**, 743-762.
282. A. Zahoor, M. Christy, Y. J. Hwang, Y. R. Lim, P. Kim and K. S. Nahm, *Appl. Catal. B-Environ.*, 2014, **147**, 633-641.
283. K. Ikemoto, S. Yang, H. Naito, M. Kotani, S. Sato and H. Isobe, *Nat. Commun.*, 2020, **11**, 6.
284. S. Detriche, G. Zorzini, J. F. Colomer, A. Fonseca and J. B. Nagy, *J. Nanosci. Nanotechnol.*, 2008, **8**, 6082-6092.
285. H. J. Um, K. Lee, Y. S. Cho, Y. S. Kim, T. Kim and C. R. Park, *Phys. Chem. Chem. Phys.*, 2014, **16**, 17466-17472.
286. C. M. Hansen, *Hansen Solubility Parameters: A User's Handbook, Second Edition*, CRC Press, 2007.
287. C. L. Yaws and P. C. Richmond, in *Thermophysical Properties of Chemicals and Hydrocarbons*, ed. C. L. Yaws, William Andrew Publishing, Norwich, NY, 2009, pp. 686-781.
288. M. J. O'Connell, P. Boul, L. M. Ericson, C. Huffman, Y. H. Wang, E. Haroz, C. Kuper, J. Tour, K. D. Ausman and R. E. Smalley, *Chem. Phys. Lett.*, 2001, **342**, 265-271.
289. Y. Shen, M. Y. Gee and A. B. Greytak, *Chem. Commun.*, 2017, **53**, 827-841.

290. H. M. Xu, Y. Q. Sang, B. Xu, L. Zhang, L. Zhang and H. Xu, *ACS Appl. Nano Mater.*, 2020, **3**, 12169-12177.
291. S. H. Qin, D. Q. Qin, W. T. Ford, D. E. Resasco and J. E. Herrera, *Macromolecules*, 2004, **37**, 752-757.
292. P. Q. Velasco, K. Porfyrakis and N. Grobert, *Phys. Chem. Chem. Phys.*, 2019, **21**, 5331-5334.
293. W. An and C. H. Turner, *J. Phys. Chem. C*, 2009, **113**, 7069-7078.
294. S. J. Kim, Y. J. Park, E. J. Ra, K. K. Kim, K. H. An, Y. H. Lee, J. Y. Choi, C. H. Park, S. K. Doo, M. H. Park and C. W. Yang, *Appl. Phys. Lett.*, 2007, **90**, 3.
295. H. M. Alshammari, A. S. Alshammari, J. R. Humaidi, S. A. Alzahrani, M. S. Alhumaimess, O. F. Aldosari and H. M. A. Hassan, *Processes*, 2020, **8**, 11.
296. S. Nardecchia, D. Carriazo, M. L. Ferrer, M. C. Gutierrez and F. del Monte, *Chem. Soc. Rev.*, 2013, **42**, 794-830.
297. M. H. Miao, *Particuology*, 2013, **11**, 378-393.
298. S. X. Qu, Y. G. Dai, D. X. Zhang, Q. W. Li, T. W. Chou and W. B. Lyu, *Funct. Compos. Struct.*, 2020, **2**, 35.
299. S. Y. Huang, Q. W. Li, Y. T. Zhu and P. S. Fedkiw, *J. Appl. Electrochem.*, 2017, **47**, 105-115.
300. Z. Y. Cao and B. Q. Wei, *Energy Environ. Sci.*, 2013, **6**, 3183-3201.
301. K. J. Wu, Y. T. Niu, Y. Y. Zhang, Z. Z. Yong and Q. W. Li, *Compos. Pt. A-Appl. Sci. Manuf.*, 2021, **144**, 18.
302. S. K. Samanta, M. Fritsch, U. Scherf, W. Gomulya, S. Z. Bisri and M. A. Loi, *Accounts Chem. Res.*, 2014, **47**, 2446-2456.
303. A. R. Boccaccini, J. Cho, J. A. Roether, B. J. C. Thomas, E. J. Minay and M. S. P. Shaffer, *Carbon*, 2006, **44**, 3149-3160.
304. W. B. Choi, Y. W. Jin, H. Y. Kim, S. J. Lee, M. J. Yun, J. H. Kang, Y. S. Choi, N. S. Park, N. S. Lee and J. M. Kim, *Appl. Phys. Lett.*, 2001, **78**, 1547-1549.
305. B. Gao, G. Z. Yue, Q. Qiu, Y. Cheng, H. Shimoda, L. Fleming and O. Zhou, *Adv. Mater.*, 2001, **13**, 1770-1773.
306. B. J. C. Thomas, A. R. Boccaccini and M. S. P. Shaffer, *J. Am. Ceram. Soc.*, 2005, **88**, 980-982.
307. C. Y. Nie, L. K. Pan, H. B. Li, T. Q. Chen, T. Lu and Z. Sun, *J. Electroanal. Chem.*, 2012, **666**, 85-88.
308. J. Cho, K. Konopka, K. Rozniatowski, E. Garcia-Lecina, M. S. P. Shaffer and A. R. Boccaccini, *Carbon*, 2009, **47**, 58-67.
309. J. L. Rigueur, S. A. Hasan, S. V. Mahajan and J. H. Dickerson, *Carbon*, 2010, **48**, 4090-4099.
310. J. Biswas, J. S. Rottman-Yang, I. Gonzalo-JuanA and J. H. Dickerson, *J. Electrochem. Soc.*, 2012, **159**, K103-K106.
311. J. Ballentine, Chemical Routes to Improved Nanomaterial Suspensions for Electrophoretic Deposition - DPhil Thesis, University of Oxford, 2023.
312. A. W. Xiao, K. Evers, M. Tkaczyk, R. S. Jones, C. Saxby, K. Dragnevski and N. Grobert, *ACS Appl. Nano Mater.*, 2019, **2**, 5190-5199.
313. D. Wang, P. C. Song, C. H. Liu, W. Wu and S. S. Fan, *Nanotechnology*, 2008, **19**, 6.
314. B. Ribeiro, E. C. Botelho, M. L. Costa and C. F. Bandeira, *Polimeros*, 2017, **27**, 247-255.
315. J. Liu, A. G. Rinzler, H. J. Dai, J. H. Hafner, R. K. Bradley, P. J. Boul, A. Lu, T. Iverson, K. Shelimov, C. B. Huffman, F. Rodriguez-Macias, Y. S. Shon, T. R. Lee, D. T. Colbert and R. E. Smalley, *Science*, 1998, **280**, 1253-1256.

316. A. G. Rinzler, J. Liu, H. Dai, P. Nikolaev, C. B. Huffman, F. J. Rodriguez-Macias, P. J. Boul, A. H. Lu, D. Heymann, D. T. Colbert, R. S. Lee, J. E. Fischer, A. M. Rao, P. C. Eklund and R. E. Smalley, *Appl. Phys. A-Mater. Sci. Process.*, 1998, **67**, 29-37.
317. S. M. Cooper, H. F. Chuang, M. Cinke, B. A. Cruden and M. Meyyappan, *Nano Lett.*, 2003, **3**, 189-192.
318. Z. Spitalsky, C. Aggelopoulos, G. Tsoukleri, C. Tsakiroglou, J. Parthenios, S. Georga, C. Krontiras, D. Tasis, K. Papagelis and C. Galiotis, *Mater. Sci. Eng. B-Adv. Funct. Solid-State Mater.*, 2009, **165**, 135-138.
319. J. L. Bahr, J. P. Yang, D. V. Kosynkin, M. J. Bronikowski, R. E. Smalley and J. M. Tour, *J. Am. Chem. Soc.*, 2001, **123**, 6536-6542.
320. S. Roy, V. Jain, R. Bajpai, P. Ghosh, A. S. Pente, B. P. Singh and D. S. Misra, *J. Phys. Chem. C*, 2012, **116**, 19025-19031.
321. Z. Wang, Z. Y. Liang, B. Wang, C. Zhang and L. Kramer, *Compos. Pt. A-Appl. Sci. Manuf.*, 2004, **35**, 1225-1232.
322. S. Y. Chew, S. H. Ng, J. Z. Wang, P. Novak, F. Krumeich, S. L. Chou, J. Chen and H. K. Liu, *Carbon*, 2009, **47**, 2976-2983.
323. K. So, Making and Manipulating Nanowires inside Carbon Nanotubes - DPhil Thesis, Univeristy of Oxford, 2017.
324. R. Arrigo, R. Teresi, C. Gambarotti, F. Parisi, G. Lazzara and N. T. Dintcheva, *Materials*, 2018, **11**, 14.
325. F. Hennrich, R. Krupke, K. Arnold, J. A. R. Stutz, S. Lebedkin, T. Koch, T. Schimmel and M. M. Kappes, *J. Phys. Chem. B*, 2007, **111**, 1932-1937.
326. L. Dumee, K. Sears, J. Schutz, N. Finn, M. Duke and S. Gray, *Nanomaterials*, 2013, **3**, 70-85.
327. V. Babenko, G. Lane, A. A. Koos, A. T. Murdock, K. So, J. Britton, S. S. Meysami, J. Moffat and N. Grobert, *Sci Rep*, 2017, **7**, 12.
328. S. Niyogi, M. A. Hamon, H. Hu, B. Zhao, P. Bhowmik, R. Sen, M. E. Itkis and R. C. Haddon, *Accounts Chem. Res.*, 2002, **35**, 1105-1113.
329. L. Y. Liang, W. Y. Xie, S. X. Fang, F. He, B. H. Yin, C. Tlili, D. Q. Wang, S. Qiu and Q. W. Li, *J. Mater. Chem. C*, 2017, **5**, 11339-11368.
330. Y. Liu, X. Z. Wang, Y. F. Dong, Z. Y. Wang, Z. B. Zhao and J. S. Qiu, *J. Mater. Chem. A*, 2014, **2**, 16832-16835.
331. V. Datsyuk, M. Kalyva, K. Papagelis, J. Parthenios, D. Tasis, A. Siokou, I. Kallitsis and C. Galiotis, *Carbon*, 2008, **46**, 833-840.
332. K. A. Wepasnick, B. A. Smith, K. E. Schrote, H. K. Wilson, S. R. Diegelmann and D. H. Fairbrother, *Carbon*, 2011, **49**, 24-36.
333. M. G. Trulli, E. Sardella, F. Palumbo, G. Palazzo, L. C. Giannossa, A. Mangone, R. Comparelli, S. Musso and P. Favia, *J. Colloid Interface Sci.*, 2017, **491**, 255-264.
334. I. D. Rosca, F. Watari, M. Uo and T. Akaska, *Carbon*, 2005, **43**, 3124-3131.
335. S. Peponas, M. Benlahsen and M. Guedda, *J. Appl. Phys.*, 2009, **106**, 8.
336. Y. Li, X. B. Zhang, J. H. Luo, W. Z. Huang, J. P. Cheng, Z. Q. Luo, T. Li, F. Liu, G. L. Xu, X. X. Ke, L. Li and H. J. Geise, *Nanotechnology*, 2004, **15**, 1645-1649.
337. H. Yu, Y. G. Jin, F. Peng, H. J. Wang and J. Yang, *J. Phys. Chem. C*, 2008, **112**, 6758-6763.
338. R. Jones, Designing Boron Nitride Nanotubes and their Macroscopic Assemblies via Sacrificial Templating - DPhil DPhil, University of Oxford, 2021.
339. Q. K. Wu, W. Wongwiriyapan, J. H. Park, S. Park, S. J. Jung, T. Jeong, S. Lee, Y. H. Lee and Y. J. Song, *Curr. Appl. Phys.*, 2016, **16**, 1175-1191.
340. L. L. Chen, H. H. Ye and Y. Gogotsi, *J. Am. Ceram. Soc.*, 2004, **87**, 147-151.
341. R. S. Jones, B. Maciejewska and N. Grobert, *Nanoscale Adv.*, 2020, **2**, 4996-5014.

342. W. L. Wang, J. Q. Bi, W. X. Sun, H. L. Zhu, J. J. Xu, M. T. Zhao and Y. J. Bai, *Mater. Chem. Phys.*, 2010, **122**, 129-132.
343. D. Xia, H. Li, P. Huang, J. Mannering, U. Zafar, D. Baker and R. Menzel, *J. Mater. Chem. A*, 2019, **7**, 24027-24037.
344. W. Yang, Y. F. Wang, Y. Li, C. Gao, X. J. Tian, N. Wu, Z. S. Geng, S. Che, F. Yang and Y. F. Li, *Compos. Pt. B-Eng.*, 2021, **224**, 9.
345. A. Anson-Casaos, J. M. Gonzalez-Dominguez, E. Terrado and M. T. Martinez, *Carbon*, 2010, **48**, 1480-1488.
346. C. X. Liu and J. W. Choi, *Nanomaterials*, 2012, **2**, 329-347.
347. S. Giordani, S. D. Bergin, V. Nicolosi, S. Lebedkin, M. M. Kappes, W. J. Blau and J. N. Coleman, *J. Phys. Chem. B*, 2006, **110**, 15708-15718.
348. W. Dai, J. Wang, X. H. Gan, H. Wang, X. G. Su and C. Xi, *Colloid Surf. A-Physicochem. Eng. Asp.*, 2020, **589**, 11.
349. P. Castel, M. Cano, W. K. Maser and A. M. Benito, *Compos. Sci. Technol.*, 2013, **80**, 101-107.
350. Z. Sun, V. Nicolosi, D. Rickard, S. D. Bergin, D. Aherne and J. N. Coleman, *J. Phys. Chem. C*, 2008, **112**, 10692-10699.
351. M. Dutta, V. Nicolosi, E. Obratzsova, A. A. Koos, A. Crossley and N. Groben, *Mater. Express*, 2011, **1**, 201-209.
352. J. G. Park, J. Smithyman, C. Y. Lin, A. Cooke, A. W. Kismarahardja, S. Li, R. Liang, J. S. Brooks, C. Zhang and B. Wang, *J. Appl. Phys.*, 2009, **106**, 6.
353. F. Pourfayaz, Y. Mortazavi, A. A. Khodadadi, S. H. Jafari, S. Boroun and M. V. Naseh, *Appl. Surf. Sci.*, 2014, **295**, 66-70.
354. W. Dalina, M. Mariatti and S. H. Tan, *Polym. Bull.*, 2019, **76**, 2801-2817.
355. S. Q. Song, H. X. Yang, R. C. Rao, H. D. Liu and A. M. Zhang, *Catal. Commun.*, 2010, **11**, 783-787.
356. H. Rennhofer and B. Zanghellini, *Nanomaterials*, 2021, **11**, 27.
357. J. W. Zhang, D. Z. Jiang and H. X. Peng, *Microporous Mesoporous Mat.*, 2014, **184**, 127-133.
358. S. C. Her and W. C. Hsu, *Sensors*, 2020, **20**, 13.
359. P. Slobodian, P. Riha and P. Saha, *Carbon*, 2012, **50**, 3446-3453.
360. X. S. Yang, J. Lee, L. X. Yuan, S. R. Chae, V. K. Peterson, A. I. Minett, Y. B. Yin and A. T. Harris, *Carbon*, 2013, **59**, 160-166.
361. A. A. Alshahrani, H. Al-Zoubi, L. D. Nghiem and M. I. H. Panhuis, *Desalination*, 2017, **418**, 60-70.
362. H. Wang, J. Jia, P. F. Song, Q. Wang, D. B. Li, S. X. Min, C. X. Qian, L. Wang, Y. F. Li, C. Ma, T. Wu, J. Y. Yuan, M. Antonietti and G. A. Ozin, *Angew. Chem.-Int. Edit.*, 2017, **56**, 7847-7852.
363. K. S. W. Sing, *Pure Appl. Chem.*, 1982, **54**, 2201-2218.
364. S. Brunauer, P. H. Emmett and E. Teller, *J. Am. Chem. Soc.*, 1938, **60**, 309-319.
365. E. P. Barrett, L. G. Joyner and P. P. Halenda, *J. Am. Chem. Soc.*, 1951, **73**, 373-380.
366. M. R. Elamin, B. Y. Abdulkhair and A. O. Elzupir, *Sci Rep*, 2019, **9**, 10.
367. I. Mustafa, I. Lopez, H. Younes, R. A. Susantyoko, R. Abu Al-Rub and S. Almheiri, *Electrochim. Acta*, 2017, **230**, 222-235.
368. L. Y. Cao, Y. S. Liu, J. Wang, Y. Pan, Y. H. Zhang, N. Wang and J. Chen, *Nanomaterials*, 2020, **10**, 16.
369. S. Sakurai, F. Kamada, D. N. Futaba, M. Yumura and K. Hata, *Nanoscale Res. Lett.*, 2013, **8**, 7.

370. B. Krause, I. Konidakis, M. Arjmand, U. Sundararaj, R. Fuge, M. Liebscher, S. Hampel, M. Klaus, E. Serpetzoglou, E. Stratakis and P. Potschke, *J. Compos. Sci.*, 2020, **4**, 17.
371. D. V. Pankratov, Y. S. Zeifman, O. V. Morozova, G. P. Shumakovich, I. S. Vasil'eva, S. Shleev, V. O. Popov and A. I. Yaropolov, *Electroanalysis*, 2013, **25**, 1143-1149.
372. K. Rajavel, M. Lalitha, J. K. Radhakrishnan, L. Senthilkumar and R. T. R. Kumar, *ACS Appl. Mater. Interfaces*, 2015, **7**, 23857-23865.
373. Y. Y. Wang, W. J. Sun, K. Dai, D. X. Yan and Z. M. Li, *Compos. Sci. Technol.*, 2021, **212**, 8.
374. J. Liu, Y. Zhang, M. I. Ionescu, R. Y. Li and X. L. Sun, *Appl. Surf. Sci.*, 2011, **257**, 7837-7844.
375. C. Ma, P. F. Hou, X. P. Wang, Z. Wang, W. T. Li and P. Kang, *Appl. Catal. B-Environ.*, 2019, **250**, 347-354.
376. X. L. Wang, Q. Li, H. Y. Pan, Y. Lin, Y. J. Ke, H. Y. Sheng, M. T. Swihart and G. Wu, *Nanoscale*, 2015, **7**, 20290-20298.
377. K. Chizari, A. Vena, L. Laureritius and U. Sundararaj, *Carbon*, 2014, **68**, 369-379.
378. P. Q. Velasco, V. Karde, Y. Ito, J. Y. Y. Heng, K. Porfyrakis and N. Grobert, *Carbon Trend.*, 2022, **6**, 8.
379. I. M. Patil, M. Lokanathan, B. Ganesan, A. Swami and B. Kakade, *Chem.-Eur. J.*, 2017, **23**, 676-683.

Appendices

Appendix – List of Abbreviations

AACVD – Aerosol Assisted Chemical Vapour Deposition

BCN – Borocarbonitride

BCN-NT – Borocarbonitride Multiwalled Nanotubes

BET – Brunauer-Emmett-Teller

BJH – Barrett-Joyner-Halenda

BN – Boron Nitride

C-Hex - Cyclohexane

CNT – Carbon Nanotube

CVD – Chemical Vapour Deposition

EDX – Energy Dispersive X-ray Analysis

EPD – Electrophoretic Deposition

FeO_xNP – Iron Oxide Nanoparticles

IO - Iron Oxide

IPA – Iso-propanol

TGA – Thermogravimetric Analysis

MW – Multiwalled

N-CNT – Nitrogen Doped Multiwalled Carbon Nanotubes

NP – Nanoparticle

NT – Nanotube

SEM – Scanning Electron Microscopy

SESP – Surface Energy Solubility Parameter

SW – Single Walled

TEM – Transmission Electron Microscopy

Tol - Toluene

UV-Vis – Ultraviolet Visible

XPS – X-ray Photoelectron Spectroscopy

XRD – X-ray Diffraction

Appendix – Supplementary Information

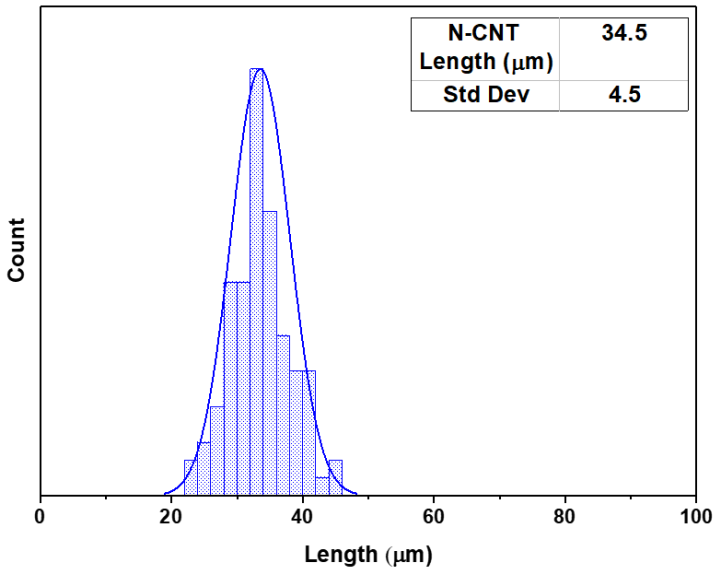


Figure S1 – Size distribution measured for the length of the as-synthesised N-CNTs utilised throughout this thesis.

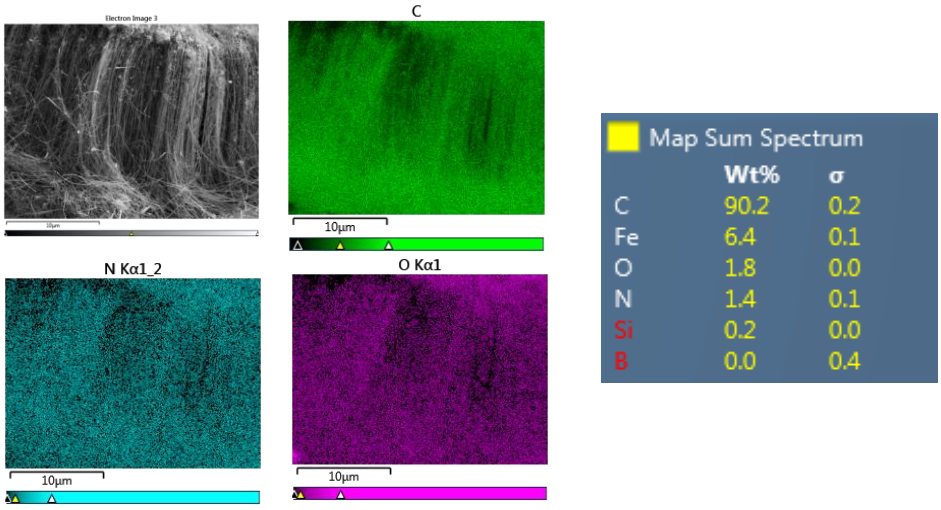


Figure S2 - SEM micrograph (a) and the respective elemental maps for carbon (b), nitrogen (c) and oxygen (d) recorded for the as-synthesised N-CNT prior to boron doping, along with the corresponding mini-quant table. This highlights the uniform distribution of nitrogen dopants across the precursor material.

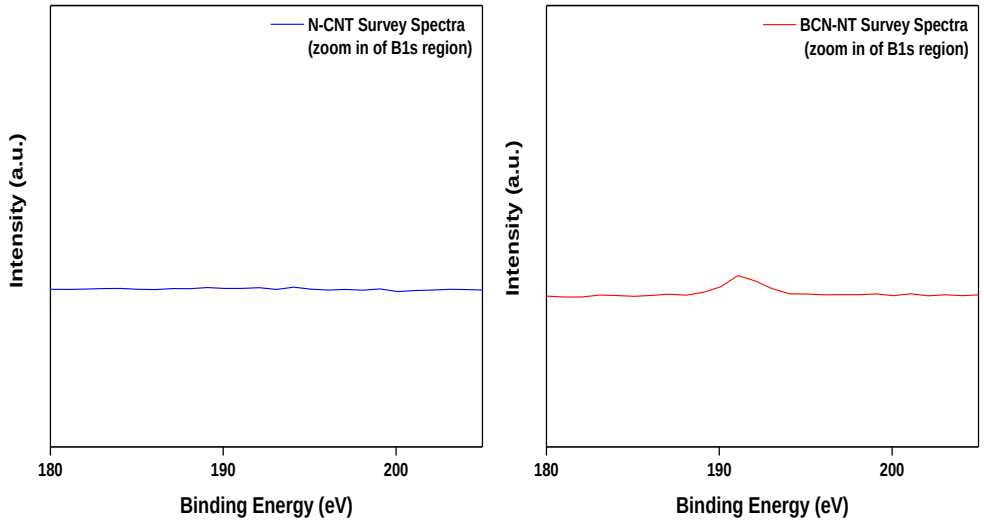


Figure S3 – A figure highlighting a magnified region of interest on the survey spectra for the N-CNTs and BCN-NTs which highlights the incorporation of boron into the nanotube sample.

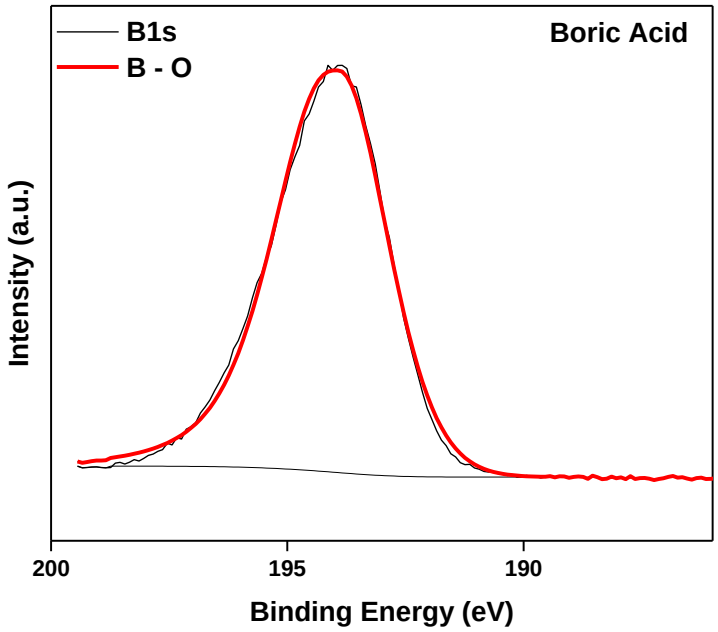


Figure S4 – B1s spectra recorded for boric acid highlights a significant shift towards higher binding energies when compared to those recorded for the boron dopant incorporated within the BCN-NTs.

Table S1 – A table summarising the elemental composition of BCN-NTs, prepared via standard conditions, in comparison to the N-CNT precursor utilised for the synthesis.

Elemental Composition *via* XPS		
Component	**N-CNT**	**BCN-NT**
C	91.3	86.6
N	3.0	3.5
B	-	3.4
O	4.9	5.4
Residual Material from Synthesis (FeO_x/Quartz/PTFE)	0.8	1.1

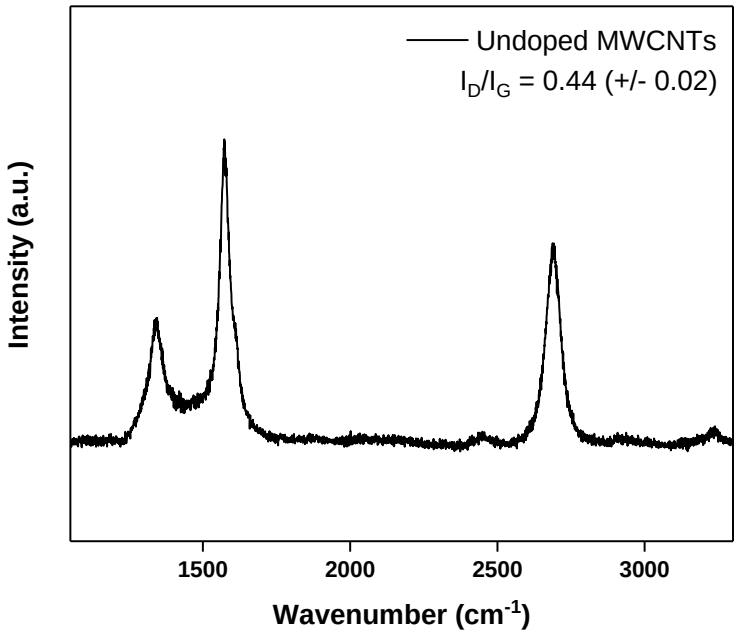


Figure S5 – Raman spectrum recorded for undoped MWCNTs highlighting the difference in defect density when compared to the doped nanotubes produced and utilised in this thesis.

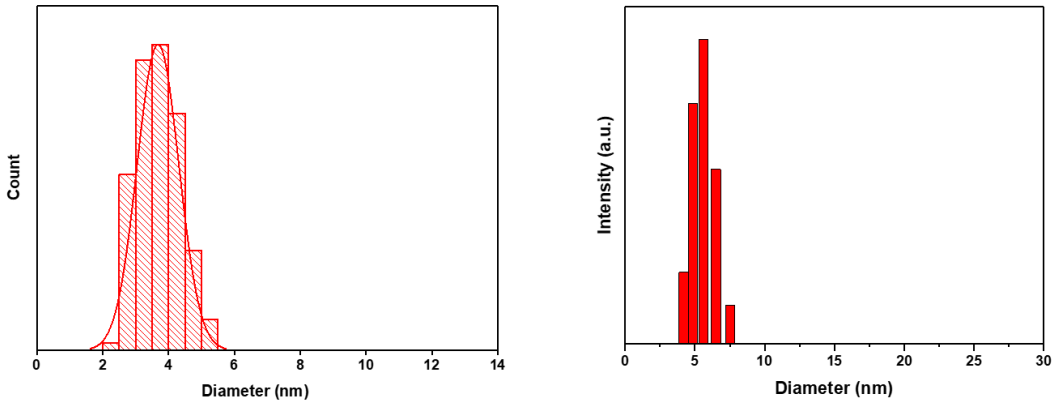


Figure S6 – Diameter distributions according to TEM (a) and DLS (b) analysis for FeO_xNPs produced using Method 2.

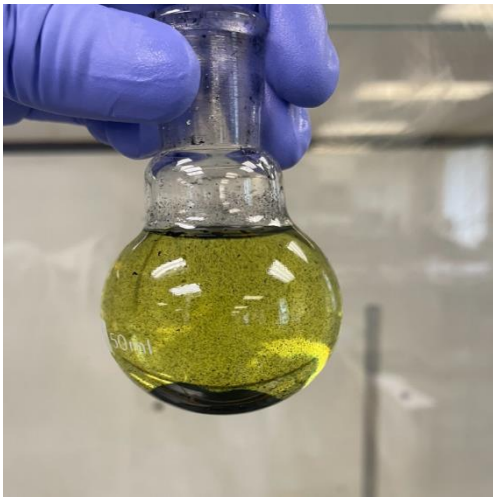


Figure S7 – Supernatant after HCl treatment to remove residual catalyst from sample.

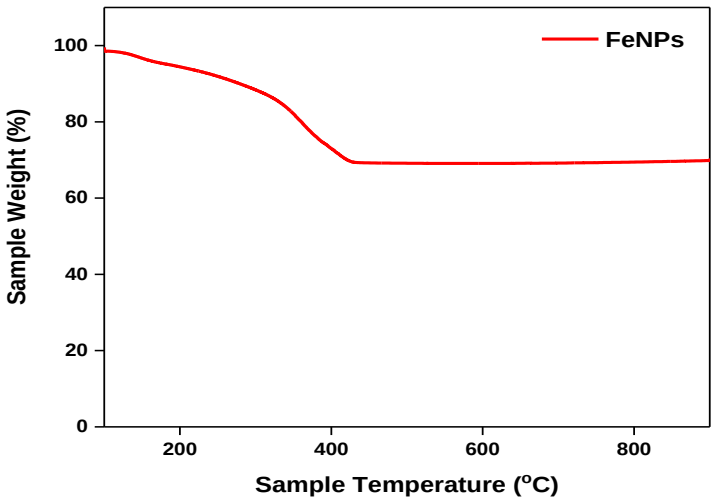


Figure S8 – TGA profile recorded for FeO_xNPs in the absence of nanotubes. This highlights the large residual mass remaining after oxidation which allows us to deduce the nanoparticle loading achieved during functionalisation.

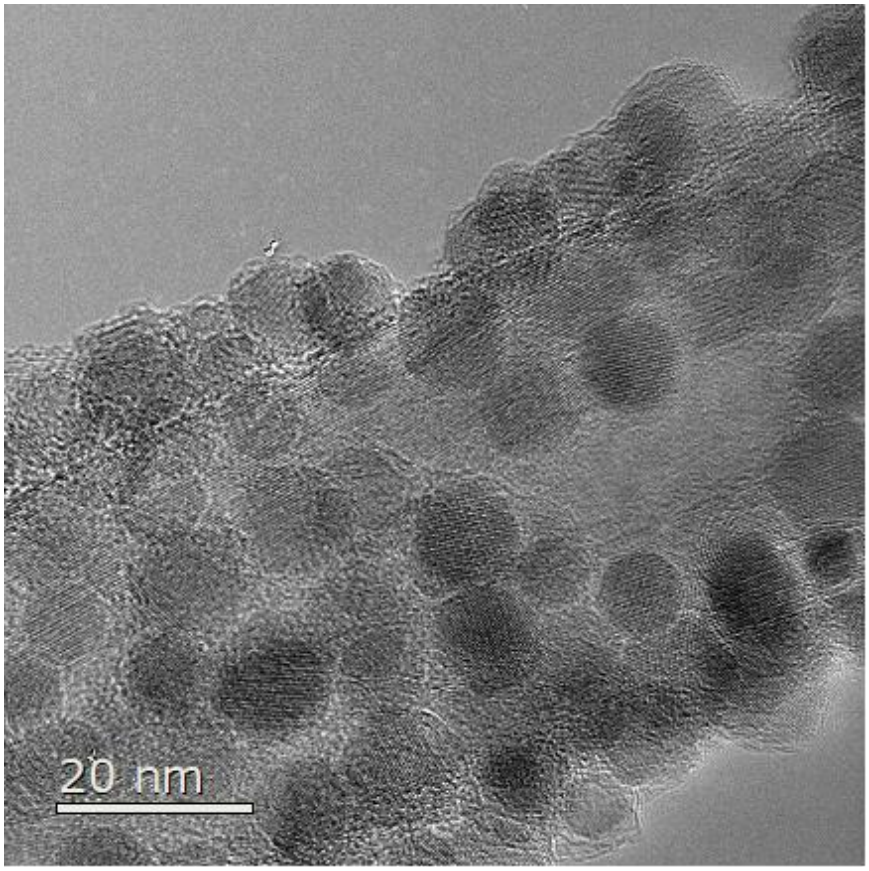


Figure S9 - High magnification TEM micrograph obtained for the BCN-NT-FeO_xNP hybrids (produced in cyclohexane) highlighting the crystalline nature of the FeO_xNPs attached to the nanotubes.

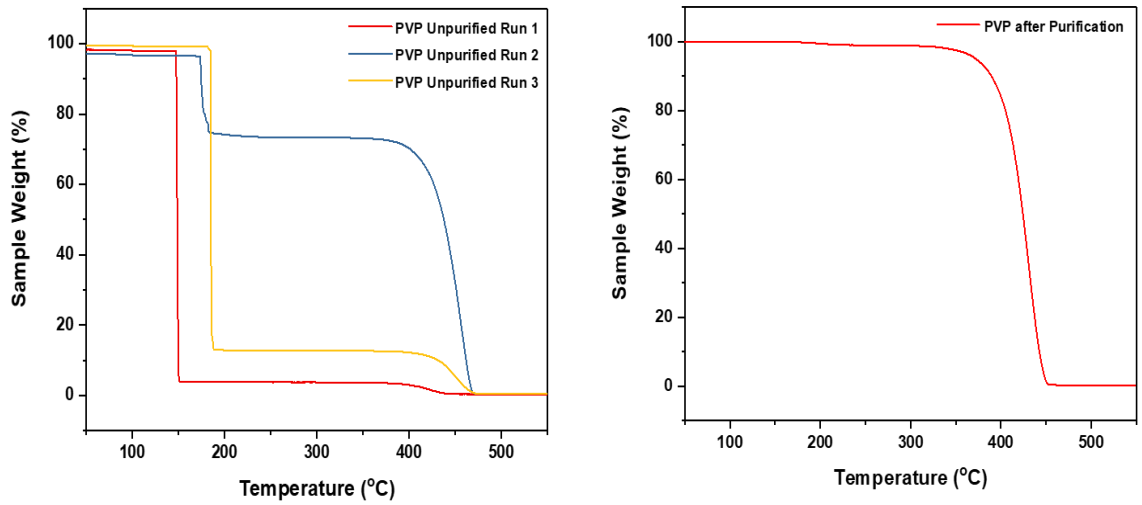


Figure S10 - TGA profiles of the polyvinylpyridine used throughout this study before (a) and after purification (b). The profiles reveal that the purity of the sample was inconsistent due to 'trapped' solvent. This consistency was improved after the removal of the 'trapped' solvent, as highlighted by the smooth TGA curve.

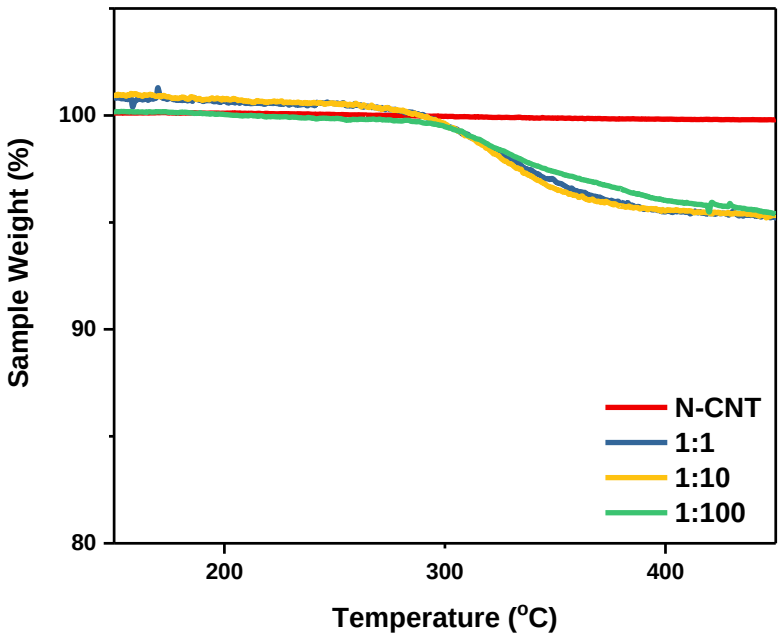


Figure S11: TGA profiles recorded in N_2 for N-CNT/PVP hybrids prepared under various stoichiometries of nanotube: polymer. From these profiles we were able to deduce the level of polymer loading achieved on the nanotubes prior to functionalisation.

Table S2: Value used for the calculation of Hansen distances. Hansen solubility parameters for the solvents were obtained from reference 276 and surface tensions from 277. Values for CNTs were obtained from reference 114.

Material	δ_D ($MPa^{0.5}$)	δ_P ($MPa^{0.5}$)	δ_H ($MPa^{0.5}$)	γ (mJ/m^2)	∂_D ($mJ^{0.5}/m$)	∂_P ($mJ^{0.5}/m$)	∂_H ($mJ^{0.5}/m$)
Cyclohexane	16.80	0.00	0.20	24.65	7.30	0.00	0.07
Tetrahydrofuran	16.80	5.70	8.00	26.65	6.80	1.80	2.60
Toluene	18.00	1.40	2.00	27.93	7.50	0.50	0.70
Iso-Propanol	15.80	6.10	16.4	20.92	5.31	1.63	4.39
Ethanol	15.80	8.80	19.40	21.99	4.89	2.16	4.77
Water	15.50	16.00	42.30	72.71	4.00	4.13	10.91
CNTs	20.50	6.70	7.20	-	10.20	2.60	2.80

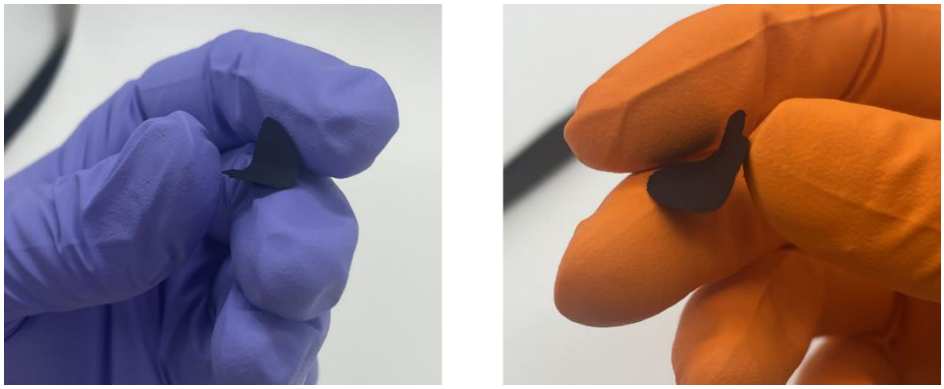


Figure S12 – Optical images highlighting the flexibility and mechanical manipulability of the as-produced BCN-NT buckypapers. These could be readily handled and returned to their original shape.

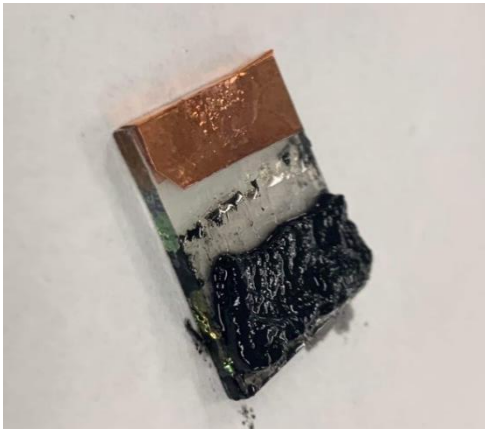


Figure S13: An image showing a wet-deposit after electrophoretic deposition. These deposits collapsed on drying to form films with varying degrees of thickness.

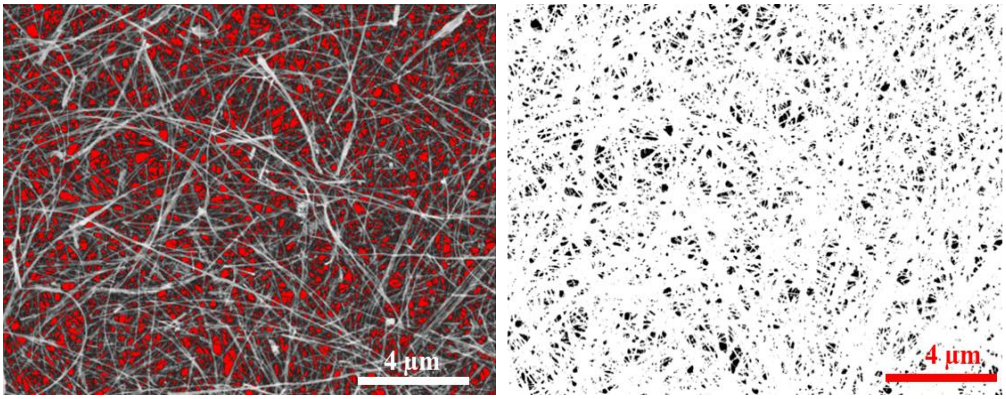


Figure S14 – Demonstration of the thresholding applied to SEM micrographs, emphasising the buckypaper pores used for Feret diameter measurements.

“There’s plenty of room at the bottom”
- Richard Feynman